Development of First Principles Paramagnetic NMR Methodologies to Probe the Complex Local Structural Properties of Li-ion Battery Materials

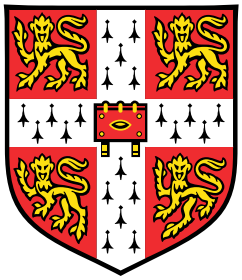

Roberta Pigliapochi

Department of Chemistry
University of Cambridge

This dissertation is submitted for the degree of
Doctor of Philosophy

December 2017

A Lussi

Declaration

I hereby declare that except where specific reference is made to the work of others, the contents of this dissertation are original and have not been submitted in whole or in part for consideration for any other degree or qualification in this, or any other University. This dissertation is the result of my own work and contains nothing which is the outcome of work done in collaboration with others, except as specified in the text. This dissertation contains less than 60.000 words excluding table of contents, figure captions, bibliography and acknowledgments.

Roberta Pigliapochi
December 2017

List of Publications

Chapter 3 contains material from this publication:
Meng, W.; **Pigliapochi, R.**; Bayley, P. M.; Pecher, O.; Gaultois, M. W.; Seymour, I. D.; Liang, H.-P.; Xu, W.; Wiaderek, K. M.; Chapman, K. W.; Grey, C. P. Unraveling the Complex Delithiation and Lithiation Mechanisms of the High Capacity Cathode Material V_6O_{13}, *Chemistry of Materials*, **2017**, 29, 5513

Chapter 4 contains material from this publication:
Pigliapochi, R.; Seymour, I. D.; Merlet, C.; Pell, A. J.; Murphy, D.; Schmid, S.; Grey, C. P. Structural characterization of the Li-ion battery cathode materials $LiTi_xMn_{2-x}O_4$ ($0.2 \leq x \leq 1.5$): A combined experimental ^{7}Li NMR and first-principles study, *Chemistry of Materials*, **2018**, 30, 817

Chapter 5 contains material from this publication:
Pigliapochi, R.; Pell, A. J.; Seymour, I. D.; Ceresoli, D.; Kaupp, M.; Grey, C. P. DFT investigation of the effect of spin-orbit coupling on the NMR shifts in paramagnetic solids, *Physical Review B*, **2017**, 95, 054412

Abstract

Development of First Principles Paramagnetic NMR Methodologies to Probe the Complex Local Structural Properties of Li-ion Battery Materials

Pigliapochi Roberta

NMR spectroscopy of paramagnetic solids provides detailed information about the local configuration and the chemical environment of the NMR observed center, as well as about the structural, magnetic and electronic properties of the coordianted paramagnetic centres. In the case of complex paramagnetic solids such as cathode materials for (rechargeable) batteries, NMR represents an invaluable tool to provide insight into the structural and electronic properties of the systems, which are at the base of the electrochemical performance of these materials. However, the paramagnetism makes the interpretation of the NMR data very challenging. This is primarily due to the interactions of the unpaired electrons with the NMR observed nucleus, and the rationalization of the NMR spectra often requires the aid of reliable theoretical and computational methods.

Often the dominant interaction contributing to the measured isotropic shifts in paramagnetic systems is the hyperfine interaction between the unpaired electrons and the observed nucleus. It results from the transfer of unpaired electrons from the paramagnetic centre(s) to the NMR observed site. In systems such as the cathode materials studied here, in which the paramagnetic ions are a major constituent of the lattice, the multitude of different local environments results in a complex distribution of resonances.

The complex lithiation mechanism upon electrochemical cycling in the $Li_xV_6O_{13}$ cathode material is analysed. A methodical investigation of the configurational stability from first principles gives insight into the preferred site configurations. The combination of experimental ^{7}Li NMR spectra and hyperfine shift DFT calculations of the identified stable Li environments aids the understanding of the complex lithiation mechanism of this material.

The series of $LiTi_xMn_{2-x}O_4$ cathode materials is studied, investigating the compositional (dis)order as a function of x throughout the series, using a combined first principle and experimental ^{7}Li NMR apporach. The ^{7}Li hyperfine shifts calculated with DFT

for a variety of Li environments are combined in a lattice model, which simulates the ^{7}Li NMR spectra for different Li/Ti/Mn configurations. The comparison between the calculated and the experimental shifts enables the assignement of the isotropic regions of the experimental ^{7}Li NMR spectra, helping to rationalize the complex cation ordering as a function of Mn/Ti content in the series.

For paramagnetic centres with an unquenched orbital component of the electron magnetic moment(s), the spin-orbit coupling effects also contribute to the paramagnetic NMR shift and shift anisotropy. A first principles model is derived, which describes how spin-orbit coupling and the single-ion g-tensor are defined and calculated in periodic paramagnetic solids, and how they can be coupled with the hyperfine interaction to model their effects on the NMR spectrum. The method is applied to a series of olivine-type $LiTMPO_4$ cathode materials (with TM = Mn, Fe, Co, and Ni) and the respective ^{7}Li and ^{31}P NMR spectra are simulated and compared with the experiments.

The other paramagnetic effect considered in this thesis involves the bulk magnetic susceptibility (BMS) shift, which is particularly important for paramagnetic single crystals and solids of complex shape. A method to analytically calculate the demagnetising field and the BMS shift in crystals of different shapes is derived, and it is applied to a series of $LiFePO_4$ single crystals for which the ^{7}Li MAS NMR spectra are also measured experimentally. The study shows a large variation in Li shift between the crystals of different shapes, indicating that the macroscopic shape-dependent BMS shift can indeed be a significant contribution to the NMR shifts or paramagnetic solids.

Acknowledgements

I am deeply grateful to my supervisor, Prof. Clare Grey, for her guidance and encouragement, for being such an inspiring scientist of great integrity, and for bearing with my Italian temper. I would also like to thank Andrew Pell for his teachings and kindness, and Ieuan Seymour for always being there to help, scientifically as much as personally.

I would like to thank the entire Grey Group and the very unique Team Theory for the friendly, dedicated and collaborative environment. A special thanks to Andy, Ieuan, David, Jae, Erlendur and Kent for kindly proof-reading parts of this Thesis. I would like to thank also Céline Merlet, Michael Gaultois, Pieter Magusin, Raphaële Clément, Davide Ceresoli, Liam O'Brien, Catherine Pitt and Sharon Connor for their help and contribution.

My greatest gratitude goes to Mamma, Babbo, Susi and the rest of my family, for their unconditionate love. I would like to thank all the nice people and dear friends that I have met everywhere I have lived, for always making me feel welcome and included. I am very thankful to the friends here in the U.K., particularly Rossana, Danila, Emma, Vess, Rod and Olli, for the great time together, and to my lifetime friends back home, particularly Giulia, Francesca, Giulia, Giovanni, Giuseppe and Lorenz, for helping me stop making sense at times, and for never letting me grow apart. A sweet special thanks to Luca for being there for us every day, and for making this journey sparkle.

Finally, I would like to thank the People Programme (Marie Curie Actions) of the European Union's Seventh Framework Programme for the generous funding.

List of Abbreviations

AU ..... Atomic Units

$\boldsymbol{B_0}$ ..... External Magnetic Field

BS–I ..... Basis Set One (Contracted)

BS–II ..... Basis Set Two (Extended)

BZ ..... Brillouin zone

CSA ..... Chemical Shielding Anisotropy

DFT ..... Density Functional Theory

e-n ..... Electron Nuclear

EFG ..... Electric Field Gradient

EPR ..... Electron Paramagnetic Resonance

ESR ..... Electron Spin Resonance

FC ..... Fermi Contact

FID ..... Free Induction Decay

GGA ..... Generalised Gradient Approximation

GTO ..... Gaussian Type Orbitals

HF ..... Hartree-Fock

HYB20 ..... Conventional B3LYP functional with 20% Hartree-Fock exchange

HYB35 ..... Modified B3LYP functional with 35% Hartree-Fock exchange

KS ..... Kohn-Sham

LAPW ..... Linear Augmented Plane Wave

LCAO ..... Linear Combination of Atomic Orbitals

LDA ..... Local Density Approximation

LIB ..... Lithium Ion Battery

LSDA ..... Local Spin Density Approximation

MAS ..... Magic-Angle Spinning

MF ..... Mean Field

NMR ..... Nuclear Magnetic Resonance

OC ..... Observed Centre

Oh ..... Octahedral Site

PAW ..... Projector Augmented Wave

PC ..... Pseudo Contact

pNMR ..... Paramagnetic Nuclear Magnetic Resonance

RF ..... Radio Frequency

SO ..... Spin-orbit

SPE ..... Single point energy

Td ..... Tetrahedral site

TM ..... Transition Metal

VASP ..... Vienna Ab Initio Simulation Package

XRD ..... X-ray Diffraction

Table of contents

List of figures

List of tables

Chapter 1

Introduction

1.1 Paramagnetic NMR

One important aspect of materials science and solid-state chemistry is the ability to modify the structure of a system in order to optimize specific properties of the materials, therefore also to understand the structure–property–function relationships in the solid state. Long-range structural information is typically obtained from characterization techniques based on Bragg diffraction. However, many properties of solids result from the variation of long-range periodicity, from local atomic-scale structural disorder and from compositional disorder arising from the non-regular distribution of two or more atomic species in a crystalline lattice. In energy storage materials and battery devices, the changes on electrochemical cycling to both the long-range and local structure of the electrodes in a battery can have profound effects on the long term cycling performance. A full understanding of the the intrinsic mechanisms of electron transport and of charge/discharge processes in the device requires also an analytical tool capable of studying the structure of the solids at the atomic level [1].

Solid-state nuclear magnetic resonance (NMR) spectroscopy is an essential characterization method to probe the local environments in crystalline as well as disordered solids. NMR enables us to obtain information about the local structure and bonding around particular atomic species, and it allows also the investigation of dynamical processes occurring in the solid state [2–5]. The wealth of information obtainable from an NMR spectrum is often the result of anisotropic interactions that affect the nuclear spins. In the case of liquid samples, despite the spins are present over a distribution of orientations, the rapid molecular tumblings cancel out the orientation dependence of the nuclear interactions. As a result, with solution NMR we only measure the orientation independent (isotropic) part of the interactions. The resulting spectra are typically

of high-resolution, from which it is possible to determine detailed information on the chemical bonding of the molecules under study [6]. Solid samples, however, do not benefit from the fast molecular motion as much as liquids. Solid-state NMR is hence also sensitive to the orientation dependent (anisotropic) interactions, which contain unique spatial and dynamic information. The measurement is nonetheless challenging, as these same anisotropic interactions give rise to broad lineshapes in the NMR spectra, which are therefore difficult to analyse [7]. The acquisition and the interpretation of solid-state NMR spectra is made even more challenging in the case of paramagnetic solids. In this Thesis, a paramagnetic system is intended as a molecule or material that contains one or more *paramagnetic* centres (atoms or ions) possessing at least one unpaired electron. This is commonly the case for solids used in energy storage materials, at least at some point in the electrochemical cycle. Although typically the nuclear spin studied with NMR is not itself a paramagnetic centre, the spectrum of the observed nucleus is significantly influenced by the interaction with neighbouring paramagentic site(s). The hyperfine interaction between the unpaired electrons and the observed nucleus is the origin of the paramagnetic shift, the shift anisotropy, as well as other additional sources of shift and broadening such as the bulk magnetic susceptibility effects and the paramagnetic relaxation enhancement [8]. The NMR spectrum of a nuclear species interacting with paramagnetic centre(s) yields information regarding the bonding between these sites, their spatial arrangement, the orbitals involved in the transfer of spin density, the oxidation state of the paramagnetic centres and the electronic and magnetic properties of the compound [9–14]. The information provided by the NMR spectrum of a paramagnetic solid is nonetheless often challenging to interpret. This difficulty arises from the fact that several different processes all contribute to the same features of the spectrum, i.e. the isotropic shift and the shift anisotropy, and it is often complicated to untangle the various contributions [8, 15–18].

1.1.1 Paramagnetic Shift and Shift Anisotropy

The theoretical description of paramagnetic NMR was initiated in 1958 by the work of McConnell on paramagnetic systems containing *d*-block transition metal ions [15, 16]. The isotropic shift observed in open-shell systems was related to the isotropic hyperfine interaction A between the unpaired electron spin and the NMR-observed nuclear spin, devided into two contributions: *i*) the Fermi contact component, due to the through-bond transfer of unpaired spin density onto the nuclear position of the observed site, *ii*) and, in the presence of spin orbit-coupling, the pseudo-contact component, due to the through-space dipolar coupling between the nuclear spin and the unpaired electron spin

moments [15, 16]. The successive work of Kurland and McGravey on transition metal complexes included a more complex description of the magnetic properties [17], whereas the contribution of Bleaney extended the formalism to systems containing lanthanide ions [19]. A modernised quantum-mechanical description of the various isotropic and anisotropic interactions occurring in paramagnetic systems had to wait almost 50 years until Moon and Patchkovskii presented a systematic theory for metal ions with a single unpaired electron, known as the doublet theory [20]. The theory was later extended by Pennanen and Vaara *et al.* to systems with arbitrary spin state and small spin-orbit couplings [21, 22]. In this modern formalism, the paramagnetic shielding tensor is defined in terms of the hyperfine interaction *via* the A tensor, and of the spin-orbit coupling effects *via* the g-tensor and the zero-field splitting $\boldsymbol{D}$ tensor. The formalism has also been extended by Soncini and van de Heuvel to any system with arbitrary spin-orbit coupling strength, although still experimentally untested [23–25].

1.1.2 Bulk Magnetic Susceptibility Effects

The effects described so far are local atomic-scale interactions between the paramagnetic centres and the observed nuclear spin. Macroscopically, the bulk magnetic properties of the system also affect the NMR spectrum [26, 27]. The bulk magnetic susceptibility (BMS) has its origin in the dipolar coupling between nuclear and unpaired electron magnetic moments. Depending on the bulk magnetic properties of the material, when the sample is placed in a magnetic field, a demagnetizing field is induced, that is proportional to the magnetic susceptibility and that either opposes or adds to the static external field [28]. Depending on the shape of the crystallite/particle, as well as the shape of the sample container and the symmetry of the magnetic susceptibility tensor, the demagnetizing field can contribute both to the shift and the line-broadening of the NMR spectrum. First presented by VanderHart *et al.* [29] and Alla and Lippmaa [30], the description of the BMS effects on the broadening was later extended in the work of Grey *et al.* on lanthanide stannates to include also the influence on the linewidth and spinning sideband intesities [31]. Later, Schwerk *et al.* [32] and Kubo *et al.* [26] presented a theoretical derivation of the isotropic and anisotropic BMS effects on the NMR spectrum of homogeneous paramagnetic powders. Dickinson *et al.* [33] extended the model based on classical electrostatics to calculate the demagnetizing fields of bulk samples, and the corresponding effects on the NMR spectrum of inhomogeneous powders.

1.2 Paramagnetic NMR Applied to Li–ion Battery Cathode Materials

Lithium intercalation or insertion materials have been extensively studied over the past few decades to meet the energy storage needs of increasingly widespread portable electronic devices [34]. The major challenges that are constantly faced in the development of rechargeable Li–ion batteries are associated with the cost and toxicity of the active materials, as well as the safety, the long term performance, the stability and the satisfactory charge storage capacity of the operating device [35].

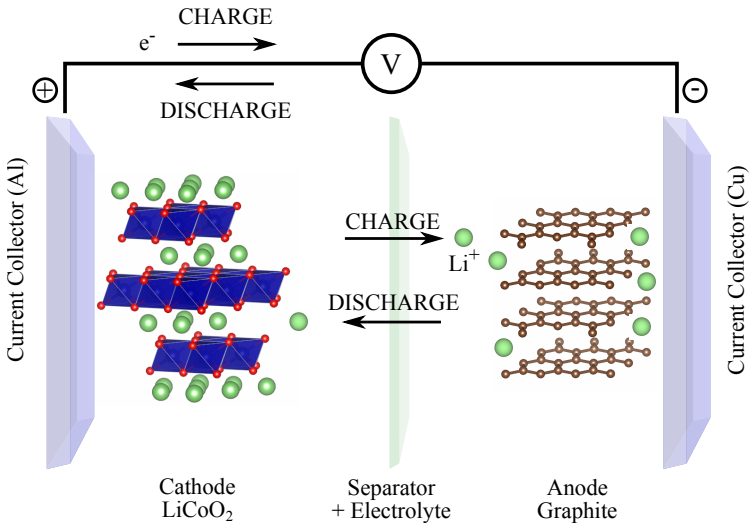

Fig. 1.1 Schematic representation of secondary Li–ion battery with a $LiCoO_2$ cathode and a graphite anode. Adapted from Ref. [36].

The basic architecture of a (rechargeable) Li–ion battery cell, schematised in Figure 1.1, consists of three main components: a cathode (positive electrode), an electrolyte, and an anode (negative electrode). The operation of the rechargeable Li–ion battery relies on the reversible intercalation and deintercalation of Li ions in and out of the structures of the electrodes. On charge driven by an external potential, the Li ions deintercalate from the cathode, flow *via* the electrolyte medium and intercalate in the anode, with the concurrent oxidation of the cathode and reduction of the anode. On discharge, the same process occurs in the opposite direction as the battery releases its stored energy [36]. The first rechargeable Li–ion battery commercialized by SONY in 1991 consisted of layered $LiCoO_2$ as cathode and of graphite as anode [37]. Despite this set-up still being the most commonly-used rechargeable battery to date, particularly for light portable electronic devices such as laptops and mobile phones, $LiCoO_2$ presents limitations related to its low

charge/discharge rates and to the low abundance (hence high cost), limited geographical distribution and high toxicity of cobalt. A large variety of alternative cathode materials with different redox active $3d$ transition metal (TM) ions have been investigated over the years, such as layered $LiTMO_2$ (TM = Mn, Ni) [38–42], spinel $LiTM_2O_4$ (TM = Mn, Ni) [43] and olivine $LiTMPO_4$ (TM = Mn, Fe) [44–46].

In the design and the understanding of the electrochemical performance and stability of the battery and its electrodes, solid-state NMR spectroscopy represents an invaluable tool to probe the local ordering of the ions directly involved in the electrochemical process, such as Li, to distinguish between insulating and conducting states, to identify the oxidation states of the metal ions involved in the redox reactions and to investigate the changes in the local structure due to the flow of ions and electrons [47]. Extensive NMR studies, primarily based on the analysis of the hyperfine isotropic and dipolar interactions, have been performed on a variety of cathode materials [48]. The rationalization of the NMR spectra of extended paramagnetic systems, such as the cathode materials in question, is based on the fact that the isotropic shift is often dominated by the hyperfine Fermi contact interaction. The resulting Fermi contact shift is proportional to the unpaired spin density transfered from the paramagnetic centre(s) towards the nearby NMR observed site. Crucially, it is an additive quantity that can be decomposed into a sum of contributions of unpaired spin density transferred from each TM ion onto the observed nucleus. A range of Li–ion paramagnetic systems have been studied with $^{6/7}$Li magic-angle spinning (MAS) NMR over the last few decades, containing transition metal ions ranging from d^1 to d^8 electronic configurations. This enabled the rationalization of the different shift mechanisms resulting from the interaction of the Li spins with the unpaired electrons in the t_{2g} and e_g orbitals of the TM centres. The investigation of cathode materials with $^{6/7}$Li MAS NMR has been reviewed by Grey and Dupré [48] and Grey and Lee [49]. A few examples will be presented herein, intended to outline how NMR can be applied and analysed for cathode materials with complex structural features.

The spinel $LiMn_2O_4$ system has been extensively studied with $^{6/7}$Li MAS NMR, as a function of the synthesis temperature as well as of the electrochemical cycling [50–53]. The structure of $LiMn_2O_4$ nominally contains only one crystallographic Li site with tetrahedral coordination. The Mn^{3+} (d^4) and Mn^{4+} (d^3) ions are present at equal ratios, however, due to the fast electron hopping, they effectively interact with the Li spins as an average $Mn^{3.5+}$, hence only one Li isotropic shift would be expected [50]. Instead, a number of peaks are present in the $^{6/7}$Li NMR spectrum, indicating the presence of a variety of Li environments. The ^{7}Li spectra of the $LiMn_2O_4$ samples synthesised at

low temperatures (∼550–600 °C) show the peak at ∼520 ppm, characteristic of the aforementioned Li tetrahedral environment in the nominal $LiMn_2O_4$ spinel structure. Additionally, a weak peak at high resonance frequency (∼2300 ppm) [49] is detected, indicative of a Li ion in an octahedral environment. This suggests that excess Li is present in the structure ($Li_{1+y}Mn_{2-y}O_4$, with y being the Li excess fraction, in octahedral sites). For every Li^+ equivalent present in excess, five $Mn^{3.5+}$ ions are oxidised to Mn^{4+} ions to balance the charge. Additional peaks are in fact present in the spectra that result from Li ions in tetrahedral environments nearby Mn^{4+} ions [48]. This is important because Mn-based spinel cathodes with excess lithium are typically reported to show improved charge/discharge cycling behaviour [54, 55]. The ^{6}Li NMR spectra of the $LiMn_2O_4$ samples synthesised at high temperature (∼800–850 °C) instead show peaks at lower frequencies than the main spinel (∼520 ppm) resonance. These shifts are indicative of the presence of Li environments nearby Mn^{3+} ions, which result from the substitution of some Li with Mn^{2+} in the tetrahedral site (for every Mn^{2+} replacing a Li^+, two $Mn^{3.5+}$ ions are reduced to Mn^{3+}). This is not beneficial for the electrochemical performance of this cathode material, because Mn^{2+} ions at the surface of the particles are easily dissolved in the electrolyte, depleting the cathode of transition metal ions [43].

A limitating factor in the application of $LiMn_2O_4$ as a cathode material arises from the Jahn–Teller distortion of the octahedral environment of the Mn^{3+} ions, which, macroscopically, contributes to large changes in the cell volume [56]. This effect becomes particularly disruptive for the mechanical stability of the cathode when the average Mn oxidation state drops below 3.5+ on discharge, contributing to the capacity fade [56, 57]. One approach to limit the effects of the Jahn–Teller distortion associated with the Mn^{3+} ions has been to partially substitute Mn for a dopant of lower oxidation state, and which does not take part in the redox process, such as Ni^{2+}, Zn^{2+}, or the excess Li^+ [49, 58, 59]. The effect of the dopant is to increase the average oxidation state of the remaining Mn ions above 3.5+. $^{6/7}$Li MAS NMR revealed however that the increase in the Mn oxidation state does not occur evenly throughout the phase. The induced oxidation to Mn^{4+} was found to predominantly occur for Mn ions nearby the dopants, while the bulk does not considerably benefit from this effect. This structural inhomogeneity has consequences on the cycling behaviour of the cathode, which, in the doped case, follows a two-phase mechanism in which the Li ions are first intercalated near the $Mn^{3.5+}$ sites, and subsequently next to the Mn^{4+} sites [60].

A breakthrough in the interpretation of the complex NMR spectra of extended paramagnetic cathode materials occurred with the application of first principles calculations. Carlier *et al.* carefully rationalized the different unpaired spin density transfer mecha-

nisms between the TM centre and the NMR observed site in terms of bonding geometries and orbital overlaps [14]. The interpretation of the hyperfine shift was presented in analogy with the Goodenough–Kanamori rules originally formulated to describe magnetic interactions between TM centres. The study was applied to model the Li NMR shift of layered $LiTMO_2$ systems (TM = Co, Cr, Mn, Fe, Ni). The computational density functional theory (DFT) approach was based on pseudopotential-based calculations that gave a qualitative interpretation of the Li hyperfine shifts by integrating the spin density over approximate Li ionic volumes [14]. Building upon this approach, Kim *et al.* performed Fermi contact shift calculations with DFT, implementing an all-electron approach in combination with hybrid exchange-correlation functionals[61]. In their work, an empirical magnetic model was derived, to include the effects of finite temperature in the hyperfine shifts calculated with DFT (hence nominally at 0 K). The study was applied to correlate the local structure of a series of Fe(III) phosphate-based cathode materials to the measured and calculated ^{7}Li and ^{31}P NMR shifts. The high accuracy of the shifts calculated following the method presented by Kim *et al.* paved the way to the clever computational strategy developed by Middlemiss *et al.* [62, 63]. In their approach, the total Fermi contact shift of a given nucleus was quantified separately for the contributions from each interacting TM centre *via* the so-called *spin flipping* approach. The method consists of performing an initial calculation of the hyperfine shift at a particular nuclear site, e.g. Li, with the magnetic moments of all the interacting paramagnetic TM centres aligned parallel to each other, i.e. ferromagnetically. This is followed by the simulation of the same system where the spin of one of the interacting TM ions is flipped, and the shift of the Li centre is recalculated for this ferrimagnetic alignment. Half the difference between the shift in the ferromagnetic state and the shift in the ferrimagnetic state corresponds to the Li(–O)–TM contribution to the overall Fermi contact shift of that Li site [63]. This relatively simple approach constituted a great step forward in the rationalization of the complex NMR spectra of cathodes, and it has since then been applied in combination with experimental NMR to study the local and electronic structure of complex systems with multiple TM species and oxidation states [62, 64, 65], as well as to rationalize the NMR spectra of less extensively studied and more problematic NMR-active nuclei such as ^{17}O [13], ^{23}Na [12] and ^{25}Mg [66] in the context of battery applications.

A comprehensive understanding of the structural and electronic processes taking place during electrochemical cycling also requires the ability to capture metastable or reactive phases. In order to be able to quickly monitor the different local structural changes as a function of capacity and potential, *in situ* NMR spectroscopy of whole

battery cells has been applied over the years to study the electrochemically-induced structural and electronic changes that occur during battery cycles [67, 68]. *In situ* NMR of such complex systems poses challenges on the experimental set-up, as well as on the interpretation of the NMR data. One difficulty arises from the need to separate the NMR resonances from the different components of the cell, which is made even more complicated by the fact that the spectra are aquired in static mode and hence suffer from severe broadening. Regarding the paramagnetic component of the cell, typically the cathode, this is often present in the battery used for the measurement as a thin film. The bulk magnetic susceptibility (BMS) effects in such paramagnetic samples induce a dependence of the shift and the linewidth on the orientation of the film with respect to the external magnetic field [68, 69]. Additionally, for a whole battery cell consisting of metallic, diamagnetic and paramagnetic parts, the BMS effects induced by the metallic and the paramagnetic components combine, and they affect the NMR response of the diamagnetic parts, making it very challenging to untangle the different contributions and to analyse the spectra. Recently, a study of the BMS effects on paramagnetic films has been presented, based on a model that considers electron-nuclear dipolar couplings within the point dipole approximation [27]. The approach was applied to optimize the orientation of the cell with respect to the NMR magnetic field, in order to minimise the BMS effects on the *in situ* ^{7}Li NMR spectra.

1.3 Motivation and Outline

This thesis aims to develop combined solid-state NMR and first principles modelling approaches to probe the local structure and the electronic properties of complex paramagnetic solids. The methods are applied to the study of a variety of Li–ion battery cathode materials.

Chapter 2 presents a brief introduction on solid-state NMR spectroscopy, a background of the quantum-mechanical theory of paramagnetic NMR and of the classical derivation of the bulk magnetic susceptibility effects, an overview of solid-state DFT calculations and a description of the application of DFT methods to calculate paramagnetic NMR properties.

Chapter 3 investigates the complex voltage profile and the local atomic and charge ordering upon electrochemical cycling of the high capacity $Li_xV_6O_{13}$ cathode material. Several phase transitions are observed during charge and discharge of this system, which are accompained by a significant rearrangement of the Li ions in the structure. A first principles methodology is performed to study the changes in the structure and in the

Li ion coordinations as a function x in the $Li_xV_6O_{13}$ series. The approach enables the identification of stable configurations and favourable Li sites throughout the composition series, by combining the computational results with experimental *in situ* XRD and ^{7}Li MAS NMR data.

Chapter 4 studies the effects of Ti doping in the compositional disorder of the $LiTi_xMn_{2-x}O_4$ series of cathode materials. Titanium doping in lithium manganese oxide spinels was shown to be beneficial for the structural stability of the potential Li-ion battery cathode materials, yet the Li/Ti/Mn distribution in $LiTi_xMn_{2-x}O_4$, pivotal for the electrochemical performance of the system, is not fully understood. A combined first principles and experimental ^{7}Li NMR methodology is presented, which investigates the changes in the local ordering of the multi-component paramagnetic solids by modelling the site-specific magnetic and Fermi contact interactions. The Li–O–Mn contributions to the ^{7}Li shifts are calculated from first principles and combined in a lattice model that simulates the NMR spectra of different site orderings. The simulated ^{7}Li NMR spectra are compared to the experimental data, and the variations in the local ordering of the Li/Mn/Ti ions in the series of structures is analysed.

Chapter 5 extends the description of the paramagnetic shielding tensor in periodic solids to include the effects of spin-orbit coupling. A first principles method is developed, which couples the hyperfine tensor with the g-tensor in periodic solids, allowing one to decompose the paramagnetic shielding into a sum of terms contributing to the NMR isotropic shift and shift anisotropy. The approach is applied to investigate the ^{7}Li and ^{31}P NMR spectra of a series of $LiTMPO_4$ cathode materials (TM = Mn, Fe, Co, Ni).

Chapter 6 treats the macroscopic effects of the bulk magnetic susceptibility on the ^{7}Li NMR shift of paramagnetic crystals. A method based on classical electrostatics is developed, which simulates the demagnetizing field in crystals modelled using the experimental dimensions and susceptibility tensors, and calculates the resulting BMS shift. The results are compared with the ^{7}Li shifts obtained from the MAS NMR spectra on a series of $LiFePO_4$ single crystals.

Chapter 7 presents the main conclusions of this work and suggests new research directions.

Chapter 2

Methodology

2.1 Principles of NMR Spectroscopy

Atomic nuclei possess an intrinsic spin, $\boldsymbol{I}$, which is defined by the nuclear spin quantum number, I. The nuclear spin is a quantised form of angular momentum that, for $I \geq 1/2$, gives rise to a non-zero nuclear magnetic moment, $\boldsymbol{\mu}_I$, of the form:

$$\boldsymbol{\mu}_I \;=\; \hbar\gamma_I \boldsymbol{I} \;=\; \mu_N g_I \boldsymbol{I} \tag{2.1}$$

where $\hbar$ is the reduced Planck constant, γ_I is the nucleus-dependent gyromagnetic ratio, μ_N is the nuclear magneton and g_I is the dimensionless nuclear g-factor. There exist $2I+1$ spin states, each described by the m_I magnetic quantum number ($m_I = -I, -I+1, ...+I$).

At thermal equilibrium and in the absence of any external magnetic field, the nuclear spin states (or nuclear energy levels) are degenerate. In nuclear magnetic resonance (NMR) spectroscopy, an external magnetic field B_0 along a certain direction (conventionally the z-direction) is applied, which interacts with the nuclear magnetic moment. Due to this so-called nuclear Zeeman interaction, the degeneracy of the manifold of the $2I+1$ states is removed, because different orientations of $\boldsymbol{\mu}_I$ with respect to B_0 will have different energies. The energy separation between consecutive m_I spin states for an isolated nucleus is proportional to the strength of the external field as well as to the size of the nuclear magnetic moment, as:

$$\Delta E \;=\; \hbar|\omega_0| \;=\; -\hbar\gamma_I B_0 \tag{2.2}$$

where ω_0 is the so-called called the Larmor frequency.

For a sample comprising a large number of individual nuclei, these thermally populate the Zeeman spin states according to a Boltzmann distribution. However, there will be a slight energetic preference for the nuclear spins to align parallel with B_0 than anti-parallel to it. This, on average over the entire collection of spins, corresponds to the formation of a bulk magnetization along the z-direction of the external field. Once the spins in an external magnetic field have reached their Boltzmann equilibrium, they need to be perturbed in some way in order to produce a measureable process associated with their return to equilibrium. Typically in NMR this is achieved *via* the application of a transverse radiofrequency (RF) pulse, generating a time-dependent magnetic field B_1 in an orientation different from B_0, and inducing a mixing of the Zeeman states. In a vector model, the effect of the RF pulse corresponds to tilting the bulk magnetization away from its equilibrium alignement along the z-axis. At the end of the RF pulse, the spins will start to re-orient to reach the Boltzmann equilibrium. This evolution of the excited spins as they return back to equilibrium corresponds to a precessional motion of the bulk magnetisation about the external magnetic field along the z-axis, at a precession frequency equal to the Larmor frequency defined earlier. This Larmor precession of the magnetization over time is measureable by the same RF coil because it induces an oscillating current detected as a free induction decay (FID), which is then Fourier transformed to obtain a spectrum comprising the Larmor frequency (or to separate the various Larmor frequencies characteristic of the multiple nuclear environments). The spectral data can be displayed in the frequency range (Hz), or in the more common chemical shift range (parts per million, ppm).

Internal interactions between the nuclear spin and the surrounding nuclear/electronic spins generate additional local perturbations to the experienced field, given by a range of contributions which are more or less significant depending on the specific system. Most commonly, these internal interactions can be summarised as: *i*) the chemical shift interaction between the nucleus and its surrounding electron shell, *ii*) the scalar (through-bond) and dipolar (through-space) coupling between two nuclear spins, *iii*) the quadrupolar interaction between the electric nuclear quadrupole moment (for $I > 1/2$) and the local electric field gradient generated by uneven charge distributions, and *iv*) the hyperfine interaction between the nuclear spin and the surrounding unpaired electrons. The final term, often dominating the NMR response of paramagnetic systems, is the major focus of this thesis, and will be discussed in detail in Section 2.3. The combination of the external B_0 field and the internal field due to the nuclear interactions with the surrounding nuclei or electrons modulates the energy separation between the nuclear spin states. Although the interaction of the nuclear spins with their environments is energetically

weak, it is responsible for the great power and versatility of NMR spectroscopy, which is to distinguish (resolution permitting) chemically or structurally different nuclear sites within the system under investigation.

The effective Hamiltonian describing the dominat interactions in an NMR epxeriment due to the external static B_0 field (nuclear Zeeman interaction, $\hat{H}_{IZ}$), the B_1 field generated by the RF pulse ($\hat{H}_{RF}$), and the collective internal interactions ($\hat{H}_{int}$) can be written as:

$$\hat{H}_{tot} = \hat{H}_{ext} + \hat{H}_{RF} + \hat{H}_{int} \tag{2.3}$$

2.2 Solid-state NMR Spectroscopy

The internal interactions described earlier and condensed in term $\hat{H}_{int}$ in equation 2.29 are typically described by anisotropic tensors. Consequently, their contributions to the NMR spectrum depend on the relative orientation of each characteristic tensor with respect to the external field. In liquids, despite the presence of a multitude of local environments or molecules with different orientations, rapid molecular tumbling effectively averages out the orientation dependence of the anisotropic tensors, resulting in a sharp isotropic peak in the NMR spectrum (Figure 2.1-a).

Solid-state powders, on the other hand, do not benefit from the fast molecular motion typical of the liquid state, and the often random distribution of molecular or particle orientations leads to the broad spectrum shown in Figure 2.1-b [7]. The anisotropic orientation dependence of the interactions in the H_{int} term in equation 2.29 is given by $3\cos^2\theta - 1$, with θ being the angle between the principal axis of the anisotropic tensor frame and the z-axis of the external B_0 field. This orientation dependence can be cleverly (at least partially) averaged out by spinning the sample about what is known as the magic angle, $\theta_{MA} = 54.74°$ (such that $3\cos^2\theta_{MA} - 1 = 0$) (Figure 2.1-c). If the spinning frequency is much greater than the size of the anisotropic interaction(s), a single resonance is observed in the NMR spectrum, at a frequency corresponding to the isotropic shift of the particular nuclear environment. Otherwise, if the spinning frequency is not fast enough, in addition to the isotropic shift, a manifold of resonances are observed, known as spinning sidebands and shown in Figure 2.1-d, that are separated from the isotropic peak by multiples of the spinning frequency.

Section 2.3 will describe how some of the internal interactions collected in the H_{int} term locally perturb the external magnetic field experienced by the NMR observed nucleus, effectively partially *shielding* (or *deshielding*) it from B_0. The effects of these local interactions can be modelled *via* a (chemical) shielding tensor, $\boldsymbol{\sigma}$, which will be

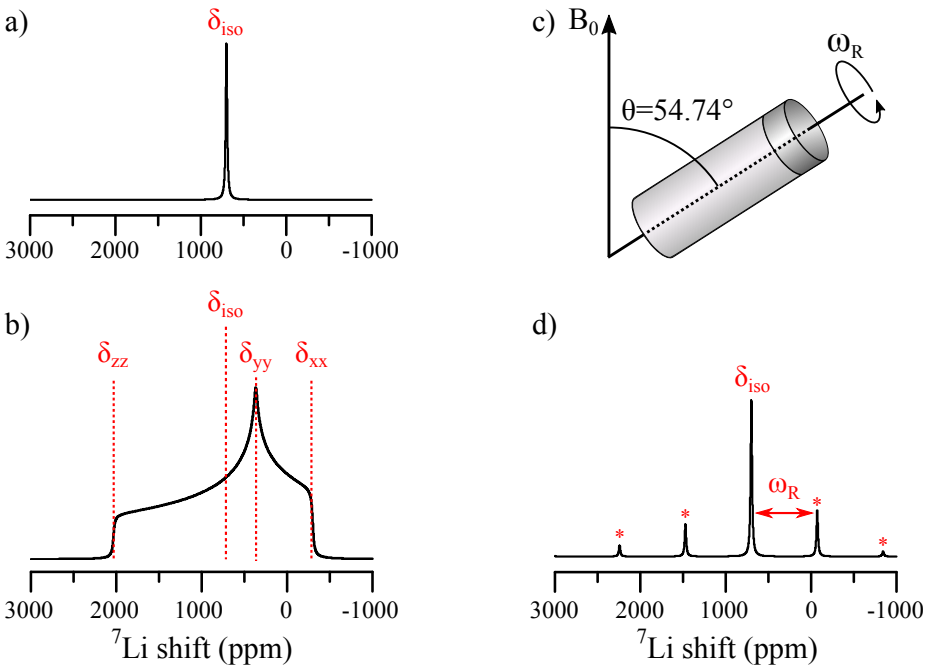

Fig. 2.1 Schematic diagrams of a) a solution state (or very fast MAS) ^{7}Li NMR spectrum, with isotropic shift $\delta_{\text{iso}} = 700$ ppm; b) a static solid-state NMR spectrum of a polycrystalline powder; c) the experimental setup in which the polycrystalline powder is rotated in a rotor at the magic angle $\theta = 54.74°$ with respect to the field B_0, at a rate ω_R; d) the NMR spectrum of a polycrystalline powder under MAS at a frequency ω_R. Adapted from Ref. [70].

defined in detail in Section 2.3.4. However, in experimental NMR, what is actually measured is the (chemical) shift tensor, $\boldsymbol{\delta}$, which is given by the difference between the shielding of a reference system and the shielding of the system under investigation. The isotropic component of the shift tensor, δ_{iso}, is equal to:

$$\delta_{\text{iso}} = \sigma_{\text{iso}}^{\text{ref}} - \sigma_{\text{iso}} \tag{2.4}$$

The shift tensor can be defined in terms of its principal components in the tensor's principal axis frame (denoted as $\tilde{\delta}_{ii}$), and the isotropic shift, the chemical shift anisotropy (CSA, $\Delta\delta$) and the asymmetry (η) are defined as:

$$\begin{aligned} \delta_{\text{iso}} &= \frac{\tilde{\delta}_{xx} + \tilde{\delta}_{yy} + \tilde{\delta}_{zz}}{3} \\ \Delta\delta &= \tilde{\delta}_{zz} - \tilde{\delta}_{\text{iso}} \\ \eta &= \frac{\tilde{\delta}_{yy} - \tilde{\delta}_{zz}}{\Delta\delta} \end{aligned} \tag{2.5}$$

using the convention: $|\tilde{\delta}_{zz} - \delta_{\text{iso}}| \geq |\tilde{\delta}_{xx} - \delta_{\text{iso}}| \geq |\tilde{\delta}_{yy} - \delta_{\text{iso}}|$ [71]. An example of a soli-state NMR spectrum showing the chemical shift components is presented in Figure 2.1-b.

2.3 Theory of Paramagnetic NMR

This section focuses on the quantum mechanical description of the internal interactions dominating the NMR response of paramagnetic systems, with a particular interest to solids in which the paramagnetic species is a major constituent of the lattice.

2.3.1 The Effective Spin Hamiltonian

Nuclear Zeeman Interaction

As introduced in the previous Section, the interaction between the nuclear spin and the external magnetic field is known as the nuclear Zeeman interaction, and the corresponding Hamiltonian takes the following form:

$$\hat{H}_{IZ} \;=\; -\hbar\gamma_I \boldsymbol{B}_0 \hat{\boldsymbol{I}} \;=\; \hbar\omega_0 \hat{\boldsymbol{I}} \;=\; \mu_N g_N \hat{\boldsymbol{I}} \tag{2.6}$$

where $\hat{\boldsymbol{I}}$ is the nuclear spin operator.

Although the nuclear Zeeman interaction accurately describes the effect of an external magnetic field on a nuclear spin, the Hamiltonian in equation 2.6 is strictly valid for an isolated nucleus. When the nucleus is part of an atom or a molecule, the motion of the surrounding electron shell induces an additional magnetic field that opposes the external $\boldsymbol{B}_0$, in other words *shielding* the nucleus from $\boldsymbol{B}_0$. This effect is included in the Hamiltonian *via* the so-called shielding tensor, $\boldsymbol{\sigma}$, and the resulting contribution takes the form $\hat{H}_{IC} = \hbar\gamma_I \boldsymbol{B}_0 \cdot \boldsymbol{\sigma} \cdot \hat{\boldsymbol{I}}$. The simple Hamiltonian in equation 2.6 is hence no longer exhaustive, and the following description has to be considered:

$$\hat{H}_I \;=\; \hat{H}_{IZ} + \hat{H}_{IC} \;=\; -\hbar\gamma_I \boldsymbol{B}_0 \cdot (\mathbf{1} - \boldsymbol{\sigma}) \cdot \hat{\boldsymbol{I}} \tag{2.7}$$

where **1** is the identity matrix.

The shielding tensor, $\boldsymbol{\sigma}$, consists of isotropic, symmetric anisotropic and antisymmetric anisotropic parts. In the absence of unpaired electrons, that is for the so-called diamagnetic systems, the chemical shielding was described by Ramsey to consist of the sum of the shielding from the electronic ground state, referred to as the *diamagnetic* term, and the shielding due to the mixing of the electronic ground and excited states, referred to as the *paramagnetic* term [72]. However, to avoid confusion, this Thesis will not adopt the terminology coined by Ramsay. Instead, the description of the shielding tensor will be extended to paramagnetic systems following the more recent distinction made by Pennanen and Vaara [21], which collects the two aforementioned contributions to the shielding in a cumulative orbital term named $\boldsymbol{\sigma}^{\text{orb}}$. This term is present in both dia- and paramagnetic systems. In the latter case, an additional shielding occurs, named $\boldsymbol{\sigma}^{s}$, which is due to the presence of unpaired electrons, and the total shielding tensor for paramagnetic systems can be expressed by the following sum:

$$\boldsymbol{\sigma} \;=\; \boldsymbol{\sigma}^{\text{orb}} \;+\; \boldsymbol{\sigma}^{s} \tag{2.8}$$

The orbital contribution to the shielding of paramagnetic solids, $\boldsymbol{\sigma}^{\text{orb}}$, is typically approximated to the shift measured for an analogous diamagnetic system [18]. The description and calculation of the paramagnetic $\boldsymbol{\sigma}^{s}$ term is the central focus of this thesis. The following Sections will introduce the interactions at its origin, and Section 2.3.5 will work through the effects of it on the NMR spectrum of a paramagnetic system.

Electron Zeeman Interaction

Analogous to the magnetic moment $\boldsymbol{\mu}_I$ associated to the nuclear spin $\boldsymbol{I}$ (equation 2.1), we can define the (unpaired) electron magnetic moment proportional to the electron spin $\boldsymbol{S}$, as:

$$\boldsymbol{\mu}_s \;=\; \hbar\gamma_S\boldsymbol{S} \;=\; -\mu_B g_e \boldsymbol{S} \tag{2.9}$$

where γ_S is the electron gyromagnetic ratio, g_e is the free-electron g-factor and μ_B is the Bohr magneton.

Paramagnetic ions with non-zero orbital angular momentum $\boldsymbol{L}$ have an orientation-dependent orbital contribution to the magnetic moment, defined as $\boldsymbol{\mu}_L \;=\; -\mu_B\boldsymbol{L}$. The total electron magnetic moment, in the Russell-Saunders ($L-S$) scheme, can be written

as [†] [73]:

$$\boldsymbol{\mu}_e \;=\; -\mu_B(\boldsymbol{L} + g_e\boldsymbol{S}) \tag{2.10}$$

Similarly to the nuclear case (equation 2.6), we can define the electron Zeeman interaction between the electron magnetic moment and the external field, which, based on equation 2.10, will correspond to the sum of the orbital Zeeman and the spin Zeeman terms, taking the total form:

$$\hat{H}_{SZ} \;=\; \mu_B\boldsymbol{B}_0 \cdot (\hat{\boldsymbol{L}} + g_e\hat{\boldsymbol{S}}) \tag{2.11}$$

The orientation dependence of the electron Zeeman interaction due to the orbital angular momentum operator can be conveniently parametrized in the so-called g-tensor, $\boldsymbol{g}$, and equation 2.11 is reformulated as:

$$\hat{H}_{SZ} \;=\; \mu_B\boldsymbol{B}_0 \cdot \boldsymbol{g} \cdot \hat{\boldsymbol{S}} \tag{2.12}$$

The g-tensor in equation 2.12 can be expressed as the following sum of contributions (up to second-order perturbation theory): [18]

$$\boldsymbol{g} \;=\; (g_e \;+\; \Delta g^{\text{iso}})\mathbf{1} \;+\; \boldsymbol{\Delta\tilde{g}} \tag{2.13}$$

The equation 2.13 breaks down as g_e, the non-relativistic free-electron g value (2.002319), and $\Delta g^{\text{iso}}\mathbf{1} \;+\; \boldsymbol{\Delta\tilde{g}}$, the relativistic isotropic and anisotropic parts of the g-shift tensor, cumulatively expressed by $\boldsymbol{\Delta g}$. Physically, the overall $\boldsymbol{\Delta g}$ corresponds to the deviation from the g_e as a consequence of the spin-orbit coupling on the paramagnetic centre when the electronic structure has a non-zero orbital angular momentum, or on heavy atoms with some fraction of unpaired-electron spin density.

Hyperfine Interaction

In addition to the distinct coupling between the nuclear magnetic moment (equation 2.7) and the electron magnetic moment (equation 2.12) with the external magnetic field, of central importance for paramagnetic systems is the so-called hyperfine interaction between the nuclear magnetic moment and the magnetic field due to the unpaired electron(s), or

[†] The Russell-Saunders coupling scheme assumes that the strength of the spin-orbit coupling interaction is much smaller than the spin-spin (and orbit-orbit) interactions. This scheme gives a good approximation for d-block transition metals, hence it is applied in this Thesis. For elements elements with greater atomic numbers such as heavy metals and lanthanides, the spin-orbit coupling interaction becomes more significant, and the $J-J$ coupling scheme is used, instead [73].

equivalently between the electron magnetic moment and the magnetic field due to the nucleus. The Hamiltonian defining the hyperfine interaction takes the following form:

$$\hat{H}_{SI} \;=\; \hat{\boldsymbol{S}} \cdot \boldsymbol{A} \;\cdot \hat{\boldsymbol{I}} \tag{2.14}$$

where $\boldsymbol{A}$ is the hyperfine tensor, which, up to second-order perturbation theory, can be defined as follows: [18]

$$\boldsymbol{A} \;=\; (A^{\mathrm{FC}} \;+\; A^{\mathrm{FC,2}})\mathbf{1} \;+\; \boldsymbol{A}^{\mathrm{dip}} \;+\; \boldsymbol{A}^{\mathrm{dip,2}} \tag{2.15}$$

In equation 2.15, the hyperfine tensor is expanded as the non-relativistic Fermi contact and dipolar contributions ($A^{\mathrm{FC}}\mathbf{1} \;+\; \boldsymbol{A}^{\mathrm{dip}}$) and the relativistic spin-orbit isotropic and dipolar terms, ($A^{\mathrm{FC,2}}\mathbf{1} \;+\boldsymbol{A}^{\mathrm{dip,2}}$). A^{FC} depends on the unpaired electron spin density transferred into the s-orbitals of the observed nucleus, whereas $\boldsymbol{A}^{\mathrm{dip}}$ accounts for the through-space dipolar interaction between the magnetic moment of the unpaired electron spin density and the nuclear magnetic moment of the observed nucleus. These two terms can be expressed as a function of the unpaired electron spin density, $\rho^{\alpha-\beta}(\boldsymbol{r})$, as follows:

$$\begin{aligned} A^{\mathrm{FC}} \;&=\; \frac{2}{3}\mu_0\mu_B\mu_N\mu_I g_I g_e \rho^{\alpha-\beta}(\mathbf{0}) \\ \boldsymbol{A}^{\mathrm{dip}} \;&=\; \frac{\mu_0\mu_B\mu_N g_I g_e}{4\pi} \int \frac{3r_i r_j \;-\; \delta_{ij}\boldsymbol{r}^2}{r^5} \rho^{\alpha-\beta}(\boldsymbol{r}) d^3r \end{aligned} \tag{2.16}$$

where $\boldsymbol{r}$ is the vector originating at the nuclear position ($\boldsymbol{r} = \mathbf{0}$) of the NMR observed site and spatially connecting the unpaired electron spin density, with ($i,\; j$) labelling the Cartesian axes. ($\alpha,\; \beta$) are the major (spin up or down) and minor (spin down or up) spin channels, respectively (hence ($\alpha - \beta$) refers to the unpaired electrons), and δ_{ij} is the Kronecker delta.

The sign and magnitude of the isotropic A^{FC} depend on the strength and covalency of the bond(s) connecting the paramagnetic centre(s) with the NMR observed nucleus, as well as on the orbitals involved in the unpaired spin transfer. The sign and magnitude of the anisotropic $\boldsymbol{A}^{\mathrm{dip}}$ depend on the distance between the nuclear and the unpaired spin magnetic moments, and on their relative orientation with respect to a common reference frame. Often, particularly for the range of paramagnetic solids studied in this thesis, the transfer of spin density from the paramagnetic centre (or transition metal, TM) to the NMR observed centre (OC) involves the bridging oxygen to form a TM–O–OC bond pathway. Experimental and first principles studies demonstrated that the limiting 90° and 180° TM–O–OC spin transfer mechanisms can be rationalized in terms of the Goodenough-Kanamori rules, originally formulated for the description of

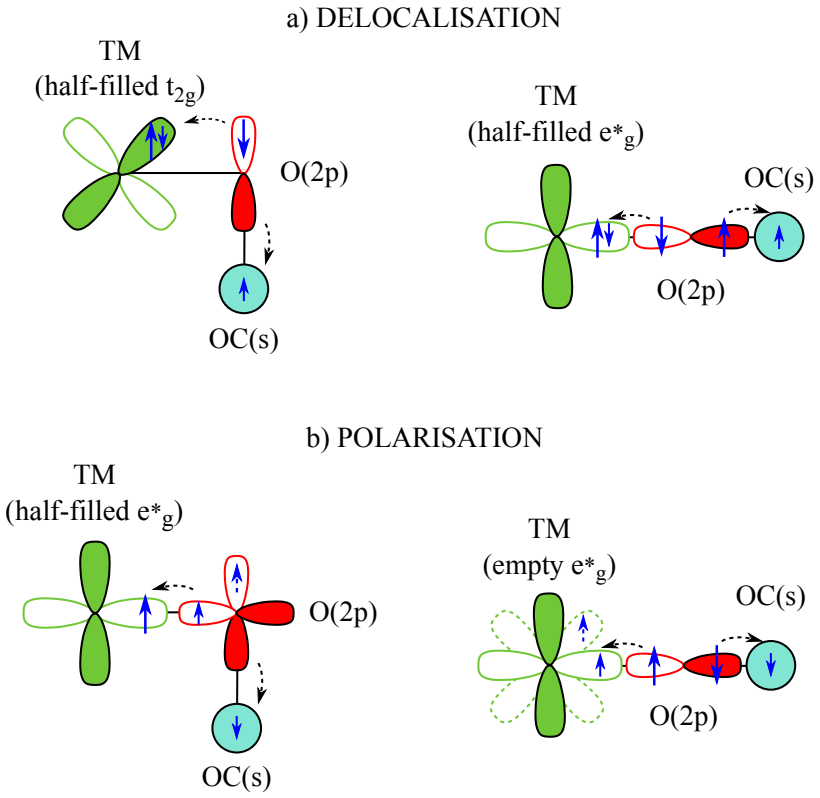

Fig. 2.2 Schematic diagrams of TM–O–Li spin transfer pathways for delocalisation (2.2-a) and polarisation (2.2-b) mechanisms.

magnetic exchange interactions between TM sites through the bridging oxygen [14]. The transfer essentially results from the combination of two contributions with opposite sign, which are schematically represented in Figure 2.2:

- *Delocalisation mechanism:* a spin polarisation in the crystal occurs along the TM–O–OC pathway if there are TM, O and OC orbitals that overlap with the correct symmetry. The unpaired spin density is delocalised along the TM–O–OC pathway, resulting in a net positive spin transfer (hence positive hyperfine shift) to the OC centre (Figure 2.2-a).

- *Polarisation mechanism:* the unpaired electron in the TM orbitals can polarise the other doubly occupied orbitals. This is due to the fact that, because of the exchange interactions, an electron with the same spin (up) as the TM-unpaired electron will spend more time near the TM than an electron with opposite spin (down), hence negative spin density is polarised towards the O and OC orbitals, leading to a net negative spin density transfer (hence negative hyperfine shift) (Figure 2.2-b).

Zero-Field Splitting Interaction

In the case of a spin multiplet with total spin $S > 1/2$, the magnetic dipolar interactions between the unpaired electrons in the system need to be considered. These interactions lead to energy differences between otherwise degenerate spin states independent of the external magnetic field strength, and the corresponding Hamiltonian describing these effects is for this reason known as the zero-field splitting Hamiltonian, with the following form:

$$\hat{H}_{ZFS} \;=\; \hat{\boldsymbol{S}} \cdot \boldsymbol{D} \cdot \hat{\boldsymbol{S}} \tag{2.17}$$

where $\boldsymbol{D}$ is a traceless and symmetric spatial tensor, and it has contributions from the direct spin-spin (contact and dipolar) coupling of the unpaired electrons, and from the spin-orbit coupling effects.

2.3.2 The EPR Effective Spin Hamiltonian

The energy splitting between the electron Zeeman states (equation 2.12) is much larger than the energy splitting between the nuclear Zeeman states (equation 2.6), which can be deduced from the three orders of magnitude difference between μ_B (9.27410^{-24} J·T^{-1}) and μ_N (5.05110^{-27} J·T^{-1}). The transitions between the electron Zeeman states can be studied in electron paramagnetic resonance (EPR) spectroscopy by applying a microwave frequency, and the effective Hamiltonian representing the interactions measureable with EPR takes the following form:

$$\hat{H}_{\text{EPR}} \;=\; \mu_B \boldsymbol{g} \cdot \boldsymbol{B}_0 \cdot \hat{\boldsymbol{S}} \;+\; \hat{\boldsymbol{S}} \cdot \boldsymbol{A} \;\cdot \hat{\boldsymbol{I}} \;+\; \hat{\boldsymbol{S}} \cdot \boldsymbol{D} \cdot \hat{\boldsymbol{S}} \tag{2.18}$$

However, in this thesis we are interested in the NMR spectroscopy, which detects transitions between nuclear energy levels. Due to the much smaller energy splitting between the nuclear Zeeman states compared to the electron states, the transitions induced in NMR will only involve nuclear energy levels, and the presence of unpaired electrons is detected through their interaction with the excited nucleus.

2.3.3 Thermal Average of the Electron Magnetic Moment

The unpaired electrons relax on a timescale ($10^{-14} - 10^{-8}$ s) much faster than the the typical nuclear longitudinal relaxation time (10^{-3} s to several minutes) [74, 75]. Consequently, the nuclear spin does not interact with the electron spin in the same way as it does with another nuclear spin in the homo/eteronuclear J-coupling. Because of the

shorter timescale of electron relaxation compared to the nuclear relaxation, on the NMR observation time the nuclear spins interact with the electronic spins that have already relaxed to their Boltzmann equilibrium. The nuclear magnetic moment hence effectively couples with the thermal (Boltzmann) average of the electronic magnetic moments. The hyperfine interaction in equation 2.14 from an NMR perspective is reformulated as:

$$\hat{H}_{SI} \;=\; \langle \hat{\boldsymbol{S}} \rangle \;\cdot\; \boldsymbol{A} \;\cdot \hat{\boldsymbol{I}} \tag{2.19}$$

with $\langle \hat{\boldsymbol{S}} \rangle$ being the thermal average (or the expectation value) of the electron spin. This can be expressed as a Boltzmann average of $\hat{\boldsymbol{S}}$ for each different Cartesian component i [21, 20]:

$$\langle \hat{S}_i \rangle \;=\; \frac{\sum_n \langle n|\hat{S}_i|n\rangle \; exp(-\beta E_n)}{\sum_n exp(-\beta E_n)} \tag{2.20}$$

where $|n\rangle$ and E_n are respectively eigenstates and eigenenergies of the total Hamiltonian in equation 2.18 and $\beta = 1/kT$ (k being the Boltzmann constant). As said, the dominant term in the equation 2.18 is the electron Zeeman interaction, corresponding to $|n\rangle = |SM_S\rangle$ and $E_n = \mu_B g_n B_0 M_S$ (M_S being the electron magnetic quantum number).

Since in the NMR experiment the external magnetic field is aligned along the z-direction, the x and y components of $\langle \hat{S}_i \rangle$ which are perpendicular to B_0 do not contribute to the net magnetic moment, while the z component parallel to B_0 results in the only non-zero contribution, $\langle \hat{S}_z \rangle$. The expectation value of the z-component of the electron spin vector in the absence of spin-orbit coupling (spin-only case) can be derived from equation 2.20 as [76]:

$$\langle \hat{S}_z \rangle \;=\; -S \; B_S(\gamma) \tag{2.21}$$

with $\langle \hat{S}_x \rangle = \langle \hat{S}_y \rangle = 0$, and $B_S(\gamma)$ being the spin-only Brillouin function defined for $\gamma = \mu_B g_e B_0 S/kT$ as:

$$B_s(\gamma) \;=\; \frac{2S+1}{2S} \coth\left(\frac{2S+1}{2S}\gamma\right) \;+\; \frac{1}{2S}\coth\left(\frac{\gamma}{2S}\right). \tag{2.22}$$

The general expression in equation 2.21 allows us to distinguish between two different regimes of temperature and magnetic field. In the spin-only case and within the so-called high-temperature limit ($\mu_B g_e B_0/kT \ll 1$), corresponding to the typical NMR experimental conditions, the Brillouin function approximates to $B_s(\gamma) \approx \gamma(S+1)/3S$, and the expectation value of $\hat{S}_z$ becomes:

$$\langle \hat{S}_z \rangle \;=\; -\frac{\mu_B g_e S(S+1) B_0}{3kT} \tag{2.23}$$

This expression for $\langle \hat{S}_z \rangle$ is commonly referred to as the *Curie spin* because of its inverse proportionality on the temperature $(1/T)$ as described by the Curie Law. Alternatively, when either B_0 is high enough or T is sufficiently low such that $\mu_B g_e B_0/kT \to \infty$ the system experiences a saturation regime where the expectation value of $\hat{S}_z$ becomes:

$$\langle \hat{S}_z \rangle_{sat} = -S. \tag{2.24}$$

Although less commonly experienced experimentally, this is an important condition for what concerns the computational representation of these systems in the solid state, as it will be better pointed out in Section 2.5.1.

Exchange Interaction

For systems where the paramagnetic centres are a major constituent of the lattice, the exchange interactions between the electron spins also affect the electronic energy levels. The interatomic exchange interaction can be expressed in terms of the Heisenberg Hamiltonian of the form [76]:

$$\hat{H}_{exc} = -\sum_{ij} J_{ij} \hat{\boldsymbol{S}}_i \cdot \hat{\boldsymbol{S}}_j \tag{2.25}$$

with J_{ij} being the isotropic exchange constant between the i^{th} and j^{th} interacting electron spins. A ferromagnetic interaction corresponds to an energetically favourable alignment of the spins parallel to one another, associated with a positive J value. Viceversa for an antiferromagnetic coupling, corresponding to an antiparallel ordering of the electron spins, hence a negative J value. The favourable magnetic alignment maintains a spontaneous ordering of the electron spins below a critical temperature, above which thermal fluctuations prevail, effectively randomizing the alignment between the spins typical of the high-temperature paramagnetic regime.

In the presence of exchange coupling between the electron spins, the expectation value of $\hat{S}_z$ in equation 2.23 in the paramagnetic regime reformulates according to the Curie-Weiss law, as:

$$\langle \hat{S}_z \rangle = -\frac{\mu_B g_e S(S+1) B_0}{3k(T-\theta)}, \tag{2.26}$$

θ in equation 2.26 is the so-called Weiss constant, which can be expressed as the sum over shells, i, of exchange constants, J_i, as:

$$\theta = \frac{2S(S+1)}{3k} \sum_i z_i J_i \tag{2.27}$$

where z_i is the number of neighbouring spins within a shell. The sign of the Weiss constant signifies whether the dominat exchange mechanisms in the system are ferromagnetic (positive θ) or antiferromagnetic (negative θ).

2.3.4 Paramagnetic Shielding Tensor

Spin-only Case

To summarise, in the high-temperature regime typical of the NMR spectroscopy and due to the much faster relaxation rate of the electrons compared to the nuclei, the interaction between the external magnetic field and the nuclear magnetic moment is affected by the thermally averaged unpaired electron magnetic moment. The total field determining the transitions between the nuclear Zeeman states is the result of the external magnetic field B_0 modulated by the shielding from the electronic ground and mixed ground-excited states, and by the hyperfine interaction between the nuclear magnetic moment and the averaged electron magnetic moment. We can express an NMR effective Hamiltonian containing these contributions and obtain:

$$\hat{H}_{\text{NMR}} \;=\; \hbar\gamma_I B_0 \,(\mathbf{1} - \boldsymbol{\sigma}^{\text{orb}})\, \hat{I}_z \;+\; \langle \hat{S}_z \rangle \;\cdot\; \boldsymbol{A} \;\cdot \hat{I}_z \tag{2.28}$$

For exchange-coupled electron spins, by substituting in 2.28 the expression of $\langle \hat{S}_z \rangle$ in equation 2.26 (in the absence of magnetic exchange interactions, equation 2.23 is considered), and by substituting the nuclear spin operator $\hat{I}_z$ with the nuclear magnetic moment operator $\hat{\mu}_{I,z} \;=\; \hbar\gamma_I \hat{I}_z \;=\; g_I \mu_N \hat{I}_z$ (equation 2.1), we obtain:

$$\hat{H}_{\text{NMR}} \;=\; -\hat{\mu}_{I,z} B_0 \;+\; B_0\, \boldsymbol{\sigma}^{\text{orb}}\, \hat{\mu}_{I,z} \;-\; B_0\, \frac{\mu_B g_e S(S+1)}{3 g_I \mu_N k (T-\theta)}\, \boldsymbol{A}\, \hat{\mu}_{I,z} \tag{2.29}$$

By comparing the second and third terms in equation 2.29, we notice that they are both linear in the external magnetic field, and that they formally modulate the interaction between the external field and the nuclear moment in the same way, that is *shielding* the nuclear moment from B_0. By analogy with the orbital term $\boldsymbol{\sigma}^{\text{orb}}$, we can identify the shielding contribution due to the presence of unpaired electrons in the third term of equation 2.29, which takes the form:

$$\boldsymbol{\sigma}^{s} \;=\; -\frac{\mu_B g_e S(S+1)}{3 g_I \mu_N k (T-\theta)}\, \boldsymbol{A}. \tag{2.30}$$

Spin-orbit Coupling - g-tensor

In the presence of spin-orbit coupling, the contribution of the non-zero orbital angular momentum $\boldsymbol{L}$ also has an effect on the paramagnetic shielding $\boldsymbol{\sigma}^s$. Neglecting the effects of zero field splitting, the derivation of Moon and Patchkovskii for $\boldsymbol{\sigma}^s$, in which we include the effects of magnetic exchange interactions, rformulates equation 2.30 to give: [20]

$$\boldsymbol{\sigma}^s = -\frac{\mu_B S(S+1)}{3g_I\mu_N k(T-\theta)}\,\boldsymbol{g}\cdot\boldsymbol{A}. \tag{2.31}$$

Spin-orbit Coupling - Zero Field Splitting

As it was derived by Soncini and Van den Heuvel [24] and by Vaara *et al.* [22], the shielding tensor presented in equation 2.30 modifies for systems with the paramagnetic site having $S > 1/2$, as

$$\sigma^s_{\epsilon\tau} = -\frac{\mu_B}{\gamma_N\hbar kT}\sum_{ab} g_{\epsilon a}\langle S_a S_b\rangle A_{b\tau} \tag{2.32}$$

with ϵ, τ, a, b being the Cartesian components of the tensor, $\langle S_a S_b\rangle$ being the second order tensor resulting from the expectation values of the product $\hat{S}_a\hat{S}_b$ evaluated with the $2S+1$ states of the ground multiplet at the limit of zero field. The term in bracket corresponds to the expectation value of the electron spin components with the ZFS modulating the Zeeman sublevels. It was also shown by Bleany that if, in the high-temperature limit, kT is sufficiently large so that the Boltzman average over the ZFS energy levels can be approximated to $1/(kT)^2$, then the effects of the ZFS on the paramagnetic shielding tensor can be expressed by the second term in the following sum [19]:

$$\boldsymbol{\sigma}^s = -\frac{\mu_B S(S+1)}{3g_I\mu_N kT}\,\boldsymbol{g}\cdot\boldsymbol{A} + \frac{\mu_B S(S+1)(2S-1)(2S+3)}{30g_I\mu_N(kT^2)}\,\boldsymbol{g}\cdot\boldsymbol{D}\cdot\boldsymbol{A} \tag{2.33}$$

Due to the $1/T^2$ dependence and to the commonly small size of the ZFS interaction ($\boldsymbol{D}$) for d-block transition metals (compared to heavier metals or lanthanides), the second term can be, to a good approximation, neglected. [77]

2.3.5 Effects of the Paramagnetic Shielding on the NMR Spectrum

We will now examine the various effects of the paramagnetic shielding tensor on the NMR spectrum by considering the product between the hyperfine and the g-tensor in

equation 2.31. For convenience, the forms of $\boldsymbol{\sigma}^s$ (in equation 2.31) and the contributing $\boldsymbol{A}$ (up to second-order perturbation theory, in equation 2.15) and $\boldsymbol{g}$ (up to second-order perturbation theory, in equation 2.13) are here repeated: [18]

$$\boldsymbol{\sigma}^s = -\frac{\mu_B S(S+1)}{3 g_I \mu_N k(T-\theta)}\, \boldsymbol{g}\cdot\boldsymbol{A}$$

with

$$\boldsymbol{A} = (A^{\mathrm{FC}} + A^{\mathrm{FC,2}})\mathbf{1} + \boldsymbol{A}^{\mathrm{dip}} + \boldsymbol{A}^{\mathrm{dip,2}}$$
$$\boldsymbol{g} = (g_e + \Delta g^{\mathrm{iso}})\mathbf{1} + \boldsymbol{\Delta\tilde{g}} \tag{2.34}$$

The individual cross terms contributing to the paramagnetic shielding tensor can be derived by substituting in the equation of $\boldsymbol{\sigma}^s$ the expressions for $\boldsymbol{A}$ and $\boldsymbol{g}$ in equation 2.34. As discussed in Ref. 21, by retaining only the terms that contain at most one leading-order spin-orbit coupling term in the product $\boldsymbol{g}\cdot\boldsymbol{A}$, the resulting contributions can be separated based on the type of the involved hyperfine term. This corresponds to retaining terms up to fourth order in the fine-structure constant. The breakdown of the various contributions arising from the product in equation 2.34 are summarised in Table 2.1.

The first group of terms named 'CONTACT' depends on the delocalization of unpaired-electron spin density to the nuclear position of the NMR observed centre; the second 'DIPOLAR' group gathers terms that depend on the electron-nuclear magnetic dipolar interaction, and therefore on the spatial position of the unpaired electrons relative to the NMR observed centre and the relative orientation of their magnetic moments.

Another useful distinction for the interpretation of $\boldsymbol{\sigma}^s$ in terms of the structural and electronic properties concerns the rank of the spherical tensors corresponding to the various terms in Table 2.1. The rank-zero terms lead to an isotropic paramagnetic shift, whereas the rank-two terms contribute to the shift anisotropy. Rank-one terms do not give rise to observable features in the spectrum under high-field conditions, and so are not considered further. The non-relativistic Fermi contact shift corresponds to the element of the shielding tensor arising from the coupling in term (a) of Table 2.1 [15]. This constitutes the isotropic contribution that depends on the electronic structure of the TM and on the degree of covalency and the orbital overlap in the bond linking the observed centre (OC) and the TM (Figure 2.2). Term (a) is commonly the dominant isotropic contact contribution in systems where the delocalization of the unpaired-electron spin

TYPE	TERM	EXPRESSION	RANK
CONTACT	a)	$g_e A^{\mathrm{FC}}$	0
	b)	$g_e A^{\mathrm{FC},2}$	0
	c)	$\Delta g_{\mathrm{iso}} A^{\mathrm{FC}}$	0
	d)	$A^{\mathrm{FC}} \boldsymbol{\Delta \tilde{g}}$	1,2
DIPOLAR	e)	$g_e \boldsymbol{A}^{\mathrm{dip}}$	2
	f)	$g_e \boldsymbol{A}^{\mathrm{dip},2}$	2
	g)	$\Delta g_{\mathrm{iso}} \boldsymbol{A}^{\mathrm{dip}}$	2
	h)	$\boldsymbol{\Delta \tilde{g}} \boldsymbol{A}^{\mathrm{dip}}$	0,1,2

Table 2.1 Comparison of the terms contributing to the paramagnetic shielding tensor from the coupling between the hyperfine and g-tensors in equation 2.34. The terms are gathered into two groups. The terms in the first group are due to an isotropic contact hyperfine interaction (CONTACT), and the second group contains terms due to an anisotropic electron-nuclear dipolar hyperfine interaction (DIPOLAR); for each product, the ranks of the resulting irreducible spherical tensor(s) contributions to the shielding are given.

density from the TM sites towards the s orbitals of the OC is prominent [78]. Terms (b), (c) and (d) represent the spin-orbit coupling contributions to the total contact shielding, either *via* the g-shift or the spin-orbit-based $A^{\mathrm{FC},2}$ term. Term (c) accounts for the spin-orbit deviation of the isotropic g-shift from the free-electron value, giving rise to a shift contribution proportional to A^{FC}. The final term that contributes to the shift is unusual, in that it does not result from the hyperfine contact component, and it is for this reason commonly referred to as the pseudo-contact shift. It is the rank-two contribution in term (h), and it derives from the coupling between the non-relativistic dipolar component of the hyperfine tensor and the g-anisotropy due to spin-orbit coupling [16]. As the pseudo-contact term arises from the dipolar hyperfine interaction, it leads to a shift that depends on the spatial position and orientation of the magnetic moment of the unpaired-electron spin density relative to the nuclear magnetic moment of the OC. Considering the rank-two terms of Table 2.1, these contribute to the spectrum in the

form of the shift anisotropy. Term (e) of Table 2.1 represents the only non-relativistic dipolar contribution to the anisotropy, and it depends on the magnitude of the electronic and nuclear magnetic moments involved in the dipolar interaction, on their relative orientation and on their separation in space. All the other terms of the group - (f), (g) and the rank-two contribution of term (h) - account for the spin-orbit corrections to this dipolar anisotropy. The other relativistic contribution to the shift anisotropy comes from the rank-two term (d), which is due to the g-anisotropy and the isotropic Fermi contact component of the hyperfine interaction.

2.3.6 Bulk Magnetic Susceptibility Effects

The local interactions between nuclear and electron spins described so far define the paramagnetic shielding tensor $\boldsymbol{\sigma}^s$ in equation 2.34, which affects the NMR spectrum as described in Section 2.3.5. In addition, the bulk magnetic properties of the system also result in a contribution to the NMR shift and shift anisotropy. The bulk magnetic susceptibility (BMS) has its origin in the dipolar coupling between the nuclear and unpaired electron magnetic moments. When the system experiences an external magnetic field, a demagnetizing field is induced, that is proportional to the magnetic susceptibility and that either opposes or adds to the static external field. Depending on the shape of the particle and on the symmetry of the magnetic susceptibility tensor, the demagnetizing field can contribute to both the shift and the line-broadening of the NMR spectrum. The treatment of the BMS effects in this Section is based on the theory of classical electrodynamics, which follows the description in Jackson's textbook [79].

A magnetic field can be described in terms of the magnetic field strength, $\boldsymbol{H}(\boldsymbol{r})$, or the magnetic flux density, $\boldsymbol{B}(\boldsymbol{r})$, which are both position-dependent and are related as:

$$\boldsymbol{B}(\boldsymbol{r}) \;=\; \mu_0(\boldsymbol{H}(\boldsymbol{r}) \;+\boldsymbol{M}(\boldsymbol{r})) \tag{2.35}$$

$\boldsymbol{M}(\boldsymbol{r})$ is the net bulk magnetization correponding to the total induced magnetic moment per unit volume. The bulk magnetization inside a crystallite is proportional to the applied field $\boldsymbol{H}_0$, with the proportionality constant being the bulk magnetic susceptibility tensor per unit volume, $\boldsymbol{\chi}_V$:

$$\boldsymbol{M} \;=\; \boldsymbol{\chi}_V \cdot \boldsymbol{H}_0 \tag{2.36}$$

The molar magnetic susceptibility tensor, $\boldsymbol{\chi}$, relates to $\boldsymbol{\chi}_V$ as $\boldsymbol{\chi} = \boldsymbol{\chi}_V V_M$, where V_M is the molar volume.

In a finite-sized paramagnetic crystallite or single crystal, the discontinuity of the induced magnetization at the sample edges generates a demagnetizing field, $\boldsymbol{H}_D$, which

modifies the total field experienced by the nucleus. The demagnetizing field is proportional to the magnetization, and it is dependent on the crystal shape, taking the form:

$$\boldsymbol{H}_D \;=\; -\,\boldsymbol{N}\cdot\boldsymbol{\chi}_V\cdot\boldsymbol{H}_0 \tag{2.37}$$

where $\boldsymbol{N}$ is two-dimensional tensor, the rank-two part describing the shape of the crystal, with trace $Tr(\boldsymbol{N}) = 1$. In analogy with the nuclear Zeeman interaction, the demagnetising field essentially induces an additional shielding at the nuclear spin, and the form of this $\boldsymbol{\sigma}^{\mathrm{BMS}}$ inside the crystallite can be derived as:

$$\boldsymbol{\sigma}^{\mathrm{BMS}}(\boldsymbol{r}) \;=\; \boldsymbol{\chi}_V\cdot(\boldsymbol{N}(\boldsymbol{r})^T \;-\; \mathbf{1}) \tag{2.38}$$

where $\mathbf{1}$ represents the identity matrix.

The treatment of the BMS effects on a single crystallite can be extended to the case of polycrystalline solids. The model presented by Kubo *et al.* [26] is adopted in the following discussion, which is schematised in Figure 2.3.

The model assumes that the observed nucleus I is inside a crystallite, and it possesses a local paramagnetic shielding tensor, $\boldsymbol{\sigma}^s$ (equation 2.34). The $\boldsymbol{\sigma}^s$ tensor is given by the sum of contributiosn from the nearby TM ions. The nuclear spin I is at the centre of an Ewald sphere, which has dimensions much smaller than those of the crystallite, and within which the sum of the contributions to $\boldsymbol{\sigma}^s$ converges. The remainder of the crystallite is then assumed to be a uniformly-magnetised continuum, in which the bulk magnetic susceptibility (BMS) effects contribute a BMS shielding tensor, $\boldsymbol{\sigma}^{\mathrm{BMS}}$. The sample contains a number of crystallites that are assumed to occupy the sites of a closed-packed lattice, and each crystallite contributes a $\boldsymbol{\sigma}^{\mathrm{BMS}}$ term to the total BMS shielding tensor of the nucleus I. The total shielding, $\boldsymbol{\sigma}^{\mathrm{TOT}}$, of the observed nucleus, I, is hence given by the sum of these contributions:

$$\boldsymbol{\sigma}^{\mathrm{TOT}} \;=\; \boldsymbol{\sigma}^s \;+\; \boldsymbol{\sigma}^{\mathrm{BMS}} \tag{2.39}$$

2.4 First Principles Modelling

In order to model the electronic structure of a system, the ultimate goal of most quantum chemical approaches is to find an approximate solution to the time-independent, non-relativistic many-body Schrödinger equation [80–82]

$$\hat{H}\Psi(\boldsymbol{r}_1,\boldsymbol{r}_2,\ldots\boldsymbol{r}_N,\boldsymbol{R}_1,\boldsymbol{R}_2,\ldots\boldsymbol{R}_M) \;=\; E\Psi(\boldsymbol{x}_1,\boldsymbol{x}_2,\ldots\boldsymbol{x}_N,\boldsymbol{R}_1,\boldsymbol{R}_2,\ldots\boldsymbol{R}_M) \tag{2.40}$$

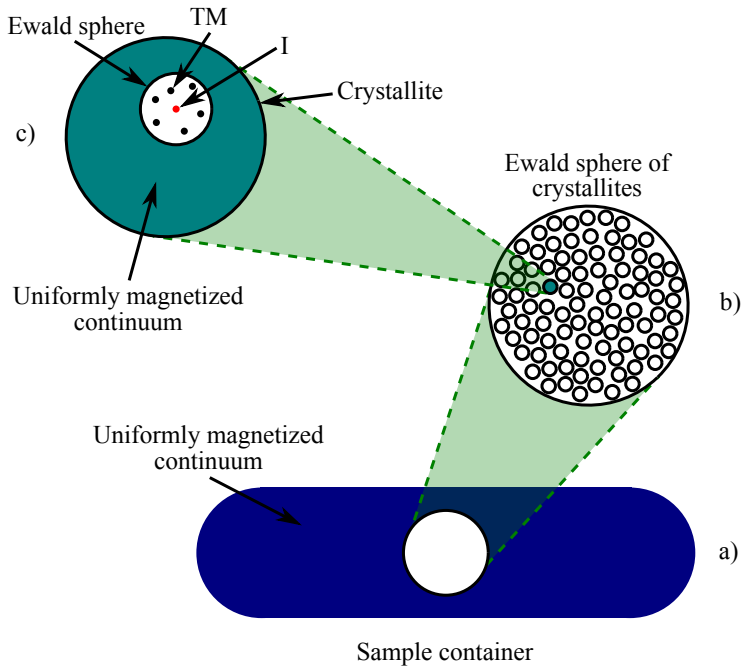

Fig. 2.3 Schematic illustration of the model of a paramagnetic policrystalline sample, adapted from Ref. [26, 8]. In a), the entire sample is shown, held in a container. The set of closesly-packed crystallites form the Ewald sphere, and the remainder of the sample is assumed to be uniformly magnetized. The Ewald sphere of crystallites is shown in b). Each of the crystallites in this sphere contributes a BMS shielding tensor $\boldsymbol{\sigma}^{\mathrm{BMS}}$. A single crystallite within the Ewald sphere is shown in c). It contains the NMR-observed nucleus I, which experiences a local paramagnetic shielding $\boldsymbol{\sigma}^{s}$ due to the nearby transition metal (TM) ions. The Ewald sphere centred at the nucleus I is defined as the region within which the sum of contributions to $\boldsymbol{\sigma}^{s}$ converges, and as having a radius much smaller than the dimensions of the crystallites. The remainder of the crystallite is modelled as a uniformly magnetized continuum which contributes to the BMS shielding tensor of I.

where $\hat{H}$, Ψ and E are respectively the Hamiltonian operator, the wavefunction and the energy of a system consisting of M nuclei with position $\boldsymbol{R}$ and N electrons with position $\boldsymbol{r}$. In the Born-Oppenheimer approximation, due to the difference in masses, and hence speed of motion of nuclei and electrons, electrons are considered as moving in the field of steady nuclei. This implies that the nuclear kinetic energy is considered zero, and that E in equation 2.40 represents the electronic energy. The Hamiltonian $\hat{H}$ in equation 2.40 reformulates as (in atomic units, and with the subscripts e signifying electrons and n nuclei) [80]:

$$\hat{H} = \hat{T} + \hat{V}_{ne} + \hat{V}_{ee} + \hat{V}_{nn} \tag{2.41}$$

where $\hat{T}$ is the kinetic energy operator:

$$\hat{T} = \sum_{i=1}^{N} -\frac{1}{2}\nabla_i^2 \tag{2.42}$$

$\hat{V}_{ne}$ is the nucleus-electron attraction energy operator:

$$\hat{V}_{ne} = \sum_{i=1}^{N} \nu(\boldsymbol{r}_i) \tag{2.43}$$

where $\nu(\boldsymbol{r})$ is the Coulomb potential between the electrons and the nuclei.

$\hat{V}_{ee}$ is the electron-electron repulsion energy operator:

$$\hat{V}_{ee} = \sum_{i<j}^{N} \frac{1}{|\boldsymbol{r}_i \boldsymbol{r}_j|} \tag{2.44}$$

and $\hat{V}_{nn}$ is the nucleus-nucleus repulsion energy operator:

$$\hat{V}_{nn} = \sum_{I<J} \frac{Z_I Z_J}{|\boldsymbol{R}_I \boldsymbol{R}_J|} \tag{2.45}$$

Despite the advances in computational power, the exact solution of the many-body Schrödinger equation is still beyond the realms of possibility. Various approaches can be followed to allow for an approximate calculation of the electronic and ground state properties of materials with sufficient accuracy. The method that will be used in this Thesis is Density Functional Theory (DFT) [80–82], of which a brief overview will be given in the following Section.

2.4.1 Principles of DFT

The basis of DFT is the proof by Hohenberg and Kohn that the wavefunction $\Psi(\boldsymbol{x}_1, \boldsymbol{x}_2, ...\boldsymbol{x}_N)$, a $3N$ dimensional function for N electrons, can be replaced with the simpler electron density $\rho(\boldsymbol{r})$, a function of three spatial variables. Hence the energy, E, is a unique functional of $\rho(\boldsymbol{r})$ and the ground-state energy of a system is also uniquely defined by $\rho(\boldsymbol{r})$ [83]. The energy functional is written as the sum of two terms:

$$E[\rho(\boldsymbol{r})] = \int V_{\text{ext}}(\boldsymbol{r})\rho(\boldsymbol{r})d\boldsymbol{r} + F[\rho(\boldsymbol{r})] \tag{2.46}$$

The first term in equation 2.46 arises from the interaction of the electrons with an external potential $V_{\text{ext}}(\boldsymbol{r})$. The second term in equation 2.46, $F[\rho(\boldsymbol{r})]$, corresponds to

the sum of the kinetic energy of the electrons and the contribution from inter-electronic interactions, and it does not depend on the external potential, $V_{\text{ext}}(\boldsymbol{r})$. Hohenberg and Kohn further showed that the energy is minimised by the exact ground-state electron density, and the corresponding minimum energy is the ground-state energy [83]. A variational approach could in principle be used to compute the ground-state energy by minimising $E[\rho(\boldsymbol{r})]$ with respect to $\rho(\boldsymbol{r})$. However, the exact form of $F[\rho(\boldsymbol{r})]$ is unknown, and the first practical approach to solve the Hohenberg and Kohn theorem for a set of interacting electrons was proposed a year later by Kohn and Sham [84]. In their work, Kohn and Sham showed that the kinetic energy of the real system of interacting electrons can be replaced by the kinetic energy of a reference system of non-interacting electrons with the same density $\rho(\boldsymbol{r})$ as the real system. In this formalism, the $F[\rho(\boldsymbol{r})]$ term in equation 2.46 can be written as:

$$F[\rho(\boldsymbol{r})] \;=\; E_{\text{KE}}[\rho(\boldsymbol{r})] \;+\; E_{\text{H}}[\rho(\boldsymbol{r})] \;+\; E_{\text{XC}}[\rho(\boldsymbol{r})] \tag{2.47}$$

$E_{\text{KE}}[\rho(\boldsymbol{r})]$ is the kinetic energy functional of the reference system of non-interacting electrons, of the form:

$$E_{\text{KE}}[\rho(\boldsymbol{r})] \;=\; \sum_{i=1}^{N} \int \psi_i(\boldsymbol{r}) \Big(-\frac{\nabla^2}{2} \Big) \psi_i(\boldsymbol{r}) d\boldsymbol{r} \tag{2.48}$$

where $\psi_i(\boldsymbol{r})$ is the set of one-electron orthonormal orbitals.

$E_{\text{H}}[\rho(\boldsymbol{r})]$ is the electron-electron Coulombic energy functional, also known as the Hartree term, which takes the classical form of the summation (or integration) over all possible pairwise interactions between two charge densities:

$$E_{\text{H}}[\rho(\boldsymbol{r})] \;=\; \frac{1}{2} \int \int \frac{\rho(\boldsymbol{r}_1 \boldsymbol{r}_2)}{|r_1 - r_2|} d\boldsymbol{r}_1 d\boldsymbol{r}_2 \tag{2.49}$$

$E_{\text{XC}}[\rho(\boldsymbol{r})]$ in equation 2.47 is the exchange and correlation energy functional, which describes the difference in kinetic energy between the reference system of non-interacting electrons and the real system of interacting electrons. This term also contains additional contributions associated with electron correlation that are not included in the classical electron-electron interaction term, $E_{\text{H}}[\rho(\boldsymbol{r})]$.

The expression of Kohn and Sham for the density of the system, $\rho(\boldsymbol{r})$, in terms of the set of one-electron orthonormal orbitals, $\psi_i(\boldsymbol{r})$ takes the form [83, 84]

$$\rho(\boldsymbol{r}) \;=\; \sum_{i=1}^{N} |\psi_i(\boldsymbol{r})|^2 \tag{2.50}$$

By using this form for the electron density and by minimising equation 2.47 variationally with respect to the density, the following set of one-electron Kohn-Sham equations is obtained:

$$\left\{ -\frac{\nabla_i^2}{2} - \left(\sum_{A=1}^{M} \int \frac{Z_A}{\boldsymbol{r}_i} \right) + \int \frac{\rho(\boldsymbol{r}_i)}{|\boldsymbol{r}_i \boldsymbol{r}'|} d\boldsymbol{r}' + V_{\mathrm{XC}}[\boldsymbol{r}_i] \right\} \psi_i(\boldsymbol{r}_i) = \epsilon_i \psi_i(\boldsymbol{r}_i) \tag{2.51}$$

ϵ_i are the orbital energies, or equivalently the Kohn-Sham eigenvalues, and $V_{\mathrm{XC}}[\boldsymbol{r}]$ is the exchange-correlation functional, which is related to the exchange-correlation energy as:

$$V_{\mathrm{XC}}[\boldsymbol{r}] = \left(\frac{\delta E_{\mathrm{XC}}[\rho(\boldsymbol{r})]}{\delta \rho(\boldsymbol{r})} \right) \tag{2.52}$$

The set of Kohn-Sham equations is solved following a self-consistent approach, in which an initial guess of the density is used to solve equation 2.51 to obtain a set of orbitals, which are used to calculate a more accurate value for the density, used in a second iteration, and so on until convergence is reached. [84]

2.4.2 Exchange-correlation Functional

The exact form of the exchange-correlation functional is unknown, and the accuracy of its approximation is central to the performance of the density functional approach. One approximation is the local density approximation (LDA), which reformulates the total exchange-correlation energy functional as [85, 86]:

$$E_{\mathrm{XC}}[\rho(\boldsymbol{r})] = \int \rho(\boldsymbol{r}) \epsilon_{\mathrm{XC}}(\rho(\boldsymbol{r})) d\boldsymbol{r} \tag{2.53}$$

ϵ_{XC} is the exchange-correlation energy per electron as a function of the density of a uniform electron gas, in which the density is constant throughout all space. LDA assumes that, at each point in the electron distribution of the real system with density $\rho(\boldsymbol{r})$, V_{XC} and ϵ_{XC} have the same values as in the homogeneous gas. Despite the model system of a homogeneous gas is not a realistic situation for the rapidly varying densities of molecules and solids, it is the only system for which the exchange-correlation energy functional is known to very high accuracy. LDA hence is a good approximation for systems of slowly varying electron density, such as simple metals. The formalism can be extended to the unrestricted case of open-shell systems introducing the so-called local spin density approximation (LSDA), which is equivalent to the LDA case, except that in the LSDA

formalism the electron density of the major spin state, ρ_α (e.g. the spin-up state) and the electron density of the minor spin state, ρ_β (e.g. the spin-down state) are treated separately [87].

To improve the description of total energies, atomisation energies and migration barriers of materials given by the local L(S)DA approximation, the generalised gradient approximation (GGA) was derived [88, 89]. The GGA approach does not just use the density $\rho(\boldsymbol{r})$ at a particular point r, but it includes also a dependence on the gradient of the charge density, $\nabla\rho(\boldsymbol{r})$, in order to better represent the non-homogeneity of the true electron density. Despite the improvements made over the years on both approaches, both L(S)DA and GGA still fail to accurately describe systems with highly correlated electrons [90].

One major problem, which is inherent to the formulation of the total energy functional in DFT, is the so-called self-interaction error. This arises from the fact that, in the electron-electron Coulombic term in equation 2.49, the electron density ρ accounts also for the contribution of the electron itself, and this contribution is not cancelled due to the approximate form of $E_{\mathrm{XC}}[\rho(\boldsymbol{r})]$ in the L(S)DA and GGA approaches. As a consequence, the self-repulsion of the electron with its own charge density induces an excessive delocalization of the wavefunction, giving a poor representation of the physics of correlated systems. The most common solutions to this limitation of the formalisms have relied on the ability of giving a more accurate description of the localised electron states, and the two major approaches to this regard are the DFT+U method and the hybrid functional implementation, which will be presented separately.

2.4.3 DFT+U

The DFT+U approach was initially formulated by Anisimov *et al.* [91] and it is based on the treatment of the correlated electronic states, such as localized d orbitals, using a Hubbard model, while the rest of the valence electrons are treated with the standard DFT formalism. The total energy of the system treated within the DFT+U method can be expressed by the sum of three components [92, 93]

$$E_{\mathrm{DFT+U}}[\rho(\boldsymbol{r})] \;=\; E_{\mathrm{DFT}}[\rho(\boldsymbol{r})] \;+\; E_{\mathrm{Hub}}[\{n^{l\sigma}_{mm'}\}] \;-\; E_{\mathrm{dc}}[\{n^{l\sigma}_{mm'}\}] \tag{2.54}$$

E_{DFT} is the standard approximate DFT energy functional, E_{Hub} corresponds to the term that contains the Hubbard Hamiltonian to treat correlated states, and E_{dc} represents the double-counting correction, due to the fact that the Hubbard term models part of the interaction energy that is already included in the DFT functional. The

variable $n^{l\sigma}_{mm'}$ is the occupation matrix of correlated electrons, with orbital quantum number l, magnetic quantum number m, and spin σ. Many different formulations of the E_{Hub} and the E_{dc} have been presented. In the scheme derived by Liechtenstein *et al.*, a unitary-transformation-invariant formulation of DFT+U is implemented, which expresses the interaction between localised states (E_{Hub}) and the double-counting correction (E_{dc}) in terms of the Coulomb parameter (Hubbard U) and of the exchange parameter (Stoner J) [94]. The double-counting term in equation 2.54 is reformulated as:

$$E_{\text{dc}}[\{n^{l\sigma}_{mm'}\}] \;=\; \sum_{l}\left\{\frac{U^l}{2}n^l(n^l-1) \;-\; \frac{J^l}{2}n^{l\uparrow}(n^{l\uparrow}-1)+n^{l\downarrow}(n^{l\downarrow}-1)\right\} \tag{2.55}$$

where n^l are generalized atomic orbital occupations, and $n^l = \; n^{l\uparrow}+n^{l\downarrow} \; = Tr(n^l_{mm'})$.

In many instances, as the study presented in Chapter 5 of this thesis, the simpler expression of the E_{Hub} term is implemented, which was derived by Dudarev *et al.* [95] to maintain the rotational invariance of the complete formulation just presented, while incorporating the Coulomb U and the exchange J terms in an overall *effective* value, $U_{\text{eff}} = U - J$.

Due to the low computational cost that is only marginally greater than standard DFT, DFT+U has rapidly become a very popular method in *ab initio* calculations of correlated and/or extended solid systems. However, the results of the DFT+U method are sensitive to the numerical values of the Hubbard U and Stoner J (or U_{eff}), which are material- and atom-specific, depend on the crystal structure and the magnetic ordering and are also sensitive to the code-specific implementation of the DFT+U scheme [92]. Although a self-consistent computation of these terms is more accurate, often they are obtained semi-empirically through comparison with some experimental properties of the system under investigation such as the oxidation energy.

2.4.4 Hybrid Functionals

As indicated earlier, an important limitation of the DFT formalism is due to the exchange contribution being significantly larger than the correlation effects. Another well studied computational method, the Hartree-Fock (HF) theory, computes the exchange energy exactly. However, the exchange term in the HF method is uncoupled with the correlation counterpart, thus leading to over-localisation of electrons [80]. The clever compromise derived by Becke in 1993 takes advantage of the combination of the *exact* (HF) exchange functional and the approximate (L(S)DA/GGA) exchange-correlation functional to partially cancel the intrinsic errors of the two formalism [96]. Becke hence proposed the

idea of hybrid functionals, which combine the HF and the L(S)DA/GGA functionals weighted by some semi-empirical coefficients, to obtain the general form:

$$E_{\mathrm{XC}} = E_{\mathrm{XC}}^{\mathrm{L(S)DA/GGA}} + a_0(E_{\mathrm{X}}^{\mathrm{HF}} - E_{\mathrm{X}}^{\mathrm{L(S)DA/GGA}}) + a_x\Delta E_{\mathrm{X}}^{\mathrm{GC}} + a_c\Delta E_{\mathrm{C}}^{\mathrm{GC}} \quad (2.56)$$

where $E_{\mathrm{X}}^{\mathrm{HF}}$ is the exact exchange energy obtained with the HF method, $E_{\mathrm{X}}^{\mathrm{L(S)DA/GGA}}$ is the exchange energy under the L(S)DA or GGA approximation, $\Delta E_{\mathrm{X}}^{\mathrm{GC}}$ is the gradient correction for the exchange, $\Delta E_{\mathrm{C}}^{\mathrm{GC}}$ is the gradient correction for the correlation, and a_0, a_x a_c are the empirical coefficients obtained from fitting of experimental data. As an example, equation 2.56 for the commonly used hybrid functional known as B3LYP takes the form [96, 97]

$$E_{\mathrm{XC}}^{\mathrm{B3LYP}} = 0.2E_{\mathrm{X}}^{\mathrm{HF}} + 0.8E_{\mathrm{X}}^{\mathrm{LDA}} + 0.72\Delta E_{\mathrm{X}}^{\mathrm{B88}} + 0.81E_{\mathrm{C}}^{\mathrm{LYP}} + 0.19E_{\mathrm{C}}^{\mathrm{VWN}} \quad (2.57)$$

where ΔE^{B88} is the Becke88 exchange functional [98] and $E_{\mathrm{C}}^{\mathrm{LYP}}$, $E_{\mathrm{C}}^{\mathrm{VWN}}$ are the semi-local LYP [99] and VWN [85] correlation functionals, respectively. Previous computational studies on paramagnetic materials showed that, while B3LYP (*i.e.* the hybrid functional containing 20 % HF exchange, named HYB20 hereafter) achieves a much better agreement with experiments for the structure than pure DFT, a higher fraction of HF exchange needs to be included (*i.e.* the B3LYP functional with 35 % HF exchange, named HYB35 hereafter) in order to more accurately predict other properties, such as the magnetism. Often, in the context of paramagnetic materials and the calculation of structural and NMR properties, a pragmatic approach has been followed, which consists of performing the calculations with HYB20 and HYB35 separately, and the respective results are considered to represent the upper and lower bounds of the experimental hyperfine shifts. [61, 90, 100]

2.4.5 Basis sets

The feasibility of the simulation of solid systems with *ab initio* calculations is based on the assumption that the atoms form an infinitely periodic lattice and they are at rest in their equilibrium positions. All the physical quantities of the system, as well as the electronic Hamiltonian, are translationally invariant with respect to the crystal, in other words the periodicity of the lattice makes the values of a function identical at equivalent points in the lattice. This allows to express the single particle electronic wavefunction as described by the Bloch theorem [101]

$$\psi_{\boldsymbol{k}\nu}(\boldsymbol{r}) \;=\; e^{i\boldsymbol{k}\cdot\boldsymbol{r}} u_{\boldsymbol{k}\nu}(\boldsymbol{r}) \tag{2.58}$$

$\boldsymbol{k}$ in equation 2.58 is the crystal momentum of the electrons describing the translational properties of the system, ν is a discrete index grouping states corresponding to the same $\boldsymbol{k}$-vector, and $u_{\boldsymbol{k}\nu}$ is a function of the same periodicity as the lattice. The translational invariance of the lattice allows to treat different $\boldsymbol{k}$-points independently. The periodicity of the Bloch equation allows to evaluate the wavefunction $\psi_{\boldsymbol{k}\nu}$ within just the so-called first Brillouin zone (BZ), which is the primitive cell in reciprocal space within which the $\boldsymbol{k}$-vectors are defined. This means that physical properties of the whole system such as charge density and band structure can be evaluated from the wavefunction within the BZ, or even in a smaller region of it depending on the symmetry of the crystal.

In order to solve the set of Kohn-Sham equations computationally, the electronic wavefunction needs to be expanded on a suitable basis set [102]. Two kinds of basis sets will be presented now, which will be used throughout this thesis.

Plane Waves

The expansion of the Bloch wavefunction in equation 2.58 in a Plane Wave (PW) basis set takes the following form:

$$\psi_{\boldsymbol{k}\nu}(\boldsymbol{r}) \;=\; \frac{1}{(N\Omega)^{\frac{1}{2}}} \sum_{\boldsymbol{G}} e^{i(\boldsymbol{k}+\boldsymbol{G})\cdot\boldsymbol{r}} c_{\nu}(\boldsymbol{k}+\boldsymbol{G}) \tag{2.59}$$

where Ω is the unit cell volume, $\boldsymbol{G}$ are the reciprocal lattice vectors and $c_{\nu}(\boldsymbol{k}+\boldsymbol{G})$ are the normalized coefficients. Although the PW expansion is exact in the limit of an infinite number of $\boldsymbol{G}$-vectors, in practice the expansion can be truncated to include only the plane waves contained within a sphere of a maximum kinetic energy value, known as the energy cut-off E_{cut}:

$$\frac{\hbar^2}{2m}|\boldsymbol{k}+\boldsymbol{G}|^2 \leq E_{cut} \tag{2.60}$$

The value of E_{cut} needs to be determined by varying it and studying the convergence of a certain property or parameter of interest, and it is in fact the only parameter that needs to be optimised to improve the accuracy of the PW basis set. However, despite the convenience of the PW expansion within a cut-off region, a very large number of $\boldsymbol{G}$-vectors (or a very large E_{cut}) would be needed to accurately describe the core electrons, due to the rapid oscillations of their wavefunction close to the nucleus. A common trade-off is the combination of the PW expansion with the pseudopotential (PP) approximation, which assumes that the majority of the physical/chemical properties mainly depend on

the behaviour of the valence electrons, while the core electrons can be considered as fixed (or frozen) in their atomic configuration [103]. Following this approach, the core electrons are not included explicitly in the calculation, and instead they are modelled as an the effective field acting on the valence electrons. Hence the potential is constructed to reproduce the true wavefunction beyond a certain distance from the nucleus, while replacing the core electron wavefunctions close to the nucleus with a smooth, *pseudo* potential.

Localised Gaussian Basis Functionals

A different approach calculates the single particle wavefunction, $\psi_{\boldsymbol{k}\nu}(\boldsymbol{r})$, as a linear combination of basis functions, $\phi_{\boldsymbol{\mu}\nu}(\boldsymbol{r})$, as:

$$\psi_{\boldsymbol{k}\nu}(\boldsymbol{r}) \;=\; \sum_{\mu} c_{n,\mu,k}\phi_{\boldsymbol{\mu}\nu}(\boldsymbol{r}) \tag{2.61}$$

where $\phi_{\boldsymbol{\mu}\nu}(\boldsymbol{r})$ is a linear combination of atomic orbitals (LCAO), in this thesis represented by a linear combination of primitive Gaussian type functions, and $c_{n,\mu,k}$ are the set of coefficients to determine [104]. Differently from the PW approach described earlier, for the localised Gaussian basis set the accuracy of the calculation depends on the number and shape of Gaussian primitives to describe each Gaussian type orbital, and in some cases a large basis set is necessary to accurately describe the wavefunction. On the other hand, compared to the PW-PP approach, the localised Gaussian type orbitals allow to explicitly treat core and valence electronic state and to perform all-electron calculations. [105–107] This is of great importance for accuracy of the calculated hyperfine interaction, which relies on the ability to calculate the unpaired spin density at the nuclear position.

2.5 Calculation of the Paramagnetic NMR Components

2.5.1 Hyperfine Tensor

In this Thesis, the DFT calculation of the Fermi contact and dipolar hyperfine terms in equation 2.16 follow the approach presented by Kim *et al.* [61] and Middlemiss *et al.* [63]. The unpaired electron spin density at the nuclear position, $\rho^{\alpha-\beta}(\mathbf{0})$, is calculated with DFT as the square modulus of the wavefunction (i.e. the probability of finding unpaired electron spins) at the NMR observed nucleus, $|\psi^{\alpha-\beta}(\mathbf{0})|^2$, and it is subsituted

into equation 2.16 to obtain A^{FC}. Similarly, the principal components of the dipolar hyperfine tensor, $\boldsymbol{A}^{\mathrm{dip}}$, in equation 2.16 are calculated with DFT as the integral over space of $|\psi^{\alpha-\beta}(\boldsymbol{r})|^2$, with $\boldsymbol{r}$ being the position vector originating at the NMR observed nucleus. The dipolar hyperfine tensor can be also computed, in the point-dipole approximation, as the sum of all the pair-wise dipolar interactions between the observed nuclear moment and each of the unpaired electron moments of the lattice. However, since in DFT the electron spin density is represented as a continuous field, the integral form in equation 2.16 needs to be implemented, instead.

The periodic DFT calculation provides the *total* $\rho^{\alpha-\beta}(\mathbf{0})$ (or $\rho^{\alpha-\beta}(\boldsymbol{r})$) at the NMR observed centre, which hence defines the *total* hyperfine tensor that we can call $\boldsymbol{A}_{\mathrm{DFT}}$. For computational convenience, the DFT single-point energy minimisations to calculate the unpaired electron spin density are performed nominally at 0 K, ignoring the electronic and lattice degrees of freedom, and in the ferromagnetic state, in which all the unpaired electron moments are aligned parallel to each other. Despite this does not necessarily correspond to the ground state magnetic configuration, it represents the system in the saturation regime of 0 K, and the expectation value of the unpaired spin moment is $\langle \hat{S}_z \rangle_{sat} = -S$, as in equation 2.24. However, experimentally the system experiences the weaker paramagnetic regime in which the average unpaired spin moment $\langle \hat{S}_z \rangle_{para}$ is defined (in the presence of magnetic exchange) by equation 2.26. Consequently, the paramagnetic shielding tensor in equation 2.34 can be obtained from the calculated $\boldsymbol{A}_{\mathrm{DFT}}$ by scaling it by $\frac{\langle \hat{S}_z \rangle_{para}}{\langle \hat{S}_z \rangle_{sat}}$: [61]

$$\boldsymbol{\sigma}^s = -\frac{\mu_B g_e S(S+1)}{3 g_i \mu_N k (T-\theta)} \frac{\boldsymbol{A}_{\mathrm{DFT}}}{S} \tag{2.62}$$

By comparing the form of $\boldsymbol{\sigma}^s$ in equation 2.62 with the expression in equation 2.34 it is clear that the *total* hyperfine tensor calculated with periodic DFT is none other than the hyperfine tensor defined in equation 2.15 multiplied by S, i.e. $\boldsymbol{A} = \frac{\boldsymbol{A}_{\mathrm{DFT}}}{S}$.

The accurate computation of the hyperfine interaction relies on the ability of evaluating the unpaired spin density (or wavefunction, $|\psi^{\alpha-\beta}(\boldsymbol{R}_N)|^2$) at the nuclear position and in space. For this reason, in previous works and in this thesis, the DFT calculations of the spin density are performed using hybrid functionals and an all electron basis of Gaussian-type orbitals [90]. A common choice as DFT code to this regard is CRYSTAL [108], which is an all-electron code using linear combination of Gaussian-type atomic orbitals, it implements hybrid functionals efficiently. It also allows to impose (i.e. *flip*) the spin orientation at the various paramagnetic centres using, as initial input, the wavefunction converged in the ferromagnetic alignment, hence reducing the computational cost of the

sequential ferrimagnetic calculations. The latter is an important feature if one wants to decompose the total (contact and/or dipolar) hyperfine interaction of a specific nuclear site into the separate contributions of each interacting paramagnetic centre, as it will be presented in Chapter 4 and 5 [63]. The calculation of the hyperfine interaction is in principle also possible with pseudo-potential based methods in the PW scheme. However, in PW methods, the accuracy of the calculated spin density at the nuclear position is poorer due to the approximate treatment of the core electrons, the implementation of hybrid functionals is more expensive due to the need to compute the long range Fock contributions, and performing ferrimagnetic calculations is more complicated due to the delocalised nature of the basis functions. Nonetheless, a recent work performed Li hyperfine shift calculations on paramagnetic solids, obtaining good agreement with the experimental NMR shifts [109].

2.5.2 Magnetic Exchange Coupling

As described earlier (equation 2.25), the magnetic Hamiltonian of an assumed Ising-type system, H_0, takes the form of

$$\hat{H}_0 \;=\; E_0 \;-\; \sum_n \sum_{i,j} J_n \hat{S}_i \hat{S}_j \tag{2.63}$$

with E_0 being the energy of the system excluding all the magnetic interactions, n the order of the interaction over the neighbouring shells, S the spin value of the (i, j) interacting sites with the respective exchange coupling constant, J_n, and where all the $2S + 1$ projections of the spin along z are included. In this Thesis as in previous works [66], J_n are determined by a multivariate linear regression of the DFT-calculated energies of the systems having different magnetic configurations of the coupled spins, obtained through the so-called spin-flipping method described in the previous Section. The total exchange interaction at a site i is expressed as a mean field, which is felt by the spin i, as well as by the neighbouring spins. The time-averaged spin of a site i, $\langle S_{z,i} \rangle$, is obtained by calculating the Brillouin function at a particular temperature and external magnetic field, and the mean field equations are solved self-consistently for all the spins in the cell. From the calculated $\langle S_{z,i} \rangle$, one can evaluate the scaling ratio in equation 2.62 either for the total cell, or for a specific site, i, such as $\frac{\langle S_{z,i} \rangle}{S_i}$.

2.5.3 g-tensor

If we compare the definition of the electron Zeeman (equation 2.12) and the hyperfine (equation 2.14) Hamiltonians, we notice that, unlike the hyperfine tensor that modulates the interaction between the nuclear and unpaired electron spins, the g-tensor modulates the interaction between the unpaired electron spin and the external magnetic field. Consequently, the g-tensor is calculated with DFT as a perturbative response of the system (or the all-electron wavefunction) to an applied uniform magnetic field. The implementation of the g-tensor that will be used in this Thesis is formulated within the PW-PP scheme. The calculation of this propety within the PW-PP approach poses two major challenges: *i*) the PW-PP description of electrons does not treat the core region explicitly but rather through the pseudopotential formalism, and *ii*) the calculation of response properties arises from the presence of a magnetic field.

To address the first problem, the projector augmented wave (PAW) method was introduced by Blöchl in 1994 [110], which allows to map the valence pseudo-wavefunction onto the corresponding all-electron wavefunction by introducing a linear transformation operator. This operator is applied to a set of pseudo-partial-waves to obtain the corresponding set of all-electron-partial-waves *via* the application of a set of projection operators. Each projector and partial wave is an atomic-like function centered at a precise position (named the gauge origin), conveniently the atomic centre. For each atomic site, a so-called augmentation region is defined such that, outside of it the pseudo- and all-electron-partial-waves coincide and the projector operators vanish, while within the augmentation region any valence all-electron wavefunction can be defined as a linear combination of all-electron-partial-waves. Also, it is assumed that the augmentation regions of different atomic sites do not overlap. This formulation allows to express the expectation value of a certain all-electron operator in terms of pseudo-wavefunctions.

However, due to the necessity of defining the origin of each augmentation region, a problematic spatial dependence arises when an external magnetic field is applied and the response properties are calculated. Although the ground-state Hamiltonian is translationally invariant, the new eigenstates pick up an additional phase factor proportional to the external magnetic field, and the exact translational invariance is no longer ensured in the PAW scheme. To restore the invariance upon translation, an additional field-dependent transformation operator is included, which contains a magnetic-field-dependent phase factor, effectively imposing translational invariance by canceling out the dependence on the gauge origin. This extension of the PAW formalism is called the Gauge Including Projector Augmanted Waves (GIPAW) method, and it constitutes the essential development to allow the accurate yet computationally affordable

calculation of magnetic perturbation properties such as chemical shielding and g-tensor in extended crystalline solids within the PW-PP approach. [111, 112]

In this thesis, the calculation of the g-tensor is based on the GIPAW method and follows the derivation of Pickard and Mauri in Ref. [113] in its implementation in the PW-PP code QuantumEspresso [114]. All g-tensor calculations were performed on the plane-wave code QuantumEspresso, as the CRYSTAL code does not support response property calculations and spin-orbit Hamiltonians. QuantumEspresso, however, does not support hybrid functionals efficiently. Hence, the pure DFT and DFT+U schemes were adopted for the calculation of the g-tensor.

Chapter 3

Unraveling the Complex Delithiation and Lithiation Mechanisms of the High Capacity Cathode Material V_6O_{13}

Abstract

This Chapter presents a first principles approach to rationalize the complex lithiation mechanisms in the V_6O_{13} cathode material. The study combines the DFT analysis with experimental *in situ* X-ray and ^{7}Li NMR characterisations to derive the local structural and electronic properties of the system during electrochemical cycling.

V_6O_{13} is a promising Li-ion battery cathode material for use in the high temperature oil field environment. The material exhibits high capacity, and the voltage profile contains several plateaux associated with a series of complex structural transformations. Understanding the underlying structural mechanisms that occur on electrochemical cycling is important in order to rationalise and improve the performance of V_6O_{13}-based materials for rechargeable batteries. In this study, the Li intercalation/deintercalation mechanisms of V_6O_{13} during charge and discharge are studied with *in situ* X-ray diffraction (XRD). The $Li_xV_6O_{13}$ unit cell expands sequentially in c, b, and a directions during discharge and reversibly contracts back during charge. The process is associated with changes in the Li ions positions as well as in the charge ordering in $Li_xV_6O_{13}$. The

complex ordering of the Li sites throughout the series is investigated with ^{7}Li MAS NMR spectroscopy. The NMR spectra indicate that the local structure and the Li environments change during electrochemical cycling in a step-wise fashion that follows the long-range structural changes identified with XRD. DFT calculations give further insight into the electronic structures and the preferred site configurations in the different structures formed upon cycling. The DFT analysis is also applied to investigate the Li migration mechanisms at early stages of lithiation, identifying low-energy migration pathways within the cavity between the VO_x single- and double-layer, and indicating the preferential Li diffusion along the *b*-axis of the lattice. DFT is also used to interpret the ^{7}Li NMR spectra for $x \leq 2$ by calculating site-specific ^{7}Li hyperfine shifts at different compositions and configurations. The combined first principles and experimental NMR analysis for the systems within Phase 1 ($x \leq 1.5$) indicate the presence of Li ions in several energetically stable sites, connected *via* a low-energy migration pathway. The analysis of the NMR spectra for Phase 2 ($1.5 < x \leq 2.0$) indicate a more complex distribution of Li environments, that is not reproduced by the ordered structures simulated with DFT. Our combined experimental and computational study sheds light into the high specific capacity of V_6O_{13} and is likely to aid in the development of this material for use as a cathode for secondary lithium batteries.

3.1 Introduction

Lithium ion batteries (LIBs) have seen widespread and rapidly expanding applications in numerous commercial and industrial fields, such as portable electronics, electric vehicles and renewable energy [115, 116]. In industries such as oil and gas, batteries have long been utilised in devices for measurement while drilling (MWD) and logging while drilling (LWD) [117, 118]. These tools provide field engineers with real-time information on the position and tilt of the wellbore, which is essential in directional drilling.

Primary (*i.e.* non rechargeable) batteries are more widely used in the oil and gas industries because the systems, such as $LiSOCl_2$, provide sufficient energy density and operate at the temperatures experienced in the downhole environment (up to 150°C), simplifying field inventory [117]. However, the high energy density of $LiSOCl_2$ results in intrinsic safety issues, including potential contact of lithium (Li) metal with water, and the susceptibility for cell explosions when externally shorted. Furthermore, primary batteries are less desirable for use in oil field applications due to the operation downtime that they cause when they need to be replaced. Field engineers have to pull out the tool kit before the batteries die and therefore interrupt the drilling. This accounts for a

significant cost, which can be minimised by using rechargeable batteries which could be recharged by mud turbines. However, common rechargeable Li-ion technologies cannot sustain such a large temperature range experienced in the downhole environment. In order to fulfill the need of downhole rechargeable batteries, materials with high specific and volumetric capacity, moderate cycle voltage and rate performance are highly sought after.

V_6O_{13} has been studied over the last 30 years as a battery cathode for rechargeable Li polymer batteries due to its high specific capacity, low cost and wide availability [119–124]. It has a theoretical capacity of 417 mAh/g, [125] corresponding to 8 Li per formula unit (vanadium being reduced from an average formal charge of +4.33 to +3), and a theoretical energy density of 890 Wh/kg [126]. Both stoichiometric and slightly oxidised V_6O_{13+y} with $y \leq 0.2$ have been prepared, resulting in differences in the maximum Li uptake and electrochemical capacity [127]. West *et al.* were able to cycle V_6O_{13} in a prototype polymer battery at 155°C, which demonstrates its suitability to be used as a high temperature secondary battery cathode material [126]. In recent years, V_6O_{13} nano-sized structures with different morphologies were fabricated to enhance performance at high rates and capacity retention after many cycles [128, 129]. However, as described in detail by Chernova *et al.*, several phase transitions are observed during charge and discharge, accompained by a significant rearrangement of the Li ions in the structure, which may contribute to the difficulties in attaining good long-term cyclability for the V_6O_{13} cells [123]. A detailed understanding of the long-range ordering as well as the local atomic structure is of central importance in order to be able to understand the electrochemical performance of the V_6O_{13} cathode material and to identify possible limiting factors.

Extensive efforts have been made to understand the discharge mechanism of V_6O_{13} using crystallographic approaches. The crystal structure of V_6O_{13} was first studied by Aebi in 1948 [130] and further refined by Wilhelmi *et al.* in 1971 [131]. These studies show that V_6O_{13} is monoclinic (space group $C2/m$) with unit cell parameters of $a = 11.922(2)$ Å, $b = 3.680(1)$ Å, $c = 10.138(2)$ Å, and $\beta = 100.88(1)°$. The crystal structure comprises edge and corner-sharing distorted VO_6 octahedra, which form alternating single and double VO_x layers connected via shared corners (Figure 3.1). It should be noted that although it is convenient to discuss the crystal structure in terms of single and double layers, the structure is fully connected in three dimensions. In fact, V_6O_{13} is not a two-dimensional layered structure as found for many intercalation materials, where there is strong bonding within layers, and weak interactions between layers.

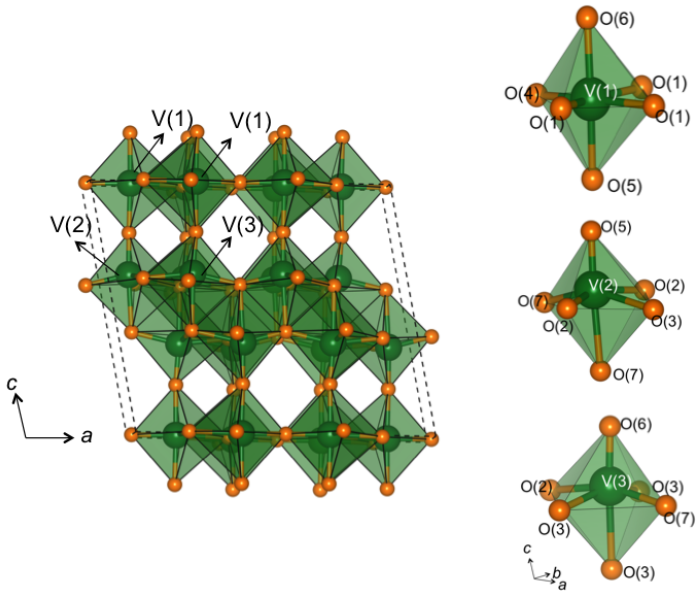

Fig. 3.1 Crystal structure of monoclinic V_6O_{13} (C2/m). The three crystallographically non-equivalent vanadium sites in V_6O_{13} are shown separately, displaying the distorted octahedral environments. Vanadium and oxygen atoms are represented by green and orange spheres respectively. The dashed lines show the unit cell. The V_6O_{13} structure is composed of layers of edge- and corner-sharing distorted VO_6 octahedra that are stacked along the *c* axis. Infinite channels extend along the *b* axis, and may facilitate intercalation of Li ions.

V_6O_{13} contains three crystallographically non-equivalent vanadium atoms, V(1), V(2), and V(3), (Figure 3.1), where the vanadium centres are mixed valence with an average vanadium formal charge of $V^{4.33+}$. The bond valences, as estimated by Wilhelmi *et al.* of 4.20, 4.67, and 4.37, respectively, suggest that the V^{5+} centres are mainly located in the $V(2)O_6$ octahedra.[131] In 1998, Bergström *et al.* performed a deformation electron density refinement on single crystal data and also assigned the oxidation state of V(2) to +5, assuming a simplistic mode of integer oxidation states [132]. V_6O_{13} is metallic at room temperature but becomes less conductive upon lithiation [126, 133].

When discharging V_6O_{13} as a cathode against a Li anode, the discharge curve shows numerous voltage plateaus corresponding to different $Li_xV_6O_{13}$ phases formed by Li ions intercalating in between the VO_6 slabs [126, 135]. Several research groups have carried out detailed investigations to understand the intercalation mechanism. Impedance spectroscopy studies of different single crystal surfaces performed by West *et al.* showed that Li ion diffusion into single crystal V_6O_{13} is a one dimensional (1D) process along the *b* axis [120]. In 1992, Gustafsson *et al.* used *in situ* X-ray diffraction (XRD) to monitor the structural changes of V_6O_{13} in a polymer battery during discharge [122].

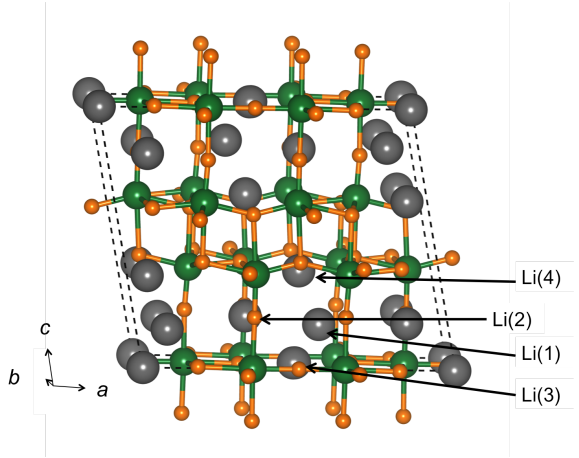

Fig. 3.2 Possible Li intercalation sites in V_6O_{13} unit cell calculated using a combination of classical pair potential and DFT methods [134]. Vanadium, oxygen and lithium atoms are represented by green, orange and grey spheres, respectively. Four possible low defect-energy Li sites were previously predicted in the V-O cavity; the Li(1) site was found to be the lowest energy site [134], and the only site observed in previous single crystal studies of $Li_xV_6O_{13}$ for $x \leq 2$ [130, 133, 135].

They observed substantial changes in both peak positions and intensities but reported only minimal details on the structural changes. Further single crystal XRD studies were performed on V_6O_{13}, [132] as well as the Li-enriched phases $Li_{0.67}V_6O_{13}$ [136], LiV_6O_{13} [136], $Li_2V_6O_{13}$ [137], $Li_3V_6O_{13}$ [134], and $Li_{3.25}V_6O_{13}$ [138], which showed that Li ions occupy the Li(1) position (Figure 3.2) and form a square pyramidal coordination with the neighbouring oxygen atoms in $Li_xV_6O_{13}$ when $x \leq 2$. The Li(1) site is proposed to be partially occupied in both $Li_{0.67}V_6O_{13}$ [136] and LiV_6O_{13} [136], but long range ordering of the Li ions and vacancies occurs, resulting in superstructures of the original V_6O_{13} phase. Based on single-crystal XRD, the Li(1) sites are fully occupied in $Li_2V_6O_{13}$, further Li insertion into the crystal structure resulting in a rearrangement of the Li ions to occupy sites in both the single and the double layers (i.e., Li(3) and Li(4)). In 2001, Braithwaite *et al.* used a combination of classical pair potential method and DFT calculations to identify Li intercalation sites [139]. These calculations indicate that there are (at least) four sites within the cavities between the single and double layers (Figure 3.2), which includes the Li(1), Li(3) and Li(4) sites observed in the single crystal studies and one additional site, Li(2).

Thackeray *et al.* reported that further lithiation to $Li_7V_6O_{13}$ can be achieved [135]. Schmitt *et al.* used soft X-ray absorption spectroscopy [140] and soft X-ray emission spectroscopy [141] to study the Li insertion, especially beyond $Li_3V_6O_{13}$, and found that $Li_4V_6O_{13}$ and $Li_5V_6O_{13}$ may be composed of two phases. The charging mechanism of

V_6O_{13} remains largely unknown. An understanding of the whole series of structural changes of V_6O_{13} during discharge and charge underpins future studies aimed at improving the performance of this material as cathode in a rechargeable Li-ion battery.

This work performs electrochemical *in situ* XRD measurements to study the lithium intercalation/deintercalation mechanisms of V_6O_{13}, and the associated changes in the lattice parameters. *Ex situ* ^{7}Li solid-state MAS NMR is also performed throughout the $Li_xV_6O_{13}$ series, to differentiate between the various Li local environments present at different lithiation stages during the electrochemical cycling. In order to identify the stable cation configurations of the series and to study the thermodynamical phase stability of the discrete members of $Li_xV_6O_{13}$ ($x = 0, 1, ... 9$), DFT calculations of the formation enthalpies of the different phases are performed. The Li-ion mobility in the V_6O_{13} host at low stage of lithiation ($x < 1$) is also studied with DFT, identifying Li migration pathways accessible at the typical battery operating conditions (~ 300 K). For $x = 1$ and 2, DFT calculations of the ^{7}Li NMR hyperfine shift are presented for different configurations, and used to rationalize the complex ^{7}Li NMR spectra obtained experimentally for $x \leq 2$.

Part of the work presented in this Chapter (*in situ* XRD and formation energy analysis with DFT) was published in the paper "Unravelling the Complex Delithiation and Lithiation Mechanisms of the High Capacity Cathode Material V_6O_{13}" [142]. The rest of the Chapter (^{7}Li MAS NMR, DFT analysis of Li migration and DFT calculations of ^{7}Li hyperfine shift) is included in the manuscript "Toward a High Temperature V_6O_{13} Based Lithium-Ion Battery", currently in preparation. The whole work presented in this Chapter benefited from the intellectual input of all the co-authors of this project, Wei Meng, Paul Bayley, Oliver Pecher, Michael Gaultois, Ieuan Seymour, Han-Pu Liang, Wenqian Xu, Kamila Wiaderek, Karena Chapman, and Clare Grey. Wei Meng performed the synthesis of the material, as well as the *in situ* XRD and the ^{7}Li NMR measurements. The current author performed all of the computational analysis.

3.2 Experimenal Methods

3.2.1 Materials

The starting material V_6O_{13} (99.6%, 20 mesh) was purchased from EVRAZ Stratcor, Inc., USA. To decrease the amount of other vanadium oxide impurities and increase crystallinity, [143] the powder was thermally annealed at 500°C under Ar for two hours.

3.2.2 *In situ* XRD Measurements

In situ synchrotron XRD data were acquired in transmission geometry at beamline 17-BM of the Advanced Photon Source at Argonne National Laboratory (wavelength 0.7295 Å, 500 μm diameter beam), using a 2D area detector (Perkin-Elmer). Measurements were performed at a sample-to-detector distance of 300 mm. Each pattern was collected for 10 seconds. Whole pattern fitting was performed using the Topas v4.1 and GSAS-II software packages [144]. The peak shape profile was determined by the modified Thompson-Cox-Hastings function; [145–147] a NIST LaB_6 standard was run separately and used to refine the instrument peak profile and the parameters, which were used for the whole series of dataset. A linear absorption correction and sample displacement were determined from one pattern and then fixed for the remaining scans. To model the complicated background (which includes the contributions from Kapton film, glassy carbon window, glass fibre separator, carbon in the electrode, and air scattering) a combination of log interpolation between 12 average values observed in regions well away from the peaks was used, along with 5 synthetic peaks to model features from amorphous materials. Unit cell parameters and isotropic strain were refined for all scans using the Pawley method [148]. Rietveld refinement [146] was performed to determine phase fractions for two-phase regions. Atomic positions were fixed to values reported in previous single crystal studies [132, 136, 137, 134], and a preferred orientation correction was also added to account for the morphology of the material and the pellet electrode.

3.2.3 *Ex situ* ^{7}Li MAS NMR Experiments

Measurement techniques and line shape fitting: Solid-state ex situ MAS ^{7}Li NMR experiments were performed on a Bruker AVANCE III spectrometer with a magnetic field of $B_0 = 4.7$ T. The corresponding resonance frequency of ^{7}Li was 77.74 MHz. The NMR signals are referenced to a 1 M solution of LiCl in D_2O [149]. MAS NMR experiments were carried out at a spinning speed of 60 kHz under ambient temperature conditions without additional temperature control, and using a ZrO_2 rotor (1.3 mm diameter) in a Bruker 1.3 mm double resonance MAS NMR probehead. ^{7}Li NMR signal line shapes were acquired by single pulse experiments with high-power pulses of 2.12 μs in length. NMR raw data handling and line shape deconvolution was done using Bruker Topspin within the SOLA program. All sample handling was done under an Ar atmosphere in a MBraun glovebox with water and oxygen levels below 0.1 ppm to avoid contamination and/or reaction with moisture and air. $Li_xV_6O_{13}$ powder samples were prepared by electrochemically cycling V_6O_{13} and Super P carbon powder mixtures (approximately 20

mg, weight ratio 8:2) at C/10 in two-electrode Swagelok cells at ambient temperature using a Biologic VSP cycler. Cell cycling was stopped at Li uptakes corresponding to nominal compositions of $Li_{1.2}V_6O_{13}$, $Li_{2.0}V_6O_{13}$, $Li_{3.9}V_6O_{13}$, and $Li_{6.4}V_6O_{13}$ upon discharge as well as $Li_{6.7}V_6O_{13}$, $Li_{3.8}V_6O_{13}$, and $Li_{1.1}V_6O_{13}$ upon charge. The powder samples were collected from disassembled cells, washed in dimethyl carbonate (DMC) three times, and dried under vacuum overnight.

3.2.4 Density Functional Theory (DFT) Calculations

DFT+U Calculations of Formation Energies

Spin-unrestricted solid-state DFT simulations of the electronic structure and phase energetics were performed in the Vienna Ab initio Simulation Package (VASP5.3) [150]. The projector–augmented wave (PAW)[151] approach was used. The plane-wave energy cutoff value was set to 520 eV. For the PAW sets, the *s* semicore states were treated as valence for Li and V, and the standard PAW set was used for O. Each simulated cell contained one $Li_xV_6O_{13}$ formula unit, hence the simulated cell of V_6O_{13} contained 19 atoms (6 × V and 13 × O), the cells of LiV_6O_{13} contained 20 atoms (1 ×Li, 6 × V and 13 × O), and likewise throughout the $0 \leq x \leq 9$ series. The Brillouin zone was sampled using a gamma-centred *k*-point mesh of 4 × 10 × 4. Full optimization of the atomic positions and cell parameters and total energy calculations were performed in the absence of symmetry constraints, in which the energy of the total cell and the root-mean-square forces was converged to 10^{-6} eV and 10^{-5} eV/Å, respectively. The Perdew–Burke–Ernzerhof (PBE) [89] exchange-correlation functional was used, applying a Hubbard U model [91, 152] within the rotationally invariant formalism proposed by Liechtenstein *et al.* [94] to correct for the known deficiencies of pure functionals for highly localized 3*d* states. The on site Coulomb (U) and exchange (J) parameters of 4.5 eV and 1 eV were chosen for vanadium in line with previous work on V_6O_{13} [153].

The thermodynamical phase stability at 10 Li compositions of the $Li_xV_6O_{13}$ series ($x = 0, 1, 2...9$) were assessed by comparing the formation enthalpy of different phases. The $Li_9V_6O_{13}$ structure was included as a model structure to enable the generation of all possible configurations for the intermediate stages of lithiation, although its formation electrochemically is thought to be unlikely. The initial $Li_9V_6O_{13}$ structure, shown in Figure 3.3 was modeled with the $C2/m$ space group, with two additional Li sites Li(5) (square pyramidal) and Li(6) (square planar LiO_4) included in addition to Li(1) – Li(4). The Li(1) site was not directly included in the $Li_9V_6O_{13}$ structure due to the small distances between neighboring Li sites at high degrees of lithiation. All intermediate Li compositions,

$Li_xV_6O_{13}$ were derived by partially delithiating the $Li_9V_6O_{13}$ structure and enumerating all symmetrically distinct orderings using the Cluster-Assisted Statistical Mechanics (CASM) software [154, 155]. The computed structures were generated from the primitive cell of $Li_9V_6O_{13}$, containing 28 atoms, in which the distortion in the vanadium octahedra was removed artificially. Consequently, the primitive cells computed with DFT contain half of the atoms of the cells reported in the single crystal studies [136, 137, 134, 138]. A total number of 272 configurations were generated, with 1, 5, 20, 44, 66, 66, 44, 20, 5, 1 configurations for V_6O_{13}, $Li_1V_6O_{13}$, $Li_2V_6O_{13}$, $Li_3V_6O_{13}$, $Li_4V_6O_{13}$, $Li_5V_6O_{13}$, $Li_6V_6O_{13}$, $Li_7V_6O_{13}$, $Li_8V_6O_{13}$ and $Li_9V_6O_{13}$, respectively. From the calculated DFT total energy, E, of each configuration, the formation energy per formula unit was calculated, as [156]

$$\Delta E(x) \;=\; E(\mathrm{Li}_x\mathrm{V}_6\mathrm{O}_{13}) \;-\; (1-\frac{x}{9})E(\mathrm{V}_6\mathrm{O}_{13}) \;-\; \frac{1}{9}E(\mathrm{Li}_9\mathrm{V}_6\mathrm{O}_{13}) \tag{3.1}$$

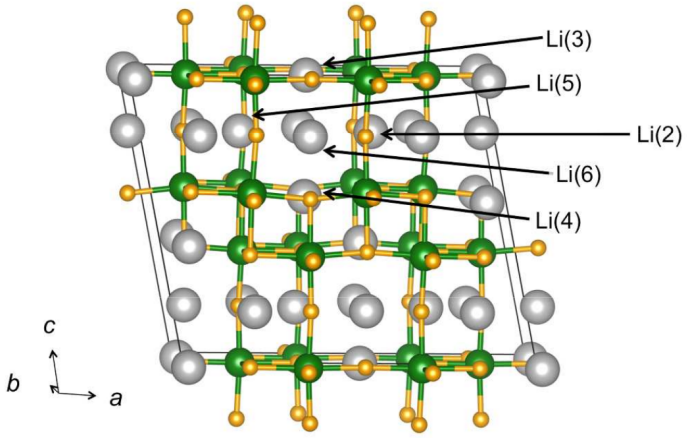

Fig. 3.3 Structure of the $Li_9V_6O_{13}$ cell, used in the convex hull analysis to generate the possible configurations in the $0 \leq x \leq 8$ range.

Transition State Searching

The migration pathways and energy barriers associated with Li diffusion were investigated for systems containing a dilute Li ion in the V_6O_{13} host structure, corresponding to an overall composition of $Li_{1/6}V_6O_{13}$. The simulated cell was obtained by applying a $3 \times b$ expansion of the V_6O_{13} unit cell, with the subsequent inclusion of one Li ion, obtaining a supercell with 115 atoms (1× Li, 78× O, 36× V).

The transition state searching was performed using a hybrid eigenvector-following approach in the OPTIM code, which interfaces with VASP to calculate energies and forces (gradients). Details of the hybrid eigenvector-following approach were described in

previous work [157–160]. For the transition-state search calculations, the convergence of the variational calculations was set to a root-mean-square gradient below 0.025 eV $Å^{-1}$, for a maximum of 50 iterations, and the change in the smallest eigenvalue was $< 25\%$ below the Rayleigh-Ritz steps. The atomic coordinate displacement step was set to 0.1 Å. The starting configurations were set by manually displacing the Li ion of interest by 0.2 Å in the direction of the proposed pathway. Regarding the VASP calculations coupled with the transition state searches, the same functional, convergence criteria and Hubbard corrections described in the previous Section were applied, with the exception of the k-point grid which was in this case set to $1 \times 1 \times 1$.

Hybrid DFT/Hartree Fock Calculations of Paramagnetic Shifts

The calculations of ^{7}Li Fermi contact shifts for LiV_6O_{13} and $Li_2V_6O_{13}$ were performed in CRYSTAL09 [161], a solid-state DFT code using all-electron Gaussian-type basis sets to accurately describe core states. All-electron atom-centred basis sets comprising fixed contractions of Gaussian primitive functions are employed. Because of the high dependence of the calculated paramagnetic shifts on the quality of the Gaussian basis sets, two levels of basis sets were used [61]. For the geometry optimizations, the basis sets used in this work were taken from the CRYSTAL online repository [162], obtained from Ref. 163 for Li, Ref. 164 for O and Ref. 165 for V. More extended sets were used for the hyperfine shift calculations, adopting the modified IGLO-III set for O [166], the flexible and extended TZDP-derived set for Li [167], and the Ahlrichs DZP-derived set for V [168].

All calculations were performed with hybrid functionals in the spin polarized state. Previous *ab initio* studies on ^{7}Li paramagnetic NMR shifts show that values obtained using 20% and 35% Hartree Fock (HF) exchange provide the upper and lower bounds for the experimental shifts [61–63]. Hence separate calculations were performed with the B3LYP functional with 20% HF exchange [169] (denoted HYB20) and a modified B3LYP with 35% of HF exchange (denoted HYB35). The starting LiV_6O_{13} and $Li_2V_6O_{13}$ structures were taken from our previous formation energy analysis performed with VASP, and subsequently re-optimized using CRYSTAL. The LiV_6O_{13} and $Li_2V_6O_{13}$ unit cells used in CRYSTAL contain, respectively, 40 atoms (2×Li, 26× O, 12× V) and 42 atoms (4×Li, 26× O, 12× V). The reciprocal space sampling was performed with a k-point grid of $4 \times 10 \times 4$ points in all the simulated cells. All geometry optimizations were performed using the CRYSTAL default convergence criteria. Self-consistent field cycles were converged to an energy difference of 2.7×10^{-6} eV.

The Fermi contact contribution to the hyperfine shift was computed directly from the spin density at the Li nuclear position in the ferromagnetic state and subsequently scaled to a value consistent with the paramagnetic state, as described previously by Kim *et al.* [61]. The Weiss constant of −100 K was obtained from a previous magneto-torque study on V_6O_{13} [170]. The spin-only magnetic moment was used, calculated as $\mu_s = g_e\sqrt{S(S+1)}$, with $g_e = 2.00023$ and $S = 0, 1/2$ for V^{5+} and V^{4+}, respectively. In the cases for which the Li shift was decomposed into Li–O–V bond-pathway contributions, the approach of Middlemiss *et al.* was followed [63]. Starting from the wavefunction converged for the system in the ferromagnetic state, the sign of the spin of one V site connected to the Li of interest is reversed, and the Fermi contact shift is calculated for this ferrimagnetic state. Half the difference between the ferromagnetic and the ferrimagnetic hyperfine shifts corresponds to the contribution of the particular Li–O–V bond-pathway. In order to avoid double-counting, for the cells used for the bond-pathway decomposition of the shift, a $2 \times b$ expansion was performed, and the $4 \times 10 \times 4$ k-point grid was applied.

3.3 Results and Discussion

3.3.1 Sequential Change of Lattice Parameters from *In situ* XRD

The changes in lattice parameters were obtained from the analysis of the *in situ* XRD patterns collected during the first cycle of the C/10 galvanostatic discharge and charge of V_6O_{13}. Full details of the procedure are presented in Ref. [142]. The analysis of the lattice parameters reveals in detail the sequential change of a, b and c, and of the volume (Figure 3.4). The results are summarised in Figure 3.5. Two main features are identified:

- *Each solid solution phase expands/shrinks in a preferred direction*

  On discharge, the most noticeable changes in cell parameters in both Phase 1 ($0 < x \leq 1.7$) and Phase 2 ($1.7 < x \leq 2.1$) occur along the c direction. Phase 1 expands in c by 4.5%, while a and b remain unchanged. Phase 2 shows a further expansion along c, with the end of Phase 2 ($x = 2.1$) showing a 7.0% expansion along the c axis with respect to the pristine cell. Phase 3 starts with $Li_3V_6O_{13}$ in which the c-axis has returned back to the pristine case (as well as a), but with b expanded by 6.4%. At the end of Phase 3 ($Li_{4.8}V_6O_{13}$), the b value reaches 7.9% expansion compared to V_6O_{13}. At the beginning of Phase 4 ($Li_{6.2}V_6O_{13}$), b is 8.9% greater than the pristine value, and also the a parameter expanded by 2.5%. By the end of Phase 4 ($Li_{6.7}V_6O_{13}$), the cell shows an overall 3.7% and

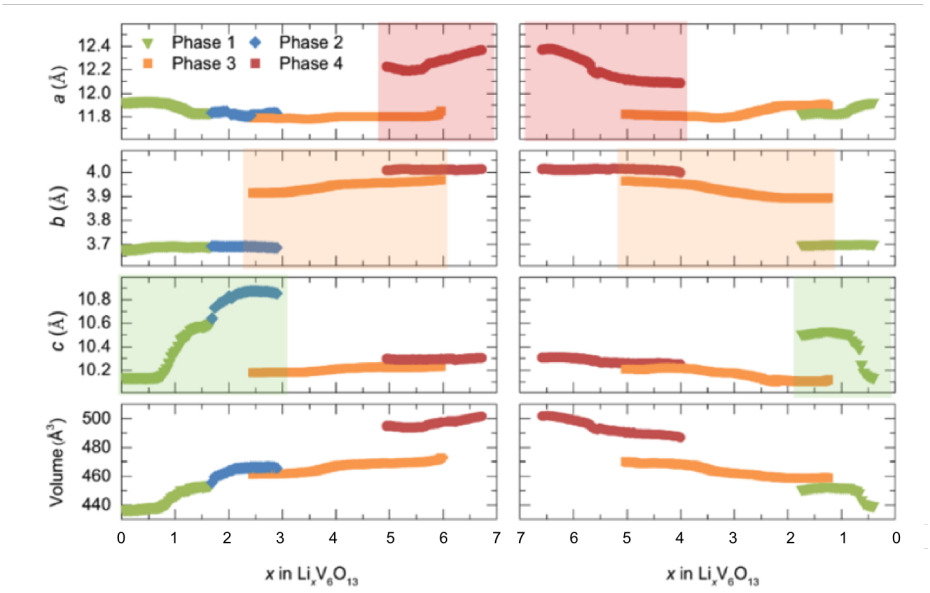

Fig. 3.4 Evolution of lattice parameters of the four phases observed during the first discharge (left) and charge (right). The unit cell expansion is driven by sequential growth along a preferred direction of the unit cell highlighted in the shaded region. While one unit cell parameter increases dramatically, the others remain relatively unchanged. Li incorporation upon discharge is accommodated first by elongating the c lattice parameter by 7.0%, after which expansion occurs predominantly in the b lattice parameter (1.6%), and finally the a lattice parameter (3.3%). The reverse process is mirrored upon charge.

9.0% expansion along a and b, respectively. The lattice changes on charge follow a similar and reversible trend, which is summarised in Figure 3.5, with the exception of an extended miscibility gap between $x = 2.3$ and $x = 1.4$, and the consequent disappearence of Phase 2 on charge.

- *First order phase transitions are accompanied by abrupt changes of lattice parameters in one or more directions*

  The first-order phase transition from Phase 2 to Phase 3 on discharge causes the lattice parameters b and c to change abruptly in opposite directions. At the end of Phase 2 ($x = 2.1$), the c parameter shows a 7.0% expansion, while the b parameter is unchanged from the pristine case. Phase 3, however, begins ($x = 3$) with a c parameter compareable to the value of the V_6O_{13} cell, and the b value expanded by 7.0%. The first-order phase transition between Phase 3 and Phase 4 causes abrupt change mainly along the a direction (3.3% expansion).

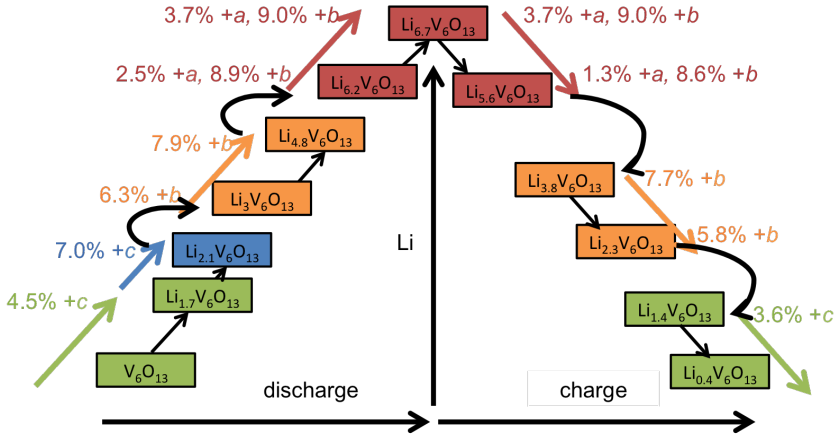

Fig. 3.5 Proposed mechanism of the first discharge and charge process of V_6O_{13} determined by in situ XRD. The most significant change in lattice parameters of Phase 1 (green), Phase 2 (blue), Phase 3 (orange) and Phase 4 (red) are shown in arrows above corresponding phases, where the %s correspond to changes within the phase and between phases. Solid solutions are represented by black arrows pointing from the starting phases to the end phases, while miscibility gaps are shown by curved black arrows.

3.3.2 Linking Structural Changes with Electronic Structure *via* DFT

The low energy structures from V_6O_{13} to $Li_9V_6O_{13}$ calculated with DFT are shown in Figure 3.6. The availability of a series of multiple configurations with the same composition allows the effect of Li positions and electronic structure on the V–O distances and cell parameters to be explored, and the lattice parameters of $Li_xV_6O_{13}$ are found to be highly sensitive to the Li positions. For $x = 1$, the DFT results show that the Li(1) position is the energetically most favourable site at this composition, with the lowest energy configuration having half-filled Li(1) sites. Although the Li(1) site was not directly included in the initial enumeration of the DFT structures, it was found to be present in a number of the structures after geometry optimization. The LiV_6O_{13} structure initially containing 1 Li atom per cell in the Li(3) site relaxed after structural optimization (and energy minimization) to cells containing Li on the Li(1) sites. As that the unit cells computed in the DFT analysis contain only one Li atom, the alternation of Li(1) occupancy reported in the single crystal study could not be captured in our DFT analysis, which would require a doubling of the unit cell in the a-direction [136]. In $Li_2V_6O_{13}$, (i.e., a composition within Phase 2), the lowest energy structure found with DFT shows half occupancy in both Li(2) and Li(5) sites. This result is different from the single crystal analysis, where the Li(1) site was reported to be fully occupied. Full

occupancy of the Li(1) site results in a significant expansion of the cell along the c axis of 8.5% in the DFT-derived structure, which is in agreement with the lattice parameter changes obtained experimentally in our *in situ* XRD. The lowest energy structure found with DFT, on the other hand, shows a reduced expansion along the c axis (2.7%). The single crystal derived (full occupancy of Li(1)) DFT-structure and the lowest energy structure differ in energy per atom by only 5 meV per atom. This energy difference is within thermal energy at room temperature ($kT \sim 26$ meV, k being the Boltzmann's constant), and the structures are both considered accessible at room temperature, as well as within DFT error. A more careful analysis of the effect of temperature, using *e.g.* phonon calculations within the harmonic approximation, would be needed in order to fully assess the relative stability of these structures with temperature, which is beyond the scope of the current work. Given the subtle energy differences, the kinetics associated with lithium reorganization and concomitant distortions of the VO_x layers may also play a role in dictating the experimentally observed Li-ordering schemes.

The *in situ* XRD results show that $Li_3V_6O_{13}$ corresponds to the beginning of a new phase (Phase 3), which is characterized by a 6% expansion of b compared to the pristine case, while the a and c are the same as the V_6O_{13} cell. The lowest energy $Li_3V_6O_{13}$ structure calculated with DFT is 5 meV above the hull, and it shows half occupancy of the Li(4) site and full occupancy of the Li(2) site, leading to a major 4.5% expansion along b, and a minor 1.5% expansion along a and c, in agreement with the lattice changes measured with XRD. All the configurations above this lowest energy structure (within $\Delta E < 0.01$ eV) contain partial occupancy of the Li(4) site, and they all show a predominant expansion of the b parameter between 4% and 6%. This suggests that the Li in the Li(4) site is the major cause of the b expansion. Previous single crystal studies of $Li_3V_6O_{13}$ proposed full occupancy of the Li(4) and Li(3) sites [134]. This configuration is found by our DFT results to have a 5.5% expansion along b, consistent with the *in situ* XRD results, and to be 6 meV higher in energy than the lowest energy configuration, i.e. within thermal energy and DFT error.

The structural rearrangements upon lithiation described so far are associated with a redistribution of electrons within the vanadium d orbitals, shown by our DFT calculations and illustrated in Figure 3.7 for $x = 0, 1, 2$ and 3 (for the DFT structures with Li site occupancies and cell parameters that are closest to those of the single-crystal derived structures). Spin density maps were generated from the (spin-polarised) DFT calculations and shown with isosurfaces, spin-density illustrating reduction of the diamagnetic V^{5+} ion. The change in oxidation states of the vanadium sites on lithiation were analysed by comparing charge density of the different $Li_xV_6O_{13}$ systems with those of the starting

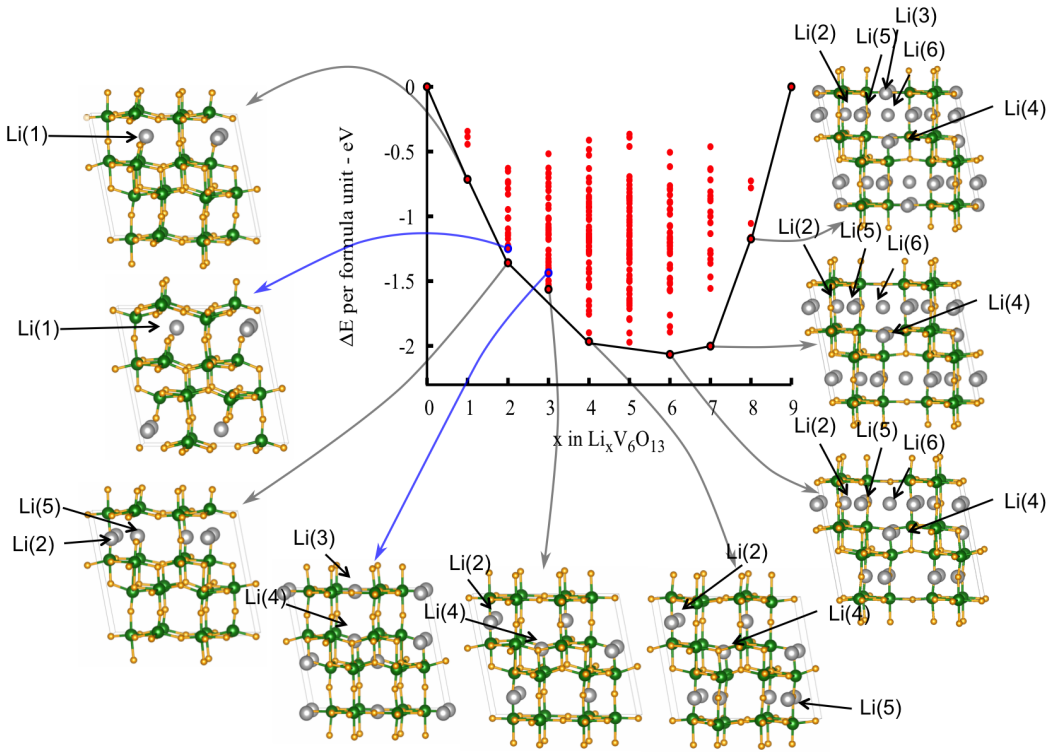

Fig. 3.6 Formation enthalpy per formula unit versus the fractional lithium concentration in $Li_xV_6O_{13}$. The convex hull, indicated by the line, is constructed by joining the stable structures obtained by the searches. The grey, green and yellow spheres in selected structures represent lithium, vanadium, and oxygen centers respectively. The structures with the lowest energy for LiV_6O_{13} to $Li_9V_6O_{13}$ (circled by black), as well as the structures with the single crystal Li-site occupancies for $Li_2V_6O_{13}$ and $Li_3V_6O_{13}$ (indicated by blue circles and arrows) are shown.

material V_6O_{13}. In the pristine V_6O_{13} phase, the V(2) sites are all V^{5+}, in agreement with previous work [132], while the unpaired electron on each of the V(3) sites is localized in the d^1_{xy} orbital. Orbital ordering of the V^{4+} V(1) centres, on the other hand, shows an alternation of d^1_{xz} and d^1_{yz} orbitals along the single layer. A previous study showed that V_6O_{13} has a metal insulator transition at 150 K and the symmetry is lower in the low temperature phase [171–173]. Given that this material is metallic at room temperature, it is likely that this orbital ordering does not persist at ambient temperatures. During the next stage of lithiation to LiV_6O_{13} (within Phase 1), the V(2) sites close to the Li inserted in Li(1) remain V^{5+}, while the other V(2) sites, opposite to the inserted Li, are reduced to V^{4+}, with the unpaired electron localised on a d^1_{yz} orbital. Similarly, the V(1) sites close to the occupied Li(1) site now show d^1_{xy} orbital occupancy, while the remaining V(1) remains d^1_{yz} , as in pristine V_6O_{13}. In the next stage of lithiation to

$Li_2V_6O_{13}$ (within Phase 2), the V(2) sites are reduced to V^{4+}, resulting in an alternation of V(2)-d^1_{xy} and V(3)-d^1_{yz} orbitals in the vanadium double layer, which is related to the different distance of V(2) and V(3) to the fully occupied Li(1) sites. The V(1) sites, now all at equal distance from the Li(1) centres, contain their unpaired electrons localized on the d^1_{xy} orbitals. These changes in the distribution of the electron density determine the elongation of both the V(1)-V(2) distance and even more so the V(1)-V(3) distance, reflecting the *c*-expansion reported for the whole range from V_6O_{13} to $Li_2V_6O_{13}$. In the next step of lithiation (to form Phase 3, $Li_3V_6O_{13}$), calculations show that the V(1) sites are preferentially reduced from V^{4+} to V^{3+}, resulting in an alternation of d^2 ($d^1_{xy} - d^1_{yz}$ or $d^1_{xy} - d^1_{xz}$) and d^1_{yz} orbital ordering along the single layer. The V(2) and V(3) centres are now both of d^1_{xy} configuration. The redistribution of charge density determines an elongation of the V(1)-V(1) distance along the *b*-axis, and a contraction of the V(1)-V(2) distance along *c*, consistent with the lattice expansion associated with this transition, as described earlier. The alternation of d^2 and d^1_{xz} in the V(1) single layer is very sensitive to the position of the Li(3) sites, as shown in detail in Figure 3.8. The $Li_3V_6O_{13}$ single crystal X-ray refinement [134] showed disorder of the lithium atom situated on the inversion centre in the single layer – the Li(3) site – and structure was modeled with a split position generating sites 0.3 Å above and below the single layer. Different $Li_3V_6O_{13}$ structures with Li(3) off-centred within this range were simulated with DFT. Following geometry relaxation, the change in the unit cell parameters is less than 1%, and the difference in energy per atom is less than 8 meV, suggesting that these conformers are degenerate at room temperature.

Upon further lithiation within the whole Phase 3 region from $Li_3V_6O_{13}$ to $Li_{4.8}V_6O_{13}$, *in situ* powder XRD shows that *b* expands continuously by 1.6%. Based on the DFT results on the $Li_4V_6O_{13}$ structures, the cells that show a major expansion along *b* (about 5% with respect to V_6O_{13}), and minor changes along *a* and *c* (below 2% with respect to V_6O_{13}) are the ones having full or partial occupancy of Li(2), and full or partial occupancy of Li(3), Li(4) or Li(5). The lowest energy structure has full Li(2) and half Li(4) and Li(5) occupancy, with an associated 4.7% expansion along *b* and a more limited expansion ($< 2\%$) of *a* and *c*, which reflect the XRD results. Among the other low energy structures, isotropic expansion along *a*, *b* and *c* of around 3% is observed for partial occupancy of Li(2), Li(5) and Li(6), while significant expansion (around 5%) of the *a* axis is observed when Li is present on the Li(1) site, which is not consistent with the *in situ* XRD results, suggesting that Li in the Li(1) site is no longer present at $x > 3$. The noticeable change in the *a*-parameter between Phase 3 ($x = 4.8$) and Phase 4 ($x = 6.2$) indicates that the Li ions redistribute again at this first order phase transition.

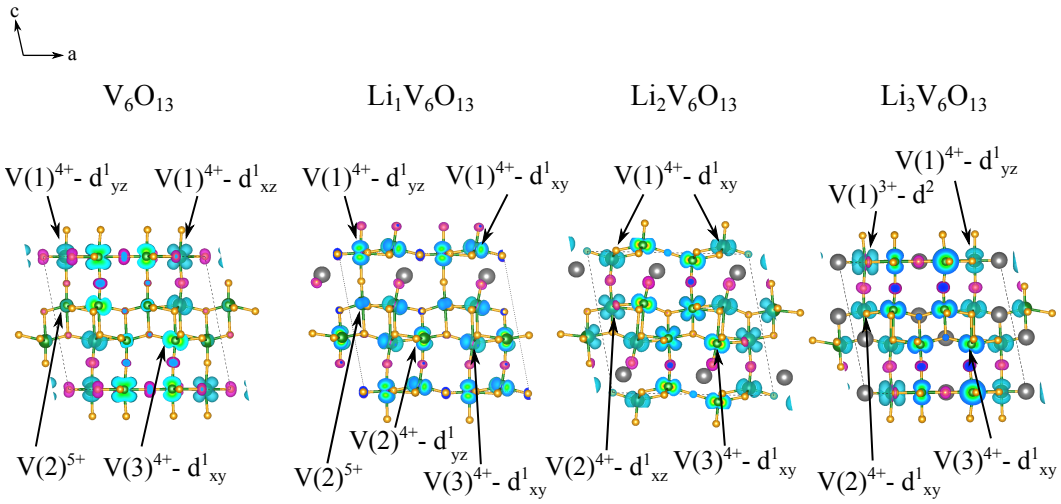

Fig. 3.7 Isosurface of the unpaired electron distribution in V_6O_{13}, LiV_6O_{13}, $Li_2V_6O_{13}$ (Phase 2), and $Li_3V_6O_{13}$ (Phase 3) calculated with DFT. Vanadium, oxygen and lithium centers are shown with green, orange and grey spheres, respectively. In V_6O_{13}, the V^{5+} ions are located in the double layer and the unpaired d electrons occupy different t_{2g} orbitals in the V^{4+} atoms. All the V^{5+} sites are reduced to V^{4+} when two Li ions are inserted into V_6O_{13} and a redistribution of the occupancy of the t_{2g} orbitals occurs for all the vanadium atoms, indicating a substantial change in electronic structure. $Li_3V_6O_{13}$ has a similar charge distribution to that found in V_6O_{13}, except for the vanadium sites ($V(2)^{5+}$ to $V(2)^{4+}$, $V(1)^{4+}$ to $V(1)^{3+}$) that are reduced. Blue and magenta isosurfaces correspond to positive and negative unpaired spin density, respectively, and are plotted with an isosurface level of 0.008.

The lattice parameters extracted from *in situ* XRD indicate that, upon lithiation to Phase 4 ($6.2 \leq x \leq 6.7$), while the b and c lattice parameters remain similar to the values of Phase 3, a expands up to almost 4%. From our DFT analysis, the majority of the lowest energy structures of $Li_6V_6O_{13}$ show half occupancy of the Li(6) site, with the associated increase in the a lattice parameter. The only low energy configuration with no Li(6) occupancy – and full occupancy of Li(2), Li(3) and Li(5) – shows a more limited expansion of a and instead a more prominent increase along b, trend which is not seen from the *in situ* XRD results. Moreover, the low energy structures of $Li_7V_6O_{13}$ all have half or full occupancy of the Li(6) site, in the latter case showing an additional expansion of another 1–2% along a. This trend reflects the changes of the lattice parameters seen from *in situ* XRD, indicating the effect of Li(6) occupancy on the expansion along a.

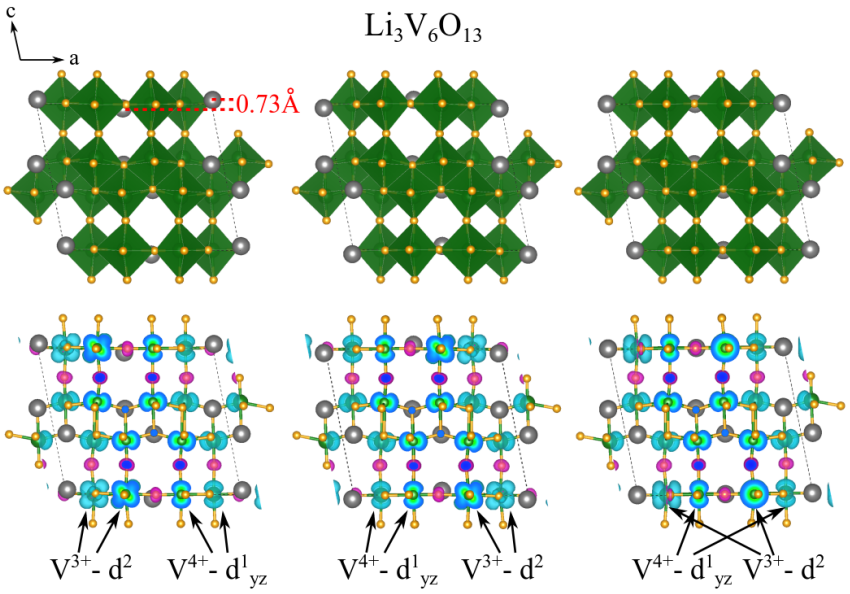

Fig. 3.8 Isosurface of the unpaired electron distribution in $Li_3V_6O_{13}$ calculated with DFT. Single crystal X-ray refinement of $Li_3V_6O_{13}$ [134] showed disorder on the lithium atom situated on the inversion centre in the single layer – the Li(3) site – and the structure was modeled with a split position generating sites 0.3 Å above and below the single layer. Three $Li_3V_6O_{13}$ structures were hence modeled with DFT, with the Li(3) off-centred above and below the single layer as as indicated by the XRD study (left-hand and central structures), as well as with the Li(3) site aligned with the single layer (right-hand structure). The structures were relaxed with DFT and the isosurfaces of the unpaired electron distribution were extracted. Vanadium, oxygen and lithium centers are shown with green, orange and grey spheres, respectively. Blue and magenta isosurfaces correspond to positive and negative unpaired spin density, respectively, and are plotted with an isosurface level of 0.008.

3.3.3 Li Migration Analysis

The migration pathways of a Li ion between the inequivalent Li sites are investigated for a dilute Li ion in the V_6O_{13} host structure, corresponding to an effective composition of $Li_{1/6}V_6O_{13}$. The calculated energy barriers (E_a), and the corresponding minima (grey spheres) and transition states (red spheres) are shown in Figure 3.9. Among all the minima, the square pyramidal Li(1) site is found to be the lowest energy site, in agreement with our previous results on the LiV_6O_{13} configurations presented in the previous Section (Figure 3.6).

The lowest-energy Li migration pathway is the Li(1)–Li(6b), involving a distorted square pyramidal transition state (migration barrier: 0.06 eV, Figure 3.9c). The Li(6b) site is a trigonal pyramidal site displaced from the Li(1) site about 1 Å in the *ab*-plane,

and only 0.05 eV higher in energy than Li(1). We label this site as Li(6b) because it is less than 1 Å distant from the Li(6) site in the *b*-direction. The Li(6b) site was not found in our previous analysis of the formation energy of the $Li_xV_6O_{13}$ series, which however found the Li(6) occupancy to be in the highest-energy configuration for the $x = 1$ composition. The results on the Li migration pathways confirm that the Li(6) site is high in energy, and in fact find it as the transition state in the Li(6b)–Li(6b) migration. The fact that, in the convex hull analysis, occupancy of the Li(6b) site was not found, and the Li(6) site was found to be a local minimum rather than a transition state, may be due to several reasons. The input structures in the formation energy study were generated starting from the fully lithiated $Li_9V_6O_{13}$ cell, with full occupancy of the sites from Li(2) to Li(6). Hence, the starting LiV_6O_{13} configuration in question was initiated with the Li already in the Li(6) site, and the geometry relaxation did not lead to significant displacement of the ions. The OPTIM calculation, however, was initiated by displacing the Li(1) site by 0.2 Å towards the Li(6) site, and the transition state search located a local minimum at the Li(6b) position which would have not been otherwise sampled. Also, the cell relaxation in the convex hull analysis allowed the atomic positions as well as the cell parameters to relax. The lattice parameters of the LiV_6O_{13} cell with half occupancy of the Li(6) site showed a 2.8% expansion of the *a*-axis compared to the pristine cell, which may have led to the localization of the Li in the Li(6) site, finding a high-energy local minimum. Geometry relaxation in the OPTIM calculations only lets the atomic positions relax, while keeping the cell parameters fixed to the values for the V_6O_{13} cell. This may be beneficial for the stabilization of the Li(6b) site, while destabilizing the Li(6) position to the point of locating it as a transition state. Furthermore, the cell used in the formation energy study contained only one formula unit, hence in this case 20 atoms of which one was a Li atom. The cell used in the OPTIM analysis was much larger, containing 115 atoms, of which one Li site. Hence, the structural distortions associated with the long-range ordering of the Li sites in the LiV_6O_{13} cell will have different effects compared to the site distortions in the dilute Li case used in the OPTIM calculations.

In addition to the Li(1)–Li(6b) pathway, we identify two other low-energy Li migrations: Li(1)–Li(2) involving a distorted square pyramidal transition state (migration barrier: 0.12 eV, Figure 3.9a), and Li(1)–Li(5) involving a distorted square pyramidal transition state (migration barrier: 0.15 eV, Figure 3.9b).

Based on these results, it appears likely that the Li ions will be able to migrate between the Li(2)–Li(1)–Li(5)–Li(6b) sites, particularly at the temperature conditions ($\sim$ 300 K) of a standard operating battery. For a comparison, the Li migration barriers for the widely used $LiCoO_2$ cathode were previously calculated to be on the order of 0.1–0.2

eV [174]. We note, however, that the Li(2)–Li(5) migration is much higher in energy (migration barrier: 0.95 eV, Figure 3.9h), due to the unfavourable distorted octahedral transition state. Based on these results, within the Li(2)–Li(1)–Li(5) migration, the Li(1) site is likely to be, on average, the more populated site of the three. The profile of the overall Li(2)–Li(1)–Li(5) migration is presented in Figure 3.10. The energetics along this pathway show that *i*) the Li(2) and the Li(5) sites are very similar in energy, and that *ii*) the Li(1) and the Li(2)–Li(5) sites are also close in energy (energy difference per atom being < 1 meV). These results are in agreement with our previous analysis for the LiV_6O_{13} (Figure 3.6), that found the Li(2) and the Li(5) sites to be almost degenerate in energy and the closest in energy to the Li on the Li(1) site.

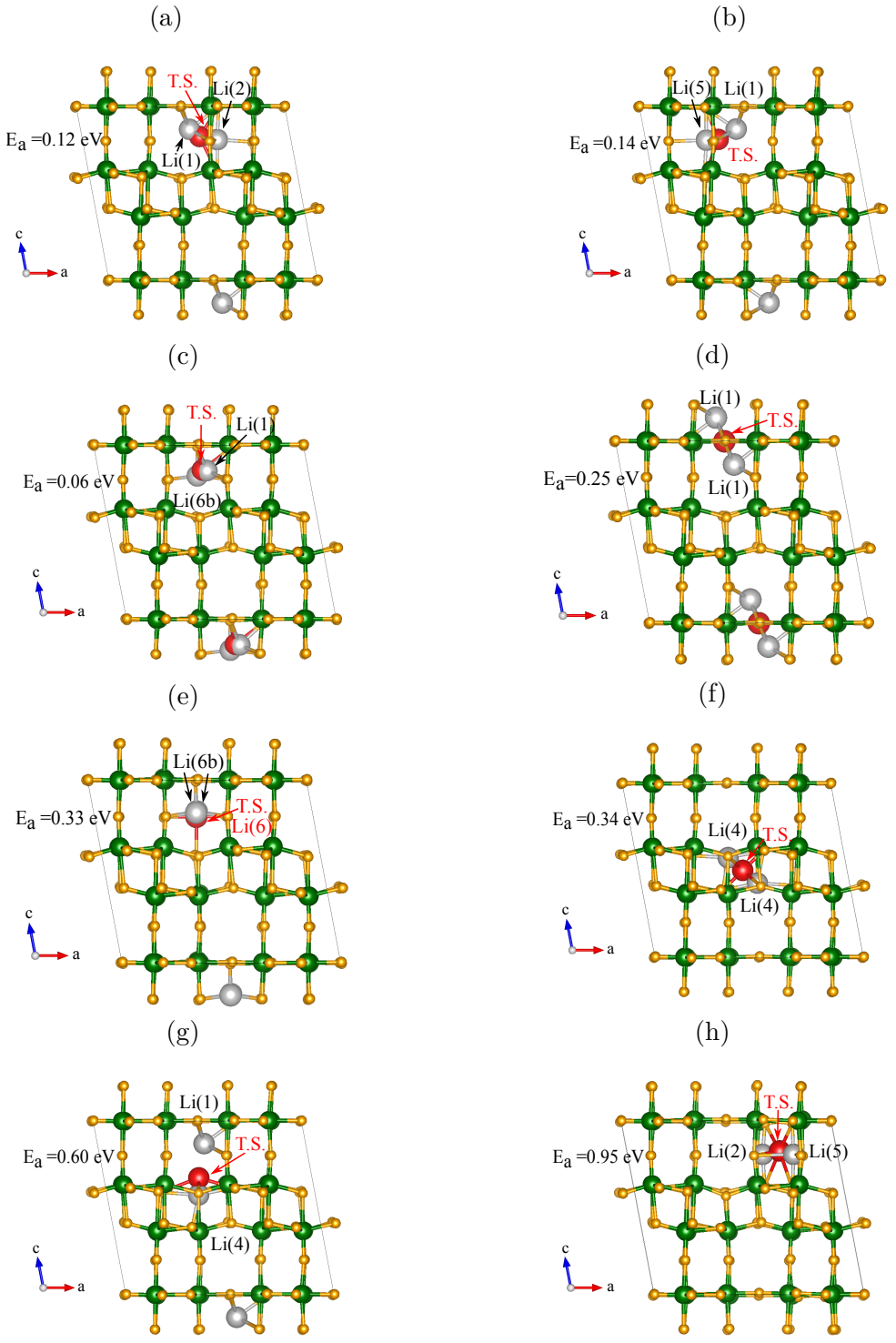

Fig. 3.9 Schematic representation of migration pathways for a dilute Li ion in an overall $Li_{1/6}V_6O_{13}$ structure. The Li local minima and transition states are shown with grey and red spheres, respectively. The energies of the transition state (E_a) are shown next to the corresponding structures.

All the other migrations are associated with for higher activation energy barriers. The Li(1)–Li(1) migration through the V–single layer involves a planar transition state, with a barrier of 0.25 eV (Figure 3.9d), the Li(6b)–Li(6b) migration through the *b*–channel also involves a planar transition state (Li(6)), with a barrier of 0.33 eV (Figure 3.9e), the Li(4)–Li(4) migration through the V–double layer (0.34 eV, Figure 3.9f) and the Li(2)–Li(5) migration (0.95 eV, Figure 3.9h) involve each a distorted octahedral transition state, while the Li(4)–Li(1) migration through the cavity (0.60 eV, Figure 3.9g) involves a distorted planar transition state.

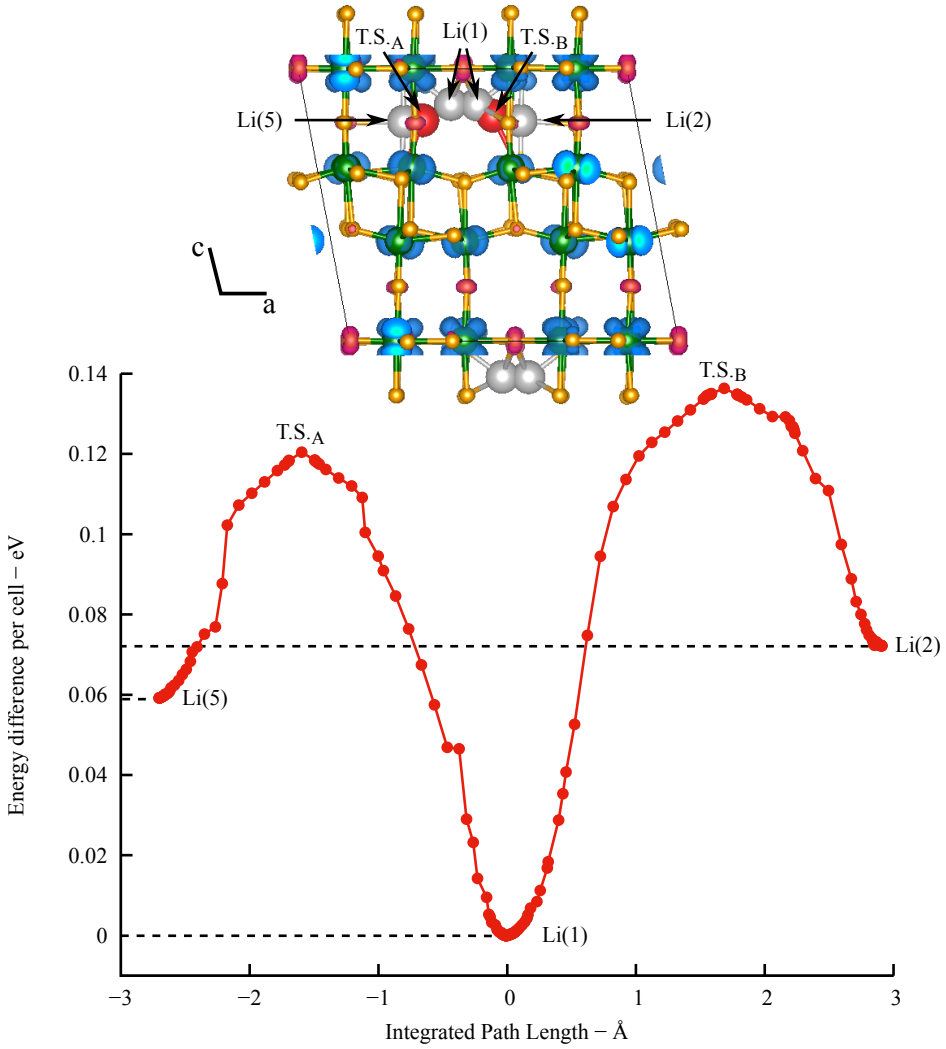

Fig. 3.10 Energy profile along the Li diffusion pathway (filled red circles) between local minima, Li(2), Li(1) and Li(5), and transition states $T.S._A$ and $T.S._B$, shown in the structure at the top as grey (minima) and red (transition states) spheres.

The combination of the different migration pathayws described so far allows us to study the diffusion of Li within the lattice. Figure 3.11 shows the overall migration pathways of Li along the a, b and c directions of the lattice (minima and transition states shown in grey and red spheres, respectively). The diffusion of Li along the a axis (Figure 3.11a) involves the energetically demanding Li(2)–Li(5) migration (Figure 3.9h), and the overall diffusion energy barrier is high (0.95 eV) and probably not accessible at the standard operating temperature of the battery. Similarly, the diffusion along the c axis (Figure 3.11c) involves the two high-energy transition states associated with the migration through the VO_x-single and double layer (Figure 3.9d and Figure 3.9f, respectively), resulting in an energetically unfavourable c-diffusion of 0.60 eV. The overall diffusion along b is the energetically most favourable (0.33 eV) and likely accessible at room temperature, suggesting that the system has facile long-range diffusion in one dimension, *i.e.* the b direction. This result is in agreement with previous impedance studies, which reported b as the major Li diffusion channel for the V_6O_{13} cathode [130]. As shown in Figure 3.9d, the migration between two adjacent Li(1) sites across the V-single layer also has a moderate migration barrier (0.25 eV), resulting in adjoined b-axis tunnels. The possible activation of this Li hop between b-tunnels would be very beneficial for the Li diffusion in the cathode, facilitating the migration of Li around blocking defects.

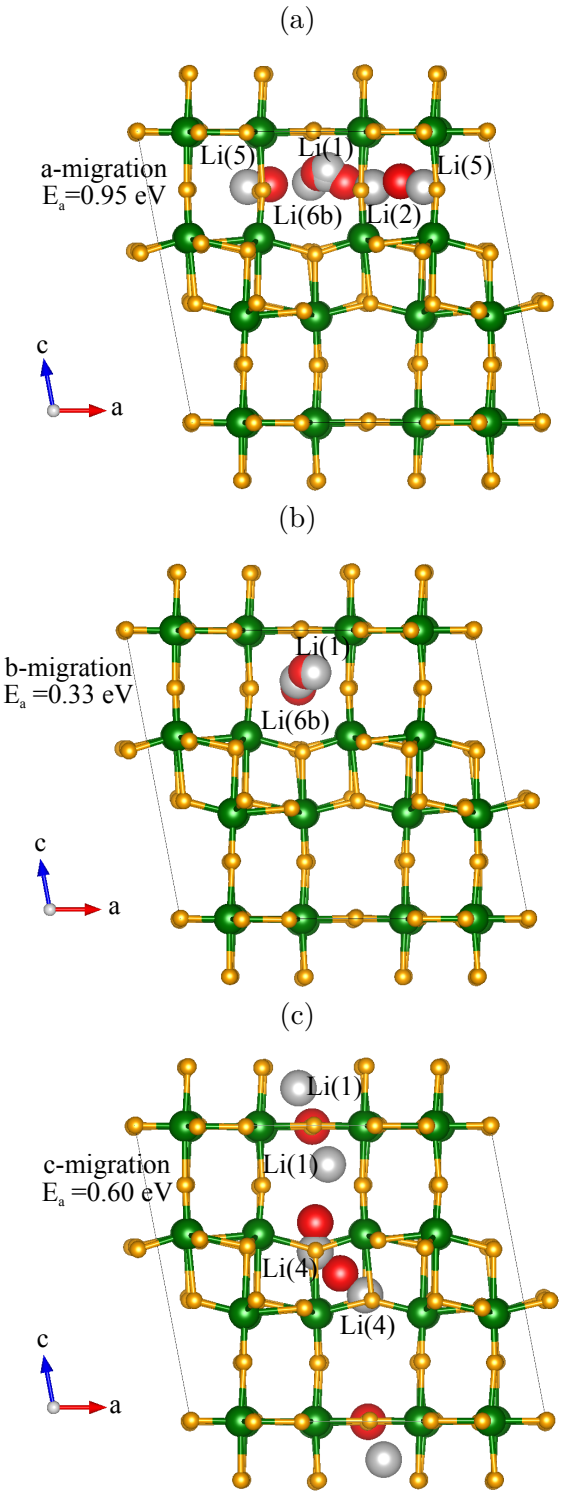

Fig. 3.11 Schematic representation of Li migration pathways through the a, b and c directions of an overall $Li_{1/6}V_6O_{13}$ structure. The Li local minima and transition states are shown with grey and red spheres, respectively. The energies of the transition states (E_a) are shown next to the corresponding structures.

3.3.4 ^{7}Li NMR of Phase 1 and Phase 2

^{7}Li NMR is a powerful technique to probe structural and electronic properties of the Li local environments present in paramagnetic solid, which are not readily analysable with diffraction studies. The spectra collected at different points of the electrochemical process are presented in Figure 3.12. In this work, as the ^{7}Li NMR experiments were done *ex situ*, some of the local structural features and orbital ordering of transient metastable phases that may be formed *in situ* may not be captured. Nonetheless, the trend of resonances throughout the series reflects the evolution of the lattice in the four main phases identified with *in situ* XRD. A more detailed analysis will now follow, which focuses on the spectra obtained for $x \leq 2$ (Phase 1 and Phase 2). Each spectrum within this range shows a complex overlap of resonances in the region between around 50 ppm and -25 ppm, which indicates the presence of multiple Li sites with different local environments (*i.e.* Li–O–V bond lengths and angles, as well as V sites with different oxidation states).

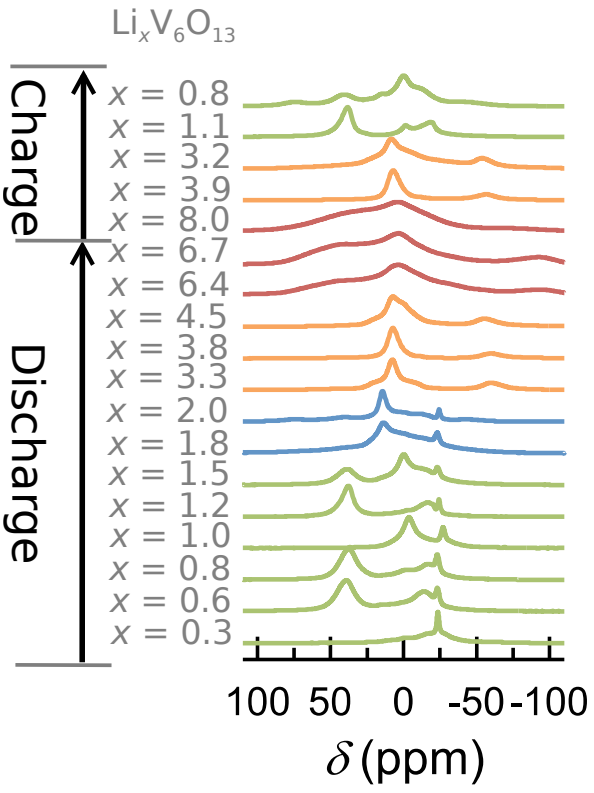

Fig. 3.12 *Ex situ* ^{7}Li MAS NMR spectra of different points in the $Li_xV_6O_{13}$ electrochemical discharge/charge process.

In an attempt to assign the isotropic shifts to different Li sites, we performed hyperfine shift calculations with DFT for a series of configurations at $x = 1$ and $x = 2$. In the majority of Li-ion cathode materials, in which the paramagnetic centre (here V) is a major constituent of the lattice, the isotropic hyperfine Fermi contact shift is the dominant contribution to the ^{7}Li NMR resonance. Hence, the calculated hyperfine shift values can be, to a good approximation, directly compared to the shifts obtained experimentally. The hyperfine calculations were performed with DFT for all the LiV_6O_{13} configurations identified in the convex hull analysis, as well as for the $Li_2V_6O_{13}$ lowest energy structure and the $Li_2V_6O_{13}$ configuration corresponding to the Li ordering previously proposed by single-crystal studies. The Fermi contact shifts were calculated using two hybrid functionals (HYB20 and HYB35), as explained in the Methodology Section. The calculated shifts for each site reported hereafter correspond to the average between the HYB20 and HYB35 results.

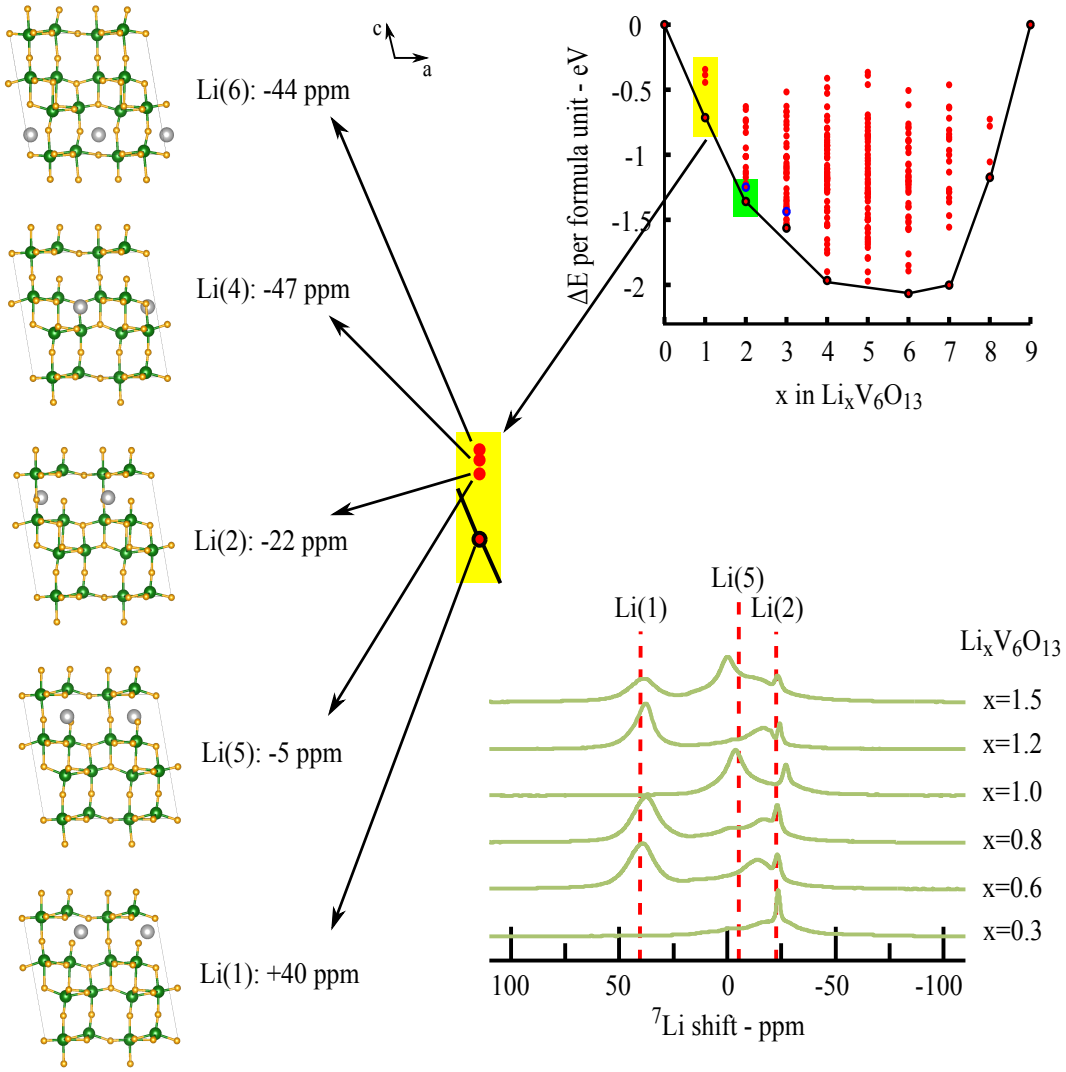

Fig. 3.13 ^{7}Li Fermi contact shifts calculated with hybrid HF-DFT for a variety of configurations in the $Li_2V_6O_{13}$ composition on and above the convex hull (top, right). The values reported are the averaged HYB20-HYB35 results. The experimental ^{7}Li NMR spectra of the Phase 1 structures ($0.3 \leq x \leq 1.5$) are shown for reference (bottom, right).

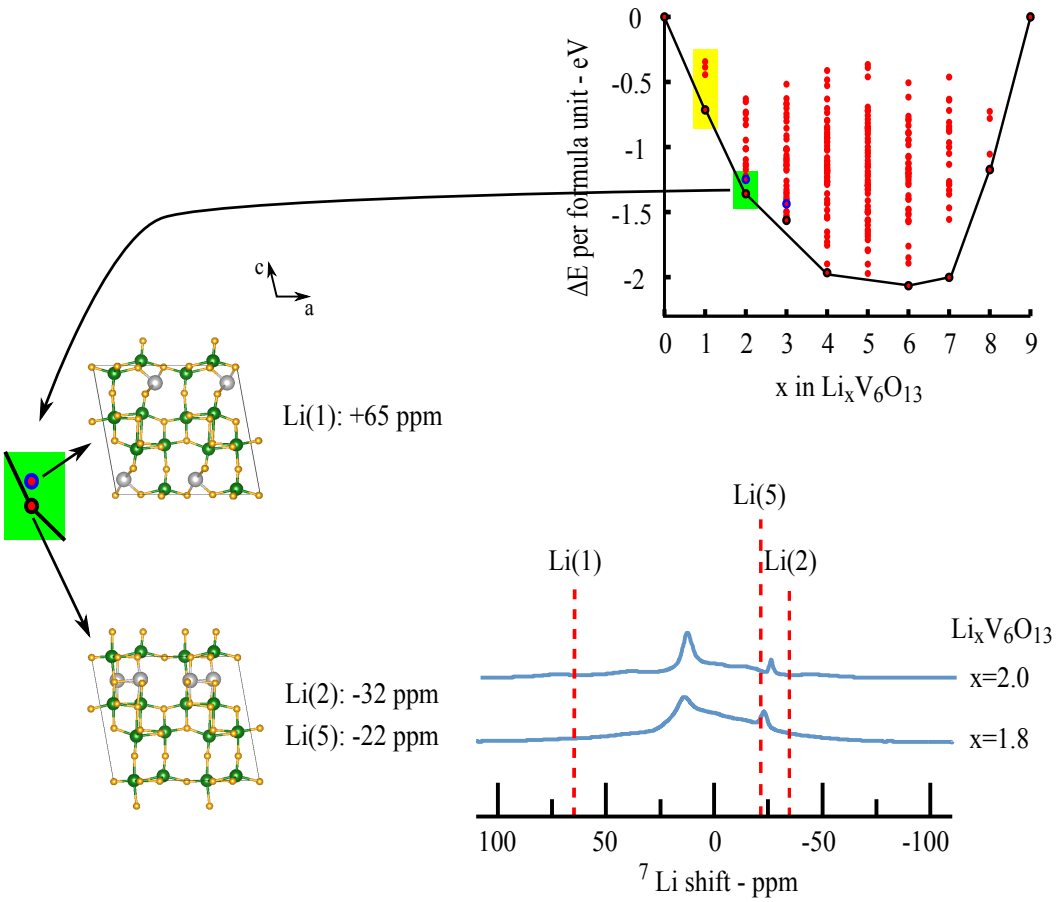

Fig. 3.14 ^{7}Li Fermi contact shifts calculated with hybrid HF-DFT for a variety of configurations in the $Li_2V_6O_{13}$ composition on and above the convex hull (top, right). The values reported are the averaged HYB20-HYB35 results. The experimental ^{7}Li NMR spectra of the Phase 2 structures ($1.8 \leq x \leq 2.0$) are shown for reference (bottom, right).

Because the isotropic hyperfine interaction results from the transfer of unpaired spin density from the paramagnetic sites to the nuclear position of the observed centre, the sign and the magnitude of the resulting Fermi contact shift for the range of Li sites in Figures 3.13 and 3.14 depend on the Li–V distance, on the Li–O–V bond angle, and on the orbitals involved in the transfer. To a good approximation, the total shift of each Li site is given by the sum of the contributions from each of the neighbouring V centres [63]. The sign and magnitude of each Li–O–V bond-pathway contribution to the ^{7}Li shift can be rationalized based on the Goodenough–Kanamori rules presented in Figure 2.2 in Section 2.3.1. As an example, we will illustrate in detail the bond-pathway contributions to the Li(1) and Li(2) shifts for the $Li_2V_6O_{13}$ case, by decomposing the total ^{7}Li shift into

the Li–O–V contributions from the neighbouring V sites *via* the spin-flipping approach described in Section 3.2.4.

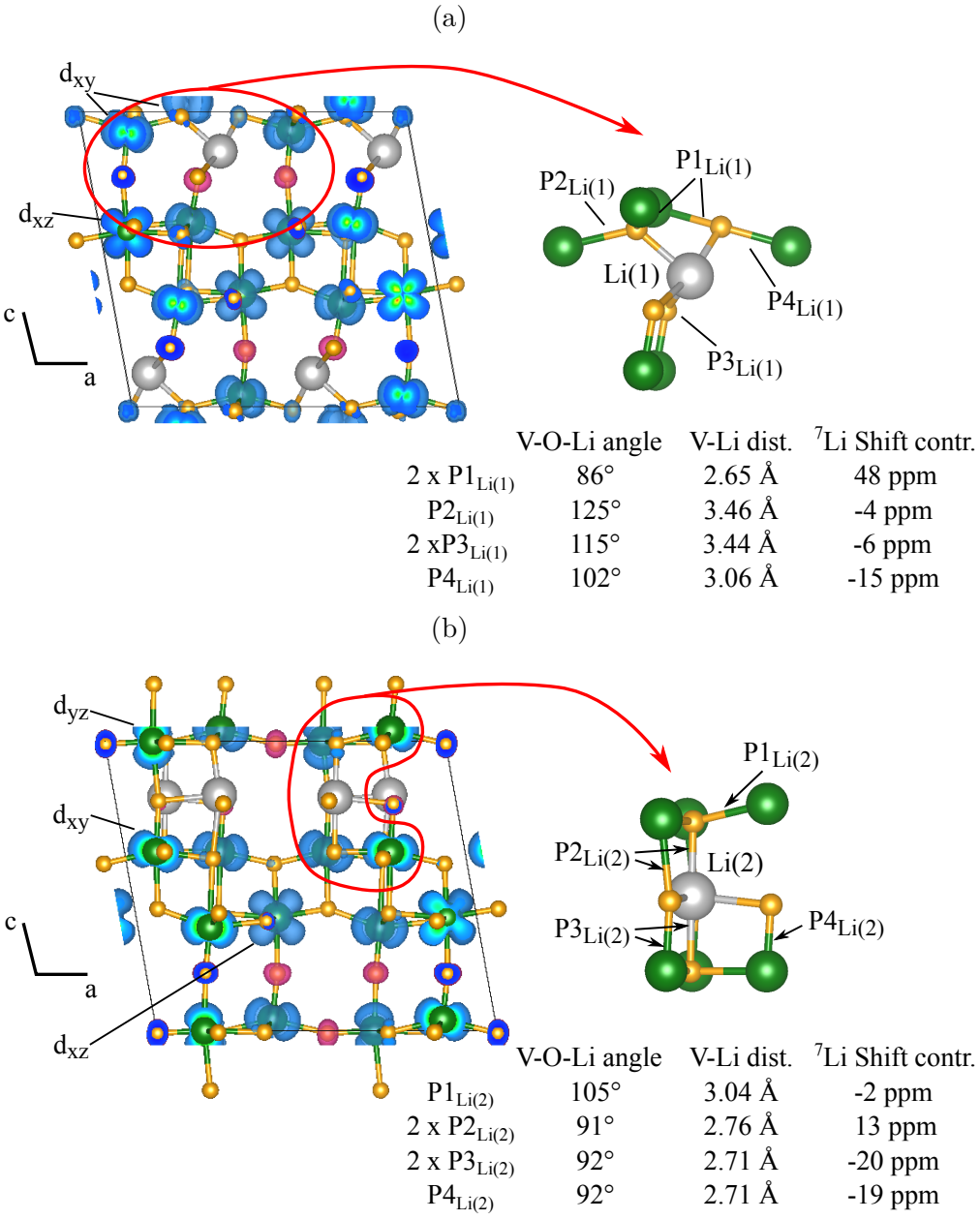

	V-O-Li angle	V-Li dist.	^{7}Li Shift contr.
2 x $P1_{Li(1)}$	86°	2.65 Å	48 ppm
$P2_{Li(1)}$	125°	3.46 Å	-4 ppm
2 x$P3_{Li(1)}$	115°	3.44 Å	-6 ppm
$P4_{Li(1)}$	102°	3.06 Å	-15 ppm

	V-O-Li angle	V-Li dist.	^{7}Li Shift contr.
$P1_{Li(2)}$	105°	3.04 Å	-2 ppm
2 x $P2_{Li(2)}$	91°	2.76 Å	13 ppm
2 x $P3_{Li(2)}$	92°	2.71 Å	-20 ppm
$P4_{Li(2)}$	92°	2.71 Å	-19 ppm

Fig. 3.15 Bond-pathway decomposition of the ^{7}Li shift calculated for a Li(1) site (Figure 3.15a) and for a Li(2) site (Figure 3.15b) in the $Li_2V_6O_{13}$ structures corresponding, respectively, to the lowest energy $Li_2V_6O_{13}$ configuration and to the $Li_2V_6O_{13}$ configuration consistent with previous single-crystal studies [135], as shown in Figure 3.6. The shift contributions presented in the Figure correspond to the average between the HYB20 and the HYB35 results.

The results for the Li(1) shift decomposition are presented in Figure 3.15a. The major contribution to the total shift results from the P1 pathway that connects Li(1) to the V in the single layer at the short distance of 2.65 Å. The Li–O–V angle characterising the P1 pathway is close to 90°, and the orbital overlap (involving the V d^1_{xy} orbital) allows the transfer of positive spin density *via* a delocalization mechanism, as described in Figure 2.2. All of the other pathways (P2, P3 and P4 in Figure 3.15a) are defined by longer Li–V distance and by intermediate Li–O–V angles between 90° and 180°. This determines a combination of both positive and negative spin density transfer, resulting in an overall shift contribution close to zero. The Li–V distance in the P4 pathway is shorter than in the P2 and P3 cases. Although, at the intermediate 102° Li–O–V angle, a combination of transfers still occurs, the orbital ordering suggests that the d^1_{xy} orbital of the V site involved in the P4 pathway will predominantly transfer positive spin density to the O(p_x) orbital, polarizing negative spin density towards the O(p_y)–L bond, hence resulting in an overall negative shift contribution.

The shift of the Li(2) site in the $Li_2V_6O_{13}$ configuration is decomposed in Figure 3.15b. In this case, there are three dominant pathways, P2, P3 and P4, which are very similar in terms of Li–V distance and Li–O–V bond angle, however contributing shifts of different sign. This can again be related to the ordering of the d^1 orbitals of the V sites in the Li(2) neighbouring shell. For the P2 pathway, the unpaired electron of the corresponding V ion is in the d_{yz} orbital, allowing delocalization of spin density *via* the O(p_z) orbital onto the Li, resulting in a positive shift, as schematized in Figure 2.2. Differently, for both the P3 and P4 pathways, the V sites have their unpaired electron in the d_{xy} orbital, of which the overlap with the O(p_x) orbital does not allow direct delocalization of spin density towards the *s* orbital of Li. Instead, the polarization mechanism dominates, inducing negative spin density towards the O(p_y)–Li bond and resulting in a net negative shift contribution. The Li(5) site has a very similar environment to the Li(2) site, resulting in a similar shift, as shown in Figure 3.13.

The description of the Li(1) and the Li(2) shifts in Figures 3.15a and 3.15b also applies to these sites in the LiV_6O_{13} configurations, as shown in Figure 3.13. The Li(5) shift in the LiV_6O_{13} case is closer to zero than in the $Li_2V_6O_{13}$ case due to the fact that some of the V sites in its neighbouring shell are V^{5+} (d^0), and do not contribute to the Fermi contact interaction. The orbital ordering in the LiV_6O_{13} configurations containing Li(4) and Li(6) sites is such that every Li–O–V bond-pathway contribution to their shift results from a ∼90° polarization mechanism determining the transfer of negative spin density from the V to the Li, hence the overall negative shifts for Li(4) and Li(6) sites shown in Figure 3.13.

The spectra for the systems within Phase 1 ($0 < x \leq 1.5$) in Figure 3.13 show main resonances at about 45 ppm, -2 ppm, -15 ppm and -25 ppm, which are very similar to the calculated shifts of Li(1) (DFT result: 40 ppm), Li(5) (DFT result: -5 ppm) and Li(2) (DFT result: -22 ppm) in the LiV_6O_{13} stoichiometry. This agreement suggests that the Li ions within Phase 1 are present in all of these sites in different ratios. This assignment is in line with the results obtained from our previously presented DFT analyses: *i*) from the formation energy study of LiV_6O_{13}, we identified Li(1) as the lowest energy site, and Li(2) and Li(5) being the sites immediately higher in energy, at an energy difference within thermal energy (and DFT error); *ii*) from the study of the Li migration pathways, we also found a low energy barrier for the Li(2)–Li(1)–Li(5) diffusion, suggesting that at room temperature and in the NMR timescale, the Li ions are likely to migrate between these sites. The DFT calculated ^{7}Li shifts for the Li(4) and Li(6) sites of -47 ppm and -44 ppm, respectively, do not correspond to any peak in the NMR spectra for Phase 1, suggesting that these two sites are not significantly populated at room temperature. This is also in line with our previous results which showed that these configurations are the most energetically unfavourable.

The spectrum of $x = 1$ shows a sudden change in the NMR trend, with the complete disappearance of the shift at $\sim$ 40 ppm and the appearance of a peak at $\sim$ 0 ppm, together with the peak at ~ -25 ppm. This change in the NMR resonances is interpreted as an indication of a cation ordering made favourable by a possible orbital ordering in the LiV_6O_{13} case. The comparison of the NMR spectrum with the ^{7}Li Fermi contact shifts calculated with DFT seems to indicate the predominant presence of Li(2) and Li(5) sites. However, as we pointed out previously, capturing a long-range ordering with our DFT approach would require significantly more expanded cells resulting in computationally demanding calculations beyond the scope of the current study.

The ^{7}Li NMR spectra of Phase 2 ($x = 1.8, 2.0$ in Figure 3.14) show a broad feature with two more distinct peaks at around 10 ppm and -25 ppm. The hyperfine shifts calculated with DFT find a +65 ppm shift for the Li(1) site, -22 ppm for the Li(5) site and -32 ppm for the Li(2) site. The DFT results of this Phase 2 are in less good agreement with the NMR resonances, compared to the shifts calculated for the spectra within Phase 1. This may be due to the approximate magnetic scaling of the hyperfine shifts calculated in our work. However, the fact that the shifts calculated with DFT on the highly ordered cells do not reproduce very well the experimental shifts of Phase 2 suggest a greater structural complexity of this Phase. The *in situ* XRD results (Figure 3.5) found that Phase 2 is only formed on discharge, but it does not occur on charge. This asymmetry may indicate that kinetic effects contribute to the formation/disappearance

of the Phase, and the simple orderings simulated with DFT do not capture the site and charge distributions in this region. More work is needed, in order to further investigate the local ordering within Phase 2, *via* a combination of a more comprehensive DFT analysis of hyperfine shifts for different configurations, as well as variable temperature NMR experiments to investigate exchange mechanisms in the systems.

3.4 Conclusions

We have investigated the first discharge and charge process of cathode material V_6O_{13} using electrochemistry, *in situ* XRD, solid-state ^{7}Li NMR and DFT calculations. An alternating solid solution and two-phase mechanism has been proposed. The material features an asymmetric six-step discharge and five-step charge, and expands/shrinks in a sequential order along *c*, *b*, and *a* axes, and reversibly upon discharge and charge. This sequential change, accompanied by significant electronic rearrangements, is related to changes in the occupancy of Li ions in different Li sites in the unit cell and charge ordering. *Via* a combined analysis of the *in situ* XRD data and the DFT-calculated cell parameters for a variety of structures constructed with different Li occupancies and arrangements, the relationship between the Li occupancies, the charge and orbital orderings and the lattice expansions is studied throughout the entire lithiation series. The DFT analysis of the Li migration pathways for $x \leq 1$ confirms that the *b*-axis is the major Li diffusion channel, as it was previously suggested by impedance spectroscopy studies. Furthermore, our DFT results identify the energetically favourable Li(2)–Li(1)–Li(5) migration pathway, likely to be accessible at the temperature condition of the operating battery. The presence of Li ions distributed among these sites at low stages of lithiation (Phase 1) is confirmed also by our combined NMR and DFT analysis of the ^{7}Li isotropic shifts. The facile Li mobility and the presence of multiple low-energy Li sites in the structure helps to explain the reason behind the high capacity of the V_6O_{13} cathode material given by a favourable interplay of Li intercalation and rearrangement in the structure.

Chapter 4

Structural characterization of the Li-ion battery cathode materials $LiTi_xMn_{2-x}O_4$ $(0.2 \leq x \leq 1.5)$: A combined experimental ^{7}Li NMR and first principles study

Abstract

This Chapter presents a combined experimental and *ab initio* approach whereby the Fermi contact shifts of a multitude of environments are calculated with DFT, combined in a lattice model which simulates the NMR spectra for different cation orderings using experimental contraints, compares the simulated and experimental ^{7}Li MAS NMR spectra and outcomes the structures which give the best agreement. The model is applied to rationalize the compositional (dis)order throughout the series of $LiTi_xMn_{2-x}O_4$ cathode materials, as a function of Mn/Ti content.

Titanium doping in lithium manganese oxide spinels was shown to be beneficial for the structural stability of the potential Li-ion battery cathode materials $LiTi_xMn_{2-x}O_4$, $0.2 \leq x \leq 1.5$, yet the distribution of Li/Ti/Mn in the structure and the cation oxidation states, both pivotal for the electrochemical performance of the system, is not fully understood. Our work investigates the changes in the local ordering of the ions throughout this series, by using a combination of ^{7}Li NMR spectroscopy and *ab initio* DFT calculations. The ^{7}Li NMR shifts are first calculated for a variety of Li configurations

with different numbers and arrangements of Mn ions in the first metal coordination shell, and then decomposed into Li-O-Mn bond pathway contributions to the shift. These Li-O-Mn shift contributions are then used to simulate and assign the experimental NMR spectra of different configurations and stoichiometries beyond those in the initial subset of configurations *via* a random distribution model and a Reverse Monte-Carlo approach. This methodology enables a detailed understanding of the experimental ^{7}Li MAS NMR spectra, allowing the variations in the local ordering of the ions in the structure to be investigated. A random distribution of Ti^{4+}-$Mn^{3+/4+}$ sites is found at low Ti-content ($x = 0.2$), an inhomogeneous lattice of Mn^{4+}-rich and Ti^{4+}-rich domains is identified for $x = 0.4$ and single-phase solid solution is observed for $x = 0.6$ and $x = 0.8$. A mixed Li-Mn^{2+} (tetrahedral) and Li-$Mn^{3+/4+}$-Ti (octahedral) configuration is identified for the $x = 1.0$ case. A specific cation ordering in the partially inverse $LiTi_{1.5}Mn_{0.5}O_4$ case is found, which transforms into a two-phase network of disordered Mn^{3+}-rich and ordered Mn^{2+}-rich domains for $x = 1.1 - 1.4$.

4.1 Introduction

Spinel-type lithium metal oxides are interesting cathode materials for rechargeable Li-ion battery applications. The robust host structure of spinel oxides retains capacity for many cycles, and the three dimensional network of interstitial sites allows high Li diffusion rates [175, 176]. $LiMn_2O_4$ spinel has been studied as a potential alternative to the more widely used $LiCoO_2$ because of its lower cost, lower toxicity and higher thermal stability [176, 177]. However, the application of $Li_xMn_2O_4$ as a positive electrode is limited by the presence of Jahn-Teller active Mn^{3+} ions, which accelerate structural degradation of the material upon cycling due to a cooperative Jahn-Teller distortion [36]. Moreover, the charge disproportionation of $2Mn^{3+} \rightarrow Mn^{4+} + Mn^{2+}$ results in the formation of Mn^{2+} ions, which dissolve in the electrolyte at the surface of the particles and deplete the spinel framework of transition metal ions [43]. The electrochemical properties and the structural stability of $LiMn_2O_4$ were shown to be improved by introducing excess Li in the spinel structure, to form $Li_{1+\alpha}Mn_{2-\alpha}O_4$ [178, 179, 55, 54]. The inclusion of the excess lithium raises the average Mn oxidation state, thereby reducing the amount of Jahn-Teller active Mn^{3+} ions. Another approach to limit the negative effects of the cooperative Jahn-Teller distortion has been to partially substitute the Mn ion with other transition metals (TM), such as Ni, Zn and Ti, hence stabilizing the structural integrity of the electrode upon cycling [180–183]. Understanding the structural ordering and the distribution of Li/TM ions in the structure is central to rationalizing the relationship between the

electrochemical performance and the physical properties of the material. As an example, the kinetic and electrochemical properties of the high-energy $LiNi_xMn_{2-x}O_4$ cathode material have been analyzed in relation with the complex cation ordering throughout the series, unraveling the key role of compositional (dis)order in the electrochemical performance of this material [184]. Here, the randomization of Ni/Mn ions among the octahedral sites of the spinel lattice was proposed to lead to improved electrochemical performance.

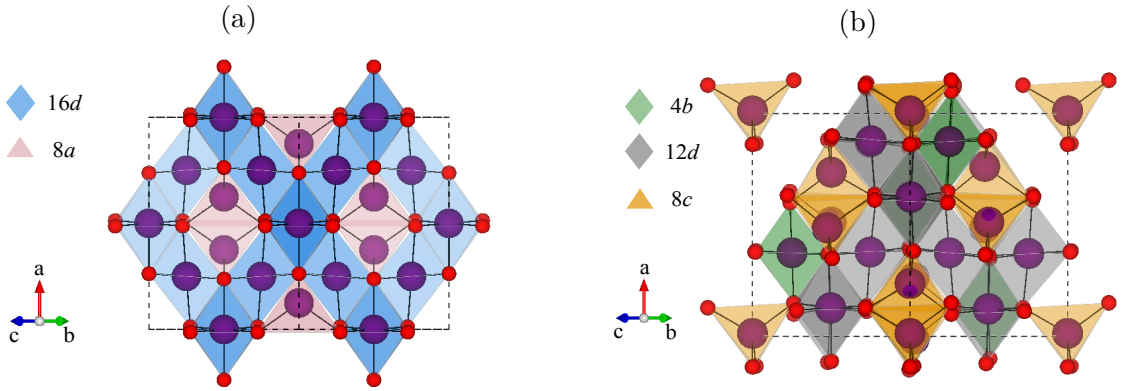

Fig. 4.1 Polyhedral representation of a general spinel-type AB_2O_4 in the $Fd\bar{3}m$ (Figure 4.1a) and $P4_332$ (Figure 4.1b) space group, with the A and B cations shown in purple spheres and the oxygens shown in red spheres. The crystallographically independent octahedral and tetrahedral sites are represented by polyhedra of different colors, as labelled in the Figure.

In this work, we focus on the series of materials $LiTi_xMn_{2-x}O_4$ with $0.2 \leq x \leq 1.5$, and study the structural changes of the Mn-oxide spinel framework as an effect of Ti doping. In spinel materials, of general formula AB_2O_4, the oxygen anions form a face-centered-cubic sublattice, within which octahedral (Oh) and tetrahedral (Td) interstitial sites are present in a 2 : 1 ratio. In a *normal* spinel, the A cations occupy the Td sites and the B cations occupy the Oh sites (denoted as $A[B_2]O_4$), while in an *inverse* spinel, the B cations occupy all of the Td sites and half of the Oh sites, and the A cations occupy the other half of the Oh sites (denoted as $B[AB]O_4$). In the case of $LiTi_xMn_{2-x}O_4$, the partial substitution of Mn with Ti results in a mixed cation occupancy on both the Oh and Td sites of the spinel lattice [185, 186]. The $LiTi_xMn_{2-x}O_4$ series was shown to adopt different space group symmetries for different doping ratios. For $0.2 \leq x \leq 1.0$, the disordered $Fd\bar{3}m$ cubic spinel preferentially forms (Figure 4.1a), with proposed partial occupancy of Li^+/Mn^{2+} and $Li^+/Ti^{4+}/Mn^{3+/4+}$ on the tetrahedral 8*a* and the octahedral 16*d* sites, respectively, and with the Li(Oh)/Mn^{2+}(Td) fraction increasing with increasing Ti content. For $x > 1.0$, the more ordered $P4_332$ cubic spinel

also starts to form (Figure 4.1b), in which it was proposed that the two inequivalent octahedral sites, 4*b* and 12*d*, are occupied by a mixture of $Li^+/Mn^{3+/4+}$ and a mixture of $Li^+/Ti^{4+}/Mn^{3+/4+}$ ions, respectively, while the tetrahedral 8*c* sites are partially occupied by Li^+/Mn^{2+} ions [185, 186]. A detailed study using synchrotron X-ray, neutron powder diffraction and XANES spectroscopy further investigated the effects of different sintering temperatures and cooling regimes during synthesis on the phase behavior of $LiTiMnO_4$ [187]. Although it is a challenge to provide an accurate description of the coordination site disorder throughout the $LiTi_xMn_{2-x}O_4$ series because of the presence of multiple mixed-valence transition metals, a detailed characterization of the structure provides the fundamental basis with which to understand and monitor the electrochemical properties of the material. Analysis based on X-ray diffraction (XRD) showed limited accuracy in determining the distribution of Li, Ti and Mn ions in the lattice, due to the difficulty of detecting Li in the presence of heavier elements, and of distinguishing between Ti and Mn which have similar X-ray scattering factors [185, 186]. Electron spin resonance (ESR) studies were also used in combination with X-ray diffraction analysis, but the presence of multiple Mn oxidation states made the assignment of the TM distribution challenging [186].

$^{6/7}$Li NMR has been successfully used to characterize the local Li environments and the cation ordering in similar systems, such as $LiMn_2O_4$ [50, 49], $LiZn_xMn_{2-x}O_4$ [188, 189, 49] and $LiNi_xMn_{2-x}O_4$ [190, 49], as well as in Li-excess Mn oxides, $Li_{1+\alpha}Mn_{2-\alpha}O_4$ [191, 27]. The dominant interaction leading to the observed ^{7}Li NMR shift in this class of paramagnetic materials is the isotropic Fermi contact (FC) hyperfine interaction [15–17], which was described in detail in Section 2.3. It results from the coupling between the nuclear moment of the Li and the time-average of the local field due to the unpaired *d* electrons present on the neighbouring TM ions [48, 49]. In the series of systems studied here, Ti is present as Ti^{4+} throughout (i.e. d^0 ion), hence the only paramagnetic centres are the $Mn^{2+/3+/4+}$ sites (i.e. $d^5/d^4/d^3$ ions, respectively). The Fermi contact interaction is proportional to the unpaired spin density transferred from the *d* orbitals of Mn to the *s* orbitals of Li. This transfer can occur either directly through the overlap of the involved orbitals, or, more prominently in the systems studied here, indirectly *via* the bridging oxygen *p* orbitals which form Mn-O-Li bond pathways. The observed ^{7}Li Fermi contact shift is hence given by the sum of the individual Mn-O-Li pathway contributions [63]. The sign and magnitude of the shift depend on the geometry and covalency of the pathway, as well as on the Mn oxidation state and on the magnetic susceptibility of the material. In mixed cation systems, the variety of Li environments often results in a multitude of paramagnetic shifts and a significant broadening of the resonances,

making the spectra difficult to interpret [62]. Computational predictions and *ab initio* calculations of paramagnetic NMR parameters constitute a robust and invaluable aid for the understanding of experimental NMR spectra of paramagnetic solids.

In this work, we report a detailed ^{7}Li magic-angle spinning (MAS) NMR spectroscopy investigation of the $LiTi_xMn_{2-x}O_4$ spinel series, using state of the art spectroscopic methods for paramagnetic materials [192]. The interpretation of the experimental spectra is supported by first-principles DFT calculations of the magnetic interactions and ^{7}Li NMR shifts. Different $LiTi_xMn_{2-x}O_4$ structures of (possibly fictitious) ferromagnetically aligned TM ions are simulated, from which we calculate the Mn-O-Li bond pathway contributions to the ^{7}Li hyperfine shift of the various environments, nominally at 0 K [63]. To compare these shifts with the experimental spectra obtained at finite temperature, we evaluate the possible Mn-Mn magnetic interactions and determine the Curie-Weiss magnetic factors, and use these to scale the shifts obtained with DFT to the paramagnetic regime of the NMR experiments (performed at room temperature) [12, 66]. The variety of bond pathway contributions is used to simulate the spectra of different $LiTi_xMn_{2-x}O_4$ configurations in a combined random distribution model and Reverse Monte Carlo approach, allowing the characterization of the cation ordering throughout the series. A random distribution of Ti^{4+}-$Mn^{3+/4+}$ sites among the octahedral 16*d* environments ($Fd\bar{3}m$) is found at low Ti-content ($x = 0.2$), which transforms into a lattice of Mn^{4+}-rich and Mn^{3+}-rich phases for $x = 0.4$ and a single-phase solid solution for $x = 0.6$ and $x = 0.8$. A partially inverse spinel configuration is identified for $x = 1.0$, with mixed Li-Mn^{2+} tetrahedral sites and mixed Li-$Mn^{3+/4+}$-Ti octahedral sites. A specific ion distribution is identified for the $LiTi_{1.5}Mn_{0.5}O_4$ case, involving ordering between the tetrahedral 8*c* and the octahedral 4*b*, 12*d* sites in the $P4_332$ lattice, corresponding to $(Li_{0.6}Ti_{0.1}Mn_{0.3})_{8c}[(Li_{0.4}Mn_{0.2})_{4b}(Ti_{1.4})_{12d}]O_4$. This further transforms into a network of Mn^{3+}-rich disordered $Fd\bar{3}m$ and Mn^{2+}-rich ordered $P4_332$ domains for $x = 1.1 - 1.4$ series. The ^{7}Li NMR shifts calculated in this work are also readily applicable to the NMR analysis of a range of similar battery materials, such as the $LiNi_xMn_{2-x}O_4$ and the $Li_{1+\alpha}Mn_{2-\alpha}O_4$ systems mentioned above, and the structural models implemented in this study can aid the analysis of the complex relationship between structural ordering and electrochemical properties.

The work presented in this Chapter is included in the paper "Structural characterization of the Li-ion battery cathode materials $LiTi_xMn_{2-x}O_4$ ($0.2 \leq x \leq 1.5$): A combined experimental ^{7}Li NMR and first principles study", currently under revision in *Chemistry of Materials*. This work benefited from the intellectual input of Ieuan Seymour, Céline Merlet, Andrew Pell, Denissa Murphy, Siegbert Schmid and Clare Grey. Denissa Murphy

synthesised the material, the current author and Andrew Pell performed the NMR, and Céline Merlet wrote the Reverse Monte Carlo code. All of the computational results were obtained by the current author.

4.2 Experimental Methods

4.2.1 Synthesis of $LiTi_xMn_{2-x}O_4$ ($0.2 \leq x \leq 1.5$)

$LiTi_xMn_{2-x}O_4$ samples ($x = 0.2, 0.4, 0.6, 0.8, 1.0, 1.2, 1.3, 1.4, 1.5$) were prepared via solid-state synthesis. Stoichiometric ratios of Li_2CO_3 (dried at 120°C, Merck, 99%), $MnCO_3$ (Sigma-Aldrich, 99%) and TiO_2 (Aithaca, 99%) were ground in a small amount of acetone until dry, then transferred into alumina crucibles and fired at 500°C for 12 hours. The calcined samples were re-ground with acetone until dry and pressed into pellets using a uniaxial pellet press at 8 tons of pressure. Samples were further sintered in air at 900°C for 24 hours, then quenched in liquid nitrogen, with the exception of $LiTi_{0.2}Mn_{1.8}O_4$, $LiTi_{1.4}Mn_{0.6}O_4$ and $LiTi_{1.5}Mn_{0.5}O_4$ which were slow-cooled in air after sintering, the latter two samples being further heated in argon for 3 hours.

4.2.2 Solid-state MAS ^{7}Li NMR

Solid-state NMR spectra of the $LiTi_xMn_{2-x}O_4$ samples ($0.2 \leq x \leq 1.5$) were acquired on a Bruker 200 Avance III spectrometer using a 1.3 mm probe, with a MAS frequency of 60 kHz. The one-dimensional ^{7}Li spectra were recorded using a double-adiabatic spin-echo sequence [192], employing a pair of 50 μs tanh/tan short high-powered adiabatic pulses (SHAPs) of 5 MHz sweep width [193, 194] and a 1.025 μs 90° excitation pulse. All pulses used a radiofrequency (RF) field strength of 244 kHz. For each spectrum, 32768 scans were acquired using a recycle delay of 30 ms. The experimental ^{7}Li NMR spectra were fitted using the DMFIT software [195]. An initial model was set up with components based on the hyperfine shifts predicted with DFT calculations, and the fitting of the isotropic region and the sideband pattern was then obtained by optimizing the shift and the amplitude of the deconvoluting regions.

4.2.3 Magnetic Susceptibility Measurements

Magnetization measurements were performed for the $LiTi_{0.4}Mn_{1.6}O_4$ powder sample with Quantum Design Material Property Measurement System (MPMS). The magnetic

susceptibility of the zero field-cooled sample was measured over the temperature range $2 - 350$K, under the external field of 100 Oe.

4.3 Computational Methods

4.3.1 Formation Energies and Thermodynamical Phase Stability

Methodology of Thermodynamical Phase Stability Analysis

The thermodynamical phase stability of the $LiTi_xMn_{2-x}O_4$ series was studied by calculating the formation enthalpy of various structures with different stoichiometries. For $LiTi_2O_4$ and $LiMn_2O_4$, crystal structures were obtained from the International Crystal Structure Database (ICSD) and fully relaxed (i.e. both the unit cell parameters and the atomic positions were allowed to vary) using Density Functional Theory (DFT). From the $LiTi_2O_4$ and $LiMn_2O_4$ unrelaxed crystal structures, selected intermediate stoichiometries of the $LiTi_xMn_{2-x}O_4$ series were generated using the Site Occupancy Disorder (SOD) [196] and the Cluster-Assisted Statistical Mechanics (CASM) [154, 155] softwares. Specifically, for $x = 0.5, 1.0, 1.5$, small cells of 14 atoms were considered, where all possible swaps between Li, Ti and Mn were enumerated. For the $x = 1.25$ and $x = 1.5$ cases, additional configurations were considered: for larger cells of 56 atoms, all configurations were enumerated starting from $LiTi_2O_4$ and replacing $(2 - x)$ Ti ions with Mn ions. Additionally, swaps between Li, Mn and Ti were allowed, in order to include inverse spinel lattices in the analysis, i.e. networks of mixed Ti-Mn-Li occupancy on both the tetrahedral and the octahedral sites were generated.

Details of GGA+U Calculations of Formation Energies

The unit cell parameters and atomic positions of each generated configuration were relaxed with DFT using the PBE [89] spin-polarized generalized gradient approximation (GGA) functional within the VASP code [150]. The projector augmented waves (PAW) [151] method was used with a plane-wave cutoff of 500 eV, an energy convergence of 4 meV/atom, and an ionic relaxation tolerance of 10^{-5} eV. The electronic energy of each relaxed structure was calculated with a single-point energy minimization. The reciprocal space sampling was performed with a k-point grid of 8×8×8 points for the smaller cells (14 atoms), and 4×4×4 points for the larger cells (56 atoms). To correct for the self-interaction error in the GGA formalism, a Hubbard U parameter was included for

the Mn ions to treat the $3d$ correlations [91]. In this work the approach proposed by Liechtenstein was used [94], where the Coulomb matrix (U) and the exchange matrix (J) are combined to give an overall effective value $U_{\text{eff}} = U - J$. The value of J was fixed to 1 eV throughout. In a previous study by Wang *et al.* [197], values of $U_{\text{eff}} = 4.5$, 4.0 and 3.5 eV were calculated for Mn^{2+}, Mn^{3+} and Mn^{4+} ions , respectively. Since in our systems the Mn ions are present in multiple oxidation states, an average U_{eff} value of 3.9 eV was chosen for all the Mn sites.

4.3.2 Paramagnetic Shift Calculations

The calculation of the Fermi contact shift, δ_{FC}, adopted in this work follows the methodology presented by Kim *et al.* [61], which has been presented in Section 2.5.1 and it is summarized here for convenience. In this method, the hyperfine coupling constant, A_{iso}, is first calculated from the system in the ferromagnetic state nominally at 0 K, and then scaled using a Curie-Weiss factor, Φ, in order to match the paramagnetic regime typical of NMR experiments.

$$\delta_{FC} = \frac{A_{iso} 10^6 \Phi}{2h\nu} \tag{4.1}$$

with

$$A_{iso} = \frac{2}{3}\mu_0 \mu_B \mu_N g_e g_I |\psi_N^{\alpha-\beta}|^2 \tag{4.2}$$

and

$$\Phi = \frac{B_0 \mu_{\text{eff}}^2}{3k_B g_e \mu_B S(T-\theta)} \tag{4.3}$$

where h is the Planck constant, ν is the Larmor frequency, $|\psi_N^{\alpha-\beta}|^2$ is the unpaired spin density at the Li nuclear position, B_0 is the static magnetic field, μ_{eff} is the effective electronic magnetic moment, μ_B is the Bohr magneton, S is the formal electronic spin of the paramagnetic center(s), k_B is the Boltzmann constant, g_e is the free-electron g-value, g_I is the nuclear g-factor, T is the temperature used in the experiments, here estimated to be 320 K to account for frictional heating due to MAS NMR, and θ is the Weiss constant. In this work, μ_{eff} is taken to be the spin-only value of $2\mu_B\sqrt{S(S+1)}$. This is considered a good approximation for the class of systems studied here. As an example, in the case of $LiMn_2O_4$ with an average oxidation state of $Mn^{3.5+}$, $S = 1.75$, and the calculated spin-only value is $\mu_{\text{eff}} = 4.39\ \mu_{\text{B}}$, in good agreement with the experimental μ_{eff} range of $4.33 - 4.36\ \mu_{\text{B}}$ reported by Masquelier *et al.* [198].

Methodology For Calculating the Magnetic Parameters, θ and Φ

Values of θ were obtained *ab initio* by calculating the magnetic exchange coupling constants, J, by a multivariate linear regression of the DFT-calculated energies of systems with different magnetic configurations of coupled spins, following the approach presented in Section 2.5.2. The calculations of the various exchange coupling constants were performed on selected structures, i.e., the lowest energy configurations for the $LiTi_{0.5}Mn_{1.5}O_4$, $LiTiMnO_4$, $LiTi_{1.25}Mn_{0.75}O_4$ and $LiTi_{1.5}Mn_{0.5}O_4$ stoichiometries, containing networks of $Mn^{3+/4+}$, Mn^{3+}, $Mn^{2+/3+}$ and Mn^{2+} ions, respectively. When equivalent Mn-Mn interactions are present in different lattices, the corresponding J values were found to differ by less than 3%, differences arising from local distortions of the optimized geometries. All of the considered structures containing Mn^{3+} ions were found to exhibit a cooperative Jahn-Teller distortion.

Methodology of Hyperfine Coupling Constant, A_{iso}, Calculation

The isotropic value of the hyperfine tensor, A_{iso}, in equation 4.2, was calculated with DFT by integrating the unpaired electron spin density, $|\psi_N^{\alpha-\beta}|^2$, directly at the Li nuclear position in the ferromagnetic state, then scaled to the paramagnetic regime by multiplying it by the scaling factor Φ (equation 4.1) [61]. The bond pathway decomposition method presented by Middlemiss *et al.* [63] was followed, to obtain the Mn-O-Li Fermi contact bond pathway contribution from each Mn ion to the total Li shift, using the computed site-specific scaling factor, Φ_i.

Details of Hybrid DFT/Hartree Fock Calculations of Paramagnetic Shifts

All calculations of magnetic and hyperfine parameters were performed in CRYSTAL09[161], a solid-state DFT code using a Gaussian-type basis set to describe core states accurately. Because of the high dependence of the calculated paramagnetic shifts on the quality of the Gaussian basis sets, two types were utilized: a smaller basis set for geometry optimizations, and a more extended basis set for hyperfine and magnetic single-point calculations. All-electron atom-centered basis sets comprising fixed contractions of Gaussian primitive functions are employed throughout for the calculations done with CRYSTAL. Two levels of basis sets are used: the first and smaller set used for geometry optimizations is of the form (7s 2p 1d)/[1s 2sp 1d] for Li; (10s 4p 1d)/[1s 2sp 1d] for O; and (20s 12p 5d)/[1s 4sp 2d] for Mn and Ti, where the values in parentheses indicate the number of primitives within each shell and the values in square brackets the contraction scheme [108]. In the more extended provision used for the calculation of hyperfine A^{FC} and A^{dip} parameters,

modified IGLO-III sets are adopted for O, taking the form (10s 6p 2d)/[6s 5p 2d] for O [63]. A flexible and extended TZDP-derived basis of the form (9s 2p)/[5s 2p] is used for Li, and Ahlrichs DZP-derived sets of the form (13s 9p 5d)/[7s 5p 3d] are applied for Mn and Ti [63]. These sets are consistent with those used in a recent previous calculation of hyperfine parameters in a series of Mn-oxides [12, 66].

All calculations were performed with hybrid functionals in the spin polarized state. Previous *ab initio* studies on ^{7}Li paramagnetic NMR shifts show that values obtained using 20% and 35% Hartree Fock (HF) exchange provide the upper and lower bounds for the experimental shifts [62, 63]. Hence separate calculations were performed with the B3LYP functional with 20% HF exchange [169] (denoted HYB20) and a modified B3LYP with 35% of HF exchange (denoted HYB35). The convergence of the energy and the spin density were checked with respect to the number of sampled points in the reciprocal space. The reciprocal space sampling was performed with a k-point grid of $4 \times 4 \times 4$ points in the simulated cells, which contain 56 atoms. Self-consistent field cycles were converged to an energy difference of 2.7×10^{-6} eV.

4.3.3 Simulation and Fitting of the ^{7}Li NMR Spectra

Random Solution Model of a Single Phase

To use the Fermi contact bond pathway contributions, calculated from DFT, to simulate model NMR spectra, one needs to know the possible cationic environments around the lithium ions and the population distribution amongst these environments. The simplest approximation that can be made to obtain such distributions of environments is to consider that there is no cation ordering and thus the cations are randomly distributed in the sites available to them. This approach corresponds to the random solid solution model. In the regular spinel structure, Li centers have the following neighbouring cations:

- each Li in a Td site has 12 neighbor cations located on Oh sites, which are each bound via an oxygen bridge and considered to contribute to the overall Fermi contact shift of this lithium;
- each Li in an Oh site has 12 neighbor cations, 6 of which are in Td sites and 6 of which are in Oh sites, which are each bound via an oxygen bridge and considered to give (different) contributions to the overall Fermi contact shift of this lithium.

To simulate the NMR spectrum we thus need to know i) how the Li ions are distributed between Td and Oh sites and ii) what ions are present in each Li neighboring shell. Once we know these possible configurations, we can calculate the corresponding Fermi contact

shifts and estimate the probability of these environments in order to simulate the NMR spectrum. In the random solution model, for each Li environment with a given number of Mn and Ti neighbors, the number of all possible configurations is calculated, with the corresponding probability p modulated by the stoichiometric ratio of the ions in the structure. For each environment, a Gaussian distribution is then generated, of the form $G = p \cdot \exp[-(\delta - \sum \delta_{\text{path}})^2/(2 \cdot \omega^2)]$. In this formula, p is the probability associated with the environment considered, δ is the range of resonance values for which the distribution is calculated, $\sum \delta_{\text{path}}$ is the sum of all relevant bond pathway contributions to the shift involved in the particular environment and ω is the Gaussian width. An approximate Gaussian peak width of 15 ppm was used to model the individual environments, based on previous NMR studies on $LiMn_2O_4$ [49]. The simulated NMR spectrum is then obtained as the sum of the Gaussian plots corresponding to the various environments present in the system.

Reverse Monte Carlo Simulations of a Single Phase

While in some cases, the random solution model provides a good agreement with the experimental data, in other cases, such as the $LiTi_{1.5}Mn_{0.5}O_4$ material studied here, it does not and there is a need to calculate the populations of lithium environments according to different conditions. Here, for this purpose, we use a simulation method inspired by Reverse Monte Carlo approaches. The idea of a Reverse Monte Carlo simulation is to build a large simulation box that is representative of the system under study and to explore the effect of configurational changes. Starting from an initial configuration, i.e. a large number of ions with defined positions in space, we allow certain moves which are accepted or rejected depending on their agreement with chosen constraints.

In the present case, we built the large simulation box by replicating an initial spinel structure corresponding to $LiTi_{1.5}Mn_{0.5}O_4$ in the $P4_332$ space group. The initial structure contained 56 atoms corresponding to i) 8 Li ions in Td sites (8*c*), ii) 12 Ti ions and 4 Mn ions in Oh sites (12*d* and 4*b*, respectively) and iii) 32 oxygen sites (8*c* and 24*e*). This simulation box was replicated 10 times in all three dimensions leading to a large simulation box containing 8,000 Li ions, 12,000 Ti ions, 4,000 Mn ions and 32,000 oxygen ions. We checked that this 10×10×10 system is large enough by simulating some of the NMR spectra with a larger box of 15×15×15 repeat units. The results from the two system sizes showed no significant differences, and so the size of the 10×10×10 cell was considered to be sufficient. Once the initial simulation box is built, the Monte Carlo method proceeds *via* the steps below:

- swap two cations;

- characterize the new Li environments;
- accept or reject the move according to a set of chosen rules.

The swaps can be done between Li, Mn and Ti belonging to octahedral sites (or to tetrahedral sites) or between cations belonging to different structural sites. If the simulations are done without constraints, all the swaps will be done randomly. If the simulations are done under constraints, the swaps which do not lead to Li environments conflicting with the set constraints will always be accepted, while the swaps leading to unwanted Li environments will be accepted with a small probability. The acceptance probability of unwanted moves is $P_{acc} = \exp(-E_a/k_BT)$. Here, for all simulations, E_a was taken to be 10 eV, i.e. the probability of having unwanted Li environments is very close to zero. In addition to the swaps between the cations present in the structure, the Monte Carlo moves can include changes between different cation types. This is needed in order to reach some of the intermediate x values in the series. For example, on going from $LiTi_{1.5}Mn_{0.5}O_4$ to $LiTi_{1.4}Mn_{0.6}O_4$, a number of Ti ions need to be replaced by Mn ions and some Mn^{2+} ions (the only Mn oxidation state possible for $LiTi_{1.5}Mn_{0.5}O_4$) will be converted to Mn^{3+} ions. These changes in cation types are also made with or without constraints. Once a satisfactory representation of the system has been reached, in terms of i) Li distribution in Td and Oh sites, and ii) stoichiometry of the structure, the number of Li cations in each environment are simply counted, the corresponding shifts are calculated and, as in the random solution model representation, the simulated NMR spectrum is then obtained by summing the Gaussian plots corresponding to the various environments present in the system.

Model for Two Phase Systems

The random solution model and Monte Carlo approaches described above were first used to simulate homogeneous (single-phase) systems. In the $LiTi_xMn_{2-x}O_4$ series, this single phase representation is able to depict only part of the series of materials. In order to investigate the possibility of having inhomogeneous systems, we simulated independently two single-phase NMR spectra and summed them according to the fractions of the structure corresponding to each of the phases present in the system. In the Monte Carlo simulations, we built a single simulation box with two regions, each of the regions corresponding to a given phase.

4.4 Results and Discussion

4.4.1 Geometry Optimization and Energy Profile

Figure 4.2 compares the formation energies of a number of structures in the $LiTi_xMn_{2-x}O_4$ series with energies below 0 eV, which are all obtained using the search strategy described in the previous section. The full set of simulated structures is shown in Figure 4.3. The convex hull (tie-line in Figure 4.2) is obtained by joining the stable structures obtained by the search. The $LiTi_{1.5}Mn_{0.5}O_4$ phase corresponds to the bottom of the hull, with the lowest energy configuration having all the Mn^{2+} ions on tetrahedral sites, in agreement with the results of Petrov *et al.* based on X-ray diffraction[186]. This configuration corresponds to the phase having a 1:1 Mn^{2+}:Li^{+} mixed occupancy of the Td sites, and a 0.75:0.25 Ti^{4+}:Li^{+} mixed occupancy of the Oh sites, i.e., in the $A[B_2]O_4$ notation, $Li_{0.5}Mn_{0.5}[Li_{0.5}Ti_{1.5}]O_4$, with cubic $P4_132$ space group symmetry. For stoichiometries with $x > 1.0$, which have mixed Mn^{2+}-Mn^{3+} oxidation states, the lowest energy structures are the ones having Mn^{2+} ions on tetrahedral sites, and Mn^{3+} and Ti^{4+} on octahedral sites, consistent with previous X-ray diffraction results[186]. For stoichiometries of $0.2 \leq x < 1.0$, which have mixed Mn^{3+}-Mn^{4+} oxidation states, the lowest energy structures are the ones having full Li occupancy of the tetrahedral *8a* sites, and Mn^{3+}-Mn^{4+}-Ti^{4+} on the octahedral *16d* sites. For the case of $x = 1.0$, the *normal* spinel ($Li[TiMn^{3+}]O_4$) has all Mn ions nominally in the 3+ oxidation state. Our results show that this ordering does not correspond to the lowest energy structure of this composition. The thermodynamically favorable ordering for $x = 1.0$ is the partially *inverse* spinel with mixed Li-Mn^{2+} occupancy of the tetrahedral ($8a$) sites, and mixed Li-Mn^{3+}-Mn^{4+}-Ti^{4+} occupancy of the octahedral ($16d$) sites, in agreement with previous X-ray diffraction studies[186, 185]. The mixed Mn oxidation state in the *inverse* spinel results from the charge dispropotionation of $Mn^{3+}_{(8a)}$+$Mn^{3+}_{(16d)} \rightarrow Mn^{2+}_{(8a)}$+$Mn^{4+}_{(16d)}$, in agreement with the preferential occupancy of the Td ($8a$) sites by Mn^{2+} over Mn^{3+}[186, 185]. However, our results show that configurations with mixed Li-Ti occupancy of the tetrahedral sites and mixed Li-Mn^{3+}-Ti occupancy of the octahedral sites are thermodynamically unfavorable, in contrast with recent results based on X-ray diffraction and absorption studies [187].

According to the presented analysis based on the calculated formation energies, we can gain some insights into the more stable cation distributions in the spinel lattice, and the results we work with are gathered in Table 4.1.

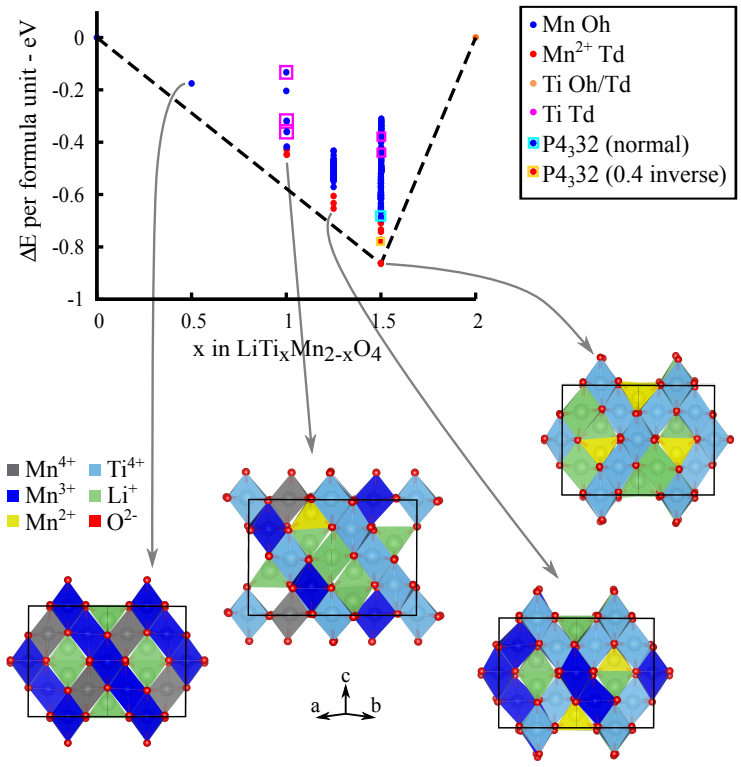

Fig. 4.2 Formation energy per $LiTi_xMn_{2-x}O_4$ formula unit *vs* fractional Ti concentration (x) in the $LiTi_xMn_{2-x}O_4$ series. The convex hull is indicated with a dashed line, and only the configurations with energies below 0 eV are shown. Insets show the minimum-energy structure for each of the studied points of the series. The majority of the structures with energies plotted on the Figure have Ti^{4+} ions on octahedral sites, those with Ti^{4+} on tetrahedral sites are indicated by blue circles corresponding to Oh Mn and outer magenta squares corresponding to Td Ti.

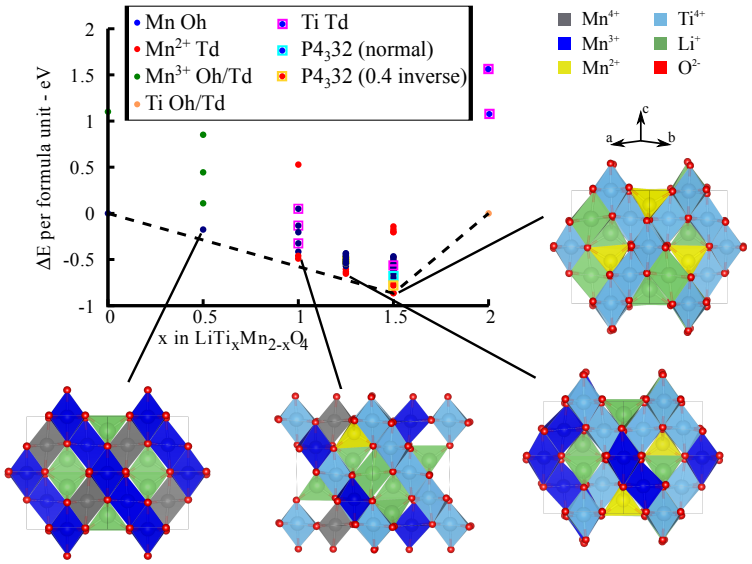

Fig. 4.3 Formation energy per $LiTi_xMn_{2-x}O_4$ formula unit *vs* fractional Ti concentration in the $LiTi_xMn_{2-x}O_4$ series. The convex hull is indicated with a dashed line, and the entire set of calculated configurations is shown. Insets show the minimum-energy structure for each of the studied points of the series. The majority of the structures with energies plotted on the Figure have Ti^{4+} ions on octahedral sites, those with Ti^{4+} on tetrahedral sites are indicated by blue circles corresponding to Oh Mn and outer magenta squares corresponding to Td Ti.

x in $LiTi_xMn_{2-x}O_4$					
$0.2 \leq x < 1.0$		$x = 1.0$		$1.1 \leq x \leq 1.5$	
Td Sites	Oh Sites	Td Sites	Oh Sites	Td Sites	Oh sites
Li^+	Mn^{3+} Mn^{4+} Ti^{4+}	Li^+ Mn^{2+}	Li^+ Mn^{3+} Mn^{4+} Ti^{4+}	Li^+ Mn^{2+}	Li^+ Mn^{2+} Mn^{3+} Ti^{4+}

Table 4.1 Summary of the energetically favorable tetrahedral (Td) and octahedral (Oh) occupancies throughout the $LiTi_xMn_{2-x}O_4$ series.

4.4.2 Solid-state NMR

Full one-dimensional ^7Li double-adiabatic spin-echo [192] spectra of the $LiTi_xMn_{2-x}O_4$ powder samples ($0.2 \leq x \leq 1.5$) are given in Figure 4.4a. The double-adiabatic spin-echo

sequence was chosen to obtain an efficient inversion of the whole spinning-sideband pattern, here of more than 400 kHz width [199]. The corresponding central regions of the spectra are shown in Figure 4.4b. The intensity ratio between the centreband and the sidebands did not change across the spectra, and for this reason we only fit the isotropic resonances. The variety of Li environments occurring in each phase leads to multiple distinct resonances, and a broad isotropic region. The resonances, on average, range from around 500 ppm to around 30 ppm with the increase in Ti concentration. We also note that the spectrum is significantly broader for intermediate x values, with the central regions covering a range of almost 600 ppm for $0.6 \leq x \leq 1.0$.

The distribution of discrete resonances giving rise to the broad spectra observed are due to Li ions in different local environments. These Li ions have different numbers of Mn^{2+}, Mn^{3+} and Mn^{4+} ions in their local coordination sphere, each contributing differently to the ^{7}Li Fermi contact shift. The shifting of the resonances to lower frequency with the increasing Ti concentration is consistent with the decrease in the average Mn oxidation state and the decrease in the overall concentration of paramagnetic Mn ions. [48]. A more detailed understanding of the structural differences across the series is now presented, based on the DFT analysis of the Fermi contact interaction.

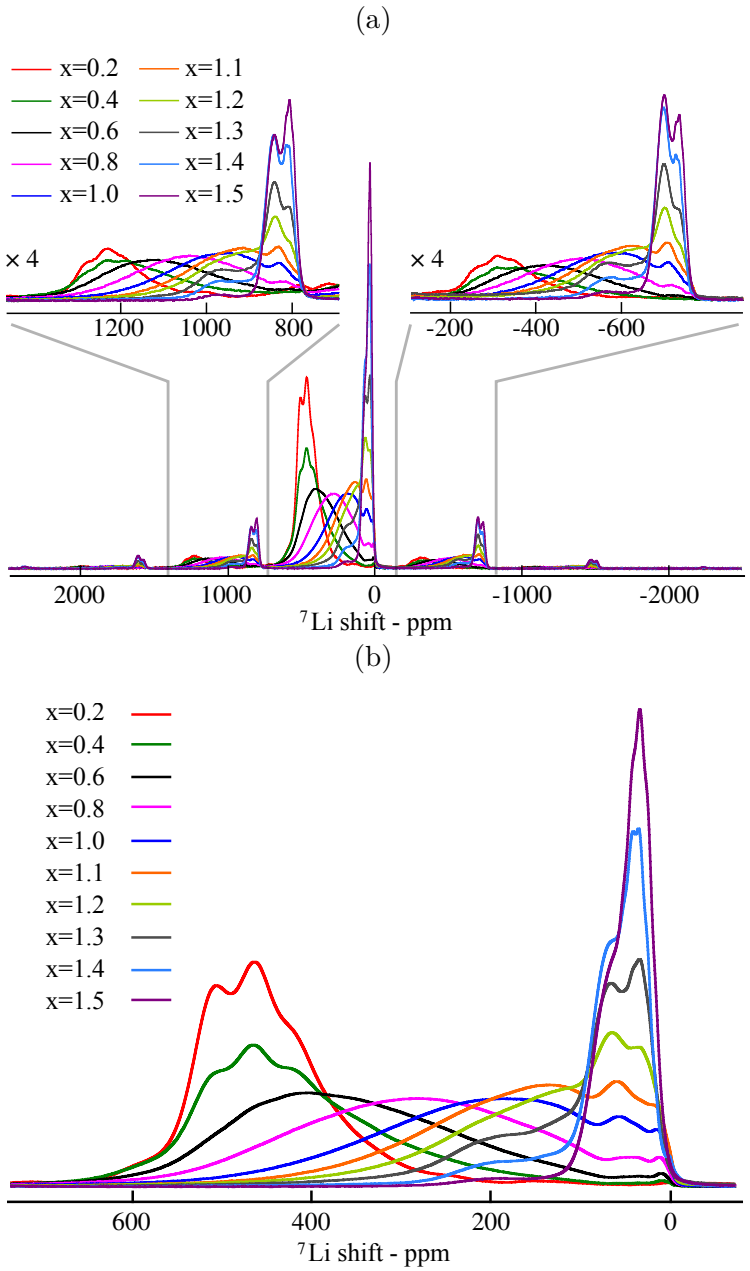

Fig. 4.4 (Figure 4.4a) ^{7}Li NMR spectra of the $LiTi_xMn_{2-x}O_4$ series, with the first-order sidebands enlarged in the top insets. Figure 4.4b shows an expanded view of the isotropic resonances of the spectra.

4.4.3 DFT Calculation of Magnetic and Hyperfine Parameters

As described previously (Equation 4.3), the magnetic scaling of the hyperfine interaction was modeled *via* a mean field approach based on the exchange coupling interaction between Mn pairs, as shown in Figure 4.6. Mn^{3+} has a $(t_{2g})^3(e_g^*)^1$ electronic configuration

which makes it Jahn-Teller active. Consequently, different exchange couplings and Fermi contact interactions were identified, depending on whether the pathway involves the Jahn-Teller lengthened or shortened Mn-O bond. The calculated J_n values are presented in Table 4.2. The results agree well with the values reported by Lee *et al.* and Clément *et al.* for similar Mn-oxides, such as $MgMn_2O_4$ [66] and $NaMnO_2$ [12]. Additionally, the accuracy of the calculated exchange integrals is tested for the $LiTi_{0.4}Mn_{1.6}O_4$ case, by comparing the magnetic scaling factors obtained with the mean field approach and by using the experimental magnetic susceptibility. The $LiTi_{0.4}Mn_{1.6}O_4$ molar magnetic susceptibility measured experimentally over the $2 - 350$K temperature range is shown in Fig. 4.5.

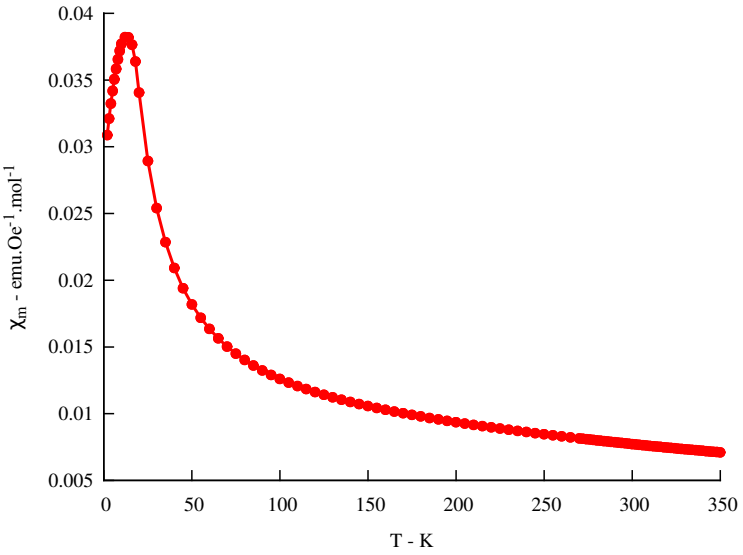

Fig. 4.5 Experimental molar magnetic susceptibility vs. temperature curve for $LiTi_{0.4}Mn_{1.6}O_4$.

As derived by Kim *et al.* [61], the bulk value for the magnetic scaling factor can be calculated from the experimental molar magnetic susceptibility (using the equivalent expression presented by Clément *et al.* [12]):

$$\Phi = \frac{B_0 \chi_m}{g_e \mu_B S N_A} \tag{4.4}$$

where B_0 is the external magnetic field strength, χ_m is the experimental molar magnetic susceptibility, g_e is the free electron g-value, μ_B is the Bohr magneton, S is the formal spin of the transition metal species and N_A is Avogadro's number.

In the case of $LiTi_{0.4}Mn_{1.6}O_4$ presented here, a bulk molar susceptibility of 7.69×10^{-3} emu.mol^{-1} is obtained at the temperature of 320 K. Taking $B_0 = 4.72$ T as the NMR external magnetic field, the net oxidation state of $Mn^{3.375+}$, hence $S = 1.8125$, and using eq. 4.4 with the experimental value of χ_m, a bulk magnetic scaling factor $\Phi_{\text{expt}} = 0.024$ is obtained. This result is compared with the value of the bulk magnetic scaling factor calculated with Mean Field approach described in Section 3.2.1, using the computed exchange coupling constants J_3 - J_4 - J_5 summarized in Table 4.2. A lattice of $LiTi_{0.4}Mn_{1.6}O_4$ composition is simulated, containing 51 Mn sites, and a bulk magnetic scaling factor $\Phi_{\text{MeanField}} = 0.018$ is obtained at the temperature of 320 K. The values obtained using the experimental χ_m and the Mean Field approach are in good agreement, indicating that the calculated exchange constants are reasonably accurate.

The magnitude of the exchange interactions is sensitive to the distance between the coupled ions, as well as to the coupling mechanism between the involved orbitals. As an example, we compare the exchange interactions between Mn^{3+}-Mn^{3+} in octahedral sites. The J_4 coupling (Figure 4.6, center) involves four Jahn-Teller shortened Mn-O bonds, which allow direct overlap between the Mn t_{2g} orbitals, leading to a strong anti-ferromagnetic exchange interaction. The J_3 coupling (Figure 4.6, center) involves two Jahn-Teller shortened and two Jahn-Teller elongated Mn-O bonds, the latter ones reducing the direct overlap between t_{2g} orbitals, and hence the strength of the direct exchange interaction. The superexchange interaction between the orbitals along the Jahn-Teller axis ($d_{z^2} - d_{xz/yz}$) results in a combination of weak ferro- and anti-ferromagnetic interactions, resulting in a significantly smaller J_3 coupling that is anti-ferromagnetic overall.

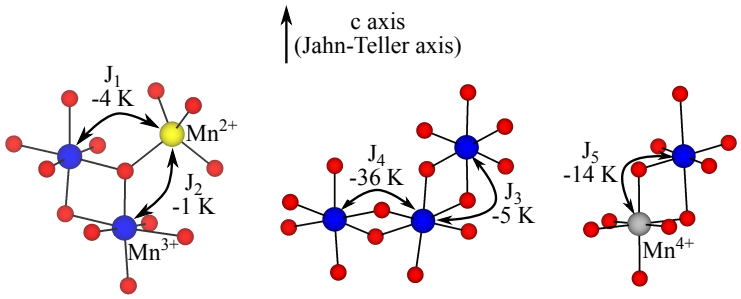

Fig. 4.6 Mn-Mn exchange coupling constants identified in the studied systems, i.e. $LiTi_{1.25}Mn_{0.25}O_4$ for J_1 and J_2, $LiTiMnO_4$ for J_3 and J_4, and $LiTi_{0.5}Mn_{1.5}O_4$ for J_5. For each J_n, the reported value corresponds to the average between the HYB20-HYB35 results.

J type	Magnetic Interaction	Mn-Mn angle degree, °	$\mathbf{J}_{exc}$	
			HYB20	HYB35
J_1	Mn^{2+} - Mn^{3+} JT short	120.2	-5 K	-3 K
J_2	Mn^{2+} - Mn^{3+} JT long	120.1	-1 K	-1 K
J_3	Mn^{3+} - Mn^{3+} JT short - JT long	90.6	-8 K	-3 K
J_4	Mn^{3+} - Mn^{3+} JT short - JT short	97.2	-41 K	-32 K
J_5	Mn^{4+} - Mn^{3+} JT short - JT long	96.1	15 K	13 K

Table 4.2 Comparison of the calculated Mn-Mn exchange coupling constants for pairs of ions interacting *via* an oxygen bridge. For the couplings involving Mn^{3+} ions, the nature of Jahn-Teller shortened or lengthened bond involved in the interaction is also specified. The results obtained with the HYB20 and HYB35 hybrid functionals are shown separately. Different J_n types are labeled as in Figure 4.6.

The possible Mn-O-Li bond pathways were identified for Li occupying Td as well as Oh sites. All the Li environments and corresponding pathways are described in Fig. 4.7, and are presented in Table 4.3. As rationalised by Carlier *et al.* [14] and summarised in Figure 2.2 of Section 2.3.1, the transfer of paramagnetic electron spin from the Mn t_{2g}/e_g^* orbitals to the *s* orbitals of the Li occur primarily *via* a superexchange-like mechanism. As presented in equation 4.1, the sign and magnitude of the Fermi contact shift are determined by a combination of factors. The extent of the transferred spin density, as well as the strength of the magnetic interaction discussed previously, strongly depend on the bond distances between the involved sites, and on the orbitals involved in the interaction [14]. The Mn-O-Li pathways in these systems involve intermediate angles (neither exactly 90° nor exactly 180°), hence the spin-density transfer deviates from a pure delocalization/polarization mechanism, and a complex combination of both processes is expected to occur. Nonetheless, we take the Li-O-Mn^{3+} pathways, P_1 and P_2 (Figure 4.7, top), as examples to give an approximate rationalization of the mechanisms involved. The P_1 pathway involves the Jahn-Teller shortened Mn-O bond, with positive transfer of spin density from the d_{xy} orbital *via* a delocalization mechanism. The P_2 pathway involves the Jahn-Teller lengthened Mn-O bond, and a combination of positive delocalization transfer from the $d_{xz/yz}$ orbitals and a negative polarisation transfer from the d_{z^2} orbital results in a weaker net Fermi contact interaction with the Li site.

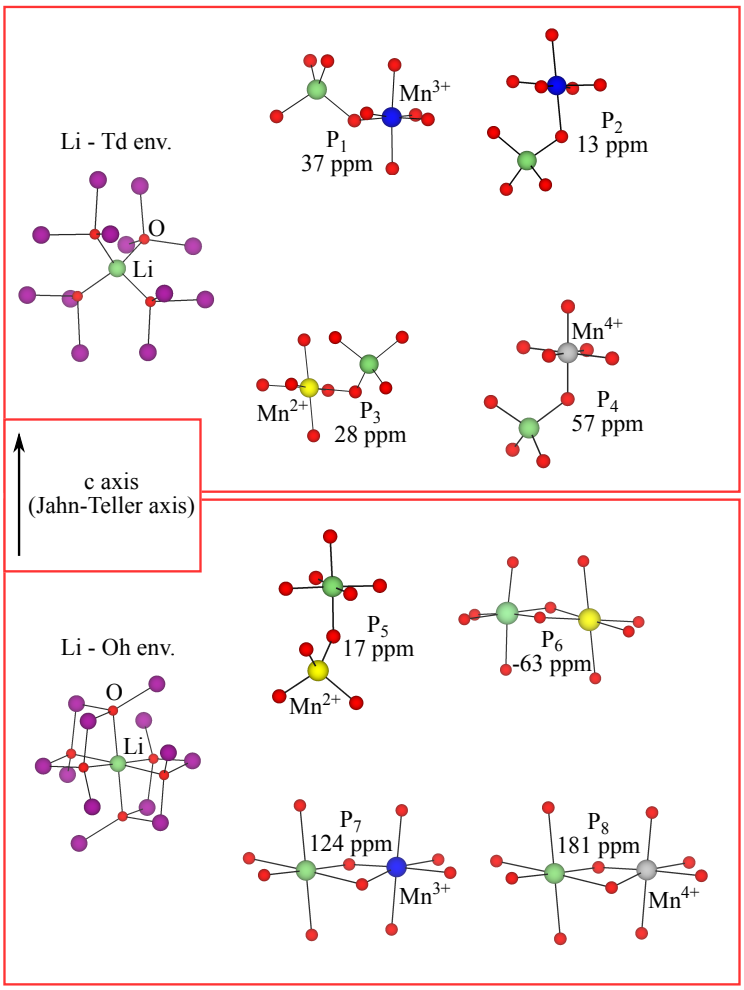

Fig. 4.7 ^{7}Li bond pathway contributions to the Fermi contact shift for a lithium center (in green) in a tetrahedral site (top) or in a octahedral site (bottom), each coordinated by twelve TM sites (in purple) via oxygen (in red) bonds. Manganese is shown in yellow, blue and grey for Mn^{2+}, Mn^{3+} and Mn^{4+}, respectively. For each bond pathway contribution, P, the reported value corresponds to the average between the HYB20-HYB35 results.

Li env.	Pathway	Mn neighbor	Mn-Li dist. Å	Mn-O-Li angle degree, °	Shift - H35; H20 ppm	Average Shift ppm
Li Td	P_1	Mn^{3+} Oh - JT short	3.5	120.2	34; 39	37
	P_2	Mn^{3+} Oh - JT long	3.6	114.0	10; 16	13
	P_3	Mn^{2+} Oh	3.5	115.2	24; 32	28
	P_4	Mn^{4+}	3.5	116.2	50; 64	57
Li Oh	P_5	Mn^{2+} Td	3.5	114.0	15; 18	17
	P_6	Mn^{2+} Oh	3.0	92.3	-54; -73	-64
	P_7	Mn^{3+} Oh - JT long	3.6	91.6	150; 98	124
	P_8	Mn^{4+} Oh	3.5	92.0	213; 151	181

Table 4.3 Comparison of the calculated Mn-O-Li pathway contributions to the ^{7}Li Fermi contact shift, obtained either with HYB20 or HYB35 functional. The table rows on the top show the possible neighbouring TM sites transferring unpaired-electron spin density to a Li center in a tetrahedral site, while the table rows on the bottom show the possible sites transferring unpaired-electron spin density to a Li center in a octahedral site. Pathways are labelled as in Figure 4.7.

4.4.4 Simulation and Fitting of the Experimental ^{7}Li NMR Spectra

We now demonstrate how the bond pathway contributions calculated in Table 4.3 can be used to model the ^{7}Li NMR spectra of the $LiTi_xMn_{2-x}O_4$ series, allowing us to extract detailed local structural information. The shift values calculated with the HYB20 and HYB35 functionals give the upper and lower bounds, however, in the following analysis we use a pragmatic approach in which the HYB20 and HYB35 results are averaged to give a single value for each pathway, P, as shown in Table 4.3. For all the systems containing Mn^{3+}, we model the Jahn-Teller distortion as a dynamic process in which the timescale of the changes in local Mn-O bond lengths is much faster than the typical NMR timescale [63]. As a consequence, we assume that the shifts corresponding to Mn^{3+}-O-Li are well represented by a weighted average with 2/3 of Jahn-Teller-short and 1/3 of Jahn-Teller-long pathway contributions.[63]

For all the systems containing exclusively Mn^{3+} and Mn^{4+} ions, i.e. the $0.2 \leq x \leq 0.8$ stoichiometries, we make an additional assumption. In this case, we consider that the timescale of electronic conduction is fast compared to the NMR timescale. This means that we can consider only one shift corresponding to an average oxidation state of the Mn ions. The weighted average depends on the stoichiometry of the system, as the average oxidation state is a function of the Ti content of the material. For example, for $LiTi_{0.2}Mn_{1.8}O_4$, the average Mn oxidation state is 3.444 while it is 3.375 for $LiTi_{0.4}Mn_{1.6}O_4$. As a result, the net shift contributions are: 41 ppm for a $Mn^{3.44+}$ in $LiTi_{0.2}Mn_{1.8}O_4$, 39 ppm for a $Mn^{3.38+}$ in $LiTi_{0.4}Mn_{1.6}O_4$, 37 ppm for a $Mn^{3.29+}$ in $LiTi_{0.6}Mn_{1.4}O_4$, and 33 ppm for a $Mn^{3.17+}$ in $LiTi_{0.8}Mn_{1.2}O_4$. This assumption, as well as the accuracy of the calculated bond pathway shift contributions, is tested with respect to the ^{7}Li NMR shift of $LiMn_2O_4$. This material has been extensively studied with NMR: as discussed in detail by Lee *et al.* [50], the NMR spectrum of $LiMn_2O_4$ with Li in the tetrahedral *8a* position, is dominated by one major resonance with an isotropic shift of $512 - 520$ ppm, the exact value varying between samples and likely the temperature of the measurement. In this stoichiometry, Mn is present in an average oxidation state of 3.5+. Combining the shift contributions that we obtained with DFT, summarised in Table 4.3, and accounting for a dynamic Jahn-Teller distortion, our calculations predict a net shift contribution of 43 ppm from a $Mn^{3.5+}$ ion. Given that in the $LiMn_2O_4$ spinel structure, each Li is bonded *via* the oxygen to 12 Mn ions, the overall calculated Li NMR shift is $12 \times 43\text{ppm} = 515$ ppm, in very good agreement with the experimental shift.[50]

$\mathbf{LiTi_{0.2}Mn_{1.8}O_4}$

We begin our analysis of the NMR results by considering the member of the series with the lowest Ti concentration, i.e. $LiTi_{0.2}Mn_{1.8}O_4$. For this system, the ^{7}Li NMR spectrum was simulated assuming a random distribution of ions in the Li local coordination shell. All Li ions are considered on the tetrahedral sites, following our observation that the presence of Ti^{4+}, Mn^{3+} and Mn^{4+} in tetrahedral sites is energetically unfavorable. The total DFT predicted spectrum is shown in Fig. 4.8a, with the individual peaks shown in Figure 4.8b. The spectrum is obtained as a Gaussian distribution of resonances corresponding to each Li environment with the associated total Fermi contact shift obtained as a sum of the DFT-calculated pathway contributions. The Li environment corresponding to each resonance differs from the others by the number of Ti centers among the 12 neighboring sites.

The experimental ^{7}Li NMR spectrum of $LiTi_{0.2}Mn_{1.8}O_4$ was then fitted, as shown in Fig. 4.8a. A good fit is obtained by using 5 more intense peaks of Voigt lineshape

and two very weak peaks. The shift contributions predicted with DFT match very well with the values obtained from the experimental fit, with a maximum discrepancy of 16 ppm. The five main peaks extracted from the fit are assigned to Li sites with 12 Mn neighbors (fit: 512 ppm, DFT: 496 ppm), 11 Mn and 1 Ti neighbors (fit: 464 ppm, DFT: 454 ppm), 10 Mn and 2 Ti neighbors (fit: 417 ppm, DFT: 413 ppm), 9 Mn and 3 Ti neighbors (fit: 370 ppm, DFT: 372 ppm), and 8 Mn and 4 Ti (fit: 324 ppm, DFT: 331 ppm), as shown in Figure 4.8a. Moreover, the relative intensities of the different peaks are accurately reproduced by the model that considers a random distribution of Ti^{4+} and $Mn^{3.44+}$ among the octahedral sites. The weak peak at 595 ppm is also predicted by DFT with the model that does not consider a dynamic exchange between Mn^{3+} and Mn^{4+}. In particular, the shift of the Li environment coordinated with 3 Mn^{3+} and 9 Mn^{4+} is calculated to be 599 ppm, in good agreement with the experimental shift of 595 ppm.

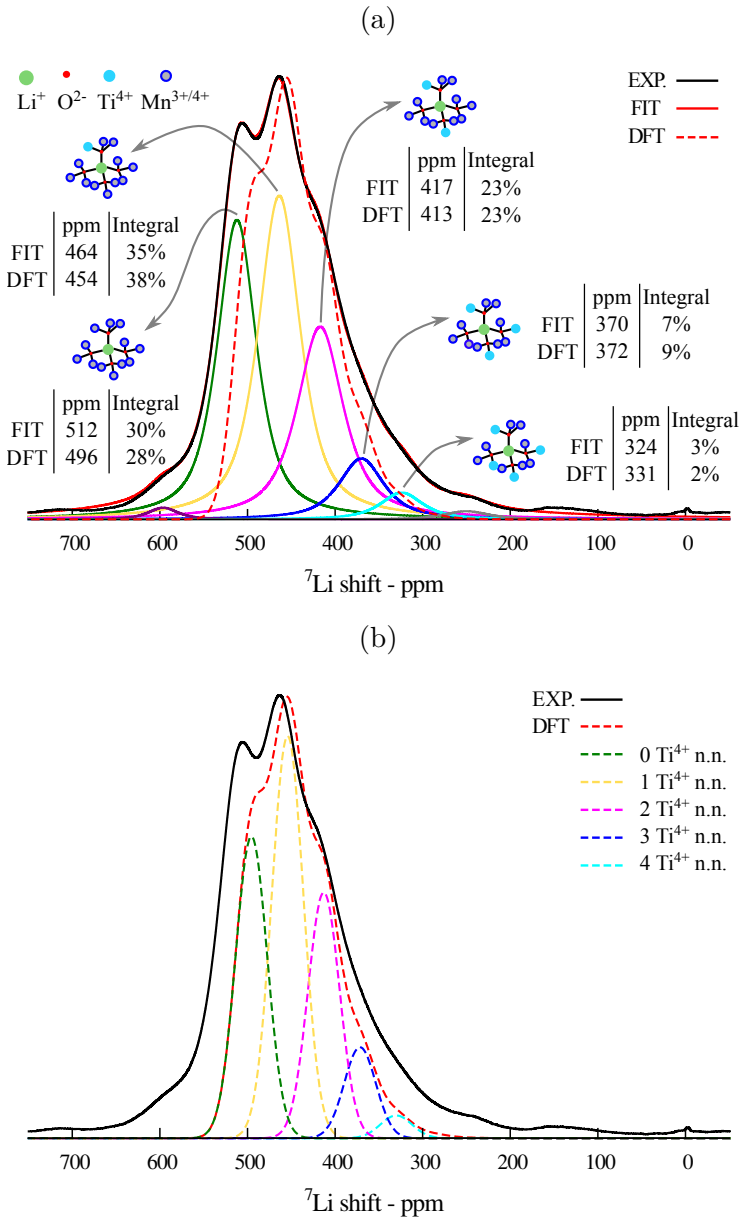

Fig. 4.8 (4.8a) Comparison of the experimental isotropic region of the ^{7}Li NMR spectrum of $LiTi_{0.2}Mn_{1.8}O_4$ (in black, with the fitting shown in red), and the DFT-simulated resonance assuming a random distribution of Ti^{4+} and $Mn^{3+/4+}$ (in dashed red). Also shown are the peaks used in the fitting of the experimental spectrum (purple, green, yellow, magenta, blue, cyan and gray peaks). (4.8b) For comparison, the peaks obtained in the DFT-simulated random distribution model are shown, following the same coloring scheme as in Figure 4.8a.

Figure 4.9 shows the results of the model that does not consider a dynamic exchange between Mn^{3+} and Mn^{4+}. The lineshape of the spectrum simulated in this way is in

less good agreement with the experimental NMR spectrum, confirming that the fast $Mn^{3+/4+}$ hopping rate in the experimental NMR conditions is a good assumption for these systems.

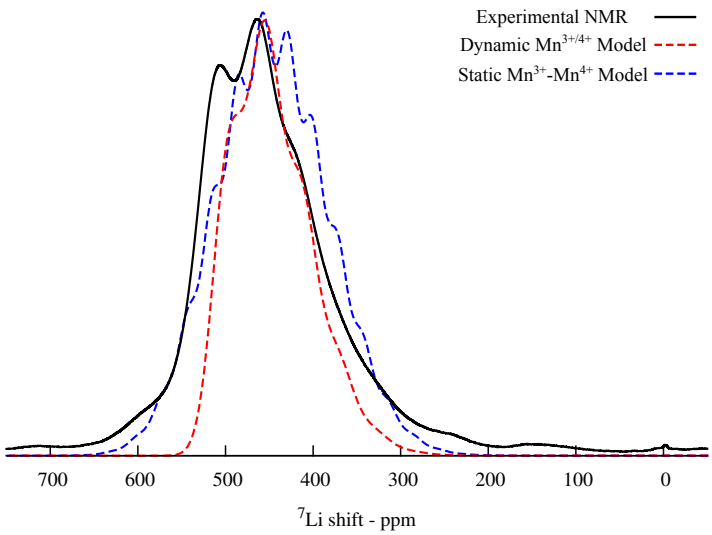

Fig. 4.9 Comparison between the experimental (solid black line) and the simulated ^{7}Li spectrum of $LiTi_{0.2}Mn_{1.8}O_4$ based on the random solution model, assuming a dynamic exchange (dotted red line) and no exchange (dotted blue line) between Mn^{3+} and Mn^{4+}.

$0.4 \leq x < 1.0$ stoichiometries

Following the successful description of the cation ordering for $LiTi_{0.2}Mn_{1.8}O_4$ with the random distribution model, we apply the same approach for the $0.4 \leq x < 1.0$ stoichiometries. As shown in Figure 4.10, the deconvolution of the isotropic region for $LiTi_{0.4}Mn_{1.6}O_4$ deviates significantly from the spectrum simulated for the random distribution model. The disagreement between the experimental NMR spectra and the simulations based on the random distribution model persists for all the $0.4 \leq x < 1.0$ cases, as shown in Figure 4.11.

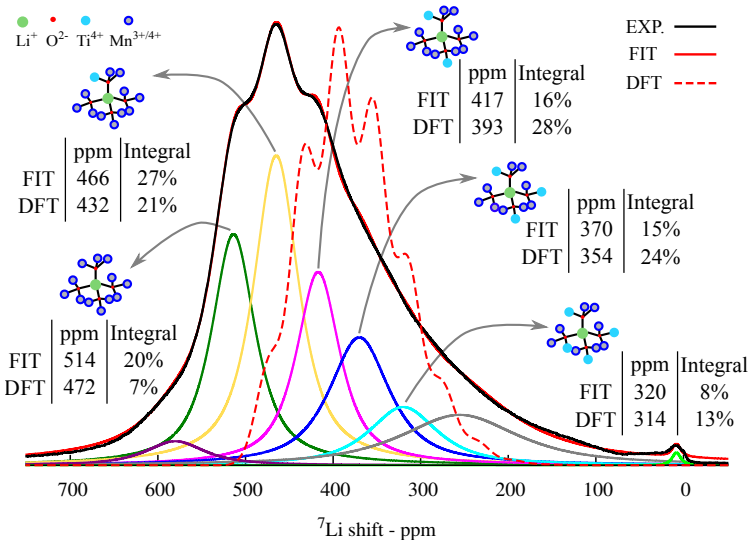

Fig. 4.10 Results of the fitting of the ^{7}Li NMR spectrum for the $LiTi_{0.4}Mn_{1.6}O_4$, and comparison with the random model predicted with DFT.

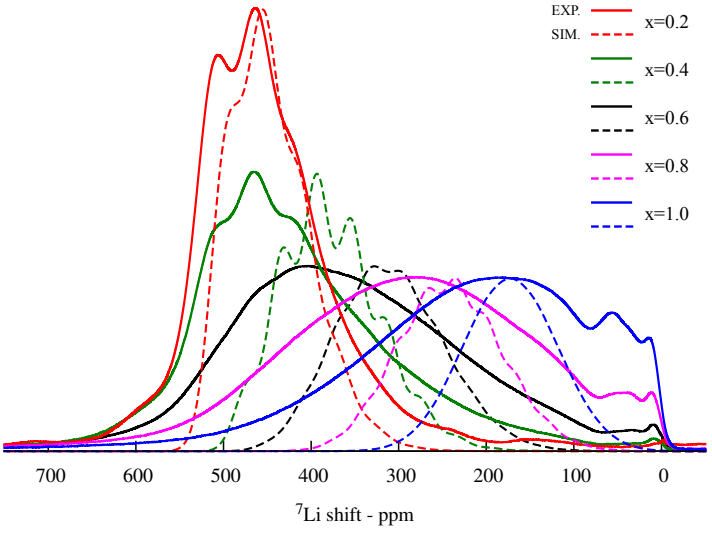

Fig. 4.11 Comparison of the experimental isotropic region (in solid line) of the ^{7}Li NMR spectrum of $LiTi_xMn_{2-x}O_4$, and the simulated region assuming a random distribution of Ti^{4+} and $Mn^{3+/4+}$ in a single-phase model (dashed line). The red, green, black, magenta and blue lines are for $x = 0.2,\ 0.4,\ 0.6,\ 0.8,\ 1$, respectively.

By comparing the NMR fit of the isotropic region for $LiTi_{0.2}Mn_{1.8}O_4$ (Figure 4.8a), and that of $LiTi_{0.4}Mn_{1.6}O_4$ (Figure S3), we notice that i) the major contributing peaks of the $x = 0.2$ spectrum have the same shifts as five of the major peaks in the $x = 0.4$ case,

and ii) the spectrum of the $x = 0.4$ case shows an additional broad feature that extends between 300 and 100 ppm, which is absent in the spectrum of $x = 0.2$. In $LiTi_{0.2}Mn_{1.8}O_4$, Mn has a net charge of 3.44+, while in $LiTi_{0.4}Mn_{1.6}O_4$, Mn has a net charge of 3.375+, each with different Fermi contact shift contributions to the neighboring Li center (41 ppm for $Mn^{3.44+}$ and 39 ppm for $Mn^{3.375+}$). The fact that the fits of the spectra for the $x = 0.2$ and for the $x = 0.4$ cases give the major peaks at exactly the same shifts indicate that in the $x = 0.4$ cases these correspond to $Mn^{4+}-$rich Li environments. The spectrum of the $x = 0.4$ case simulated for the random $Mn^{3.375+}$-Ti distribution does not show shifts lower than 240 ppm, in disagreement with the experimental spectrum. This suggests the presence of Mn^{3+}-rich Li environments in the structure. The ^{7}Li isotropic region for $LiTi_{0.4}Mn_{1.6}O_4$ is hence modeled as a 1 : 1 combination (i.e. an average) of the $LiTi_{0.2}Mn_{1.8}O_4$ and $LiTi_{0.6}Mn_{1.4}O_4$ experimental spectra. The resulting peaks, shown in Figure 4.12, reproduce the experimental spectrum of the $x = 0.4$ case very well, indicating a coexistence of $Mn^{4+}-$rich and $Mn^{3+}-$rich domains.

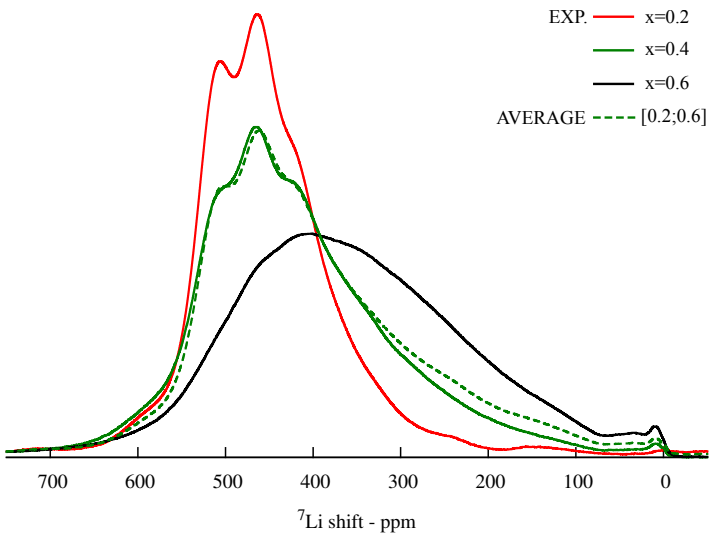

Fig. 4.12 Comparison of the experimental isotropic region of the ^{7}Li NMR spectrum of $LiTi_{0.2}Mn_{1.8}O_4$ (in red), $LiTi_{0.4}Mn_{1.6}O_4$ (in green), and $LiTi_{0.6}Mn_{1.4}O_4$ (in black), and the calculated $LiTi_{0.4}Mn_{1.6}O_4$ (in dashed green) isotropic peak. This is obtained by taking the average of the peaks of ($x = 0.2, x = 0.6$).

The spectra for the $x = 0.6$ and $x = 0.8$ show a gradual shift of resonances towards lower frequency with the increasing Ti concentration, indicative of a continuous solid solution behavior [186].

$\mathbf{LiTiMnO_4}$

As described in Figure 4.2 and in Table 4.1, for the $x = 1$ case our calculations predicted that the configuration with mixed Li-Mn^{2+} tetrahedral and Li-$Mn^{3+/4+}$-Ti octahedral occupancies is more favorable than the *normal* spinel ($Li[Mn^{3+}Ti]O_4$). Studies based on X-ray diffraction reported $20\% - 30\%$ Li occupancy of the Oh site (or, equivalently, $20\% - 30\%$ Mn^{2+} on the Td site) [186, 185]. In an attempt to model the spectrum for $LiTiMnO_4$, we hence consider a random cation distribution for the *normal* spinel lattice ($Li[Mn^{3+}Ti]O_4$), as well as for the partially inverse lattice with 30% site inversion ($Li_{0.7}Mn^{2+}_{0.3}[Li_{0.3}Mn^{4+}_{0.3}Mn^{3+}_{0.4}Ti]O_4$). The results are shown in Figure 4.13.

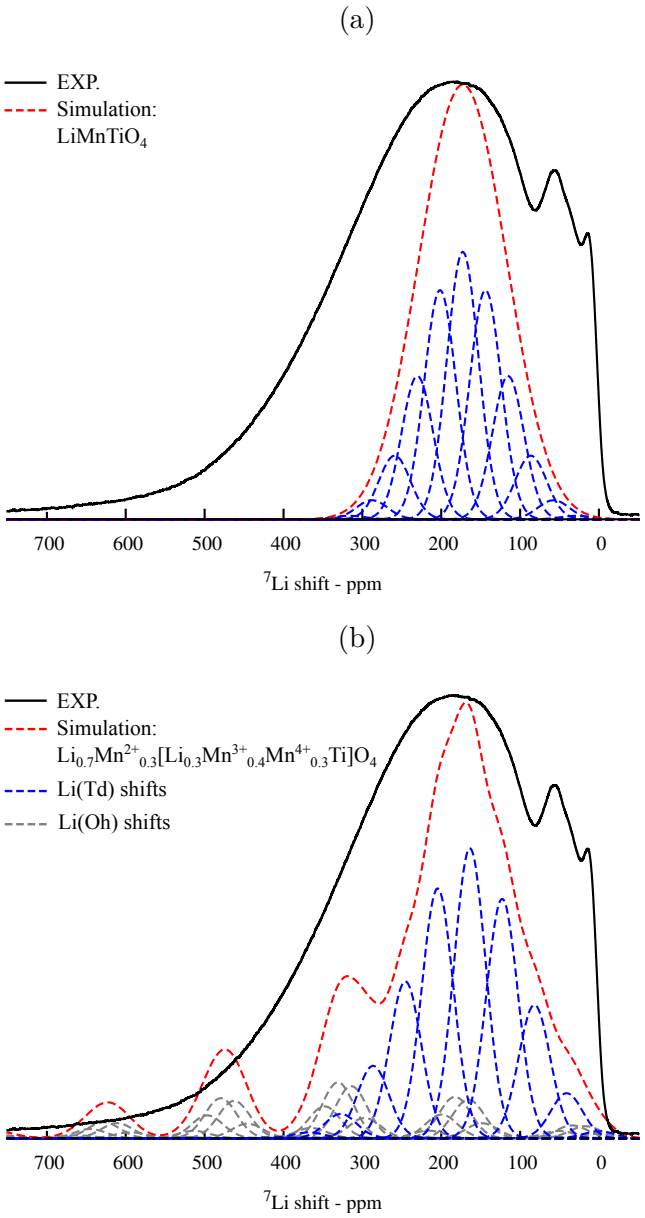

Fig. 4.13 Comparison of the experimental isotropic region of the ^{7}Li NMR spectrum of $LiTiMnO_4$ (in solid black line), with the simulated spectrum of the *normal* $Li[TiMn^{3+}]O_4$ (in dashed red line, Fig. 4.13a), and the simulated spectrum of the partially inverse $Li_{0.7}Mn^{2+}_{0.3}[Li_{0.3}Mn^{3+}_{0.4}Mn^{4+}_{0.3}Ti]O_4$ (in dashed red line, Fig. 4.13b). Also shown are the peaks corresponding to Li(Td) environments (in dashed blue lines), and to Li(Oh) environments (in dashed gray lines).

The spectrum simulated for the partially inverse case (Figure 4.13b) shows shifts over the entire $0-700$ ppm region of the experimental spectrum, while the simulation for the *normal* spinel (Figure 4.13a) only shows shifts between $20-300$ ppm. This confirms

the presence of both Li(Td) and Li(Oh) environments in the structure, as predicted by our calculations (Table 4.1). However, the lineshape of the experimental spectrum is not well reproduced by the simulation for the disordered $Li_{0.7}Mn^{2+}_{0.3}[Li_{0.3}Mn^{3+}_{0.4}Mn^{4+}_{0.3}Ti]O_4$ lattice, particularly between $0-100$ ppm and $350-450$ ppm. This indicates that the cations are not distributed randomly in the structure, and cation ordering determines the preferential presence of certain environments over others. Due to the configurational complexity of the system, which contains $Li/Mn^{2+,3+,4+}/Ti$ ions and mixed occupancy of the Td and Oh sites, further work would be needed in order to systematically analyze the configurational energies of different orderings [200], as well as to possibly account for the electroneutrality principle [201].

$\mathbf{LiTi_{1.5}Mn_{0.5}O_4}$

We now turn to the interpretation of the NMR spectra for the Ti-rich part of the series, starting with the end member $LiTi_{1.5}Mn_{0.5}O_4$. In this system, we expect Li^+, Mn^{2+} and Ti^{4+} cations to be present. The formation energies calculated with DFT shown in Figure 4.2 indicate that it is energetically favorable for Mn^{2+} ions to be on tetrahedral sites, leading to (at least) a fraction of the Li ions on the octahedral sites, also suggested by previous X-ray studies [186]. This fraction is referred to as the inverted fraction of Li, y, in the notation $Li_{1-y}Mn_y[Li_yTi_{1.5}Mn_{0.5-y}]O_4$. The first model we test is a random distribution of Mn^{2+}/Li^+ ions on tetrahedral sites and $Li^+/Mn^{2+}/Ti^{4+}$ on octahedral sites. The simulated NMR spectra are shown in Figure 4.14 for various inverted fractions of Li from $y = 0.0$ (i.e. $Li[Ti_{1.5}Mn_{0.5}]O_4$) to $y = 0.5$ (i.e.$Li_{0.5}Mn_{0.5}[Li_{0.5}Ti_{1.5}]O_4$). When the inverted fraction is $y = 0.5$, all Mn^{2+} are on tetrahedral sites while half Li ions are on octahedral sites and half Li ions are on tetrahedral sites. None of the spectra show good agreement with the experiment. The simulated spectra show two main features in strong disagreement with the experimental data, i.e. resonances at 0 ppm and some at negative frequencies, which are clearly not present in the experimental NMR spectrum. In order to use this information, we thus turn to another strategy and follow an approach similar to Reverse Monte Carlo where constraints are imposed. We use as a starting point a spinel structure with a $P4_332$ symmetry, as this was suggested by X-ray studies on this material [186]. In our starting $P4_332$ structure, the lattice is characterized by a full Li occupancy on the tetrahedral sites, and a full Ti/Mn occupancy of the octahedral sites (i.e. a regular spinel structure). This ordering corresponds to the presence of only one type of Li environment with 9 Ti^{4+} and 3 Mn^{2+}_{Oh} neighbors. The calculated shift is 3×28 ppm$=$ 85 ppm, in clear disagreement with the experimental NMR. Starting from the fully regular structure, the Monte Carlo simulation then allowed for some fraction of

Li to move onto the octahedral environment, with the consequent swap of Mn onto the tetrahedral sublattice. After each swap, the Li coordination environments are checked and the corresponding shifts are calculated. If the swap leads to a "wrong" shift (a shift ≤ 0 ppm), it will be accepted but only with a very low probability.

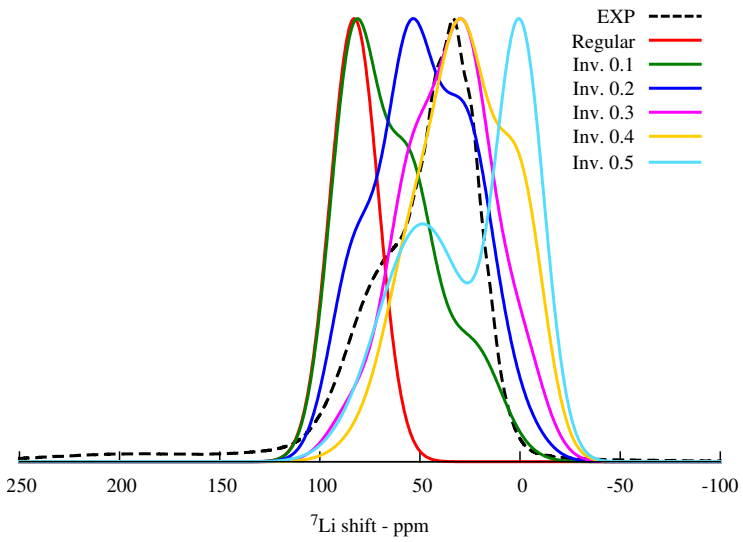

Fig. 4.14 Isotropic region of the experimental ^{7}Li NMR spectrum of $LiTi_{1.5}Mn_{0.5}O_4$ (dotted black line), and the NMR results of the Monte Carlo simulation of $Li_{1-y}Mn_y[Li_yTi_{1.5}Mn_{0.5-y}]O_4$. Red, green blue, magenta, yellow and cyan lines for y=0, 0.1, 0.2, 0.3 and 0.4, respectively.

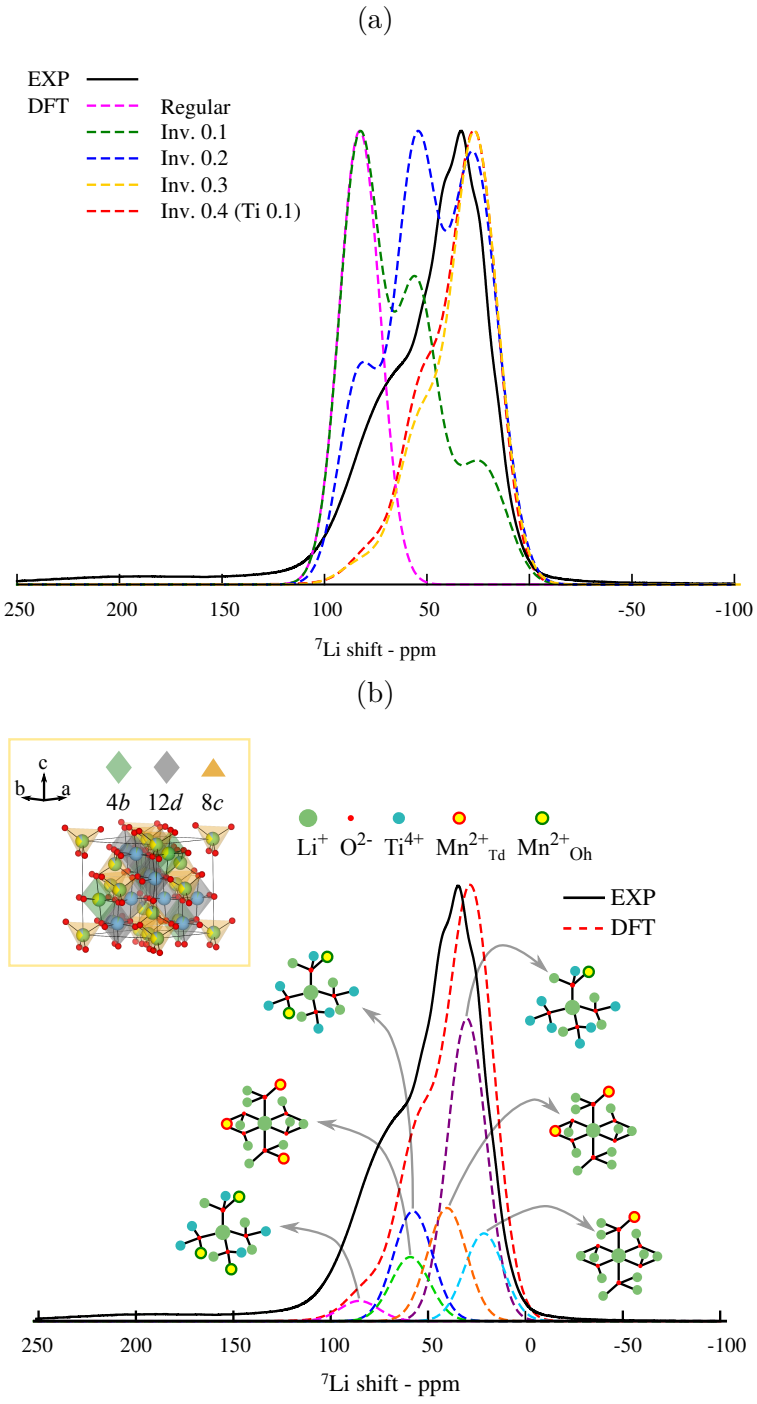

Fig. 4.15 (Fig. 4.15a) Isotropic region of the experimental ^{7}Li NMR spectrum of $LiTi_{1.5}Mn_{0.5}O_4$ (solid black line), and the NMR results of the Reverse Monte Carlo simulation of $Li_{1-y}Mn_y[Li_yTi_{1.5}Mn_{0.5-y}]O_4$. Dotted magenta, green, blue and yellow lines for y=0, 0.1, 0.2, and 0.3, respectively, and dotted red line for $Li_{0.6}Ti_{0.1}Mn_{0.3}[Li_{0.4}Ti_{1.4}Mn_{0.2}]O_4$. (Fig. 4.15b) Isotropic region of the experimental ^{7}Li NMR spectrum (in solid black line) and the simulated spectrum (in dotted red line) of $Li_{0.6}Ti_{0.1}Mn_{0.3}[Li_{0.4}Ti_{1.4}Mn_{0.2}]O_4$. For each Li coordination, the corresponding peak is shown, as calculated with the Monte Carlo method. The corresponding cation ordering in the $P4_332$ lattice is shown in the top-left inset.

The results of the Reverse Monte Carlo approach are shown in Figure 4.15a. The best agreement between simulation and experiment is obtained for the y=0.4 case, shown more in detail in Figure 4.15b, corresponding to $Li_{0.6}Ti_{0.1}Mn_{0.3}[Li_{0.4}Ti_{1.4}Mn_{0.2}]O_4$ lattice of $P4_332$ symmetry, with the repeated unit shown in the inset of Figure 4.15b. The Li environments present in the lattice are also shown in the Figure with the associated NMR peaks. The good agreement between the model and the experimental spectrum allows us to conclude that the spinel network of the $LiTi_{1.5}Mn_{0.5}O_4$ system, of $P4_332$ symmetry as previously reported [186], contains mixed cation occupancy of Li, Mn^{2+} and Ti in both tetrahedral and octahedral environments. The presented analysis also allows us to derive a specific cation ordering within $P4_332$ network, i.e. $(Li_{0.6}Ti_{0.1}Mn_{0.3})_{8c}[(Li_{0.1}Ti_{1.4})_{12d}(Li_{0.3}Mn_{0.2})_{4b}]O_4$.

$1.1 \leq x \leq 1.4$ **Stoichiometries**

The Reverse Monte Carlo approach was implemented further, to analyse the NMR spectra of the intermediate $1.1 \leq x \leq 1.4$ systems. We first look at the $LiTi_{1.4}Mn_{0.6}O_4$ material using exactly the same approach as for $LiTi_{1.5}Mn_{0.5}O_4$ but now having a mix of Mn^{3+} and Mn^{2+} ions. As highlighted previously from the DFT results, the presence of Mn^{3+} on tetrahedral sites is unfavourable. The NMR spectra simulated for an homogeneous $LiTi_{1.4}Mn_{0.6}O_4$ system and various inverted fractions are shown in Figure 4.16. It is clear from the comparison with experiments that this model is not sufficient to describe the system. In particular, there is a broad peak with a large shift ($\sim$ 200 ppm) which cannot be explained by this model, while the region of the spectrum between 0$-$100 ppm decreases in intensity but does not vary in shift compared to the $LiTi_{1.5}Mn_{0.5}O_4$ case.

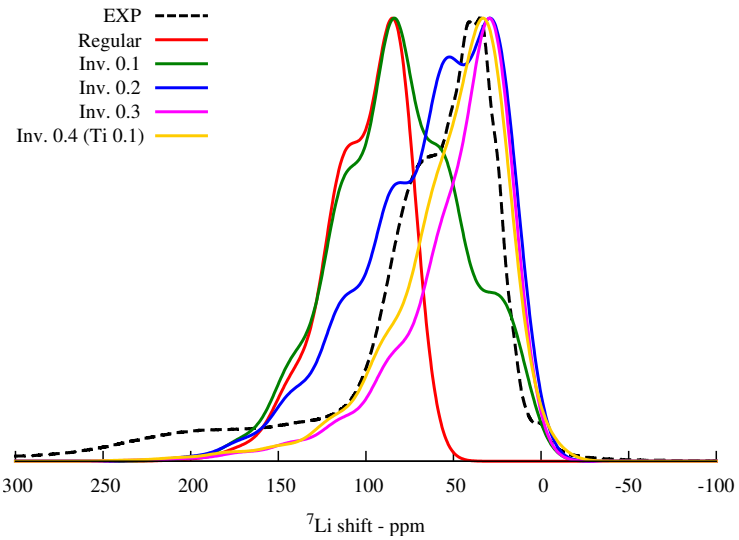

Fig. 4.16 Isotropic region of the experimental ^{7}Li NMR spectrum of $LiTi_{1.4}Mn_{0.6}O_4$ (dotted black line), and the NMR results of the constrained Monte Carlo simulation of $Li_{1-y}Mn_y[Li_yTi_{1.4}Mn_{0.6-y}]O_4$. Red, green, blue and magenta lines for y=0, 0.1, 0.2, and 0.3, respectively, and yellow line for $Li_{0.6}Ti_{0.1}Mn_{0.3}[Li_{0.4}Ti_{1.3}Mn_{0.3}]O_4$

In order to use this information, we modify the model so to retain the $P4_332$ ordering of the Mn^{2+}-rich phase, as shown for the $x = 1.5$ case, while including a random distribution of cations in the $Fd\bar{3}m$ Mn^{3+}-rich phase, as shown for the $0.2 \leq x \leq 1.0$ cases. In these simulations, a Gaussian width of 50 ppm was found to be required to model the $Fd\bar{3}m$ domain, while a Gaussian width of 12 ppm was again found to be sufficient to model the $P4_332$ domain. This difference between the peak widths may be rationalized in terms of the higher degree of disorder among the Li environments present in the $Fd\bar{3}m$ phase compared to the more ordered $P4_332$ phase. The approach is followed for the entire $1.1 \leq x \leq 1.4$ series. Furthermore, for each composition the Monte Carlo simulation also optimized the inverted fraction, y, within the $P4_332$ phase, and so we obtain: for $x = 1.4$ $Li_{0.8}Mn^{2+}_{0.2}[Li_{0.2}Mn^{2+}_{0.2}Mn^{3+}_{0.2}Ti_{1.4}]O_4$, for $x = 1.3$ $Li_{0.86}Mn^{2+}_{0.14}[Li_{0.14}Mn^{2+}_{0.16}Mn^{3+}_{0.4}Ti_{1.3}]O_4$, for $x = 1.2$ $Li_{0.92}Mn^{2+}_{0.08}[Li_{0.08}Mn^{2+}_{0.12}Mn^{3+}_{0.6}Ti_{1.2}]O_4$. The results are shown in Figure 4.17. The good agreement between the simulated and the experimental NMR spectra throughout the $1.1 \leq x \leq 1.5$ series suggests that as Mn^{2+} starts to be formed in the system, it preferentially occupies the tetrahedral environment, determining a partial ordering between Li−Mn^{2+} Td-Oh sites in the $P4_332$ symmetry, while the regular Mn^{3+}-rich component retains a random distribution of cations consistent with the $Fd\bar{3}m$ symmetry. As NMR probes structural short-range ordering, it does not allow us to distinguish the sizes of the $Fd\bar{3}m$ and the $P4_332$ phases. Since previous diffraction studies [186],

which are sensitive to long-range ordering, reported a single $P4_332$ phase behavior for $1.2 \leq x \leq 1.4$, this may suggest that the $Fd\bar{3}m - P4_332$ phase segregation is on the local scale, potentially forming small domains.

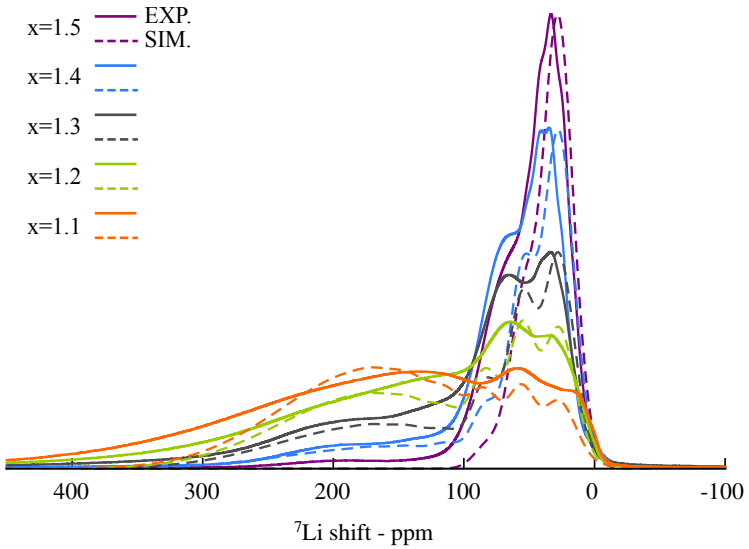

Fig. 4.17 Comparison of the experimental isotropic region (in solid line) of the ^{7}Li NMR spectrum of $LiTi_xMn_{2-x}O_4$, and the simulated region (in dashed line) assuming a distribution of Ti^{4+}, Mn^{2+} and Mn^{3+} in a two-component model (purple, blue, grey, green and orange for $x = 1.5,\ 1.4,\ 1.3,\ 1.2,\ 1.1$, respectively).

The combination of first-principles shift calculations, random solution / Monte Carlo model and experimental NMR enabled us to acquire a detailed understanding of the complex trend of cation ordering in the mixed $LiTi_xMn_{2-x}O_4$ series. This is of particular interest in regards to the application of this material as a cathode in rechargeable Li-ion batteries. The high degree of cation disorder found at intermediate $0.2 \leq x < 1$ values of the series may hinder a cooperative Jahn-Teller distortion in the bulk, and facilitate the mechanical stability during electrochemical cycling. On the other hand, the observed increasing ratio of Li(Oh)/Mn^{2+}(Td) mixing with increasing x may hinder the extraction of Li^+ from the structure, effectively resulting in a lower capacity.

4.5 Conclusions

A detailed solid-state ^{7}Li NMR and first-principles DFT study of the cation ordering and the structural changes in the $LiTi_xMn_{2-x}O_4$ series ($0.2 \leq x \leq 1.5$) was presented. ^{7}Li MAS NMR spectra were obtained for the $LiTi_xMn_{2-x}O_4$ series, using state of the art spectroscopic methods for paramagnetic solids. The methodology used to analyse the

NMR results involved the *ab initio* calculation of the magnetic and hyperfine parameters, obtaining a breakdown of the possible contributions to the ^{7}Li NMR shift. These were combined into random distribution and Reverse Monte Carlo models to simulate the ^{7}Li NMR spectra of the $LiTi_xMn_{2-x}O_4$ series. For $x = 0.2$, a random distribution of octahedra $Mn^{3+/4+}/Ti^{4+}$ cations in the $Fd\bar{3}m$ structure was determined, evolving into an inhomogeneous lattice of Mn^{3+}-rich / Mn^{4+}-rich phases for $x = 0.4$, and a single-phase solid solution for $x = 0.6$ and $x = 0.8$. The $x = 1.0$ case showed partially inverse ordering of $Mn^{3+/4+}-Ti^{4+}-$Li (Oh) and $Mn^{2+}-$Li(Td) sites. In the $1.1 \leq x \leq 1.5$ structures, the results showed the preferential formation of co-existing disordered $Mn^{3+}-$rich ($Fd\bar{3}m$) and ordered $Mn^{2+}-$rich (partially-inverse $P4_332$) phases. Additionally, for $LiTi_{1.5}Mn_{0.5}O_4$ a specific cation ordering within the partially inverse spinel framework of $P4_332$ symmetry was determined, i.e. $(Li_{0.6}Ti_{0.1}Mn_{0.3})_{8c}[(Li_{0.1}Ti_{1.4})_{12d}(Li_{0.3}Mn_{0.2})_{4b}]O_4$. The ability of the DFT results to reproduce the experimental ^{7}Li NMR data is promising. The presented methodology in general, and the DFT-calculated ^{7}Li NMR shifts in particular, pave the way to a detailed rationalization of the solid-state NMR spectra of other paramagnetic solids. The combination of the calculated NMR shifts with the random distribution and Reverse Monte Carlo methods represents a robust approach, which can be extended to include additional energetic / configurational constraints to analyse other complex systems of interest to the battery field, such as $LiZn_xMn_{2-x}O_4$, $LiNi_xMn_{2-x}O_4$, and the Li-excess $Li_{1+\alpha}Mn_{2-\alpha}O_4$ materials.

Chapter 5

DFT Investigation of the Effect of Spin-orbit Coupling on the NMR Shifts in Paramagnetic Solids

Abstract

Chapters 3 and 4 described how the combination of first principles and experimental methods can be used to obtain strucutral information from the NMR spectra of structurally complex paramagnetic solids, based on the analysis of magnetic and hyperfine interactons in the spin-only case.

In this Chapter, the formalism of the paramagnetic NMR shielding in the presence of spin-orbit coupling is extended to solid systems with multiple paramagnetic centres. This Chapter demonstrates how the single-ion Electron Paramagnetic Resonance (EPR) g-tensor is defined and calculated in periodic paramagnetic solids. The hyperfine tensor and the g-tensor are calculated with density functional theory (DFT) to show the validity of the presented model and to demonstrate how these interactions can be combined to give the overall paramagnetic shielding tensor, $\boldsymbol{\sigma}^s$. The method is applied to a series of olivine-type $LiTMPO_4$ materials (with TM=Mn, Fe, Co and Ni) and the corresponding ^{7}Li and ^{31}P NMR spectra are simulated. The analysis of the effects of spin-orbit coupling and of the electron-nuclear magnetic interactions on the calculated NMR parameters is discussed. A detailed comparison is presented between contact and dipolar interactions across the $LiTMPO_4$ series, in which the magnitudes and signs of the non-relativistic and

relativistic components of the overall isotropic shift and shift anisotropy are computed and rationalized.

5.1 Introduction

It has been presented in the previous sections how particularly the hyperfine interaction in paramagnetic solids provides detailed information concerning the structural and chemical environment of the NMR observed centre (OC) [9–11, 63, 14]. However, the interpretation of these spectra proves very challenging, as the presence of the paramagnetic centres results in multiple effects on the observed NMR lineshapes [15–18]. It was shown that the through-bond transfer of unpaired-electron spin density onto the nuclear position of the OC induces hyperfine Fermi contact shift, and the through-space hyperfine dipolar interaction between the magnetic moments of the unpaired-electron spin density and that of the observed nucleus results in a significant broadening of the spectrum. In the presence of spin-orbit coupling, the deviation of the g-tensor from the free-electron g-factor, known as the g-shift, modifies both the Fermi-contact and dipolar contributions to the shift. In particular, the combination of the anisotropy of the g-tensor and the zero-field splitting interaction with the dipolar coupling lead to a through-space contribution to the paramagnetic shift, referred to as pseudo-contact shift. The spin-orbit correction to the Fermi contact term *via* the isotropic g-shift also adds a contribution to the NMR shift. All these terms depend on the electronic structure of the TM. The pseudo-contact term depends on the distance between the OC and the paramagnetic centre(s), and on the relative orientation of the g- and hyperfine tensors, and the contact term depends on the through-bond transfer of unpaired electron density to the OC. In addition, the coupling between the g-shift and the hyperfine dipolar tensor modifies the NMR shift anisotropy. To help with the often challenging interpretation of the paramagnetic NMR spectra, first principles quantum-mechanical studies can provide detailed insight at the atomic and electronic level, and substantial progress has been made particularly in the computational modeling of the hyperfine interaction in extended paramagnetic systems [14, 61, 63]. However, in most of the previous works on solids in which the paramagnetic ion is a major constituent of the lattice, the spin-orbit coupling effects on the NMR shift are included in an empirical effective magnetic moment.

The explicit inclusion of the g-tensor in the description of the NMR spectrum is less extensively formulated for solid systems, and has mainly been presented for isolated paramagnetic centres [202–204], with only a preliminary study on paramagnetic networks [205]. This Chapter extends the current methodology to include a description of the

g-tensor in solids with multiple TM centres, and to investigate the resulting effects of spin-orbit coupling on the NMR spectra of periodic solids, which is of central importance in the analysis of many technologically relevant systems, such as battery materials. An analysis of the g- and hyperfine tensors in periodic solids is presented. A model for the derivation of the paramagnetic shielding is described, that allows the separation of the contributions to the isotropic shift and shift anisotropy. The method is applied to the investigation of the ^{7}Li and ^{31}P NMR shifts of olivine-type $LiTMPO_4$ (TM=Mn, Fe, Co and Ni). These materials, and in particular $LiFePO_4$ [44] and its Mn-substituted derivatives [206], are commercially relevant lithium-ion battery positive electrode (cathode) materials. Computational results from solid-state Density Functional Theory (DFT) are compared to the experimental shifts obtained for the corresponding powder samples [207, 208] and a method to extract individual g-tensors in solids containing high concentration of paramagnetic centres from DFT calculations is demonstrated.

The work presented in this Chapter is included in the paper "DFT investigation of the effect of spin-orbit coupling on the NMR shifts in paramagnetic solids" [209]. This work benefited from the intellectual input of Andrew Pell, Ieuan Seymour, Davide Ceresoli, Martin Kaupp and Clare Grey. All of the computational results and the analysis was done by the current author.

5.2 Theory

The theoretical background of this study is based on the derivation, by Moon and Patchkovski, of a formalism to describe the entire shift tensor including the effects of spin-orbit coupling [20], later extended to the presence of zero-field splitting by Vaara *et al.* [21, 22] and Soncini and Van den Heuvel [23]. The description of the paramagnetic shielding tensor that will be adopted in this Chapter has been presented in Section 2.3.5, and it will be briefly repeated for convenience.

In the presence of a single paramagnetic centre, the specific form of $\boldsymbol{\sigma}^s$ is derived to be [18, 20, 21]

$$\boldsymbol{\sigma}^s \;=\; -\frac{\mu_B \; S(S+1)}{3 \; \hbar \; \gamma_N \; k \; T} \; \boldsymbol{g} \;\cdot\; \boldsymbol{A} \tag{5.1}$$

where the general form of the hyperfine tensor (up to second-order perturbation theory), $\boldsymbol{A}$, and the g-tensor, $\boldsymbol{g}$, are [18]

$$\begin{aligned} \boldsymbol{A} &= (A^{\mathrm{FC}} + A^{\mathrm{FC,2}})\mathbf{1} + \boldsymbol{A}^{\mathrm{dip}} + \boldsymbol{A}^{\mathrm{dip,2}} \\ \boldsymbol{g} &= (g_e + \Delta g^{\mathrm{iso}})\mathbf{1} + \boldsymbol{\Delta\tilde{g}} \end{aligned} \tag{5.2}$$

In eq. 5.1, μ_B is the Bohr magneton, S the electronic spin quantum number, $\hbar$ the reduced Planck constant, γ_N the gyromagnetic ratio of the observed nucleus, k the Boltzmann's constant and T the absolute temperature. The complete form of the shielding tensor (equation 2.8) includes also the orbital component that is typically approximated to the shift measured for an analogous diamagnetic system [18].

5.2.1 Contributions to the Paramagnetic Shielding Tensor

By substituting the expressions of $\boldsymbol{A}$ and $\boldsymbol{g}$ in equation 5.2 into the expression of $\boldsymbol{\sigma}^s$ in equation 5.1, and retaining terms up to fourth order in the fine-structure constant, we can break down the paramagnetic shielding tensor into the following terms. A detailed description of the contributions to the shielding tensor was presented in Section 2.3.5 (Table 2.1).

- CONTACT TERMS
  - a) $g_e A^{\mathrm{FC}}$, non-relativistic. Contribution: isotropic shift
  - b) $g_e A^{\mathrm{FC,2}}$, relativistic. Contribution: isotropic shift
  - c) $\Delta g_{\mathrm{iso}} A^{\mathrm{FC}}$, relativistic. Contribution: isotropic shift
  - d) $A^{\mathrm{FC}} \boldsymbol{\Delta \tilde{g}}$, relativistic. Contribution: shift anisotropy
- DIPOLAR TERMS
  - e) $g_e \boldsymbol{A}^{\mathrm{dip}}$, non-relativistic. Contribution: shift anisotropy
  - f) $g_e \boldsymbol{A}^{\mathrm{dip,2}}$, relativistic. Contribution: shift anisotropy
  - g) $\Delta g_{\mathrm{iso}} \boldsymbol{A}^{\mathrm{dip}}$, relativistic. Contribution: shift anisotropy
  - h) $\boldsymbol{\Delta \tilde{g}} \boldsymbol{A}^{\mathrm{dip}}$, relativistic. Contribution: isotropic shift and shift anisotropy

Solid-state density functional theory (DFT) calculations have been shown to be extremely helpful in unravelling the NMR response of paramagnetic solids containing multiple paramagnetic centres [14, 61, 62, 210]. The approach for the calculation of the Fermi contact shifts and shift anisotropy in paramagnetic solids [63] is here extended to include the spin-orbit coupling effect. In Ref. 63, the methodology for computing Fermi contact interactions in solids was developed in which, among other systems, the olivine-type $LiTMPO_4$ materials were used as model systems. In the following discussion of the treatment of spin-orbit coupling effects in solids the same systems are used to allow direct comparison with prior work.

5.2.2 Analysis of the g-tensor in Solids

The unit cell of the olivine-type $LiTMPO_4$ structure with an orthorhombic *Pnma* space group is shown in Figure 5.1. In order to explore the relationship between the overall magnetic structure of the $LiTMPO_4$ unit cell and that of an individual magnetic centre, we now explore the symmetry relationships between the different TM sites.

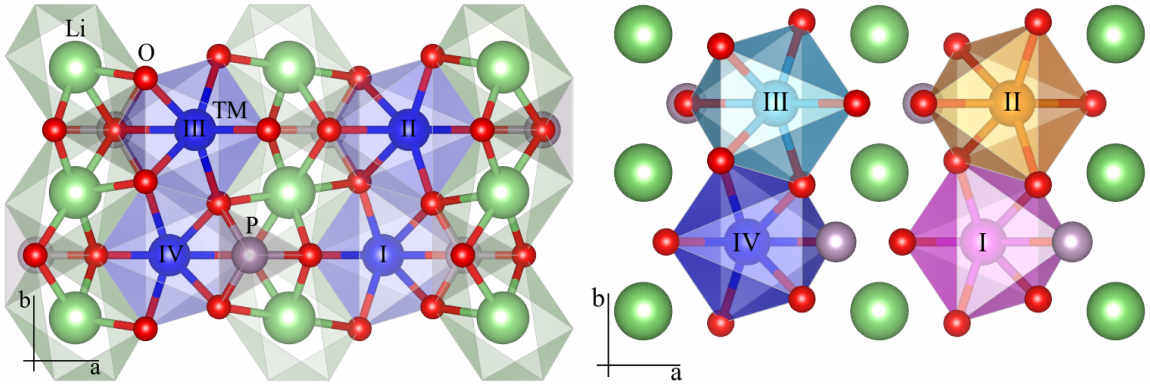

(a) (b)

Fig. 5.1 (5.1a) Structure of the repeating unit of the olivine-type phase of $LiTMPO_4$ (TM=Mn, Fe, Co, Ni) consisting of a distorted hexagonal close-packed oxygen (red) framework. Phosphorus (pink) occupies an eighth of the tetrahedral sites, while the two octahedral sites are occupied by lithium (green) and the TM (blue). (5.1b) The four octahedral TM sites are labelled I, II, III, IV and occupy different spatial positions: their environments (in pink, orange, light blue and blue respectively) are related to one another as according to the orthorhombic symmetry of the *Pnma* space group.

The four TM sites I − IV occupy the same 4 c Wyckoff positions and have the following coordinates:

$$\begin{aligned} \text{I} &: x+\frac{1}{2},\ \frac{1}{4},\ \bar{z}+\frac{1}{2} \\ \text{II} &: \bar{x},\ \frac{3}{4},\ \bar{z} \\ \text{III} &: \bar{x}+\frac{1}{2},\ \frac{3}{4},\ z+\frac{1}{2} \\ \text{IV} &: x,\ \frac{1}{4},\ z \end{aligned} \tag{5.3}$$

These equivalent positions are related by symmetry operations as defined by the space group. For example, if we focus on the metal ion in site I, it transforms into site II *via* either a two-fold screw rotation with the axis parallel to c, or a diagonal glide reflection with the plane perpendicular to a; it transforms into III *via* either a rotoinversion or a

two-fold screw rotation with the axis parallel to b and it transforms into IV *via* either a two-fold screw rotation with the axis parallel to a or an axial glide reflection with the plane perpendicular to c [211–213]. All these relations are summarised in eq. 5.4:

$$\begin{aligned} &\mathrm{I} \leftrightarrow \mathrm{II} : 2(0,0,\frac{1}{2})\ \frac{1}{4},0,z\ ;\ n(0,\frac{1}{2},\frac{1}{2})\ \frac{1}{4},y,z \\ &\mathrm{I} \leftrightarrow \mathrm{III} : \bar{1}\ 0,0,0\ ;\ 2(0,\frac{1}{2},0)\ 0,y,0 \\ &\mathrm{I} \leftrightarrow \mathrm{IV} : 2(\frac{1}{2},0,0)\ x,\frac{1}{4},\frac{1}{4}\ ;\ a\ x,y,\frac{1}{4} \end{aligned} \tag{5.4}$$

In the case where the system contains a unique TM species in a particular electronic state in the weak exchange-coupling regime [214], the orientations of the site-specific g-tensors are related by the same operations defining the symmetry of the unit cell. In the *Pnma* space group discussed here, these are the same operations summarised in eq. 5.4 [215, 216]. Consider for instance the g-tensor of site I in Figure 5.1b and its relation with those of the other sites: because of the operations given above, when expressed with respect to the same reference frame, such as the unit-cell frame, the g-shift tensors of sites I – IV are found to be:

$$\boldsymbol{\Delta g}_{\mathrm{I}} = \begin{pmatrix} \Delta g_{\mathrm{I}}^{x,x} & \Delta g_{\mathrm{I}}^{x,y} & \Delta g_{\mathrm{I}}^{x,z} \\ \Delta g_{\mathrm{I}}^{y,x} & \Delta g_{\mathrm{I}}^{y,y} & \Delta g_{\mathrm{I}}^{y,z} \\ \Delta g_{\mathrm{I}}^{z,x} & \Delta g_{\mathrm{I}}^{z,y} & \Delta g_{\mathrm{I}}^{z,z} \end{pmatrix} \tag{5.5a}$$

$$\boldsymbol{\Delta g}_{\mathrm{II}} = \begin{pmatrix} \Delta g_{\mathrm{I}}^{x,x} & -\Delta g_{\mathrm{I}}^{x,y} & -\Delta g_{\mathrm{I}}^{x,z} \\ -\Delta g_{\mathrm{I}}^{y,x} & \Delta g_{\mathrm{I}}^{y,y} & \Delta g_{\mathrm{I}}^{y,z} \\ -\Delta g_{\mathrm{I}}^{z,x} & \Delta g_{\mathrm{I}}^{z,y} & \Delta g_{\mathrm{I}}^{z,z} \end{pmatrix} \tag{5.5b}$$

$$\boldsymbol{\Delta g}_{\mathrm{III}} = \begin{pmatrix} \Delta g_{\mathrm{I}}^{x,x} & -\Delta g_{\mathrm{I}}^{x,y} & \Delta g_{\mathrm{I}}^{x,z} \\ -\Delta g_{\mathrm{I}}^{y,x} & \Delta g_{\mathrm{I}}^{y,y} & -\Delta g_{\mathrm{I}}^{y,z} \\ \Delta g_{\mathrm{I}}^{z,x} & -\Delta g_{\mathrm{I}}^{z,y} & \Delta g_{\mathrm{I}}^{z,z} \end{pmatrix} \tag{5.5c}$$

$$\boldsymbol{\Delta g}_{\mathrm{IV}} = \begin{pmatrix} \Delta g_{\mathrm{I}}^{x,x} & \Delta g_{\mathrm{I}}^{x,y} & -\Delta g_{\mathrm{I}}^{x,z} \\ \Delta g_{\mathrm{I}}^{y,x} & \Delta g_{\mathrm{I}}^{y,y} & -\Delta g_{\mathrm{I}}^{y,z} \\ -\Delta g_{\mathrm{I}}^{z,x} & -\Delta g_{\mathrm{I}}^{z,y} & \Delta g_{\mathrm{I}}^{z,z} \end{pmatrix} \tag{5.5d}$$

As a result of the symmetry relations among the various TM environments in the orthorhombic group, the overall repeated-unit deviation from g_e results in a diagonal tensor, $\boldsymbol{\Delta g}_{\mathrm{r.u.}}$, being the sum of the Δg values of all the spin centres in the cell, with the form shown in eq. 5.6. Thus, the diagonal components of the per-site $\boldsymbol{\Delta g}$ are obtained by dividing the repeated-unit g-shift by the number of TM centres of the cell. It is important to stress that this result is not general and only occurs when all of the g-tensors of the individual transition metal centres are constrained to be collinear by the symmetry operations inherent to the space group symmetry of the lattice. We present a more general approach below that can be utilised under conditions where this is not the

case.

$$\begin{aligned}\boldsymbol{\Delta g}_{\text{r.u.}} &= \boldsymbol{\Delta g}_{\text{I}} + \boldsymbol{\Delta g}_{\text{II}} + \boldsymbol{\Delta g}_{\text{III}} + \boldsymbol{\Delta g}_{\text{IV}} \\ &= \begin{pmatrix} 4\ \Delta g_{\text{I}}^{x,x} & 0 & 0 \\ 0 & 4\ \Delta g_{\text{I}}^{y,y} & 0 \\ 0 & 0 & 4\ \Delta g_{\text{I}}^{z,z} \end{pmatrix}\end{aligned} \tag{5.6}$$

5.2.3 Analysis of the Hyperfine Tensor in Solids

The hyperfine tensor determining the paramagnetic shift of a particular observed site modulates the contact and dipolar interactions between the nuclear spin of the OC and the total spin of the unpaired electrons. In analogy to the analysis presented in the previous Chapter, in a system such as the above example in Figure 5.1 where the weakly exchange-coupled TM ions are a major constituent of the lattice, the hyperfine tensor defined at the OC nuclear position is equal to the sum of the contact and dipolar interactions with each of the surrounding TM sites. It has shown in the previous Chapter also that the total Fermi contact term, A^{FC}, can be decomposed into the sum of all relevant pair-wise TM-O-OC *bond-pathway* contributions, allowing the unpaired-electron spin density transferred for each individual TM site to the nuclear position of the OC to be computed [63]. For the dipolar component of the hyperfine tensor, the long-range anisotropic electron-nuclear interaction depends on the position vector originating at the OC which connects it to the unpaired-electron spin density of each TM site. For the olivine structure (Figure 5.2) the dipolar interaction between an OC, such as Li A, and a particular paramagnetic site, such as TM-I, is different to the interaction between Li A and TM-II because of their respective orientation. Also, the strength of the dipolar interaction weakens with the distance between the involved centres, r, as $1/r^3$ [77].

5.2.4 Treatment of the Paramagnetic Shielding in Solids *via* DFT

A detailed insight into the NMR response in solids containing multiple paramagnetic centres is obtainable directly *via* periodic solid-state DFT studies. The *bond-pathway* decomposition of the isotropic Fermi contact component of the total hyperfine tensor can be calculated with DFT *via* the *spin-flipping* approach presented in the previous Chapter [63]. In general the approach proves particularly accurate [63] because the unpaired-electron delocalization is a short-range interaction. In the present study, we demonstrate how the total dipolar hyperfine coupling can be decomposed using a similar method. Firstly, the total dipolar hyperfine tensor is calculated at the OC as a result of

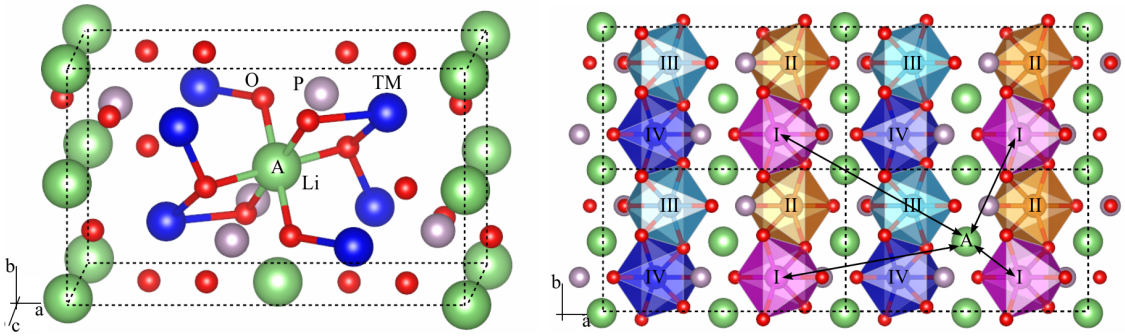

(a) (b)

Fig. 5.2 (5.2a) Repeating unit of the olivine-type $LiTMPO_4$ delimited by the dashed box. The solid lines represent the pair-wise TM-O-Li bonds and denote the pathways of delocalization of unpaired-electron spin density from each TM site to the nuclear position of the OC, here the lithium site labelled *A*, as in Ref. 63. (5.2b) Periodic expansion of the $LiTMPO_4$ repeating unit; the arrows highlight the TM-OC pairs interacting *via* magnetic dipolar coupling, and specifically underline the interactions between the lithium site labelled *A* and one of the four inequivalent TM sites, here labelled as I, throughout the periodically repeating units.

its magnetic interactions with all the TM sites in the ferromagnetic state. Subsequently, the TM-specific contributions to the total dipolar term are obtained separately by flipping each of the four TM spins labelled $\mathrm{I}-\mathrm{IV}$ in the cell in Figure 5.2b. The difference in the OC dipolar tensor due to the flip gives the contribution from each TM site. As shown in Figure 5.2b for TM-I, flipping the spin of a paramagnetic centre in the unit cell results in the spins of the same site in *all* neighbouring cells being flipped. The resulting contribution to the dipolar tensor calculated at a particular OC, such as Li *A* in Figure 5.2b, is then due to the interaction of its nuclear moment with the electronic moment of *all* the TM I ions throughout the lattice. This approach ensures that the spatial and orientational dependence of the coupling are properly treated *via* the periodic boundary conditions (PBC). The additivity of the contributions can be assessed by comparison with the ferromagnetic alignment of all the TM spins, as for the Fermi contact analysis [63].

In the current DFT approach, the *g*-tensor for a material containing multiple paramagnetic centres is calculated by linear response [112, 113], which results in a single overall *g*-tensor for the cell. The contribution to the *g*-tensor from a particular TM site can be calculated by replacing the other TM sites in the cell with diamagnetic atoms. Care must be taken in order to make sure that the resulting local distortions are negligible and that the repeated unit is expanded enough so to avoid long-range interactions between

TM sites through the PBC. Using this procedure, the only source of spin-orbit coupling is due to the remaining paramagnetic centre and hence we obtain the g-tensor of this ion. By calculating the $\boldsymbol{\Delta g}$ for each TM site, the off-diagonal components of the g-tensor are computed, which are required to give an accurate description of the coupling with the $\boldsymbol{A}^{\mathrm{dip}}$ tensor. Once the $\boldsymbol{g}$ and $\boldsymbol{A}^{\mathrm{dip}}$ tensors have been computed, they are combined to give the shielding tensor in eq. 5.1. As a result of the limitations of the available computational methods for solid-state DFT, to the best of our knowledge the calculation of the hyperfine relativistic corrections ($A^{\mathrm{FC},2}$, $\boldsymbol{A}^{\mathrm{dip},2}$) are not currently possible, and so we do not comment further on terms (b) and (f) in Section 5.2.1, which are expected to be small for ligand hyperfine couplings, except for nuclei directly bonded to truly heavy centres [217, 218]. The overall isotropic paramagnetic shift for an OC is calculated as the sum of the contact terms (a) and (c) and the rank-zero component of term (h). For the former two terms, we calculate the total A^{FC} in the ferromagnetic state and the sum of the four TM-specific Δg_{iso} separately; for the latter we calculate separately the coupling between the $\boldsymbol{\Delta g}$ of each of the four TM sites and the corresponding $\boldsymbol{A}^{\mathrm{dip}}$ tensor isolated *via* the aforementioned *spin-flip* approach. To obtain the total shielding tensor, we sum the various products of these contributions and extract the corresponding isotropic, anisotropic and asymmetry values.

5.3 Computational Methods

First-principles solid-state DFT calculations were performed within the Linear Combination of Atomic Orbital (LCAO) scheme with the CRYSTAL09 Code [161, 108] and the Generalized Gradient Approximation (GGA) scheme with the QuantumEspresso Package [114]. The calculation of the hyperfine properties was performed in CRYSTAL09 as previous studies [63, 90] have shown that the use of hybrid functionals in an all-electron treatment provides good agreement with experiments. For this, three hybrid exchange-correlation functionals were used: the PBE0 incorporating 25% Hartree-Fock (HF) exchange [89, 219], shown to provide satisfactory performances for the electronic and magnetic structures of the class of materials of interest [90], and the related 20% HF hybrid (PBE20) and 35% HF hybrid (PBE35). The choice of studying these systems with a range of hybrid functionals was motivated by the known sensitivity of the electronic delocalisation and spin polarisation on the percent of HF exchange included [90, 63, 220, 221]. Two levels of all-electron atom-centered basis set were used, a smaller set used for structure optimisation and a more extended one used for hyperfine calculations [63]. A total energy tolerance of 10^{-7} a.u. was chosen and the reciprocal-space

sampling was performed with k-point grids of $2 \times 3 \times 4$ points in the $LiTMPO_4$ unit cell. All-electron atom-centered basis sets comprising fixed contractions of Gaussian primitive functions are employed throughout for the calculations done with CRYSTAL. Two levels of basis sets are used: the first and smaller set used for geometry optimizations is of the form (7s 2p 1d)/[1s 2sp 1d] for Li; (10s 4p 1d)/[1s 2sp 1d] for O; (16s 8p 1d)/[1s 3sp 1d] for P; and (20s 12p 5d)/[1s 4sp 2d] for Mn, Fe, Co and Ni, where the values in parentheses indicate the number of primitives within each shell and the values in square brackets the contraction scheme [108]. In the more extended provision used for the calculation of hyperfine A^{FC} and A^{dip} parameters, modified IGLO-III sets are adopted for O and P, taking the form (10s 6p 2d)/[6s 5p 2d] for O, and (11s 7p 3d)/[7s 6p 3d] for P [63]. A flexible and extended TZDP-derived basis of the form (9s 2p)/[5s 2p] is used for Li, and Ahlrichs DZP-derived sets of the form (13s 9p 5d)/[7s 5p 3d] are applied for Mn, Fe, Co and Ni [63]. These sets are consistent with those used in a recent previous calculation of hyperfine parameters in a series of Fe^{3+} phosphates [61]. In all cases, Coulomb and exchange integral series tolerances were set at 10^{-7}, 10^{-7}, 10^{-7}, 10^{-7} and 10^{-14} (as defined in the CRYSTAL09 documentation [108]).

As spin-orbit coupling effects are not treated in the version of CRYSTAL used in this study, the Projector Augmented Wave (PAW) [151] QuantumEspresso package was used to calculate g-tensors for the same systems, supported by previously presented results obtained within this scheme [205]. For these calculations, the PBE exchange functional was chosen [89]. Scalar-relativistic norm-conserving pseudopotentials with nonlinear core correction were used, and the all-electron information was reconstructed using PAW and gauge-including projector augmented-wave (GIPAW) [112, 113]. A plane wave cutoff energy of 900 eV was chosen, yielding an energy convergence to within 6 meV per atom. The same energy tolerance and k-mesh sampling as used in the CRYSTAL calculations were once again used. For the calculation of per-site g-tensors, a $1 \times 2 \times 2$ supercell expansion of the crystallographic primitive cell was required, associated with a k-sampling of $2 \times 2 \times 2$. These supercells were made almost entirely diamagnetic by substituting all but the TM site under study with Mg^{2+} ions. In the GIPAW implementation in the Quantum-Espresso package, a mean-field approximation to the many-body Hamiltonian is made and as a result, the spin-orbit and spin-other-orbit operators are represented as a sum of one-electron terms, according to Ref. 113. Hybrid functionals were not used as the calculation of the g-tensor *via* the linear response method is not currently supported with these. Hence, calculations of g-tensors were compared for a pure GGA method and a GGA+U method with the PBE functional. As will be discussed below, the former is more appropriate for g-tensor calculations. The latter method, which is widely used in

periodic DFT calculations of transition metal-contain systems, is an alternative approach to the hybrid treatment and it involves the addition of a Hubbard U correction [91] to specific subshells - here the 3*d* TM orbitals - to correct for effects due to the incorrect treatment of electron correlations with the DFT approach [222]. This has previously been shown to improve the description of the magnetic coupling constants and the electronic structure of transition metal oxide systems [223, 224, 46], and to accurately predict the respective ground-state d-level splitting pattern [225]. The rotationally invariant treatment of U proposed by Dudarev *et al.* was here used [95], in which a single U_{eff} parameter is applied to the d electrons of the transition metal species. The values of U_{eff} were chosen from previous self-consistent determinations [223] and are reported in Table 5.1. The effect and validity of the addition of U to *g*-tensor calculations is explored.

The structures of $LiMnPO_4$ [226], $LiFePO_4$ [227] and $LiNiPO_4$ [226] were fully relaxed with both DFT packages independently. For $LiCoPO_4$, the experimental structure (Ref. 228) was used without further relaxation in order to avoid the difficulties in optimising the distinct sublattice anions, as described in detail by Middlemiss *et al.* [63]. Furthermore, as derived in Ref. 61, the bulk magnetic properties of the materials affect the paramagnetic shift. These effects are included in the treatment by modifying the temperature dependence of the shift *via* the inclusion of the Weiss constant Θ. Hence, the prefactor in eq. 5.1 used to calculate all terms in the $\boldsymbol{\sigma}^{\boldsymbol{s}}$ becomes $-\frac{\mu_B S(S+1)}{3\hbar\gamma_N K_B(T-\Theta)}$. The temperature used in this work was 320 K to approximate the frictional heating due to Magic Angle Spinning (MAS). The Weiss constants used for $LiMnPO_4$, $LiFePO_4$, $LiCoPO_4$ and $LiNiPO_4$ are summarised in Table 5.1 [207]. For all of the materials considered, the magnitude of the Weiss constant was found to be much lower than the experimental temperature $T = 320\ K$, which suggests that the spins can be treated as being essentially uncoupled from each other as a result of thermal fluctuations. As presented in equation 5.7, for every calculated tensor, λ, the resulting isotropic term λ_{iso}, symmetric anisotropic value $\Delta\lambda$ and asymmetry parameter η were calculated following the convention in Ref. 71. For any symmetric tensor in the principal axis frame, the diagonal components are ordered such that $|\lambda_{zz} - \lambda_{\text{iso}}| > |\lambda_{yy} - \lambda_{\text{iso}}| > |\lambda_{xx} - \lambda_{\text{iso}}|$, with λ_{iso} being the isotropic value defined in eq. 5.7, together with the second-rank tensor anisotropy, $\Delta\lambda$, and the asymmetry parameter, η:

$$\begin{aligned} \lambda_{\text{iso}} &= \frac{\lambda_{xx} + \lambda_{yy} + \lambda_{zz}}{3} \\ \Delta\lambda &= \lambda_{zz} - \lambda_{\text{iso}} \\ \eta &= \frac{\lambda_{xx} - \lambda_{yy}}{\Delta\lambda} \end{aligned} \tag{5.7}$$

For the systems studied in this work, no explicit calculation of the orbital component of the shielding tensor was included [18], as this contribution is very close to 0 ppm for the diamagnetic analogue material $LiMgPO_4$ [229].

Phosphate	S	$\mu_{\text{eff}}^{\text{theo}}$ [a] $[\mu_B]$	$\mu_{\text{eff}}^{\text{expt}}$ [a] $[\mu_B]$	Θ [a] [K]	U_{eff} [b] [eV]
$LiMnPO_4$	2.5	5.91	5.4	-58	3.92
$LiFePO_4$	2	4.89	6.8	-161	3.71
$LiCoPO_4$	1.5	3.87	5.0	-77	5.05
$LiNiPO_4$	1	2.82	3.1	-60	5.26

Table 5.1 Summary of the parameters used in the calculation of hyperfine shifts: S, the spin quantum number of the TM ion involved in each phosphate; the theoretical ($\mu_{\text{eff}}^{\text{theo}}$) and experimental ($\mu_{\text{eff}}^{\text{expt}}$) magnetic moments in terms of the Bohr magneton (μ_B); Θ, the Weiss constant in Kelvin; U_{eff}, the effective Hubbard correction applied to the relative TM ion in eV. [a] Ref. 207. [b] Ref. 223.

5.4 Results and Discussion

For all the olivine $LiTMPO_4$ structures considered in this work, the experimentally observed unit cell parameters were in reasonable agreement with the optimised unit cell parameters obtained from hybrid functionals (LCAO), GGA and GGA+U approaches, as shown in Table 5.2.

The results of the g-tensor calculations are also shown in detail in Appendix A. As discussed previously for systems of orthorhombic symmetry, for all the studied phosphates the spin-orbit coupling effects at each TM site of the repeated unit are found to lead to g-tensors with the same principal components, which are oriented relative to each other according to the symmetry operations of the cell (eq. 5.5). The site-specific g-tensors and the values obtained for the whole repeated unit comprising all paramagnetic ions are compared in the Appendix A, the sum of the per-site g-tensors being very close to the *repeated unit* $\boldsymbol{g}_{\text{u.c.}}$ as expected from equation 5.6. Table 5.3 shows the isotropic g_{iso} values calculated for an individual TM site for the four studied phosphates. Firstly it is clear from Table 5.3 that the range of experimentally-determined isotropic g values obtained

		a [Å]	b [Å]	c [Å]	V [Å^3]
$LiMnPO_4$	LCAO	10.14	5.94	4.64	289.78
	GGA	10.39	6.09	4.72	299.5
	GGA+U	10.42	6.14	4.75	297.90
	Expt.[226]	10.33	6.01	4.79	302.00
$LiFePO_4$	LCAO	9.92	5.75	4.63	279.57
	GGA	9.82	5.71	4.63	259.61
	GGA+U	9.76	5.70	4.56	303.74
	Expt.[227]	10.02	5.85	4.68	291.39
$LiNiPO_4$	LCAO	10.28	6.02	4.68	264.69
	GGA	10.41	6.12	4.63	253.36
	GGA+U	10.38	6.08	4.72	253.36
	Expt.[226]	10.43	6.10	4.74	274.49

Table 5.2 Comparison of the cell parameters (in Ångstroms) of the olivine structures optimized within the LCAO, the GGA and the GGA+U schemes and the experimental values used as starting point for the DFT relaxations.

TM	TM conf.	$\tilde{g}_{aa}$, $\tilde{g}_{bb}$, $\tilde{g}_{cc}$		$g_{\rm iso}$		$g_{\rm iso}^{\rm expt}$
		GGA	GGA+U	GGA	GGA+U	
Mn^{2+}	$t_{2g}^3\ e_g^{*2}$	2.00	2.00	2.00	2.00	2.00 [a]
Fe^{2+}	$t_{2g}^4\ e_g^{*2}$	2.17, 2.23, 2.10	2.06, 2.03, 2.11	2.17	2.07	2.02 – 2.22 [b]
Co^{2+}	$t_{2g}^5\ e_g^{*2}$	2.26, 2.40, 2.39	2.16, 2.12, 2.12	2.35	2.13	2.17 – 2.36 [c]
Ni^{2+}	$t_{2g}^6\ e_g^{*2}$	2.25, 2.23, 2.25	2.14, 2.14, 2.13	2.24	2.14	2.15 [d]

Table 5.3 Comparison of the electronic configuration and the calculated g-tensors for each different TM site in an octahedral crystal field as involved in the studied systems. For each ion, the occupation of the $3d$ orbitals in an octahedral field is specified. For each calculated TM-specific g-tensor the corresponding principal components ($\tilde{g}_{aa}$, $\tilde{g}_{bb}$, $\tilde{g}_{cc}$) and isotropic value ($g_{\rm iso}$), calculated with pure GGA and with GGA+U, are reported and compared with theisotropic g value determined experimentally with EPR ($g_{\rm iso}^{\rm expt}$). [a] Ref. 230, 231. [b] Ref. 232, 233. [c] Ref. 232, 234, 235. [d] Ref. 236.

from electron paramagnetic resonance (EPR) is broad for this class of $LiTMPO_4$ olivine systems, justifying further calculations to extract this parameter. All the calculated

values of g_{iso} show a positive deviation from the free-electron g-value as expected for TM ions with a more-than-half-filled $3d$ shell. The results reflect the trends expected based on the electronic structure of the involved ions [77, 237]. The deviation from g_e is found to be negligible for Mn^{2+} as it has zero spin-orbit coupling as a result of the half-filled $3d$ shell. For Fe^{2+}, the effects of spin-orbit coupling result in a small deviation from g_e, with a calculated isotropic g-shift that falls within the experimental values shown in Table 5.3. The effect of the spin-orbit coupling increases for octahedral Co^{2+}, largely due to the increased value of the spin-orbit coupling parameter moving across the 3d series, which results in a larger deviation from g_e.

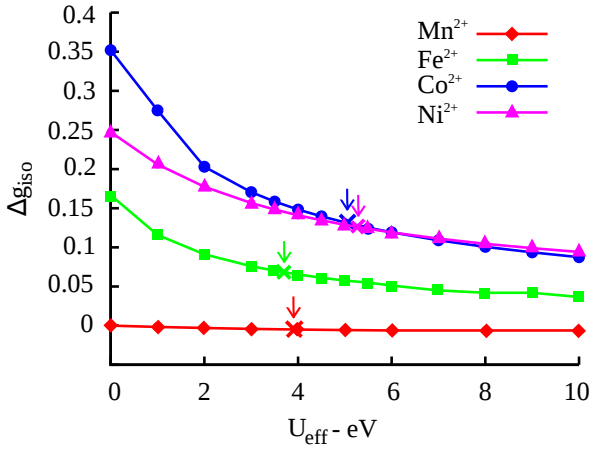

Fig. 5.3 Calculated isotropic value of the g-tensor shift, Δg_{iso}, as a function of the U_{eff} correction applied on Mn^{2+} (in red prisms), Fe^{2+} (in green squares), Co^{2+} (in blue circles) and Ni^{2+} (in magenta triangles). For each case the isotropic value obtained with the U_{eff} value used in prior DFT+U studies is indicated with a cross.

The dependence of Δg_{iso} on the applied U_{eff} was studied, and the results are shown in Figure 5.3. In all cases the deviation from the free-electron g-value is found to decrease with increasing U_{eff} (converging to a plateau at high U_{eff} [238]). This is at first sight surprising, as it is known that the Fermi contact shift for the same systems [239] decreases with increasing U_{eff}, due to a reduction of the spin delocalisation from the $3d$ orbitals to the nucleus of interest - which, in the study in Ref. 239, is Li. One would expect the resulting larger spin density at the metal centre to enhance the g-tensor, due to larger spin-orbit contributions from the heavier centre. This is what one observes in g-tensor calculations on molecular $3d$-complexes, where adding more exact exchange to a hybrid functional increases the g-tensors [221]. Then why do Hubbard $+U$ corrections provide a change in the opposite direction? The reason is the increased energy gap, which weakens the spin-orbit response contributions to the g-tensor (the gap enters the energy denominator of the perturbation expressions). While the same increase of the gap also

occurs with increasing HF exchange in hybrid functionals, in the latter case the effect is overcompensated by the enhanced coupling terms contributed by the non-local HF exchange potential [221], leading to an overall increased linear response. Such coupling terms are absent in the DFT+U scheme, and thus the Hubbard terms move the results in the wrong direction. While comparison with experimental Δg_{iso} (Table 5.3) might suggest improved agreement for DFT+U, this would indeed be due to compensation with other errors. We thus have to conclude that, while DFT+U improves hyperfine interactions, magnetic moments, band gap, and other aspects of electronic structure in the present $LiTMPO_4$ systems [240–243, 223], it is not suitable for response properties, unless one finds a way to mimic the response coupling terms. A correct treatment of solid-state g-tensors with hybrid functionals may provide a better route for future improvement. Here we will pragmatically use the uncorrected GGA results for the g-tensors and will combine them with hybrid-functional data for the hyperfine tensors. The results obtained within the GGA+U scheme are reported in the Appendix for completeness.

The paramagnetic shielding tensor is calculated by combining the g-tensor data with the hyperfine results according to eq. 5.1. The breakdown of the contributing terms presented in Section 5.2.1 is shown for the studied systems in Table 5.4. The hyperfine parameters are sensitive to the amount of Hartree-Fock exchange in the hybrid functional, as smaller amounts of HF exchange lead to more delocalization of the d orbitals. For simplicity, in Table 5.4 we only show the PBE0 results, while the PBE20 and PBE35 results, which can be considered as upper and lower bounds of the acceptable range [90, 63], are shown in Appendix A. We now draw attention to the contributions to the isotropic shift resulting from the non-relativistic - term (a) - and relativistic - terms (c) and (h). With regards to the Fermi contact shift (a), the value of the isotropic term depends on the fraction of unpaired-electron spin density transferred from the d orbitals of the TM onto the s orbitals of the OC and on the covalency of the TM-O-OC bonds. From the ^{31}P results, the Fermi contact shift is found to decrease across the series going from Mn^{2+} towards Ni^{2+}, in line with the decrease of the number of unpaired electrons in the t_{2g} orbitals of the d-shell of the respective ions. Different unpaired-electron spin density transfer mechanisms are involved in the different bond-pathway configurations, as elucidated by Carlier *et al.* [14] for oxide based systems. This can be seen by comparing the values of term (a) in Table 5.4 for ^{7}Li: after the decrease of the Fermi contact shift from the Mn^{2+} to Fe^{2+}, caused by the smaller number of unpaired t_{2g} electrons, we see that the sign of the shift, and hence of the transferred spin density, inverts on going from Fe^{2+} to Co^{2+} and Ni^{2+}. For the Fe site, there is an equal contribution of spin density transferred *via* a 90° pathway from the unpaired electrons in t_{2g} orbitals and a 180°

pathway from the unpaired electrons in e_g orbitals towards the Li site. In the first case this corresponds to a positive transfer *via* a delocalization mechanism while in the second case, this leads to a negative transfer *via* a polarization mechanism. Hence the overall ^{7}Li Fermi contact shift in $LiFePO_4$ is the result of these opposite contributions. For the high-spin Co^{2+} case, the majority of spin density is transferred from e_g orbitals and the overall sign of the resulting Fermi contact shift becomes negative; finally for the Ni^{2+} case all the spin density is transferred from the e_g orbitals of the TM, leading to a larger and still negative shift. Regarding the term (c) in Table 5.4, this contribution to the isotropic shift represents the spin-orbit coupling correction to the Fermi contact interaction *via* the isotropic g-shift. By comparing the results for the different cases, this term scales with the extent of spin-orbit coupling for the involved TM ion. Term (c) for ^{7}Li is negligible for the Mn^{2+} case (0.3 ppm) and becomes progressively more significant when going from Fe^{2+} (9.0 ppm) to Ni^{2+} (-31.4 ppm). This term depends on the strength of the Fermi contact interaction, and it is interestingly shown to be non-negligible, particularly for the ^{31}P shift, due to the magnitude of A^{FC} for this nucleus.

We focus now on the isotropic term resulting from the product (h) in Table 5.4 corresponding to the aforementioned pseudo-contact shift. We notice how the combination of spin-orbit coupling and dipolar interaction results in a non obvious trend for this isotropic shift. Although the deviation from the g-value almost doubles in going from Fe^{2+} to Co^{2+}, the dipolar interaction is reduced to the point where the magnitude of the overall pseudo-contact shift is larger for the former than for the latter. This result suggests that although the ^{7}Li shift is dominated by the contact contribution, the pseudo-contact term can be non-negligible in these systems. The agreement between the total isotropic shift obtained with DFT and the experimental value is still not particularly good for the ^{7}Li site. Part of the discrepancy is thought to be due to the neglect of the zero-field splitting effects. Also, a careful analysis of the basis set and of structural optimization is under investigation by some of the authors of this work, which are expected to have an effect on the accuracy of the spin-density calculated at the nuclear position. For ^{31}P the agreement is more satisfactory, mainly because of the predominance of the Fermi contact contribution to the total shift, as previously described. We now discuss the terms in Table 5.4 contributing to the shift anisotropy, both non-relativistic (e) and due to spin-orbit coupling ((d), (g), (h)). Focusing on the dipolar component of the hyperfine tensor, $\boldsymbol{A}^{\mathrm{dip}}$, there is a decrease along the series from Mn to Ni, hence giving a progressively smaller contribution to the shift anisotropy, as seen by comparing terms (e) of Table 5.4. The calculated tensor with no spin-orbit coupling inclusion corresponds to the dipolar interaction between the magnetic moments of the observed nucleus and

		CONTACT TERMS									DIPOLAR TERMS									ISOTROPIC TERM	
		a) $g_e A^{FC}$			c) $\Delta g_{iso} A^{FC}$			d) $A^{FC}\Delta\tilde{g}$			e) $g_e \boldsymbol{A}^{dip}$			g) $\Delta g_{iso} \boldsymbol{A}^{dip}$			h) $\Delta\tilde{g}\boldsymbol{A}^{dip}$			DFT	EXP
		δ_{iso} [ppm]	$\Delta\delta$ [ppm]	η	δ_{iso} [ppm]	$\Delta\delta$ [ppm]	η	δ_{iso} [ppm]	$\Delta\delta$ [ppm]	η	δ_{iso} [ppm]	$\Delta\delta$ [ppm]	η	δ_{iso} [ppm]	$\Delta\delta$ [ppm]	η	δ_{iso} [ppm]	$\Delta\delta$ [ppm]	η	δ_{iso} [ppm]	δ_{iso} [ppm]
^{7}Li	$LiMnPO_4$	109.9	0	—	0.3	0	—	0	0.1	0.3	0	1234.2	0.2	0	0.9	0.2	-0.1	0.2	0.4	110.1	57[a], 68[b]
	$LiFePO_4$	27.2	0	—	9.0	0	—	0	-3.6	0.9	0	881.0	0.2	0	72.7	0.2	-1.2	-15.3	0.7	35.0	-15[a], -8[b]
	$LiCoPO_4$	-19.6	0	—	-13.5	0	—	0	3.6	0.1	0	700.3	0.2	0	121.0	0.2	-17.8	-14.5	0.4	-50.9	-92[a], -86[b]
	$LiNiPO_4$	-64.8	0	—	-31.4	0	—	0	2.0	0.1	0	433.8	0.2	0	52.6	0.2	-0.9	-1.6	0.3	-97.1	-49[b], -41[a]
^{31}P	$LiMnPO_4$	8397.3	0	—	25.3	0	—	0	11.3	0.3	0	795.9	0.5	0	-1.2	0.5	-0.1	0.2	0.3	8404.5	7296[a]
	$LiFePO_4$	3219.0	0	—	1062.9	0	—	0	-432.2	0.96	0	795.4	0.4	0	65.7	0.4	-2.4	13.4	0.2	4279.5	3352[a]
	$LiCoPO_4$	2012.6	0	—	1391.5	0	—	0	-369.3	0.1	0	652.6	0.4	0	112.8	0.4	-3.8	9.2	0.6	3400.3	2756[a]
	$LiNiPO_4$	1658.7	0	—	804.3	0	—	0	-50.4	0.4	0	576.1	0.1	0	69.9	0.1	1.1	-2.2	0.1	2462.1	1706[a]

Table 5.4 Comparison of the various terms contributing to the shielding tensor for the series of $LiTMPO_4$ compounds (TM= Mn, Fe, Co, Ni) at the ^{7}Li and ^{31}P sites broken down into the contact and dipolar isotropic shift (δ_{iso}, ppm), symmetric anisotropic value ($\Delta\delta$, ppm) and asymmetry parameter (η, dimensionless). The hyperfine tensor for this Table is obtained with the PBE0 hybrid functional and the g-tensor is calculated at PBE GGA level. Every tensorial term of the Table is reported oriented with respect to its own principal axis frame. All the reported terms are scaled by the pre-factor $-\frac{\mu_B S(S+1)}{3\hbar\gamma_N K_B(T-\Theta)}$, with the respective Weiss constant of the system reported in Table 5.1. The last column compares the sum of the calculated isotropic terms (a, c, h) with the experimental isotropic shift. [a] Ref. [208]. [b] Ref. [207].

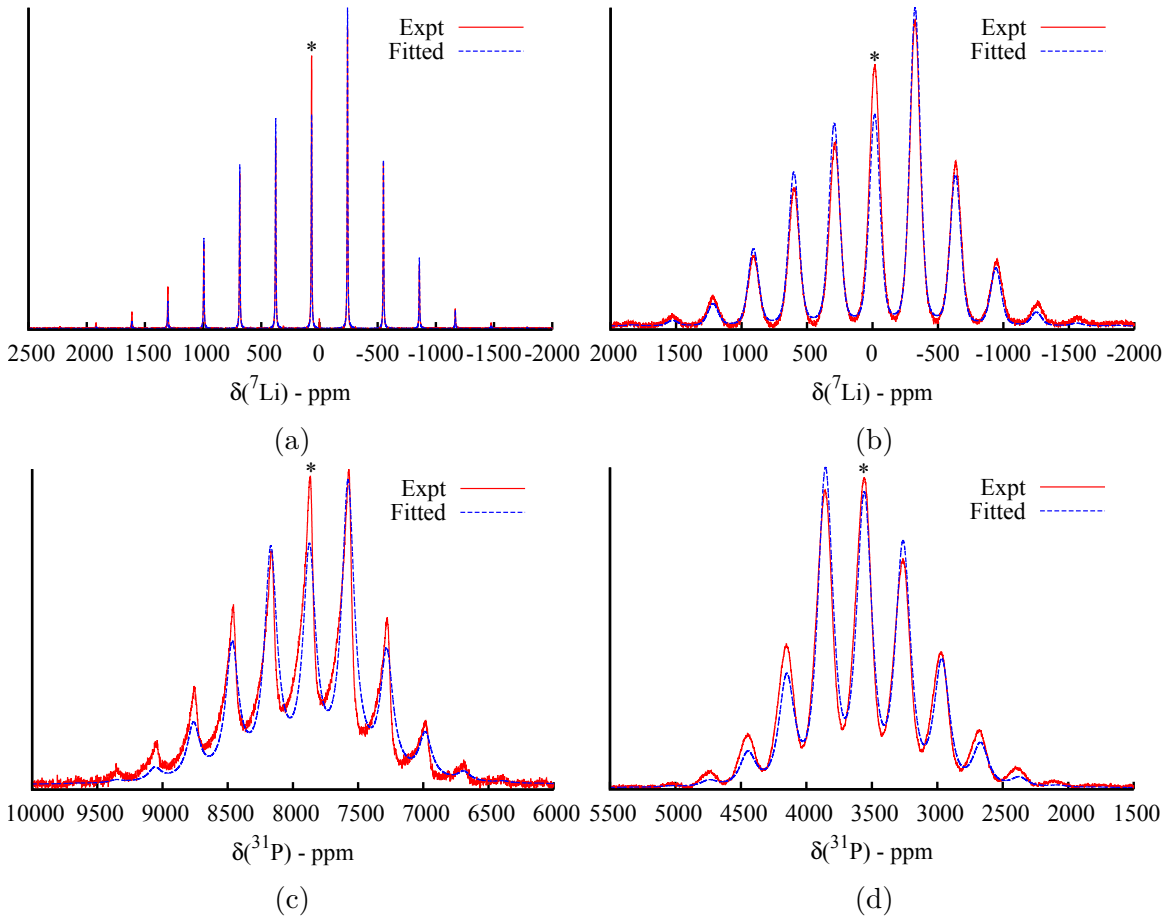

Fig. 5.4 Experimental (in solid red line) and fitted (in dashed blue line) ^{7}Li and ^{31}P spectra of $LiMnPO_4$ (Figure 5.4a and 5.4c respectively) and $LiFePO_4$ (Figure 5.4b and 5.4d respectively). Isotropic peaks are marked with an asterisk. The experimental spectra are taken from Ref. 62.

magnetic moment of the TM ion [61, 78]. Following the trend of $\mu_{\text{eff}}^{\text{theo}}$ for the considered ions reported in Table 5.1, a progressively weaker dipolar interaction is observed when going from Mn^{2+} towards Ni^{2+}. The trend is more complex when spin-orbit coupling is included, as seen from Tables 5.1 and 5.3: the $\boldsymbol{\Delta}g$ and $\boldsymbol{A}^{\text{dip}}$ tensors involved in terms (g) and (h) of Table 5.4 follow opposite trends along the series of studied systems. The contributions to the shift anisotropy are the product of these two terms, resulting in an increase in the anisotropy when going from Mn^{2+} to Fe^{2+} and a decrease when going from Fe^{2+} to Ni^{2+}. For ^{31}P the relativistic corrections to the shift anisotropy are found to contribute significantly to the total value. For $LiMnPO_4$ and $LiFePO_4$, the total shift anisotropy $\Delta\delta^{\text{DFT}}$ is calculated from the coupling of the full $\boldsymbol{A}$ and $\boldsymbol{g}$ tensors as in eq. 5.1. We stress that these values cannot be obtained by directly summing the

	^{7}Li				^{31}P			
	δ_{iso} [a] [ppm]	$\Delta\delta^{DFT}$ [ppm]	$\Delta\delta^{FIT}$ [ppm]	η^{FIT}	δ_{iso} [a] [ppm]	$\Delta\delta^{DFT}$ [ppm]	$\Delta\delta^{FIT}$ [ppm]	η^{FIT}
$LiMnPO_4$	67.9	1241.3	1159.9	0.8	7879	1098.9	963.3	0.8
$LiFePO_4$	-16.8	884.6	1115.1	0.7	3558	-830.6	-865.0	0.7

Table 5.5 Results of the DFT calculated and fitted shielding anisotropy for ^{7}Li and ^{31}P spectra of $LiMnPO_4$ (shown in Figure 5.4a and 5.4c respectively) and of $LiFePO_4$ (shown in Figure 5.4b and 5.4d respectively). The results are reported as the isotropic shift (δ_{iso}, ppm), the symmetric anisotropic value ($\Delta\delta$, ppm) and the asymmetry parameter (η, dimensionless). [a] The experimental spectra as well as the reported values for the isotropic shifts (δ_{iso}) are taken from Ref. 62.

relevant terms - terms (d), (e), (g) and (h) in Table 5.4 - since each of these terms is expressed with respect to its own principal frame, which is not necessarily unique for all the tensorial products. Thus, the direct sum of the reported $\Delta\delta$ values is not necessarily appropriate because of the different reference frames of the various terms. By coupling the whole hyperfine tensor and g-tensor we then obtain for ^{7}Li $\Delta\delta^{DFT}(Mn) = 1241.3$ ppm and $\Delta\delta^{DFT}(Fe) = 884.6$ ppm, while for the ^{31}P, $\Delta\delta^{DFT}(Mn) = 1098.9$ ppm and $\Delta\delta^{DFT}(Fe) = -830.6$ ppm. These values can be compared with the values of spin-dipolar anisotropy obtained by fitting the solid-state MAS ^{7}Li and ^{31}P NMR spectra of the $LiMnPO_4$ and $LiFePO_4$ powders (previously reported and shown in Figure S1 and Figure 1 of Ref. 62 for ^{7}Li and ^{31}P respectively). The results of the fitting carried out within the DMFIT software [195] are shown in Figure 5.4 and summarised in Table 5.5. We point out that the values for the ^{7}Li and ^{31}P isotropic shifts measured in Ref. 208 and in Ref. 62, and reported in this work in Tables 5.4 and 5.5 respectively, are not exactly equal. The NMR spectra of the two studies were acquired at different MAS speeds - 22.5 KHz in Ref. 208 and 60 KHz in Ref. 62. Hence, the discrepancy between the measured isotropic shifts is thought to be mainly due to the different temperatures experienced by the powder sample during the acquisition due to frictional heating caused by MAS. It is interesting to note that the DFT results predict, for the ^{7}Li spectra, a sideband pattern of comparable width and anisotropy for both $LiMnPO_4$ and $LiFePO_4$, while for the ^{31}P spectra of the two phosphates the patterns are calculated to be of comparable width

but of opposite anisotropy. These results are in reasonable agreement with the fitting of the experimental NMR spectra, as summarised in Table 5.5. Of note, without the inclusion of spin-orbit coupling we would not have been able to reproduce the correct sign of the anisotropy for the ^{31}P shift of $LiFePO_4$. Errors between the fits and the observed spectra are largely caused by bulk magnetic susceptibility (BMS) effects, which vary from particle to particle and within a particle; BMS effects also contribute to the discrepancy between the calculations and the fits [244]. Despite our neglect of this term, this work represents to the best of our knowledge the first example of a paramagnetic NMR anisotropy pattern simulation where hyperfine and spin-orbit coupling parameters are obtained from first principles.

5.5 Conclusions

A method was presented, to include spin-orbit coupling effects in the calculation of the paramagnetic NMR shielding for solid systems with multiple paramagnetic centres. It was demonstrated how to combine the Fermi contact and dipolar hyperfine interactions between the NMR-observed nucleus and multiple TM sites, with the g-tensor. The hyperfine interactions and g-tensors in this study are calculated from first principles through the use of solid-state DFT calculations. An accurate description of spin-orbit coupling effects on the NMR signal of such systems can only be obtained by including the g-tensor associated with each individual paramagnetic site of the solid. A calculation performed for a system containing multiple paramagnetic ions leads to an overall g-tensor for the whole unit cell. If the system contains paramagnetic ions with principal components along different directions (as dictated by the symmetry operations of the crystallographic space group of the material), or different types of paramagnetic ions, then the overall tensor is not a simple sum of the individual tensors of the different ions, unless they are all expressed with respect to a common reference frame. Furthermore, the overall computed tensor cannot be used to determine the tensors for the individual ions. Since the NMR and EPR parameters are influenced by the g-tensor of the individual ions, we adopted a simple approach to extract these parameters, which involved substituting all but one ion within the cell by diamagnetic ions. The first-principles approach is used to study the NMR response of a series of olivine $LiTMPO_4$ materials (TM=Mn, Fe, Co, Ni). In particular, we show the importance of including spin-orbit coupling effects in combination with the hyperfine interaction in order to obtain an accurate description of the observed NMR chemical shift and shift anisotropy. The approach outlined here can be readily applied to aid in the interpretation of the NMR spectra of a wide range of

solid systems with multiple (and different) paramagnetic centres, allowing more detailed structural and electronic information to be extracted from these systems.

Chapter 6

Bulk Magnetic Susceptibility Effects on the ^{7}Li NMR Shift of $LiFePO_4$ Single Crystals

Abstract

In the previous Chapters, the analysis of the NMR spectra of paramagnetic solids has focused on the description and calculation of the local hyperfine and spin-orbit coupling interactions between the observed nucleus and the nearby paramagnetic centres. In addition to these interactions, the bulk magnetic properties of the paramagnetic system may also affect the NMR spectrum of the observed nuclear spin. In this Chapter, a study of the ^{7}Li MAS NMR spectra of four $LiFePO_4$ single crystals of different macroscopic shapes is presented. The experimental shifts are compared to the bulk magnetic susceptibility (BMS) shifts calculated for each of the four $LiFePO_4$ crystals. The large variation in ^{7}Li shift observed between the various samples is confirmed to be predominantly due to the shape-dependent macroscopic shift effect, and the BMS shift in crystals of very anisotropic shapes is found to be a major contribution to the total ^{7}Li shift. The wider aim of this work is to develop a methodology to calculate the isotropic and anisotropic BMS effects on the NMR spectra of paramagnetic solids of complex shapes, as well as of powder samples.

6.1 Introduction

The previous Chapters of this Thesis have focused on the theoretical description and interpretation of the local paramagnetic shielding tensor of an NMR observed nucleus. As discussed in detail in Chapter 3 and Chapter 4, the presence of paramagnetic ions coordinated with the NMR observed site results in the hyperfine interaction between the observed nuclear spin and the unpaired spin density of the paramagnetic centers. The isotropic hyperfine interaction results in a shift of the isotropic resonance of the observed spin, known as Fermi contact shift [48]. The anisotropic hyperfine interaction results in a broadening of the spectrum. As discussed in detail in Chapter 5, in the presence of spin-orbit coupling, the interaction between the dipolar hyperfine coupling and the anisotropic electron magnetic moment of the unpaired spin density leads to a dipolar contribution to the paramagnetic shift, known as pseudo-contact shift. The effects described so far are local interactions between the paramagnetic centers and the observed nuclear spin.

In addition to these local interactions, the macroscopic magnetic properties of the system may also affect the NMR spectrum [67, 26, 27]. When a finite-sized diamagnetic or paramagnetic sample is placed in a magnetic field, the induced moment arising from the bulk magnetic susceptibility (BMS) of the material generates a demagnetizing field. This field either opposes or adds to the static external field [28], and, depending on the sample shape and on the symmetry of the magnetic susceptibility tensor, can contribute to both the shift and the line-broadening of the NMR spectrum. Typically, in weakly paramagnetic materials the induced demagnetizing field is small, and the hyperfine Fermi contact term is the dominant contribution to the measured NMR shift [48, 63]. However, in materials with large BMS the demagnetizing field can be sizeable, and hence the induced shifts appreciable. This can be the case for paramagnetic powders of highly anistropic crystallite shapes. The ^{7}Li NMR shift of $LiFePO_4$ powder, for example, is reported in the literature for a range of resonances between -56 ppm to -8 ppm [207, 208, 245, 246]. One contributing factor to this variation may in fact be due to the difference in the particle shapes, hence BMS shifts, between the different powder samples.

Ultimately, the Fermi contact, pseudo-contact and BMS shifts, as well as the hyperfine dipolar and BMS broadenings, are additive, and untangling these contributions to rationalize the NMR spectrum of a paramagnetic material requires the ability to quantify them separately.

Computational approaches, mainly based on density functional theory (DFT) methods have been successfully developed, allowing a detailed first principles description of the electronic structure and of the Fermi contact and pseudo-contact shifts, as well as the

hyperfine dipolar broadening [14, 61, 63, 209]. Examples of this were presented in Chapters 3, 4 and 5. For BMS contributions, however, the explicit dependence on the single crystal geometry, or, in the case of powders, crystallite geometry, distribution, and even container shape, means that the BMS shift calculations must typically be made on a sample–to–sample basis.

This Chapter investigates the BMS shift in paramagnetic $LiFePO_4$ single crystals with a variety of different macroscopic shapes. The ^{7}Li shift of each crystal is measured using magic-angle spinning (MAS) NMR, employing an innovative 3D-printed rotor insert design. The ^{7}Li NMR spectra show a significant variation in the measured isotropic ^{7}Li shifts between crystals. BMS effects for each precise crystal geometry are calculated using finite element micromagnetic simulations of the demagnetising field distribution and the anisotropic magnetic susceptibility tensors experimentally determined for the $LiFePO_4$ crystal samples. The calculated BMS shift contributions, summed to the local paramagnetic shift contributions, are in close agreement with the experimental results, confirming that the large variation in shift is predominantly due to the shape-dependent macroscopic BMS term.

The work presented in this Chapter benefited from the intellectual input of Liam O'Brien, Andrew Pell, Michael Gaultois and Clare Grey. The $LiFePO_4$ single crystals were prepared by Yuri Janssen. Liam O'Brien performed the BMS shift calculations. The current author performed all of the experimental work.

6.2 Theory

The theoretical description of the paramagnetic shielding tensor, $\boldsymbol{\sigma}^s$, and the BMS shielding tensor, $\boldsymbol{\sigma}^{\mathrm{BMS}}$, were presented in Section 2.3.5 and Section 2.3.6, respectively, and a summary will be given here for convenience.

When an external magnetic field, H_0, is applied to a paramagnetic crystal, a net magnetic moment μ_{ind} is induced parallel to H_0. In a macroscopic continuum approximation, this moment can be described by a magnetisation per unit volume, $M = \frac{\mu_{\mathrm{ind}}}{V}$, which is proportional to the external field [78]

$$M = \frac{\mu_{\mathrm{ind}}}{V} = \chi_{\mathrm{V}} H_0 \tag{6.1}$$

where V is the total crystal volume, and the volume magnetic susceptibility, χ_{V}, is given by the magnetic susceptibility per molecule, χ, divided by the Avogadro number.

If the electron orbital angular momentum is non-negligible, the total magnetic moment $\boldsymbol{\mu}$ becomes anisotropic as an effect of spin-orbit coupling, as does the magnetic susceptibility. For an ensemble of paramagnetic ions, $\boldsymbol{\chi}$ is represented by replacing the free-electron g-value with an anisotropic g-tensor that parametrizes the non-zero electron orbital angular momentum. The magnetic susceptibility tensor for systems containing d-block transition metal ions (neglecting the effects of zero-field splitting, as discussed in Section 2.3.4) can then be formulated as [77, 8]

$$\boldsymbol{\chi} = \frac{\mu_0 \mu_B^2 S(S+1)}{3kT} \boldsymbol{g} \cdot \boldsymbol{g}^T \tag{6.2}$$

where μ_0 is the permeability of free space, μ_B is the Bohr magneton, g_e is the free-electron g-value, S is the electronic spin, k is the Boltzmann's constant and T the absolute temperature, and $\boldsymbol{g}^T$ is the transpose of the g-tensor.

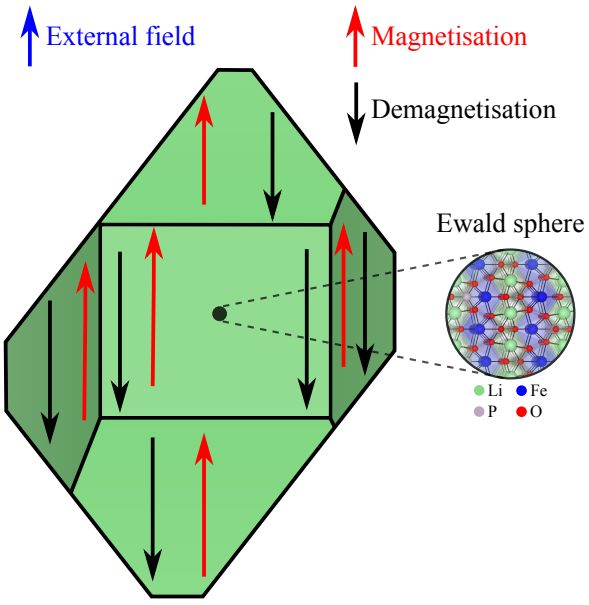

Fig. 6.1 Schematic representation of the model of a paramagnetic $LiFePO_4$ crystal. A crystal of arbitrary shape is shown, subject to an external magnetic field aligned along a certain direction (blue arrow). The Ewald sphere is shown in the inset on the right-hand side, with a radius much smaller than the dimensions of the crystal, but large enough so that the sum of the local interactions contributing to $\boldsymbol{\sigma}^S$ converges. The remainder of the crystal is treated as an uniformly magnetized continuum within which the bulk magnetic susceptibility effects generate the $\boldsymbol{\sigma}^{\mathrm{BMS}}$ contribution to the total shielding tensor of the nucleus I, in this example being ^{7}Li.

We now examine how the presence of paramagnetic centres affects the NMR spectrum of the observed nucleus, with a particular focus on the BMS effects. Schwerk *et al.* [32]

and Kubo *et al.* [26] presented a theoretical derivation of the isotropic BMS and the anisotropic BMS effects on the NMR spectrum of homogeneous paramagnetic powders. Dickinson *et al.* [33] extended the model based on classical electrostatics to calculate the demagnetising fields of bulk samples, and the corresponding effects on the NMR spectrum of inhomogenheous materials. Here, we use a similar approach to that of the Kubo model, which is schematically represented in Figure 6.1 [26]. The model assumes that the observed nucleus I is at the center of a local region, referred to as the Ewald sphere, which has dimensions much smaller than those of the crystal. Within this region, the nucleus experiences a local paramagnetic shielding tensor, $\boldsymbol{\sigma}^s$, resulting from the sum of hyperfine and spin-orbit interactions with the nearby paramagnetic centres, with the radius of the Ewald sphere being large enough so that the sum converges. The remainder of the crystal is then assumed to be a uniformly magnetised continuum, in which the bulk magnetic susceptibility (BMS) effects contribute a BMS shielding tensor, $\boldsymbol{\sigma}^{\mathrm{BMS}}$. The total shielding, $\boldsymbol{\sigma}^{\mathrm{TOT}}$, at the observed nucleus, I, is hence given by the sum of these contributions:

$$\boldsymbol{\sigma}^{\mathrm{TOT}} \;=\; \boldsymbol{\sigma}^{s} \;+\; \boldsymbol{\sigma}^{\mathrm{BMS}} \tag{6.3}$$

In the presence of spin-orbit coupling, $\boldsymbol{\sigma}^s$ takes the form in equation 2.34. [78, 8]

As presented in Chapters 3, 4, 5, and in many other studies [202, 204, 12, 13, 66], first principles calculations of hyperfine interactions have been successfully applied to various paramagnetic systems, from molecules containing a single paramagnetic site to solids with substantial paramagnetic centres throughout the lattice. Alternatively, the contributions of $\boldsymbol{\sigma}^s$ to the NMR spectrum of a crystal can be experimentally approximated with the shift of a powder sample of the same material, provided that the particle shape is approximately spherical, so as to approximate the Ewald sphere described earlier (Figure 6.1). The latter is the approach that will be followed in this work.

As it was introduced in Section 2.3.6, to determine $\boldsymbol{\sigma}^{\mathrm{BMS}}$ in equation 6.3, one must consider the uniformly magnetised continuum, external to the Ewald sphere, as schematically represented in Figure 6.1. In relatively simple crystal shapes (e.g. ellipsoids), the demagnetising field, $\boldsymbol{H}_D$, generated due to the discontinuity of $\boldsymbol{M}$ at the sample edges, takes the form [28, 76]

$$\boldsymbol{H}_D \;=\; -\boldsymbol{N} \cdot \boldsymbol{M} \;=\; -\boldsymbol{N} \cdot \boldsymbol{\chi} \cdot \boldsymbol{H}_0 \tag{6.4}$$

where $\boldsymbol{N}$ is the two-dimensional demagnetising tensor, the rank-two part describing the shape of the crystal, and with trace $Tr(\boldsymbol{N}) = 1$. As described in Section 2.3.4, in analogy with the nuclear Zeeman interaction, the demagnetising field essentially induces

an additional shielding at the nuclear spin, and the form of $\boldsymbol{\sigma}^{\mathrm{BMS}}$ inside the crystal can be derived as

$$\boldsymbol{\sigma}^{\mathrm{BMS}}(\boldsymbol{r}) \;=\; \boldsymbol{\chi}_V \cdot (\boldsymbol{N}(\boldsymbol{r})^T \;-\; \mathbf{1}) \tag{6.5}$$

where $\mathbf{1}$ is the identity matrix. In this work we will be concerned with the isotropic component of $\boldsymbol{\sigma}^{\mathrm{BMS}}$, which is determined by the on-diagonal components of $\boldsymbol{N}$ and $\boldsymbol{\chi}$, so to obtain:

$$\delta^{\mathrm{iso,BMS}} = \frac{1}{3} Tr[\boldsymbol{\chi}_V \cdot (\boldsymbol{N}(\boldsymbol{r})^T \;-\; \mathbf{1})] \tag{6.6}$$

In order to quantify the demagnetising field, and to compute $\boldsymbol{\sigma}^{\mathrm{BMS}}$, one needs to know $\boldsymbol{N}$ and $\boldsymbol{\chi}_V$. In simple geometries, $\boldsymbol{N}$ can be analytically determined from the dimensions of the sample. In more complex shapes, however, $\boldsymbol{H}_D$ must be calculated numerically using the precise sample geometry[26], as is the approach taken here. We note that the local dipolar contribution to $\boldsymbol{\sigma}^s$ will inherently include the BMS contribution due to the Ewald sphere itself. Therefore, to avoid double-counting the BMS contribution inside the Ewald sphere, equation 6.6 is reformulated as

$$\delta^{\mathrm{iso,BMS}}_{\mathrm{calc.}} = \frac{1}{3} Tr[\boldsymbol{\chi}_V \cdot (\boldsymbol{N}(\boldsymbol{r})^T \;-\; \frac{1}{3}\mathbf{1})] \tag{6.7}$$

where $\frac{1}{3}\boldsymbol{\chi}_V$ is the demagnetising field inside the Ewald sphere. It is worth noting at this stage that, considering equation 6.7, substantial BMS shifts are only observed in samples where both $\boldsymbol{\chi}_V$ and $\boldsymbol{N}$ are anisotropic, i.e., in crystals that are far from spherical in shape.

6.3 Experimental Methods

6.3.1 $LiFePO_4$ Crystal Growth, Basic Characterization, Single Crystal Diffraction

Single crystals of $LiFePO_4$ were prepared and characterized by Janssen *et al.*, as described in detail in Ref. [247]. To briefly summarize, the crystals were prepared by flux growth techniques, using Li_3PO_4, LiCl, $FeCl_2$ as reagents, heated to 810 °C, held at this temperature for 2 h and then slowly cooled to 480°C, after which the furnace was allowed to cool naturally. The growth boules were then taken out of the crucibles, and the LiCl-$FeCl_2$ flux was dissolved with water or ethanol in an ultrasonic bath to reveal the crystals. Single crystal alignments were done using both X-ray and neutron diffraction, both collected at room temperature.

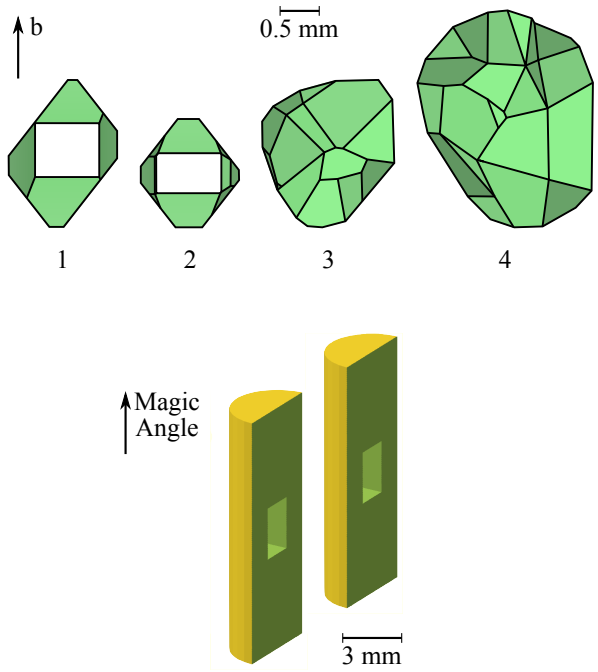

Fig. 6.2 (Top) Schematic representation of the four $LiFePO_4$ single crystals, labelled Crystal $1-4$. (Bottom) Schematic representation of the 3D-printed insert for the 4 mm rotor. The cavity in the middle of the insert is designed to host the crystal under investigation. A set of inserts is fabricated, each with a cavity shaped to host a specific crystal shape.

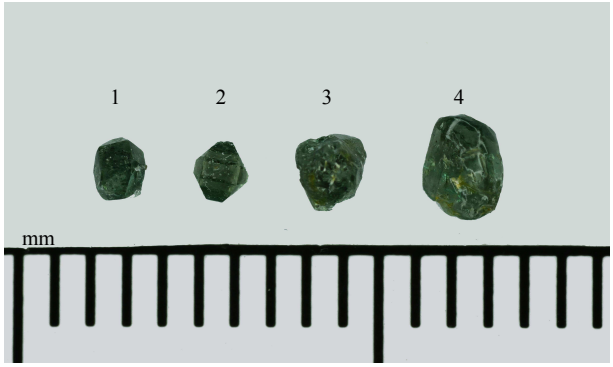

Fig. 6.3 Picture showing the four $LiFePO_4$ single crystals, labelled Crystal $1-4$.

The four $LiFePO_4$ single crystals used in this study, labelled Crystal $1-4$ hereafter, are schematically shown in Figure 6.2 (Top) (real photograph in Figure 6.3), and have the following dimensions along the principal crystallographic directions, (a, b, c), respectively: $(1.0 \times 1.9 \times 1.0)$ mm for Crystal 1, $(1.1 \times 1.4 \times 1.7)$ mm for Crystal 2, $(1.7 \times 1.9 \times 2.1)$ mm for Crystal 3, and $(2.3 \times 2.8 \times 0.9)$ mm for Crystal 4. For convenience, the dimensions of the crystals are also summarised in Table 6.1.

6.3.2 $LiFePO_4$ Powder XRD and TEM

The carbon-coated $LiFePO_4$ powder was synthesized by Strobridge *et al.* *via* the solid-method described in Ref. [246]. The particle size of the $LiFePO_4$ powder was determined with powder X-ray diffraction (XRD) and transmission electron microscopy (TEM). Laboratory X-ray diffraction (XRD) was performed with a PANalytical Empyrean diffractometer using Cu Kα radiation ($\lambda = 1.5406$ Å), and Rietveld refinement was performed using the Topas Academic software package [248] using an initial model of $LiFePO_4$ from Nyten and Thomas [249]. A NIST Si standard was run prior to refinements to determine the instrument profile parameters, after which a size-strain analysis of the $LiFePO_4$ analyzed was performed during the Rietveld refinement using a voigt convolution as described and discussed by Balzar *et al.* [250, 251] A total of 17 TEM images of the $LiFePO_4$ powder were obtained using a JEOL JEM-3010 Transmission Electron Microscope (300 kV). The particle size distribution was calculated by directly measuring the size of 30 different particles and averaging over their determined sizes.

6.3.3 Magnetic Measurements

Magnetization measurements were performed with a Quantum Design Material Property Measurement System (MPMS). Magnetic moments of zero field-cooled crystals were measured at temperatures from 2 K up to 301 K to obtain the dependence of magnetic susceptibility on temperature, $\chi(T) = dM/dH \approx M/H$. Each measurement was conducted by mounting the crystal under investigation in epoxy resin aligned along one of the a, b and c principal axes with respect to the external field. This allowed the characterization of the susceptibility tensor along the three principal components of each crystal.

6.3.4 Solid-state MAS ^{7}Li NMR

Solid-state ^{7}Li NMR spectra of the four $LiFePO_4$ crystals and of the $LiFePO_4$ powder sample were acquired on a Bruker 200 Avance III spectrometer using a 4 mm probe, with a magic angle spinning (MAS) frequency of 12.5 kHz; the one-dimensional ^{7}Li spectra were recorded using a double-adiabatic spin-echo sequence [192], employing a pair of 50 μs tanh/tan short high-powered adiabatic pulses (SHAPs) of 5 MHz sweep width [193, 194] and a 1.025 μs 90° excitation pulse. All pulses used a radiofrequency (RF) field strength of 244 kHz. For each spectrum, 8192 scans were acquired using a recycle delay of 30 ms. The pulse sequence used for the single-crystal NMR was modified to include a *trigger* function, which allowed, within the same acquisition, each scan to

start at the same rotor rotation angle, hence to obtain the side-band profile typical of single crystals [252]. As a benchmark, the same pulse sequence is also used without the inclusion of the *trigger* function. Without this option, the whole carousel is sampled, i.e. each pulse sequence starts at a random and potentially different rotor (hence crystal) rotation angle [253]. Over the entire set of scans, the sum over the collected spectra will correspond to an average of the rotation-specific side-band profiles, hence giving a fully in-phase side-band pattern. The spectra acquired without the *trigger* function are performed to make sure that the determination of the isotropic shift is not affected by the phasing of the spectrum.

The NMR spectra are performed under MAS. A set of rotor inserts was designed, intended to encapsulate the crystal inside the rotor and to keep it firm in a fixed position during the acquisition. A schematic of the insert is presented in Figure 6.2 (Bottom). The insert consists of a plastic cylinder with a cavity in the middle that hosts the crystal. The cavity of each insert is designed to host a specific crystal aligned in a certain orientation. The insert is 3D-printed as two detached halves, which, once the crystal is aligned inside the cavity, are put together and the resulting cylinder is tightened in Teflon seal tape to ensure firmness inside the rotor. The plymer used for the 3D-print was acrylonitrile butadiene styrene.

6.3.5 Calculation of the BMS Shift

Our approach to the calculation of the BMS shift implements a finite numerical model to calculate the internal demagnetizing field distribution within a crystal of a given shape, using the OOMMF code [254]. The precise crystal shape is extracted from the analysis of high-resolution calibrated microscope images of the $LiFePO_4$ single crystals, and converted into a 3D mask. Where possible, individual face orientations and positions are determined to create the 3D mask. For highly irregular and multifaceted samples (e.g. Crystal 4), where such an approach is unfeasible, an outline mask is built up from images of the sample oriented along specific crystal planes (e.g. *ab*, *ac*, *bc* planes). The mask is then broken into a discrete mesh of cuboid cells, size, and uniform magnetization $\boldsymbol{M}$. $\boldsymbol{M}$is aligned in turn along the three principal axes of the crystal, and the demagnetizing self-energy ($\mu_0 \boldsymbol{H}_D \cdot \boldsymbol{M}$) is calculated. The code determines the volume average $\boldsymbol{H}_D$ in each cell, and then calculates the demagnetizing self-energy using a fast Fourier transform method. As $\boldsymbol{M}$ is uniform and constant throughout the crystal, the ratio of the demagnetising self-energies along each axis is equivalent to the ratios of the three on-diagonal components of $\boldsymbol{N}$. This, plus the requirement that $Tr(\boldsymbol{N}) = 1$, allows us

to calculate the exact values of N_a, N_b, N_c. These values are then combined with the experimentally measured $\boldsymbol{\chi}$ of each crystal to give $\boldsymbol{\sigma}^{\mathrm{BMS}}$ using equations 6.5 and 6.7.

6.4 Results and Discussion

Figure 6.4 shows the variation of the zero-field cooled magnetic susceptibilies with temperature in the range of $2-301$ K for the four $LiFePO_4$ single crystals. The curves show that all the crystals are characterized by typical paramagnetic features over a wide temperature range and become antiferromagnetic at a Néel temperature (T_N) of about 53 K. Crystal 1, however, shows a second transition at 130 K, which is ascribed to $Fe_3^{II,III}O_4$ magnetite impurities, as previously reported [247]. Below 52 K a substantial drop is observed in χ_b , while the change in both χ_a and χ_c is less prominent from 52 K down to 2 K. This indicates the presence of antiferromagnetic long-range order below T_N with the crystallographic b axis being the magnetic easy axis of the $LiFePO_4$ system. These results are in agreement with previously reported magnetic data on $LiFePO_4$ single crystals. [255]

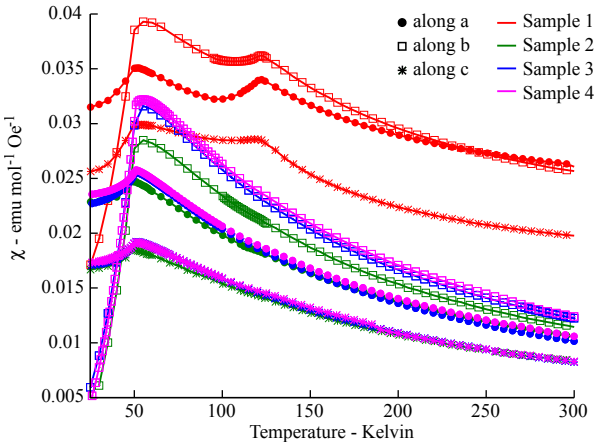

Fig. 6.4 Experimental molar magnetic susceptibility curves as a function of temperature for the four different crystals (red, green, blue and magenta for Crystal 1, 2, 3 and 4, respectively). The measurement for each crystal mounted with the $a-$, $b-$ or $c-$ axis aligned with the field is represented with circle, square and star symbols, respectively.

For each susceptibility curve, the Weiss constant, θ, is extracted by fitting the Curie-Weiss law $\frac{1}{\chi} = \frac{T-\theta}{C}$, with C being the Curie constant, in the temperature range of $150-301$ K. The fitted curves are shown in Figure 6.5, the obtained Weiss constants are summarised in Table 6.1, and the details of the fittings are listed in Table 6.2. The trend $\theta(\parallel b) < \theta(\parallel a) < \theta(\parallel c)$ is obtained for all the crystals. The observed values and

trend with respect to the alignment are in agreement with previously reported magnetic results [255]. The significant difference of the θ values for Crystal 1 compared to the values of Crystals $2-4$ is ascribed to the presence of the $Fe_3^{II,III}O_4$ impurity and the corresponding second transition. From the fitting of the susceptibilities, shown in Figure 6.5, the value of χ at room temperature is extracted (Table 6.1), which, combined with the measured dimensions of each crystal along the principal components, is used to calculate the demagnetising field, $\boldsymbol{N}$, for each crystal.

	Dimensions mm			θ K			χ (320 K) emu mol^{-1} Oe^{-1}		
	a	b	c	a	b	c	a	b	c
Crystal 1	1.0	1.9	1.0	-417	-375	-605	0.0251	0.0243	0.0186
Crystal 2	1.1	1.4	1.7	-127	-86	-135	0.0100	0.0109	0.0079
Crystal 3	1.7	1.9	2.1	-105	-89	-119	0.0097	0.0116	0.0079
Crystal 4	2.3	2.8	0.9	-112	-80	-121	0.0101	0.0118	0.0079

Table 6.1 Dimensions (in mm), Weiss constants (in K) and χ values (in emu mol^{-1} Oe^{-1}) at 320 K, for each Crystal $1-4$ for each a, b and c crystallographic axis.

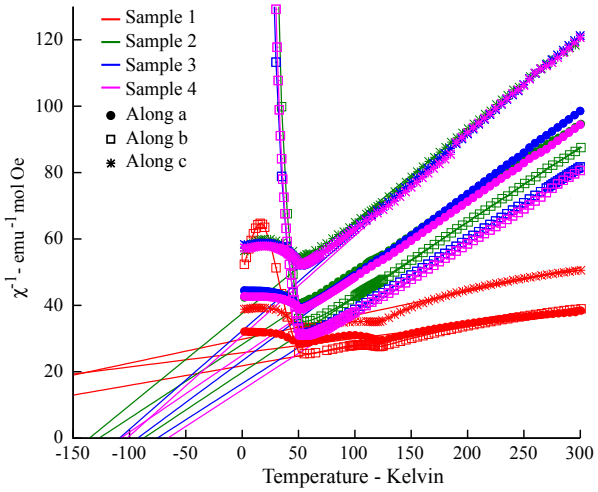

Fig. 6.5 Experimental inverse molar magnetic susceptibility as a function of temperature curves for the four different crystals (red, green, blue and magenta for Crystal 1, 2, 3 and 4, respectively).The fitting is shown with the solid lines following the same colouring scheme. The measurement for each crystal mounted with the $a-$, $b-$ or $c-$ axis aligned with the field is represented with circle, square and star symbols, respectively.

	Along a	Along b	Along c
Crystal 1	$y = 0.05x + 24.26$, $R^2 = 0.97$	$y = 0.06x + 21.80$, $R^2 = 0.99$	$y = 0.07x + 29.80$, $R^2 = 0.98$
Crystal 2	$y = 0.22x + 28.24$, $R^2 = 0.99$	$y = 0.23x + 19.79$, $R^2 = 0.99$	$y = 0.28x + 37.57$, $R^2 = 0.99$
Crystal 3	$y = 0.30x + 32.36$, $R^2 = 0.99$	$y = 0.22x + 16.43$, $R^2 = 0.99$	$y = 0.25x + 23.31$, $R^2 = 0.99$
Crystal 4	$y = 0.23x + 24.90$, $R^2 = 0.99$	$y = 0.21x + 14.63$, $R^2 = 0.99$	$y = 0.30x + 30.68$, $R^2 = 0.99$

Table 6.2 Results of the linear regression fit of the curves ($\frac{1}{\chi}$ vs T) shown in Figure 6.5. The R^2 refers to the coefficient of determination in the linear regression.

The average particle size and shape of the $LiFePO_4$ powder sample was analysed with TEM, and two illustrative images are presented in Figure 6.7. A total of 30 particles was measured. An average particle size of 126 nm was calculated, and an averaged featureless particle shape was determined. Since the particle detection with TEM was made difficult by the carbon coating of the powder, we compared the results with the analysis based on X-ray diffraction. The unit-cell volume obtained from the Rietveld refinement is 297.31 Å, in agreement with previous literature [227]. The volume-weighted domain size, D_V, was determined by Rietveld refinement to be 100(3) nm. The fitting of the XRD pattern is shown in Figure 6.6. Under the assumption that the powder is a monodisperse system of spherical crystallites, this corresponds to an average crystallite diameter of 133(4) nm, and is consistent with the direct particle measurement performed using TEM. This confirms that the particles have an average size (130 nm) four orders of magnitude smaller than the average size of the single crystals (1.7 mm).

The ^{7}Li NMR spectrum of the $LiFePO_4$ powder is shown in Figure 6.8, and an isotropic shift of $\delta^{iso} = -16$ ppm is measured, in agreement with previous studies [208]. Since we confirmed that the powder particles are featureless and approximately spherical, of average size (130 nm) significantly smaller than the average single crystal size (1.7 mm), the isotropic shift of the $LiFePO_4$ powder is considered as resulting only from the local hyperfine and spin-orbit coupling interactions within the Ewald sphere, i.e. only $\boldsymbol{\sigma}^s$ in equation 6.3.

The NMR spectra of the four $LiFePO_4$ single crystals were acquired for each principal axis aligned along the magic angle. The spectra obtained for the *a*-, *b*-, and *c*-axis aligned along the magic angle are shown in Figure 6.9, 6.10 and 6.11, respectively. For each crystal, the variation in the isotropic shift between the different alignments is within ±

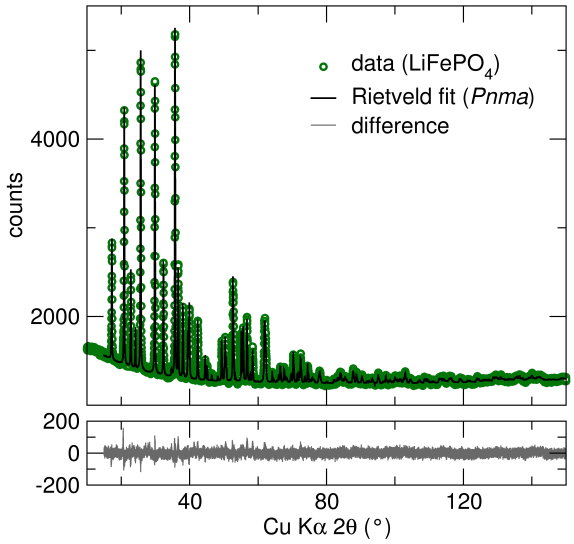

Fig. 6.6 X-ray diffraction pattern for $LiFePO_4$, showing the collected data (green circles), the Rietveld fit (black line) and their difference (lower panel, grey line).

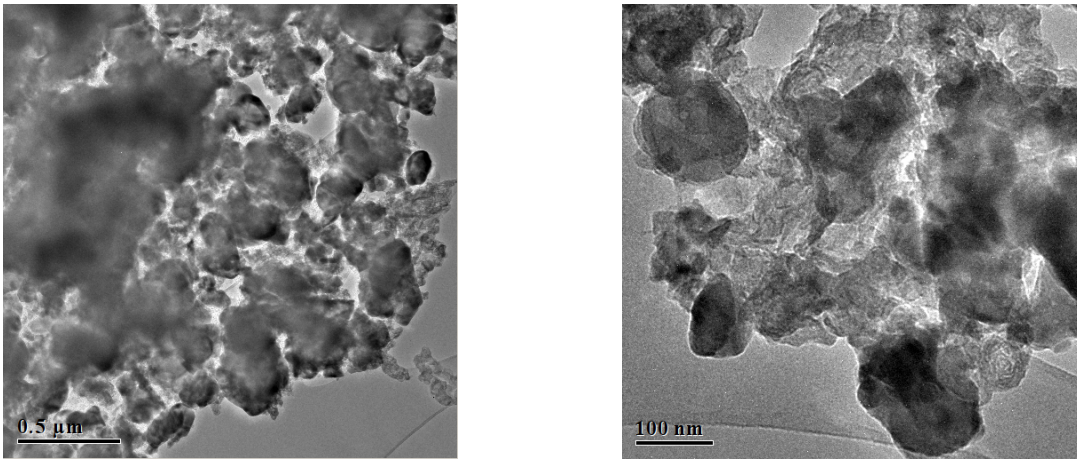

Fig. 6.7 Two Transmission Electron Microscopy (TEM) images of the $LiFePO_4$ powder sample.

3 ppm. The obtained shifts are summarised in Table 6.3. In order to make sure that the values of the isotropic shifts did not depend on the phasing of the spectra, for every orientation the ^{7}Li NMR of the four samples was also acquired without applying the *triggering* in the NMR pulse sequence, as described in the Experimental Section. This resulted in all in-phase spectra. The ^{7}Li NMR spectra obtained with this approach are presented in the Appendix B. The results are consistent with the shifts obtained from the spectra in Figures 6.9, 6.10 and 6.11, and summarised in Table 6.3.

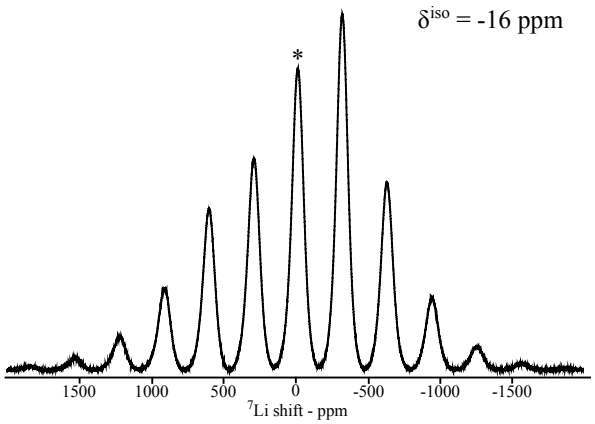

Fig. 6.8 Experimental ^{7}Li NMR spectrum of the $LiFePO_4$ powder sample.

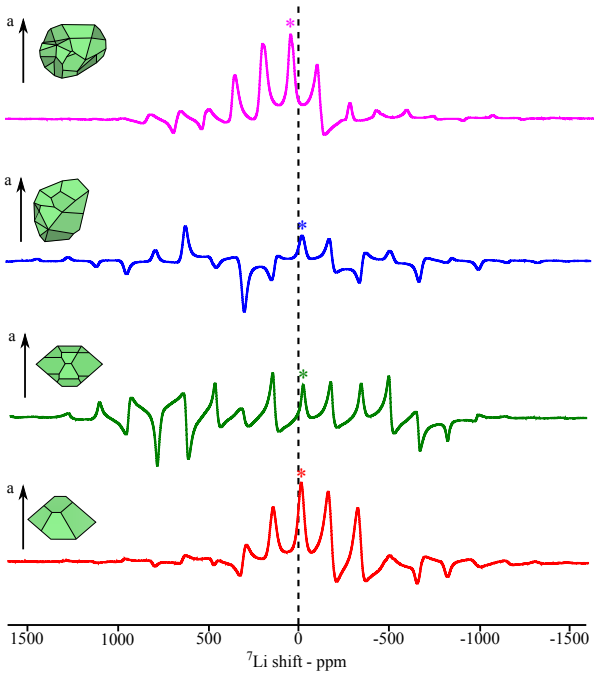

Fig. 6.9 Experimental ^{7}Li NMR spectra of the four $LiFePO_4$ single crystals oriented with the a-axis aligned along the magic angle. The spectrum of Crystal 1 is shown with the red line, for Crystal 2 with the green line, for Crystal 3 with the blue and for Crystal 4 with the magenta line. The isotropic peak of each spectrum is marked with an asterisk. The dotted line marking the 0 ppm is included to facilitate the visualization of positive and negative isotropic resonances.

A very large variation in δ^{iso} of almost 60 ppm is found across the series, and the shift of each crystal deviates from the ^{7}Li shift of the powder sample, assumed to correspond to the paramagnetic shift due to the local interactions within the Ewald sphere. Since

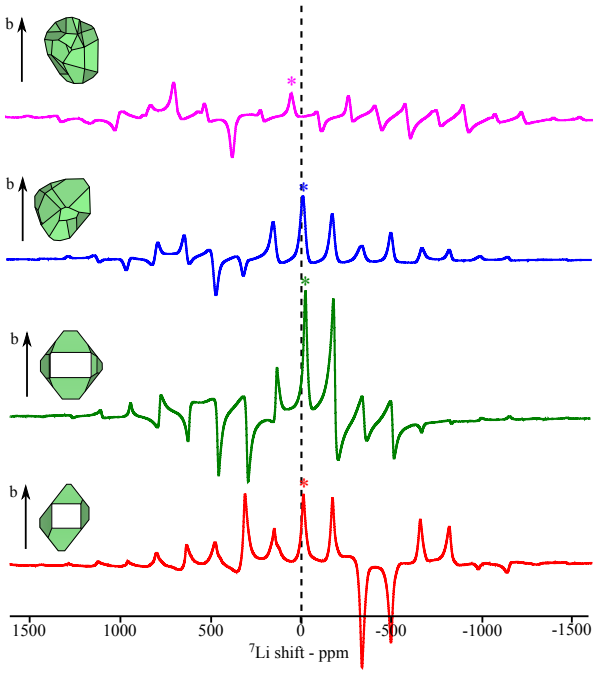

Fig. 6.10 Experimental ^{7}Li NMR spectra of the four $LiFePO_4$ single crystals oriented with the *b*-axis aligned along the magic angle. The spectrum of Crystal 1 is shown with the red line, for Crystal 2 with the green line, for Crystal 3 with the blue and for Crystal 4 with the magenta line. The isotropic peak of each spectrum is marked with an asterisk. The dotted line marking the 0 ppm is included to facilitate the visualization of positive and negative isotropic resonances.

	$\delta^{\mathrm{BMS}}_{\mathrm{calc.}}$ ppm	$\delta^{\mathrm{iso,TOT}}_{\mathrm{calc.}}$ ppm	$\delta^{\mathrm{iso}}_{\mathrm{exp.}}(a)$ ppm	$\delta^{\mathrm{iso}}_{\mathrm{exp.}}(b)$ ppm	$\delta^{\mathrm{iso}}_{\mathrm{exp.}}(c)$ ppm
Crystal 1	10	-6	-12	-11	-14
Crystal 2	-5	-21	-19	-22	-23
Crystal 3	-1	-17	-20	-21	-20
Crystal 4	58	42	38	36	38

Table 6.3 Calculated bulk magnetic susceptibility ^{7}Li shift ($\delta^{\mathrm{BMS}}_{\mathrm{calc.}}$ as in eq. 6.6), calculated total isotropic ^{7}Li shift ($\delta^{\mathrm{iso,TOT}}_{\mathrm{calc.}}$ as in eq. 6.7) and experimental isotropic ^{7}Li shift obtained for each crystal aligned along a ($\delta^{\mathrm{iso}}_{\mathrm{exp.}}(a)$), b ($\delta^{\mathrm{iso}}_{\mathrm{exp.}}(b)$), and c ($\delta^{\mathrm{iso}}_{\mathrm{exp.}}(c)$).

the major difference between the crystals is the shape, the large variation in their ^{7}Li NMR shifts is interpreted as primarily ascribed to the bulk magnetic susceptibility effects. The calculated $\delta^{\mathrm{BMS}}_{\mathrm{calc.}}$ values are presented in Table 6.3. The results indeed support the

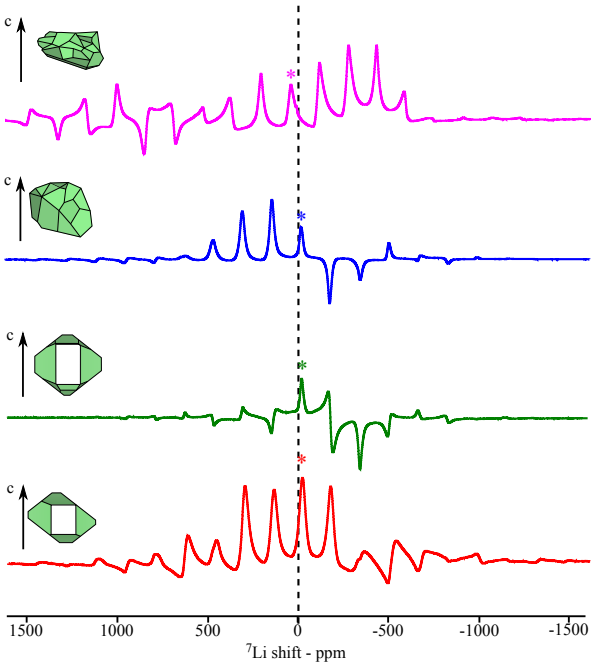

Fig. 6.11 Experimental ^{7}Li NMR spectra of the four $LiFePO_4$ single crystals oriented with the *c*-axis aligned along the magic angle. The spectrum of Crystal 1 is shown with the red line, for Crystal 2 with the green line, for Crystal 3 with the blue and for Crystal 4 with the magenta line. The isotropic peak of each spectrum is marked with an asterisk. The dotted line marking the 0 ppm is included to facilitate the visualization of positive and negative isotropic resonances.

hypothesis that the BMS shift varies significantly between the crystals as an effect of the different shapes and shape anisotropies of the four samples. The BMS shift is in fact found to constitute a significant, if not major as in the case of Crystal 4, contribution to the total shift. The computed total shifts, calculated as $\delta^{\mathrm{iso,TOT}}_{\mathrm{calc.}} = \delta^{\mathrm{BMS}}_{\mathrm{calc.}} + \delta^{s}_{\mathrm{local}}$, where $\delta^{s}_{\mathrm{local}} = -16$ ppm (i.e. the $LiFePO_4$ powder ^{7}Li shift) are also presented in Table 6.3. The trend of the calculated shifts across the crystals repoduces well the trend obtained experimentally. The deviation between the calculated and the measured isotropic shift for the Crystal 1 is primarily ascribed to the presence of $Fe_3^{\mathrm{II,III}}O_4$ impurity. The experimental magnetic susceptibility used for the calculation of the BMS effect is very much affected by the presence of this impurity (Figure 6.4). Without knowing the amount and the distrubution of $Fe_3^{\mathrm{II,III}}O_4$ in the crystal, it is complicated to work out its effect on the local paramagnetic interaction to the Li shift, and a more carefull characterization to this regard would be needed. Additional sources of errors may be due to possible slight misalignments of the crystals in the SQUID holder when measuring the susceptibility. Nevertheless, the calculations are overall in good agreement with the experimental shifts.

This comparison confirms that the BMS shift can indeed be a significant contribution to the total shift, and that, depending on the magnetism and the macroscopic shape of the crystal, it can be of comparable or even greater size than the local hyperfine and pseudo-contact shift contributions. This approach can be readily extended to the analysis of BMS shifts in paramagnetic powder samples, paving the way to the understanding of crystallites shape dependence of the isotropic paramagnetic shift.

6.5 Conclusions

This work presents an accurate approach to the calculation of demagnetising fields and BMS shifts for paramagnetic crystals based on classical electrodynamics. A set of four $LiFePO_4$ single crystals is used, for which the shape and the magnetization are measured along each of the three (a, b, c) crystallographic axes. An innovative rotor insert is designed and 3D-printed, which allows to measure the ^{7}Li NMR shift of each crystal for different alignements and under magic angle spinning, so to partially suppress the line-broadening and obtain a well resolved isotropic resonance.

The measured ^{7}Li NMR shifts of the four crystals vary significantly, covering a shift range of almost 60 ppm. The calculated BMS shift contributions confirm that the large variation in the shift between the samples is due to the different macroscopic shape of the crystals. The BMS shift is indeed found to be a significant component of the total ^{7}Li shift, in some cases even greater than the local hyperfine and pseudo-contact shifts. This is particularly relevant in the study of systems with large spin-orbit coupling effects and susceptibility anisotropy such as solids containing lanthanide ions, for which the demagnetizing field and the shape-dependent BMS shift can constitute a significant portion of the measured shift. By showing the relevance of the BMS shift contribution in the ^{7}Li NMR of paramagnetic solids, the present work also points out the importance of accounting for this term when validating computational methods, normally involved in the calculation of the local hyperfine and pseudo-contact shifts only, but aimed at reproducing the total experimental NMR shifts of paramagnetic solids. The versatility of the presented computational approach enables its broadening towards the study of shape-dependent BMS shifts in more complex samples, such as paramagnetic powders.

Chapter 7

Conclusions

NMR spectroscopy has been shown to be a powerful technique to probe the local atomic and electronic structure of paramagnetic solids, aiding the investigation the structure–properties relationships in complex systems, such as cathode materials for Li–ion batteries. The structural complexity of such solids, and the elaborate interplay between the various paramagnetic electron-nuclear interactions, result in NMR spectra that are dense of structural, electronic and magnetic information, yet often very complicated to interpret. The synergy of the state of the art NMR spectroscopy methods for paramagnetic solids, and the advanced first principles approaches to model open-shell periodic systems, enables to obtain an in-depth characterisation of the studied materials.

During the electrochemical cycling of a Li–ion battery, the Li ions are (de)intercalated into (out of) the cathode. The process induces changes in the electronic configuration and the orbital ordering of the paramagnetic sites involved in the redox process, as well as structural changes of atomic coordinations and lattice parameters. A combined experimental and first principles investigation of the structural changes induced by electrochemical cycling to the V_6O_{13} cathode material is presented in Chapter 3. *In situ* XRD is performed to monitor the evolution of the lattice expansions/contractions during cycling. The underlying atomic rearrangements as a function of lithiation are studied with DFT calculations. This is performed by implementing a first principles approach that calculates the optimized structure and the electronic properties of the manifold of possible configurations throughout the lithiation process. The analysis of the calculated formation energies of the different structures and the comparison between the lattice parameters obtained with DFT and the ones extracted from the *in situ* XRD refinement allows the identification of energetically favourable Li sites and orbital orderings as a function of lithiation. The occupancy of specific Li sites during cycling is further investigated by a combined experimental and computational ^{7}Li MAS NMR study

of different compositions during the electrochemical process. The migration pathways between different Li sites are also investigated with DFT, identifying preferential Li diffusion channels in the cathode host. The complex phase evolution of the material during cycling still needs more work to be fully understood. Further analysis on the ^{7}Li NMR spectra, combined with additional first principles hyperfine shift calculations, can aid in interpreting the structural rearrangements as a function of lithiation throughout the entire series, also investigating the differences between charge and discharge processes. Furthermore, since the V_6O_{13} material has attracted interest as a possible cathode in battery devices operated at high temperatures, the study can be further extended towards the analysis of the electrochemical performance and the structural changes under more extreme thermal conditions.

Often materials used as cathodes are composed of multiple transition metal species, each of which can be present at more than one oxidation state. The electrochemical performance and the structural stability of the cathode (and of the whole cell) crucially rely on the distribution of TM and Li sites in the lattice, and the characterisation of the structure at the atomic level is of central importance. A combined ^{7}Li MAS NMR experimental and computational methodology is developed in Chapter 4, and applied to study the compositional (dis)order of the $LiTi_xMn_{2-x}O_4$ series of cathode materials. The Li isotropic shift, dominated by the Fermi contact interaction, allows to distinguish (resolution permitting) between different Li coordination environments, e.g. Li in tetrahedral or octahedral sites, and between different TM ions connected to the Li *via* oxygen bonds, e.g. Ti^{4+}, $Mn^{2+/3+/4+}$. The analysis of the complicated experimental ^{7}Li NMR spectra requires the support of first principles calculations. Because of the additivity of the Li–O–TM Fermi contact contributions to the total shift of any given Li environment, the computational approach follows the following steps. Firstly, the pair-wise TM–TM exchange interactions are calculated with DFT, to model the local magnetic properties of the material. Secondly, the Li Fermi contact shift contributions are computed for all the Li–O–TM bond pathways possibly present in the structures, using the previously calculated magnetic scalings. Thirdly, configurations of different site orderings are simualated, and the isotropic shift of the occurring Li centres are obtained by summing the respective Li–O–TM contributions relevant to each Li environment. The configurations are generated either as a random distribution of sites, or in a more ordered site arrangement by implementing a Reverse Monte Carlo approach. Finally, the total spectrum of each simulated configuration is obtained by summing the shifts of all the Li sites present in the structure, and it is compared with the experimental ^{7}Li NMR spectrum for the relevant stoichiometry. The best agreement between simulated and

experimental spectra allows the validation of the specific site arrangement throughout the $LiTi_xMn_{2-x}O_4$ series. This approach enables the investigation of the variations in the local ordering of the ions in the structure, a function of composition and Mn oxidation state. The approach presented in this Chapter, as well as the specific Li–O–Mn shift contributions, can be readily extended to the NMR analysis of similar Li–Mn spinel systems of interest in the battery field. The discussed methodology can also be improved by including additional parameters in the Reverse Monte Carlo simulation, such as for instance the electroneutrality principle, enabling the analysis of the ion pairing within a disordered crystalline network.

Depending on the electronic configuration of the paramagnetic centres, the NMR spectrum of a given system may be influenced not only by the hyperfine interaction between nuclear spins and unpaired electrons, but also by the effects of spin-orbit coupling at the transition metal sites. In such cases, in addition to the Fermi contact and dipolar interactions, the analysis of the NMR shift and shift anisotropy needs to include also the spin-orbit coupling contribution. This is investigated in Chapter 5, and applied to analyse the ^{7}Li and ^{31}P NMR spectra of $LiTMPO_4$ systems (TM = Mn, Fe, Co, Ni). For NMR-observed nuclei interacting with TM ions which have unquenched orbital angular momenta, the paramagnetic shielding tensor is defined by the coupling between the hyperfine $\boldsymbol{A}$ tensor and the spin-orbit $\boldsymbol{g}$-tensor. This coupling results in several contributions to both the shift and the shift anisotropy of observed site. Ideally, $\boldsymbol{A}$ and $\boldsymbol{g}$ are calculated from first principles and combined to obtain a breakdown of the various contributions to the NMR spectrum. However, solid-state DFT methods to calculate the g-tensor have been primarily developed to model isolated paramagnetic sites in diamagnetic host structures. This is not often representative of cathode materials, in which the paramagnetic species is a major constituent of the lattice. In Chapter 5, a method is developed to obtain site-specific g-tensors in paramagnetic solids, which uses the current DFT implementation of spin-orbit coupling calculations, and which exploits the symmetry operations defining the structure under investigation. The ability to calculate site-specific $\boldsymbol{A}$ and $\boldsymbol{g}$ tensors enables the fully decomposition of the shift and shift anisotropy into the various contributing terms. The derived method allows to rationalize the experimental spectra in light of the effects of spin-orbit coupling and electron-nuclear interactions in the systems under investigation. The model can be further extended to include also the effects of zero-field splitting, and hence be applied to a wider range of paramagnetic solids, such as systems including lanthanides or heavy metals.

Particularly important for single crystals and powder samples of complex crystallite shapes, the paramagnetic NMR shift and shift anisotropy may have, in addition to the contributions from hyperfine and spin-orbit interactons at the atomic level, also significant contributions from the bulk magnetic susceptibility effects. This is investigated in Chapter 6, which considers a solid-state ^{7}Li MAS NMR study of $LiFePO_4$ single crystals, combined with sample-specific BMS shift calculations. The BMS effects are modelled using classical electrostatics, simulating the solids by implementing the geometries of the paramagnetic single crystal samples, and the magnetic susceptibility tensors at the experimentally determined orientation with respect to the bulk. Depending on the anisotropy of the susceptibility tensor and on the anisotropy of the sample shape, the BMS shift can be significant, in some cases having a comparable or even greater contribution to the total shift than the Fermi contact term. The approach can be extended to the analysis of the BMS shift of paramagnetic powders with crystallites of different shapes.

References

[1] Bruce, P. G. *Solid state electrochemistry*, vol. 5 (Cambridge university press, 1997).

[2] Levitt, M. H. *Spin dynamics: basics of nuclear magnetic resonance* (John Wiley & Sons, 2001).

[3] Emsley, L. & Bertini, I. *Frontiers in solid-state NMR technology* (ACS Publications, 2013).

[4] Apperley, D. C., Harris, R. K. & Hodgkinson, P. *Solid-State NMR: Basic Principles and Practice* (Momentum Press, 2012).

[5] Ashbrook, S. E. & Sneddon, S. New methods and applications in solid-state NMR spectroscopy of quadrupolar nuclei. *Journal of the American Chemical Society* **136**, 15440–15456 (2014).

[6] Keeler, J. *Understanding NMR spectroscopy* (John Wiley & Sons, 2013).

[7] Duer, M. J. *Solid state NMR spectroscopy: principles and applications* (John Wiley & Sons, 2008).

[8] Pell, A. J., Pintacuda, G. & Grey, C. P. *Theory and Application of Paramagnetic NMR Spectroscopy* (In Review, 2017).

[9] Blanc, F., Copéret, C., Lesage, A. & Emsley, L. High resolution solid state NMR spectroscopy in surface organometallic chemistry: access to molecular understanding of active sites of well-defined heterogeneous catalysts. *Chemical Society Reviews* **37**, 518–526 (2008).

[10] Bertini, I., Luchinat, C., Parigi, G. & Pierattelli, R. Perspectives in paramagnetic NMR of metalloproteins. *Dalton Transactions* 3782–3790 (2008).

[11] Knight, M. J. *et al.* Structure and backbone dynamics of a microcrystalline metalloprotein by solid-state NMR. *Proceedings of the National Academy of Sciences* **109**, 11095–11100 (2012).

[12] Clément, R. J., Middlemiss, D. S., Seymour, I. D., Ilott, A. J. & Grey, C. P. Insights into the Nature and Evolution upon Electrochemical Cycling of Planar Defects in the β-NaMnO2 Na-Ion Battery Cathode: An NMR and First-Principles Density Functional Theory Approach. *Chemistry of Materials* **28**, 8228–8239 (2016).

[13] Seymour, I. *et al.* Characterizing oxygen local environments in paramagnetic battery materials via ^{17}O NMR and DFT calculations. *Journal of the American Chemical Society* **138**, 9405–9408 (2016).

[14] Carlier, D., Ménétrier, M., Grey, C. P., Delmas, C. & Ceder, G. Understanding the NMR shifts in paramagnetic transition metal oxides using density functional theory calculations. *Physcal Review B* **67**, 174103 (2003).

[15] McConnell, H. M. & Chesnut, D. B. Theory of Isotropic Hyperfine Interactions in π-Electron Radicals. *The Journal of Chemical Physics* **28**, 107–117 (1958).

[16] McConnell, H. M. & Robertson, R. E. Isotropic nuclear resonance shifts. *The Journal of Chemical Physics* **29**, 1361–1365 (1958).

[17] Kurland, R. J. & McGarvey, B. R. Isotropic NMR shifts in transition metal complexes: the calculation of the Fermi contact and pseudocontact terms. *Journal of Magnetic Resonance* **2**, 286–301 (1970).

[18] Kaupp, M. & Köhler, F. H. Combining NMR spectroscopy and quantum chemistry as tools to quantify spin density distributions in molecular magnetic compounds. *Coordination Chemistry Reviews* **253**, 2376–2386 (2009).

[19] Bleaney, B. Nuclear magnetic resonance shifts in solution due to lanthanide ions. *Journal of Magnetic Resonance (1969)* **8**, 91–100 (1972).

[20] Kaupp, M., Bühl, M. & Malkin, V. G. *Calculation of NMR and EPR parameters: theory and applications - Chapter 20 by S. Moon and S. Patchkovskii* (John Wiley & Sons, 2006).

[21] Pennanen, T. O. & Vaara, J. Nuclear magnetic resonance chemical shift in an arbitrary electronic spin state. *Physical review letters* **100**, 133002 (2008).

[22] Vaara, J., Rouf, S. A. & Mareŝ, J. Magnetic couplings in the chemical shift of paramagnetic NMR. *Journal of chemical theory and computation* **11**, 4840–4849 (2015).

[23] Van den Heuvel, W. & Soncini, A. NMR Chemical Shift in an Electronic State with Arbitrary Degeneracy. *Physical review letters* **109**, 073001 (2012).

[24] Soncini, A. & Van den Heuvel, W. Communication: Paramagnetic NMR chemical shift in a spin state subject to zero-field splitting. *The Journal of chemical physics* **138**, 021103 (2013).

[25] Van den Heuvel, W. & Soncini, A. NMR chemical shift as analytical derivative of the Helmholtz free energy. *The Journal of chemical physics* **138**, 054113 (2013).

[26] Kubo, A., Spaniol, T. P. & Terao, T. The effect of bulk magnetic susceptibility on solid state NMR spectra of paramagnetic compounds. *Journal of Magnetic Resonance* **133**, 330–340 (1998).

[27] Zhou, L., Leskes, M., Ilott, A. J., Trease, N. M. & Grey, C. P. Paramagnetic electrodes and bulk magnetic susceptibility effects in the in situ NMR studies of batteries: Application to $Li_{1.08}Mn_{1.92}O_4$ spinels. *Journal of Magnetic Resonance* **234**, 44–57 (2013).

[28] O'handley, R. C. *Modern magnetic materials: principles and applications* (Wiley, 2000).

[29] VanderHart, D., Earl, W. L. & Garroway, A. Resolution in ^{13}C NMR of organic solids using high-power proton decoupling and magic-angle sample spinning. *Journal of Magnetic Resonance (1969)* **44**, 361–401 (1981).

[30] Alla, M. & Lippmaa, E. Resolution limits in magic-angle rotation NMR spectra of polycrystalline solids. *Chemical Physics Letters* **87**, 30–33 (1982).

[31] Grey, C. P., Dobson, C. M. & Cheetham, A. K. Susceptibility matching in MAS NMR. The determination of hyperfine tensors from paramagnetic stannates. *Journal of Magnetic Resonance (1969)* **98**, 414–420 (1992).

[32] Schwerk, U., Michel, D. & Pruski, M. Local magnetic field distribution in a polycrystalline sample exposed to a strong magnetic field. *Journal of Magnetic Resonance, Series A* **119**, 157–164 (1996).

[33] Dickinson, R., Royappa, A. T., Tone, F., Ujj, L. & Wu, G. Distribution of non-uniform demagnetization fields in paramagnetic bulk solids. *Journal of Applied Physics* **110**, 013902 (2011).

[34] Whittingham, M. S. History, evolution, and future status of energy storage. *Proceedings of the IEEE* **100**, 1518–1534 (2012).

[35] Whittingham, M. S. Ultimate limits to intercalation reactions for lithium batteries. *Chemical reviews* **114**, 11414–11443 (2014).

[36] Goodenough, J. B. & Park, K.-S. The Li-ion rechargeable battery: a perspective. *Journal of the American Chemical Society* **135**, 1167–1176 (2013).

[37] Nagaura, T. & Tozawa, K. Lithium ion rechargeable battery. *Prog. Batteries Solar Cells* **9**, 209 (1990).

[38] Armstrong, A. R. & Bruce, P. G. Synthesis of layered $LiMnO_2$ as an electrode for rechargeable lithium batteries. *Nature* **381**, 499–500 (1996).

[39] Capitaine, F., Gravereau, P. & Delmas, C. A new variety of $LiMnO_2$ with a layered structure. *Solid State Ionics* **89**, 197–202 (1996).

[40] Ohzuku, T., Ueda, A. & Nagayama, M. Electrochemistry and structural chemistry of $LiNiO_2$ ($R3m$) for 4 volt secondary lithium cells. *Journal of the Electrochemical Society* **140**, 1862–1870 (1993).

[41] Dahn, J., Von Sacken, U., Juzkow, M. & Al-Janaby, H. Rechargeable $LiNiO_2$/carbon cells. *Journal of the Electrochemical Society* **138**, 2207–2211 (1991).

[42] Broussely, M. *et al.* Li_xNiO_2, a promising cathode for rechargeable lithium batteries. *Journal of Power Sources* **54**, 109–114 (1995).

[43] Thackeray, M., Johnson, P., De Picciotto, L., Bruce, P. & Goodenough, J. Electrochemical extraction of lithium from $LiMn_2O_4$. *Materials Research Bulletin* **19**, 179–187 (1984).

[44] Padhi, A. . K., Nanjundaswamy, K. & Goodenough, J. B. d. Phospho-olivines as positive-electrode materials for rechargeable lithium batteries. *Journal of the electrochemical society* **144**, 1188–1194 (1997).

[45] Delacourt, C. *et al.* Toward understanding of electrical limitations (electronic, ionic) in LiMPO4 (M= Fe, Mn) electrode materials. *Journal of the Electrochemical Society* **152**, A913–A921 (2005).

[46] Hautier, G. *et al.* Phosphates as lithium-ion battery cathodes: an evaluation based on high-throughput ab initio calculations. *Chemistry of Materials* **23**, 3495–3508 (2011).

[47] Pecher, O., Carretero-González, J., Griffith, K. J. & Grey, C. P. Materials' methods: NMR in battery research. *Chem. Mater* **29**, 213–242 (2017).

[48] Grey, C. P., & Dupré, N. NMR Studies of Cathode Materials for Lithium-Ion Rechargeable Batteries. *Chemical Reviews* **104**, 4493–4512 (2004).

[49] Grey, C. P. & Lee, Y. J. Lithium MAS NMR studies of cathode materials for lithium-ion batteries. *Solid State Sciences* **5**, 883–894 (2003).

[50] Lee, Y. J., Wang, F. & Grey, C. P. ^{6}Li and ^{7}Li MAS NMR studies of lithium manganate cathode materials. *Journal of the American Chemical Society* **120**, 12601–12613 (1998).

[51] Gee, B., Horne, C. R., Cairns, E. J. & Reimer, J. A. Supertransferred hyperfine fields at ^{7}Li: variable temperature ^{7}Li NMR studies of $LiMn_2O_4$-based spinels. *The Journal of Physical Chemistry B* **102**, 10142–10149 (1998).

[52] Morgan, K. R., Collier, S., Burns, G. & Ooi, K. A ^{6}Li and ^{7}Li MAS NMR study of the spinel-type manganese oxide $LiMn_2O_4$ and the rock salt-type manganese oxide Li_2MnO_3. *Journal of the Chemical Society, Chemical Communications* 1719–1720 (1994).

[53] Mustarelli, P., Massarotti, V., Bini, M. & Capsoni, D. Transferred hyperfine interaction and structure in $LiMn_2O_4$ and Li_2MnO_3 coexisting phases: mA XRD and ^{7}Li NMR-MAS study. *Physical Review B* **55**, 12018 (1997).

[54] Xia, Y. & Yoshio, M. Optimization of Spinel $Li_{1+x}Mn_{2-y}O_4$ as a 4 V Li-Cell Cathode in Terms of a Li-Mn-O Phase Diagram. *Journal of The Electrochemical Society* **144**, 4186–4194 (1997).

[55] Gao, Y. & Dahn, J. Synthesis and Characterization of $Li_{1+x}Mn_{2-x}O_4$ for Li-Ion Battery Applications. *Journal of The Electrochemical Society* **143**, 100–114 (1996).

[56] Thackeray, M. M. Manganese oxides for lithium batteries. *Progress in Solid State Chemistry* **25**, 1–71 (1997).

[57] Yamada, A. Lattice instability in $Li(Li_xMn_{2-x})O_4$. *Journal of Solid State Chemistry* **122**, 160–165 (1996).

[58] Tucker, M. C., Reimer, J. A. & Cairns, E. J. A ^{7}Li Nuclear Magnetic Resonance Study of Metal-Substituted Lithium Manganese Oxide Spinels. *Journal of the Electrochemical Society* **148**, A951–A959 (2001).

[59] Amatucci, G., Du Pasquier, A., Blyr, A., Zheng, T. & Tarascon, J.-M. The elevated temperature performance of the $LiMn_2O_4$/C system: failure and solutions. *Electrochimica Acta* **45**, 255–271 (1999).

[60] Lee, Y. J., Wang, F., Mukerjee, S., McBreen, J. & Grey, C. P. ^{6}Li and ^{7}Li Magic-Angle Spinning Nuclear Magnetic Resonance and In Situ X-Ray Diffraction Studies of the Charging and Discharging of $Li_xMn_2O_4$ at 4 V. *Journal of The Electrochemical Society* **147**, 803–812 (2000).

[61] Kim, J. *et al.* Linking Local Environments and Hyperfine Shifts: A Combined Experimental and Theoretical ^{31}P and ^{7}Li Solid-State NMR Study of Paramagnetic Fe(III) Phosphates. *Journal of the American Chemical Society* **132**, 16825–16840 (2010).

[62] Clément, R. J. *et al.* Spin-transfer pathways in paramagnetic lithium transition-metal phosphates from combined broadband isotropic solid-state MAS NMR spectroscopy and DFT calculations. *Journal of the American Chemical Society* **134**, 17178–17185 (2012).

[63] Middlemiss, D. S., Ilott, A. J., Clément, R. J., Strobridge, F. C. & Grey, C. P. Density functional theory-based bond pathway decompositions of hyperfine shifts: Equipping solid-state NMR to characterize atomic environments in paramagnetic materials. *Chemistry of Materials* **25**, 1723–1734 (2013).

[64] Strobridge, F. C. *et al.* Identifying the structure of the intermediate, $Li_{2/3}CoPO_4$, formed during electrochemical cycling of $LiCoPO_4$. *Chemistry of Materials* **26**, 6193–6205 (2014).

[65] Trease, N. M. *et al.* Identifying the Distribution of Al^{3+} in $LiNi_{0.8}Co_{0.15}Al_{0.05}O_2$. *Chemistry of Materials* **28**, 8170–8180 (2016).

[66] Lee, J., Seymour, I. D., Pell, A. J., Dutton, S. E. & Grey, C. P. A systematic study of ^{25}Mg NMR in paramagnetic transition metal oxides: applications to Mg-ion battery materials. *Physical Chemistry Chemical Physics* **19**, 613–625 (2017).

[67] Klett, M. *et al.* Quantifying mass transport during polarization in a Li Ion battery electrolyte by in situ ^{7}Li NMR imaging. *Journal of the American Chemical Society* **134**, 14654–14657 (2012).

[68] Trease, N. M., Zhou, L., Chang, H. J., Zhu, B. Y. & Grey, C. P. In situ NMR of lithium ion batteries: Bulk susceptibility effects and practical considerations. *Solid state nuclear magnetic resonance* **42**, 62–70 (2012).

[69] Zhou, L., Leskes, M., Liu, T. & Grey, C. P. Probing Dynamic Processes in Lithium-Ion Batteries by In Situ NMR Spectroscopy: Application to $Li_{1.08}Mn_{1.92}O_4$ Electrodes. *Angewandte Chemie International Edition* **54**, 14782–14786 (2015).

[70] Ashbrook, S. E. & McKay, D. Combining solid-state NMR spectroscopy with first-principles calculations–a guide to NMR crystallography. *Chemical Communications* **52**, 7186–7204 (2016).

[71] Harris, R. K. *et al.* Further Conventions for NMR Shielding and Chemical Shifts. *Magnetic Resonance in Chemistry* **46**, 582–598 (2008).

[72] Ramsey, N. F. Electron coupled interactions between nuclear spins in molecules. *Physical Review* **91**, 303 (1953).

[73] Atkins, P. W. & Friedman, R. *Molecular quantum mechanics* (Oxford university press, 2011).

[74] Bertini, I., Luchinat, C. & Parigi, G. *Solution NMR of paramagnetic molecules; application to metallobiomolecules and models* (Elsevier, London, 2001).

[75] Editorial Board. *Coordination Chemistry Reviews* **150** (1996).

[76] Blundell, S. *Magnetism in Condensed Matter - Oxford Master Series in Condensed Matter Physics* (Oxford University Press USA, 2001).

[77] Abragam, A. & Bleaney, B. *Electron paramagnetic resonance of transition ions* (Oxford University Press, 2012).

[78] Bertini, I., Luchinat, C. & Parigi, G. Magnetic susceptibility in paramagnetic NMR. *Progress in Nuclear Magnetic Resonance Spectroscopy* **40**, 249–273 (2002).

[79] Jackson, J. D. *Classical electrodynamics* (AAPT, 1999).

[80] Parr, R. & Yang, W. Density-Functional Theory of Atoms and Molecules Oxford Univ. *Press, New York* (1989).

[81] Sholl, D. & Steckel, J. A. *Density functional theory: a practical introduction* (John Wiley & Sons, 2011).

[82] Dreizler, R. M. & Gross, E. K. *Density Functional Theory: An Approach to the Quantum Many-Body Problem* (Springer, 1990).

[83] Hohenberg, P. & Kohn, W. Inhomogeneous electron gas. *Physical review* **136**, B864 (1964).

[84] Kohn, W. & Sham, L. J. Self-consistent equations including exchange and correlation effects. *Physical review* **140**, A1133 (1965).

[85] Vosko, S. H., Wilk, L. & Nusair, M. Accurate spin-dependent electron liquid correlation energies for local spin density calculations: a critical analysis. *Canadian Journal of physics* **58**, 1200–1211 (1980).

[86] Perdew, J. P. & Wang, Y. Accurate and simple analytic representation of the electron-gas correlation energy. *Physical Review B* **45**, 13244 (1992).

[87] Gunnarsson, O. & Lundqvist, B. I. Exchange and correlation in atoms, molecules, and solids by the spin-density-functional formalism. *Physical Review B* **13**, 4274 (1976).

[88] Perdew, J. P. & Yue, W. Accurate and simple density functional for the electronic exchange energy: Generalized gradient approximation. *Physical review B* **33**, 8800 (1986).

[89] Perdew, J. P., Burke, K. & Ernzerhof, M. Generalized gradient approximation made simple. *Physical review letters* **77**, 3865 (1996).

[90] Corà, F. *et al.* The performance of hybrid density functionals in solid state chemistry. In *Principles and Applications of Density Functional Theory in Inorganic Chemistry II*, 171–232 (Springer, 2004).

[91] Anisimov, V. I., Zaanen, J. & Andersen, O. K. Band theory and Mott insulators: Hubbard U instead of Stoner I. *Physical Review B* **44**, 943 (1991).

[92] Himmetoglu, B., Floris, A., Gironcoli, S. & Cococcioni, M. Hubbard-corrected DFT energy functionals: The LDA+ U description of correlated systems. *International Journal of Quantum Chemistry* **114**, 14–49 (2014).

[93] Cococcioni, M. *A LDA+ U study of selected iron compounds.* Ph.D. thesis (2002).

[94] Liechtenstein, A., Anisimov, V. & Zaanen, J. Density-functional theory and strong interactions: Orbital ordering in Mott-Hubbard insulators. *Physical Review B* **52**, R5467 (1995).

[95] Dudarev, S., Botton, G., Savrasov, S., Humphreys, C. & Sutton, A. Electron-energy-loss spectra and the structural stability of nickel oxide: An LSDA+U study. *Physical Review B* **57**, 1505 (1998).

[96] Becke, A. D. A new mixing of Hartree–Fock and local density-functional theories. *The Journal of chemical physics* **98**, 1372–1377 (1993).

[97] Stephens, P., Devlin, F., Chabalowski, C. & Frisch, M. J. Ab initio calculation of vibrational absorption and circular dichroism spectra using density functional force fields. *The Journal of Physical Chemistry* **98**, 11623–11627 (1994).

[98] Becke, A. D. Density-functional exchange-energy approximation with correct asymptotic behavior. *Physical review A* **38**, 3098 (1988).

[99] Lee, C., Yang, W. & Parr, R. G. Development of the Colle-Salvetti correlation-energy formula into a functional of the electron density. *Physical review B* **37**, 785 (1988).

[100] Middlemiss, D. S. & Wilson, C. C. Ferromagnetism and spin transitions in prussian blue: A solid-state hybrid functional study. *Physical Review B* **77**, 155129 (2008).

[101] Dovesi, R., Civalleri, B., Orlando, R., Roetti, C. & Saunders, V. R. Ab initio quantum simulation in solid state chemistry. *Reviews in computational chemistry* **21**, 1 (2005).

[102] Payne, M. C., Teter, M. P., Allan, D. C., Arias, T. & Joannopoulos, J. Iterative minimization techniques for ab initio total-energy calculations: molecular dynamics and conjugate gradients. *Reviews of modern physics* **64**, 1045 (1992).

[103] Kresse, G. & Joubert, D. From ultrasoft pseudopotentials to the projector augmented-wave method. *Physical Review B* **59**, 1758 (1999).

[104] Bush, I. *et al.* Parallel implementation of the ab initio CRYSTAL program: electronic structure calculations for periodic systems. In *Proceedings of the Royal Society of London A: Mathematical, Physical and Engineering Sciences*, vol. 467, 2112–2126 (The Royal Society, 2011).

[105] Tosoni, S., Tuma, C., Sauer, J., Civalleri, B. & Ugliengo, P. A comparison between plane wave and Gaussian-type orbital basis sets for hydrogen bonded systems: Formic acid as a test case. *The Journal of chemical physics* **127**, 154102 (2007).

[106] Ulian, G., Tosoni, S. & Valdrè, G. Comparison between Gaussian-type orbitals and plane wave ab initio density functional theory modeling of layer silicates: Talc $[Mg_3Si_4O_{10}(OH)_2]$ as model system. *The Journal of chemical physics* **139**, 204101 (2013).

[107] Seymour, I. D. *A Combined Experimental and Theoretical Investigation of the Local Structure of Lithium Manganese Oxide Cathode Materials for Lithium Ion Batteries*. Ph.D. thesis (2016).

[108] Dovesi, R. *et al. CRYSTAL09 User's Manual*, vol. Torino (Università di Torino, 2009).

[109] Bamine, T. *et al.* Understanding Local Defects in Li-Ion Battery Electrodes through Combined DFT/NMR Studies: Application to $LiVPO_4F$. *The Journal of Physical Chemistry C* **121**, 3219–3227 (2017).

[110] Van de Walle, C. G. & Blöchl, P. E. First-principles calculations of hyperfine parameters. *Physical Review B* **47**, 4244 (1993).

[111] Yates, J. R. & Pickard, C. J. Computations of magnetic resonance parameters for crystalline systems: principles. *eMagRes* (2008).

[112] Pickard, C. J. & Mauri, F. All-electron magnetic response with pseudopotentials: NMR chemical shifts. *Physical Review B* **63**, 245101 (2001).

[113] Pickard, C. J. & Mauri, F. First-principles theory of the EPR g-tensor in solids: Defects in quartz. *Physical review letters* **88**, 086403 (2002).

[114] Giannozzi, P. *et al.* QUANTUM ESPRESSO: a modular and open-source software project for quantum simulations of materials. *Journal of Physics: Condensed Matter* **21** (2009).

[115] Tarascon, J.-M. & Armand, M. Issues and challenges facing rechargeable lithium batteries. *Nature* **414**, 359–367 (2001).

[116] Armand, M. & Tarascon, J.-M. Building better batteries. *Nature* **451**, 652–657 (2008).

[117] Hensley, D., Milewits, M. & Zhang, W. The Evolution of Oilfield Batteries. *Oilfield Review* 42–57 (1998).

[118] Guidotti, R. A., Reinhardt, F. W. & Odinek, J. Overview of high-temperature batteries for geothermal and oil/gas borehole power sources. *Journal of power sources* **136**, 257–262 (2004).

[119] Murphy, D., Christian, P., DiSalvo, F. & Carides, J. Vanadium oxide cathode materials for secondary lithium cells. *Journal of The Electrochemical Society* **126**, 497–499 (1979).

[120] West, K., Zachau-Christiansen, B., Jacobsen, T. & Atlung, S. V_6O_{13} As cathode material for lithium cells. *Journal of Power sources* **14**, 235–245 (1985).

[121] Bruce, P. & Krok, F. Studies of the interface between V_6O_{13} and poly (ethylene oxide) based electrolytes. *Electrochimica acta* **33**, 1669–1674 (1988).

[122] Gustafsson, T., Thomas, J., Koksbang, R. & Farrington, G. The polymer battery as an environment for in situ X-ray diffraction studies of solid-state electrochemical processes. *Electrochimica acta* **37**, 1639–1643 (1992).

[123] Chernova, N. A., Roppolo, M., Dillon, A. C. & Whittingham, M. S. Layered vanadium and molybdenum oxides: batteries and electrochromics. *Journal of Materials Chemistry* **19**, 2526–2552 (2009).

[124] West, K., Zachau-Christiansen, B., Østergård, M. & Jacobsen, T. Vanadium oxides as electrode materials for rechargeable lithium cells. *Journal of Power Sources* **20**, 165–172 (1987).

[125] Macklin, W., Neat, R. & Sandhu, S. Structural changes in vanadium oxide-based cathodes during cycling in a lithium polymer electrolyte cell. *Electrochimica acta* **37**, 1715–1720 (1992).

[126] West, K., Zachau-Christiansen, B. & Jacobsen, T. Electrochemical properties of non-stoichiometric V_6O_{13}. *Electrochimica acta* **28**, 1829–1833 (1983).

[127] Murphy, D., Christian, P., DiSalvo, F., Carides, J. & Waszczak, J. Lithium incorporation by V 6 O 13 and related vanadium (+ 4,+ 5) oxide cathode materials. *Journal of The Electrochemical Society* **128**, 2053–2060 (1981).

[128] Tian, X. *et al.* Ultrathin pre-lithiated V 6 O 13 nanosheet cathodes with enhanced electrical transport and cyclability. *Journal of Power Sources* **255**, 235–241 (2014).

[129] Ding, Y.-L. *et al.* 3D V_6O_{13} nanotextiles assembled from interconnected nanogrooves as cathode materials for high-energy lithium ion batteries. *Nano letters* **15**, 1388–1394 (2015).

[130] Aebi, F. Phasenuntersuchungen im System Vanadin-Sauerstoff und die Krystallstruktur von $V_{12}O_{26}$. *Helvetica chimica acta* **31**, 8–21 (1948).

[131] Wilhelmi, K.-A. *et al.* A Refinement of the Crystal Structure of V_6O_{13}. *Acta Chem. Scand* **25**, 2675 (1971).

[132] Bergström, Ö., Gustafsson, T. & Thomas, J. O. Lithium insertion into V 6 O 13 studied by deformation electron density refinement of single-crystal X-ray data. *Solid State Ionics* **110**, 179–186 (1998).

[133] Chaklanabish, N. & Maiti, H. Phase stability and electrical conductivity of lithium intercalated nonstoichiometric V_6O_{13}. *Solid State Ionics* **21**, 207–212 (1986).

[134] Bergström, Ö., Gustafsson, T. & Thomas, J. O. Electrochemically Lithiated Vanadium Oxide, $Li_3V_6O_{13}$. *Acta Crystallographica Section C: Crystal Structure Communications* **54**, 1204–1206 (1998).

[135] Thackeray, M. M., Thomas, J. O. & Whittingham, M. S. Science and applications of mixed conductors for lithium batteries. *MRS bulletin* **25**, 39–46 (2000).

[136] Björk, H., Lidin, S., Gustafsson, T. & Thomas, J. O. Superlattice formation in the lithiated vanadium oxide phases $Li_{0.67}V_6O_{13}$ and LiV_6O_{13}. *Acta Crystallographica Section B: Structural Science* **57**, 759–765 (2001).

[137] Bergström, Ö., Gustafsson, T. & Thomas, J. Electrochemically Lithiated Vanadium Oxide, $Li_2V_6O_{13}$. *Acta Crystallographica Section C: Crystal Structure Communications* **53**, 528–530 (1997).

[138] Höwing, J., Gustafsson, T. & Thomas, J. O. $Li_{3+\delta}V_6O_{13}$: a short-range-ordered lithium insertion mechanism. *Acta Crystallographica Section B: Structural Science* **60**, 382–387 (2004).

[139] Braithwaite, J. S., Catlow, C. R. A., Harding, J. H. & Gale, J. D. A theoretical study of lithium intercalation into V 6 O 13—a combined classical, quantum mechanical approach. *Physical Chemistry Chemical Physics* **3**, 4052–4059 (2001).

[140] Schmitt, T. *et al.* Electronic structure studies of V 6 O 13 by soft x-ray emission spectroscopy: Band-like and excitonic vanadium states. *Physical Review B* **69**, 125103 (2004).

[141] Schmitt, T. *et al.* Electronic structure of Li-inserted V 6 O 13 battery cathodes: Rigid band behavior and effects of hybridization. *Applied Physics Letters* **86**, 064101 (2005).

[142] Meng, W. *et al.* Unraveling the Complex Delithiation and Lithiation Mechanisms of the High Capacity Cathode Material V_6O_{13}. *Chemistry of Materials* (2017).

[143] Liang, H.-P., Du, J., Jones, T. G., Lawrence, N. S. & Meredith, A. W. Large-Scale Production of V_6O_{13} Cathode Materials Assisted by Thermal Gravimetric Analysis–Infrared Spectroscopy Technology. *ACS applied materials & interfaces* **8**, 25674–25679 (2016).

[144] Toby, B. H. & Von Dreele, R. B. GSAS-II: the genesis of a modern open-source all purpose crystallography software package. *Journal of Applied Crystallography* **46**, 544–549 (2013).

[145] Thompson, P., Cox, D. & Hastings, J. Rietveld refinement of Debye–Scherrer synchrotron X-ray data from Al_2O_3. *Journal of Applied Crystallography* **20**, 79–83 (1987).

[146] Rietveld, H. A profile refinement method for nuclear and magnetic structures. *Journal of applied Crystallography* **2**, 65–71 (1969).

[147] Young, R. & Wiles, D. Profile shape functions in Rietveld refinements. *Journal of Applied Crystallography* **15**, 430–438 (1982).

[148] Pawley, G. Unit-cell refinement from powder diffraction scans. *Journal of Applied Crystallography* **14**, 357–361 (1981).

[149] Harris, R. K., Becker, E. D., Cabral de Menezes, S. M., Goodfellow, R. & Granger, P. NMR nomenclature: nuclear spin properties and conventions for chemical shifts. *Magnetic Resonance in Chemistry* **40**, 489–505 (2002).

[150] Kresse, G. & Furthmüller, J. Efficient iterative schemes for ab initio total-energy calculations using a plane-wave basis set. *Physical Review B* **54**, 11169 (1996).

[151] Blöchl, P. E. Projector augmented-wave method. *Physical Review B* **50**, 17953 (1994).

[152] Anisimov, V. I., Solovyev, I., Korotin, M., Czyżyk, M. & Sawatzky, G. Density-functional theory and NiO photoemission spectra. *Physical Review B* **48**, 16929 (1993).

[153] Toriyama, T., Nakayama, T., Konishi, T. & Ohta, Y. Charge and orbital orderings associated with metal-insulator transition in V 6 O 13. *Physical Review B* **90**, 085131 (2014).

[154] Van der Ven, A., Thomas, J. C., Xu, Q., Swoboda, B. & Morgan, D. Nondilute diffusion from first principles: Li diffusion in Li_xTiS_2. *Physical Review B* **78**, 104306 (2008).

[155] Van der Ven, A., Thomas, J., Xu, Q. & Bhattacharya, J. Linking the electronic structure of solids to their thermodynamic and kinetic properties. *Mathematics and Computers in Simulation* **80**, 1393–1410 (2010).

[156] Van der Ven, A., Thomas, J. C., Xu, Q., Swoboda, B. & Morgan, D. Nondilute diffusion from first principles: Li diffusion in Li_xTiS_2. *Physical Review B* **78**, 104306 (2008).

[157] Munro, L. J. & Wales, D. J. Defect migration in crystalline silicon. *Physical Review B* **59**, 3969 (1999).

[158] Kumeda, Y., Wales, D. J. & Munro, L. J. Transition states and rearrangement mechanisms from hybrid eigenvector-following and density functional theory: application to $C_{10}H_{10}$ and defect migration in crystalline silicon. *Chemical physics letters* **341**, 185–194 (2001).

[159] Chill, S. T. *et al.* Benchmarks for characterization of minima, transition states, and pathways in atomic, molecular, and condensed matter systems. *Journal of chemical theory and computation* **10**, 5476–5482 (2014).

[160] Zeng, Y., Xiao, P. & Henkelman, G. Unification of algorithms for minimum mode optimization. *The Journal of chemical physics* **140**, 044115 (2014).

[161] Dovesi, R. *et al.* CRYSTAL: a computational tool for the ab initio study of the electronic properties of crystals. *Zeitschrift für Kristallographie* **220**, 571–573 (2005).

[162] *CRYSTAL09 on-line basis set repository.*

[163] Mérawa, M., Labeguerie, P., Ugliengo, P., Doll, K. & Dovesi, R. The structural, electronic and vibrational properties of LiOH and NaOH: an ab initio study. *Chemical Physics Letters* **387**, 453–459 (2004).

[164] Gatti, C., Saunders, V. & Roetti, C. Crystal field effects on the topological properties of the electron density in molecular crystals: The case of urea. *The Journal of Chemical Physics* **101**, 10686–10696 (1994).

[165] Ruiz, E., Llunell, M. & Alemany, P. Calculation of exchange coupling constants in solid state transition metal compounds using localized atomic orbital basis sets. *Journal of Solid State Chemistry* **176**, 400–411 (2003).

[166] Kutzelnigg, W., Fleischer, U. & Schindler, M. The IGLO-Method: ab-initio calculation and interpretation of NMR chemical shifts and magnetic susceptibilities. In *Deuterium and shift calculation*, 165–262 (Springer, 1990).

[167] Schäfer, A., Horn, H. & Ahlrichs, R. Fully optimized contracted Gaussian basis sets for atoms Li to Kr. *The Journal of Chemical Physics* **97**, 2571–2577 (1992).

[168] Dolg, M., Wedig, U., Stoll, H. & Preuss, H. Energy-adjusted abinitio pseudopotentials for the first row transition elements. *The Journal of chemical physics* **86**, 866–872 (1987).

[169] Becke, A. D. Density-functional thermochemistry. III. The role of exact exchange. *The Journal of Chemical Physics* **98**, 5648–5652 (1993).

[170] Ueda, Y., Kosuge, K. & Kachi, S. Magneto-torque measurement on V_6O_{13}. *Materials Research Bulletin* **11**, 293–298 (1976).

[171] Adler, D. Mechanisms for metal-nonmental transitions in transition-metal oxides and sulfides. *Reviews of Modern Physics* **40**, 714 (1968).

[172] Kawashima, K., Ueda, Y., Kosuge, K. & Kachi, S. Crystal growth and some electric properties of V_6O_{13}. *Journal of Crystal Growth* **26**, 321–322 (1974).

[173] Dernier, P. Structural investigation of the metal-insulator transition in V_6O_{13}. *Materials Research Bulletin* **9**, 955–963 (1974).

[174] Ong, S. P. *et al.* Voltage, stability and diffusion barrier differences between sodium-ion and lithium-ion intercalation materials. *Energy & Environmental Science* **4**, 3680–3688 (2011).

[175] Thackeray, M., David, W., Bruce, P. & Goodenough, J. Lithium insertion into manganese spinels. *Materials Research Bulletin* **18**, 461–472 (1983).

[176] Tarascon, J. M., Wang, E., Shokoohi, F., McKinnon, W. & Colson, S. The Spinel Phase of $LiMn_2O_4$ as a Cathode in Secondary Lithium Cells. *Journal of the Electrochemical Society* **138**, 2859–2864 (1991).

[177] Hunter, J. C. Preparation of a new crystal form of manganese dioxide: λ-MnO_2. *Journal of Solid State Chemistry* **39**, 142–147 (1981).

[178] Chan, H., Duh, J. & Sheen, S. $LiMn_2O_4$ cathode doped with excess lithium and synthesized by co-precipitation for Li-ion batteries. *Journal of Power Sources* **115**, 110–118 (2003).

[179] Rossouw, M. *et al.* Structural aspects of lithium-manganese-oxide electrodes for rechargeable lithium batteries. *Materials Research Bulletin* **25**, 173–182 (1990).

[180] Gummow, R., De Kock, A. & Thackeray, M. Improved capacity retention in rechargeable 4 V lithium/lithium-manganese oxide (spinel) cells. *Solid State Ionics* **69**, 59–67 (1994).

[181] Zhong, Q., Bonakdarpour, A., Zhang, M., Gao, Y. & Dahn, J. Synthesis and Electrochemistry of $LiNi_xMn_{2-x}O_4$. *Journal of The Electrochemical Society* **144**, 205–213 (1997).

[182] Song, J. *et al.* Role of Oxygen Vacancies on the Performance of $Li[Ni_{0.5-x}Mn_{1.5+x}]O_4$ (x= 0, 0.05, and 0.08) Spinel Cathodes for Lithium-Ion Batteries. *Chemistry of Materials* **24**, 3101–3109 (2012).

[183] Wang, S. *et al.* Toward high capacity and stable manganese-spinel electrode materials: A case study of Ti-substituted system. *Journal of Power Sources* **245**, 570–578 (2014).

[184] Duncan, H., Hai, B., Leskes, M., Grey, C. P. & Chen, G. Relationships between Mn3+ Content, Structural Ordering, Phase Transformation, and Kinetic Properties in $LiNi_xMn_{2-x}O_4$ Cathode Materials. *Chemistry of Materials* **26**, 5374–5382 (2014).

[185] Krins, N. *et al.* $LiMn_{2-x}Ti_xO_4$ spinel-type compounds ($x \leq 1$): Structural, electrical and magnetic properties. *Solid State Ionics* **177**, 1033–1040 (2006).

[186] Petrov, K. *et al.* Cation distribution and phase transformations in $LiMn_{2-y}Ti_yO_4$ ($0.2 \leq y \leq 1.5$) solid solutions. *Solid state sciences* **7**, 277–286 (2005).

[187] Murphy, D. T., Schmid, S., Hester, J. R., Blanchard, P. E. & Miiller, W. Coordination Site Disorder in Spinel-Type LiMnTiO4. *Inorganic Chemistry* **54**, 4636–4643 (2015).

[188] Lee, Y. J., Park, S.-H., Eng, C., Parise, J. B. & Grey, C. P. Cation Ordering and Electrochemical Properties of the Cathode Materials $LiZn_xMn_{2-x}O_4$, $0 < x \leq 0.5$: A ^{6}Li Magic-Angle Spinning NMR Spectroscopy and Diffraction Study. *Chemistry of materials* **14**, 194–205 (2002).

[189] Lee, Y. J. & Grey, C. P. Determining the lithium local environments in the lithium manganates $LiZn_{0.5}Mn_{1.5}O_4$ and Li_2MnO_3 by analysis of the ^{6}Li MAS NMR spinning sideband manifolds. *The Journal of Physical Chemistry B* **106**, 3576–3582 (2002).

[190] Lee, Y. J., Eng, C. & Grey, C. P. ^{6}Li Magic Angle Spinning NMR Study of the Cathode Material $LiNi_xMn_{2-x}O_4$: The Effect of Ni Doping on the Local Structure during Charging. *Journal of The Electrochemical Society* **148**, A249–A257 (2001).

[191] Lee, Y. J. & Grey, C. P. ^{6}Li Magic Angle Spinning Nuclear Magnetic Resonance Study of the Cathode Materials $Li_{1+\alpha}Mn_{2-\alpha}O_{4-\delta}$ The Effect of Local Structure on the Electrochemical Properties. *Journal of The Electrochemical Society* **149**, A103–A114 (2002).

[192] Pell, A. J. & Pintacuda, G. Broadband solid-state MAS NMR of paramagnetic systems. *Progress in nuclear magnetic resonance spectroscopy* **84**, 33–72 (2015).

[193] Kervern, G., Pintacuda, G. & Emsley, L. Fast adiabatic pulses for solid-state NMR of paramagnetic systems. *Chemical Physics Letters* **435**, 157–162 (2007).

[194] Hwang, T.-L., van Zijl, P. C. & Garwood, M. Fast broadband inversion by adiabatic pulses. *Journal of Magnetic Resonance* **133**, 200–203 (1998).

[195] Massiot, D. *et al.* Modelling one-and two-dimensional solid-state NMR spectra. *Magnetic Resonance in Chemistry* **40**, 70–76 (2002).

[196] Grau-Crespo, R., Hamad, S., Catlow, C. & De Leeuw, N. Symmetry-adapted configurational modelling of fractional site occupancy in solids. *Journal of Physics: Condensed Matter* **19**, 256201 (2007).

[197] Wang, L., Maxisch, T. & Ceder, G. Oxidation energies of transition metal oxides within the GGA+U framework. *Physical Review B* **73**, 195107 (2006).

[198] Masquelier, C. *et al.* Chemical and Magnetic Characterization of Spinel Materials in the $LiMn_2O_4$ - $Li_2Mn_4O_9$ - $Li_4Mn_5O_{12}$ System. *Journal of Solid State Chemistry* **123**, 255–266 (1996).

[199] Pell, A. J. *et al.* Broadband inversion for MAS NMR with single-sideband-selective adiabatic pulses. *The Journal of Chemical Physics* **134**, 024117 (2011).

[200] Bhattacharya, J. & Van der Ven, A. Phase stability and nondilute Li diffusion in spinel $Li_{1+x}Ti_2O_4$. *Physical Review B* **81**, 104304 (2010).

[201] Harris, K. J. *et al.* Structure Solution of Metal-Oxide Li Battery Cathodes from Simulated Annealing and Lithium NMR Spectroscopy. *Chemistry of Materials* **29**, 5550–5557 (2017).

[202] Hrobárik, P. *et al.* Density functional calculations of NMR shielding tensors for paramagnetic systems with arbitrary spin multiplicity: Validation on 3d metallocenes. *The Journal of chemical physics* **126**, 024107 (2007).

[203] Martin, B. & Autschbach, J. Temperature dependence of contact and dipolar NMR chemical shifts in paramagnetic molecules. *The Journal of chemical physics* **142**, 054108 (2015).

[204] Liimatainen, H., Pennanen, T. O. & Vaara, J. ^{1}H chemical shifts in nonaxial, paramagnetic chromium (III) complexes-Application of novel pNMR shift theory 1. *Canadian Journal of Chemistry* **87**, 954–964 (2009).

[205] Mali, G., Sirisopanaporn, C., Masquelier, C., Hanzel, D. & Dominko, R. Li_2FeSiO_4 polymorphs probed by ^{6}Li MAS NMR and ^{57}Fe Mossbauer spectroscopy. *Chemistry of Materials* **23**, 2735–2744 (2011).

[206] Whittingham, M. S. Ultimate limits to intercalation reactions for lithium batteries. *Chemical reviews* **114**, 11414–11443 (2014).

[207] Tucker, M. C. *et al.* Hyperfine Fields at the Li Site in $LiFePO_4$-Type Olivine Materials for Lithium Rechargeable Batteries: A ^{7}Li MAS NMR and SQUID Study. *Journal of the American Chemical Society* **124**, 3832–3833 (2002).

[208] Wilcke, S., Lee, Y.-J., Cairns, E. & Reimer, J. Covalency measurements via NMR in lithium metal phosphates. *Applied Magnetic Resonance* **32**, 547–563 (2007).

[209] Pigliapochi, R. *et al.* DFT investigation of the effect of spin-orbit coupling on the NMR shifts in paramagnetic solids. *Physical Review B* **95**, 054412 (2017).

[210] Chazel, C., Ménétrier, M., Croguennec, L. & Delmas, C. $^{6/7}$Li NMR study of the $Li_{1-z}Ni_{1+z}O_2$ phases. *Magnetic Resonance in Chemistry* **43**, 849–857 (2005).

[211] Aroyo, M. I. *et al.* Bilbao Crystallographic Server: I. Databases and crystallographic computing programs. *Zeitschrift für Kristallographie* **221**, 15–27 (2006).

[212] Aroyo, M. I., Kirov, A., Capillas, C., Perez-Mato, J. & Wondratschek, H. Bilbao Crystallographic Server. II. Representations of crystallographic point groups and space groups. *Acta Crystallographica Section A: Foundations of Crystallography* **62**, 115–128 (2006).

[213] Aroyo, M. *et al.* Crystallography online: Bilbao crystallographic server. *Bulg. Chem. Commun* **43**, 183–97 (2011).

[214] Mobbs, F. & Collison, D. *Electron Paramagnetic Resonance of d Transition Metal Compounds, Vol. 16* (Elsevier, Amsterdam, 1992).

[215] Harriman, J. E. *Theoretical Foundations of Electron Spin Resonance* (Academic Press INC., 1978).

[216] Powell, R. C. *Symmetry, Group Theory, and the Physical Properties of Crystals* (Springer, 2010).

[217] Remenyi, C., Reviakine, R., Arbuznikov, A. V., Vaara, J. & Kaupp, M. Spin-orbit effects on hyperfine coupling tensors in transition metal complexes using hybrid density functionals and accurate spin-orbit operators. *The Journal of Physical Chemistry A* **108**, 5026–5033 (2004).

[218] Remenyi, C., Reviakine, R. & Kaupp, M. Density functional study of EPR parameters and spin-density distribution of azurin and other blue copper proteins. *The Journal of Physical Chemistry B* **111**, 8290–8304 (2007).

[219] Adamo, C. & Barone, V. Toward reliable density functional methods without adjustable parameters: The PBE0 model. *The Journal of chemical physics* **110**, 6158–6170 (1999).

[220] Munzarová, M. & Kaupp, M. A critical validation of density functional and coupled-cluster approaches for the calculation of EPR hyperfine coupling constants in transition metal complexes. *The Journal of Physical Chemistry A* **103**, 9966–9983 (1999).

[221] Kaupp, M. *et al.* Calculation of electronic g-tensors for transition metal complexes using hybrid density functionals and atomic meanfield spin-orbit operators. *Journal of computational chemistry* **23**, 794–803 (2002).

[222] Verma, P. & Truhlar, D. G. Does DFT+U mimic hybrid density functionals? *Theoretical Chemistry Accounts* **135**, 1–15 (2016).

[223] Zhou, F., Cococcioni, M., Marianetti, C. A., Morgan, D. & Ceder, G. First-principles prediction of redox potentials in transition-metal compounds with LDA+ U. *Physical Review B* **70**, 235121 (2004).

[224] Zhou, F., Cococcioni, M., Kang, K. & Ceder, G. The Li intercalation potential of $LiMPO_4$ and $LiMSiO_4$ olivines with M = Fe, Mn, Co, Ni. *Electrochemistry communications* **6**, 1144–1148 (2004).

[225] Xiang, H., Lee, C., Koo, H.-J., Gong, X. & Whangbo, M.-H. Magnetic properties and energy-mapping analysis. *Dalton Transactions* **42**, 823–853 (2013).

[226] Garcia-Moreno, O. *et al.* Influence of the structure on the electrochemical performance of lithium transition metal phosphates as cathodic materials in rechargeable lithium batteries: a new high-pressure form of $LiMPO_4$ (M= Fe and Ni). *Chemistry of materials* **13**, 1570–1576 (2001).

[227] Rousse, G., Rodriguez-Carvajal, J., Patoux, S. & Masquelier, C. Magnetic structures of the triphylite $LiFePO_4$ and of its delithiated form $FePO_4$. *Chemistry of materials* **15**, 4082–4090 (2003).

[228] Kubel, F. Crystal structure of lithium cobalt double orthophosphate, $LiCoPO_4$. *Zeitschrift fur Kristallographie - New Crystal Structures* **209**, 755 (1994).

[229] Enciso-Maldonado, L. *et al.* Computational Identification and Experimental Realization of Lithium Vacancy Introduction into the Olivine $LiMgPO_4$. *Chemistry of Materials* **27**, 2074–2091 (2015).

[230] Koleva, V., Zhecheva, E. & Stoyanova, R. Facile synthesis of $LiMnPO_4$ olivines with a plate-like morphology from a dittmarite-type $KMnPO_4 \times H_2O$ precursor. *Dalton Transactions* **40**, 7385–7394 (2011).

[231] Wizent, N. *et al.* Single-crystal growth of $LiMnPO_4$ by the floating-zone method. *Journal of Crystal Growth* **311**, 1273–1277 (2009).

[232] Singh, V. *et al.* Magnetism in olivine-type $LiCo_{1-x}Fe_xPO_4$ cathode materials: bridging theory and experiment. *Physical Chemistry Chemical Physics* **17**, 31202–31215 (2015).

[233] Liang, G. *et al.* Anisotropy in magnetic properties and electronic structure of single-crystal $LiFePO_4$. *Physical Review B* **77**, 064414 (2008).

[234] Vaknin, D., Zarestky, J., Miller, L., Rivera, J.-P. & Schmid, H. Weakly coupled antiferromagnetic planes in single-crystal $LiCoPO_4$. *Physical Review B* **65**, 224414 (2002).

[235] Baek, S.-H. *et al.* Unusual spin fluctuations and magnetic frustration in olivine and non-olivine $LiCoPO_4$ detected by ^{31}P and ^{7}Li nuclear magnetic resonance. *Physical Review B* **89**, 134424 (2014).

[236] Goni, A. *et al.* Magnetic properties of the $LiMPO_4$ (M= Co, Ni) compounds. *Journal of magnetism and magnetic materials* **164**, 251–255 (1996).

[237] Boča, R. Zero-field splitting in metal complexes. *Coordination chemistry reviews* **248**, 757–815 (2004).

[238] Jiang, H., Gomez-Abal, R. I., Rinke, P. & Scheffler, M. First-principles modeling of localized d states with the GW LDA+ U approach. *Physical Review B* **82**, 045108 (2010).

[239] Castets, A. *et al.* Multinuclear NMR and DFT calculations on the $LiFePO_4 \times OH$ and $FePO_4 \times H_2$ O homeotypic phases. *The Journal of Physical Chemistry C* **115**, 16234–16241 (2011).

[240] Zhou, F., Kang, K., Maxisch, T., Ceder, G. & Morgan, D. The electronic structure and band gap of $LiFePO_4$ and $LiMnPO_4$. *Solid State Communications* **132**, 181–186 (2004).

[241] Forti, M., Alonso, P., Gargano, P. & Rubiolo, G. Transition metals monoxides. An LDA+U study. *Procedia Materials Science* **1**, 230–234 (2012).

[242] Jena, A. & Nanda, B. Unconventional Magnetism and Band Gap Formation in $LiFePO_4$: Consequence of Polyanion Induced Non-planarity. *Scientific reports* **6** (2016).

[243] Le Bacq, O., Pasturel, A. & Bengone, O. Impact on electronic correlations on the structural stability, magnetism, and voltage of $LiCoPO_4$ battery. *Physical Review B* **69**, 245107 (2004).

[244] Drain, L. The broadening of magnetic resonance lines due to field inhomogeneities in powdered samples. *Proceedings of the Physical Society* **80**, 1380 (1962).

[245] Cabana, J., Shirakawa, J., Chen, G., Richardson, T. J. & Grey, C. P. MAS NMR study of the metastable solid solutions found in the LiFePO4/FePO4 system. *Chemistry of Materials* **22**, 1249–1262 (2010).

[246] Strobridge, F. C. *et al.* Characterising local environments in high energy density Li-ion battery cathodes: a combined NMR and first principles study of $LiFe_xCo_{1-x}PO_4$. *Journal of Materials Chemistry A* **2**, 11948–11957 (2014).

[247] Janssen, Y. *et al.* Reciprocal salt flux growth of $LiFePO_4$ single crystals with controlled defect concentrations. *Chemistry of Materials* **25**, 4574–4584 (2013).

[248] Coelho, A. A. TOPAS V2.0: General Profile and Structure Analysis Software for Powder Diffraction Data. *Bruker AXS: Karlsruhe, Germany* (2000).

[249] Nytén, A. & Thomas, J. O. A neutron powder diffraction study of $LiCo_xFe_{1-x}PO_4$ for x= 0, 0.25, 0.40, 0.60 and 0.75. *Solid State Ionics* **177**, 1327–1330 (2006).

[250] Balzar, D. *et al.* Size–strain line-broadening analysis of the ceria round-robin sample. *Journal of Applied Crystallography* **37**, 911–924 (2004).

[251] Balzar, D. Voigt-function model in diffraction line-broadening analysis. *International union of crystallography monographs on crystallography* **10**, 94–126 (1999).

[252] Levitt, M. H. Why do spinning sidebands have the same phase? *Journal of Magnetic Resonance (1969)* **82**, 427–433 (1989).

[253] Pell, A. J., Clément, R. J., Grey, C. P., Emsley, L. & Pintacuda, G. Frequency-stepped acquisition in nuclear magnetic resonance spectroscopy under magic angle spinning. *The Journal of chemical physics* **138**, 114201 (2013).

[254] Donahue, M. J. & Porter, D. G. *OOMMF User's Guide, Version 1.0*, vol. Interagency Report NISTIR 6376 (National Institute of Standards and Technology, Gaithersburg, MD, 1999).

[255] Chen, D. *et al.* Magnetic anisotropy in doped and undoped $LiFePO_4$ single crystals. *Journal of applied physics* **101**, 09N512 (2007).

Appendix A

A1 Details of g-shift Calculations performed with GGA

Calculated $\boldsymbol{\Delta g}$ tensors for $LiFePO_4$, $LiCoPO_4$ and $LiNiPO_4$: the results are presented as the TM site-specific $\boldsymbol{\Delta g}$ tensors for sites labelled as I and II and the total unit-cell $\boldsymbol{\Delta g}$ tensor, following the labelling scheme of Figure 5.1.

$$\boldsymbol{\Delta g}_{\mathrm{I}}^{\mathrm{Fe}} = \begin{pmatrix} 0.168 & -0.004 & -0.003 \\ -0.004 & 0.229 & 0.003 \\ -0.004 & 0.003 & 0.098 \end{pmatrix}$$

$$\boldsymbol{\Delta g}_{\mathrm{II}}^{\mathrm{Fe}} = \begin{pmatrix} 0.168 & 0.004 & 0.003 \\ 0.004 & 0.229 & 0.003 \\ 0.004 & 0.003 & 0.098 \end{pmatrix}$$

$$\boldsymbol{\Delta g}_{\mathrm{u.c.}}^{\mathrm{Fe}} = \begin{pmatrix} 0.671 & 0 & 0 \\ 0 & 0.916 & 0 \\ 0 & 0 & 0.392 \end{pmatrix}$$

$$\boldsymbol{\Delta g}_{\mathrm{I}}^{\mathrm{Co}} = \begin{pmatrix} 0.254 & 0 & -0.010 \\ 0 & 0.398 & 0 \\ -0.010 & 0 & 0.385 \end{pmatrix}$$

$$\boldsymbol{\Delta g}_{\mathrm{II}}^{\mathrm{Co}} = \begin{pmatrix} 0.254 & 0 & 0.010 \\ 0 & 0.398 & 0 \\ 0.010 & 0 & 0.385 \end{pmatrix}$$

$$\boldsymbol{\Delta g}_{\mathrm{u.c.}}^{\mathrm{Co}} = \begin{pmatrix} 1.020 & 0 & 0 \\ 0 & 1.593 & 0 \\ 0 & 0 & 1.539 \end{pmatrix}$$

$$\boldsymbol{\Delta g}_{\mathrm{I}}^{\mathrm{Ni}} = \begin{pmatrix} 0.250 & 0 & 0 \\ 0 & 0.228 & 0 \\ 0 & 0 & 0.251 \end{pmatrix}$$

$$\boldsymbol{\Delta g}_{\mathrm{II}}^{\mathrm{Ni}} = \begin{pmatrix} 0.250 & 0 & 0 \\ 0 & 0.225 & 0 \\ 0 & 0 & 0.251 \end{pmatrix}$$

$$\boldsymbol{\Delta g}_{\mathrm{u.c.}}^{\mathrm{Ni}} = \begin{pmatrix} 1.000 & 0 & 0 \\ 0 & 0.912 & 0 \\ 0 & 0 & 1.004 \end{pmatrix}$$

A2 Details of g-shift Calculations performed with GGA+U

Calculated $\boldsymbol{\Delta g}$ tensors for $LiFePO_4$, $LiCoPO_4$ and $LiNiPO_4$: the results are presented as the TM site-specific $\boldsymbol{\Delta g}$ tensors for sites labelled as I and II and the total unit-cell $\boldsymbol{\Delta g}$ tensor, following the labelling scheme of Fig. 1 of the main paper.

$$\boldsymbol{\Delta g}_{\mathrm{I}}^{\mathrm{Fe}} = \begin{pmatrix} 0.058 & -0.002 & -0.002 \\ -0.002 & 0.111 & 0.003 \\ -0.002 & 0.004 & 0.003 \end{pmatrix}$$

$$\boldsymbol{\Delta g}_{\mathrm{II}}^{\mathrm{Fe}} = \begin{pmatrix} 0.058 & 0.002 & 0.003 \\ 0.002 & 0.111 & 0.003 \\ 0.002 & 0.004 & 0.003 \end{pmatrix}$$

$$\boldsymbol{\Delta g}_{\mathrm{u.c.}}^{\mathrm{Fe}} = \begin{pmatrix} 0.232 & 0 & 0 \\ 0 & 0.433 & 0 \\ 0 & 0 & 0.130 \end{pmatrix}$$

$$\boldsymbol{\Delta g}_{\mathrm{I}}^{\mathrm{Co}} = \begin{pmatrix} 0.147 & 0 & -0.014 \\ 0 & 0.113 & 0 \\ -0.015 & 0 & 0.131 \end{pmatrix}$$

$$\boldsymbol{\Delta g}_{\mathrm{II}}^{\mathrm{Co}} = \begin{pmatrix} 0.147 & 0 & 0.014 \\ 0 & 0.113 & 0 \\ 0.015 & 0 & 0.131 \end{pmatrix}$$

$$\boldsymbol{\Delta g}_{\mathrm{u.c.}}^{\mathrm{Co}} = \begin{pmatrix} 0.583 & 0 & 0 \\ 0 & 0.449 & 0 \\ 0 & 0 & 0.521 \end{pmatrix}$$

$$\boldsymbol{\Delta g}_{\mathrm{I}}^{\mathrm{Ni}} = \begin{pmatrix} 0.137 & 0 & 0 \\ 0 & 0.126 & 0 \\ 0 & 0 & 0.139 \end{pmatrix}$$

$$\boldsymbol{\Delta g}_{\mathrm{II}}^{\mathrm{Ni}} = \begin{pmatrix} 0.137 & 0 & 0 \\ 0 & 0.126 & 0 \\ 0 & 0 & 0.139 \end{pmatrix}$$

$$\boldsymbol{\Delta g}_{\mathrm{u.c.}}^{\mathrm{Ni}} = \begin{pmatrix} 0.501 & 0 & 0 \\ 0 & 0.470 & 0 \\ 0 & 0 & 0.516 \end{pmatrix}$$

A3 Details of paramagnetic shielding Calculations performed with GGA/GGA+U and PBE0/PBE20/PBE35

		CONTACT TERMS									DIPOLAR TERMS									ISOTROPIC TERM	
		a) $g_e A^{FC}$			c) $\Delta g_{iso} A^{FC}$			d) $A^{FC}\Delta\tilde{g}$			e) $g_e \boldsymbol{A}^{dip}$			g) $\Delta g_{iso} \boldsymbol{A}^{dip}$			h) $\Delta\tilde{g}\boldsymbol{A}^{dip}$			DFT	EXP
		δ_{iso} [ppm]	$\Delta\delta$ [ppm]	η	δ_{iso} [ppm]	$\Delta\delta$ [ppm]	η	δ_{iso} [ppm]	$\Delta\delta$ [ppm]	η	δ_{iso} [ppm]	$\Delta\delta$ [ppm]	η	δ_{iso} [ppm]	$\Delta\delta$ [ppm]	η	δ_{iso} [ppm]	$\Delta\delta$ [ppm]	η	δ_{iso} [ppm]	δ_{iso} [ppm]
^{7}Li	$LiMnPO_4$	109.9	0	—	0.3	0	—	0	0.1	0.3	0	1234.2	0.2	0	0.9	0.2	-0.1	0.2	0.4	110.1	57[a], 68[b]
	$LiFePO_4$	27.2	0	—	3.7	0	—	0	2.4	0.6	0	881.0	0.2	0	29.7	0.2	-3.3	9.0	0.7	27.6	-15[a], -8[b]
	$LiCoPO_4$	-19.6	0	—	-5.1	0	—	0	0.7	0.9	0	700.3	0.2	0	45.7	0.2	2.6	-5.5	0.1	-22.1	-92[a], -86[b]
	$LiNiPO_4$	-64.8	0	—	-17.4	0	—	0	1.1	0.4	0	433.8	0.2	0	29.1	0.2	0.3	-0.7	0.1	-81.9	-49[b], -41[a]
^{31}P	$LiMnPO_4$	8397.3	0	—	25.3	0	—	0	11.3	0.3	0	795.9	0.5	0	-1.2	0.5	-0.1	0.2	0.3	8404.5	7296[a]
	$LiFePO_4$	3219.0	0	—	434.1	0	—	0	282.3	0.6	0	795.4	0.4	0	26.8	0.4	-2.3	7.9	0.3	3650.8	3352[a]
	$LiCoPO_4$	2012.6	0	—	524.8	0	—	0	-70.3	0.9	0	652.6	0.4	0	42.5	0.4	-0.7	2.6	0.6	2536.7	2756[a]
	$LiNiPO_4$	1658.7	0	—	444.8	0	—	0	-27.1	0.4	0	576.1	0.1	0	38.7	0.1	0.5	-1.1	0.1	2104.0	1706[a]

Table A1 Comparison of the various terms contributing to the shielding tensor for the series of $LiTMPO_4$ compounds (TM= Mn, Fe, Co, Ni) at the ^{7}Li and ^{31}P sites broken down into the contact and dipolar isotropic shift (δ_{iso}, ppm), symmetric anisotropic value ($\Delta\delta$, ppm) and asymmetry parameter (η, dimensionless). The hyperfine tensor for this Table is obtained with the PBE0 hybrid functional and the g-tensor is calculated with pure GGA+U. Every tensorial term of the Table is reported oriented with respect to its own principal axis frame. All the reported terms are scaled by the pre-factor $-\frac{\mu_B S(S+1)}{3\hbar\gamma_N K_B(T-\Theta)}$, with the respective Weiss constant of the system. The last column compares the sum of the calculated isotropic terms (a, c, h) with the experimental isotropic shift. [a] Ref. [208]. [b] Ref. [207].

		CONTACT TERMS								DIPOLAR TERMS						ISOTROPIC TERM	
		a) $g_e A^{FC}$			c) $\Delta g_{iso} A^{FC}$			d) $A^{FC} \Delta \tilde{g}$		e) $g_e \boldsymbol{A}^{dip}$			g) $\Delta g_{iso} \boldsymbol{A}^{dip}$			h) $\Delta \tilde{g} \boldsymbol{A}^{dip}$			DFT	EXP
		δ_{iso} [ppm]	$\Delta\delta$ [ppm]	η	δ_{iso} [ppm]	$\Delta\delta$ [ppm]	η	δ_{iso} [ppm]	$\Delta\delta$ [ppm]	η	δ_{iso} [ppm]	$\Delta\delta$ [ppm]	η	δ_{iso} [ppm]	$\Delta\delta$ [ppm]	η	δ_{iso} [ppm]	$\Delta\delta$ [ppm]	η	δ_{iso} [ppm]	δ_{iso} [ppm]
^{7}Li	$LiMnPO_4$	123.9	0	—	0.4	0	—	0	0.2	0.3	0	1230.6	0.2	0	0.9	0.2	-0.1	0.2	0.4	124.2	57^a, 68^b
	$LiFePO_4$	36.4	0	—	4.9	0	—	0	3.2	0.6	0	869.6	0.2	0	29.3	0.2	-3.3	-8.9	0.7	38.0	-15^a, -8^b
	$LiCoPO_4$	-15.2	0	—	-4.0	0	—	0	0.5	0.9	0	695.7	0.2	0	45.4	0.2	2.5	-5.4	0.1	-16.7	-92^a, -86^b
	$LiNiPO_4$	-64.6	0	—	-17.3	0	—	0	1.1	0.4	0	434.7	0.2	0	29.2	0.2	0.3	-0.7	0.6	-81.6	-49^b, -41^a
^{31}P	$LiMnPO_4$	8877.7	0	—	26.8	0	—	0	12.0	0.3	0	1118.8	0.3	0	0.8	0.3	0	-0.1	0.7	8907.5	7296^a
	$LiFePO_4$	3419.3	0	—	461.1	0	—	0	299.8	0.6	0	821.9	0.5	0	27.7	0.5	-2.2	18.1	0.4	3878.2	3352^a
	$LiCoPO_4$	2132.7	0	—	556.1	0	—	0	-74.5	0.9	0	662.7	0.4	0	43.2	0.4	-0.8	2.6	0.4	2688.0	2756^a
	$LiNiPO_4$	1821.9	0	—	489.1	0	—	0	-29.8	0.0	0	595.8	0.1	0	40.0	0.1	0.5	-1.1	0.1	2311.5	1706^a

Table A2 Comparison of the various terms contributing to the shielding tensor for the series of $LiTMPO_4$ compounds (TM= Mn, Fe, Co, Ni) at the ^{7}Li and ^{31}P sites broken down into the contact and dipolar isotropic shift (δ_{iso}, ppm), symmetric anisotropic value ($\Delta\delta$, ppm) and asymmetry parameter (η, dimensionless). The hyperfine tensor for this Table is obtained with the PBE20 hybrid functional and the g-tensor is calculated with GGA. Every tensorial term of the Table is reported oriented with respect to its own principal axis frame. All the reported terms are scaled by the pre-factor $-\frac{\mu_B S(S+1)}{3\hbar\gamma_N K_B (T-\Theta)}$, with the respective Weiss constant of the system. The last column compares the sum of the calculated isotropic terms (a, c, h) with the experimental isotropic shift. [a] Ref. [208]. [b] Ref. [207].

		CONTACT TERMS									DIPOLAR TERMS									ISOTROPIC TERM	
		a) $g_e A^{FC}$			c) $\Delta g_{iso} A^{FC}$			d) $A^{FC} \Delta \tilde{g}$			e) $g_e \boldsymbol{A}^{dip}$			g) $\Delta g_{iso} \boldsymbol{A}^{dip}$			h) $\Delta \tilde{g} \boldsymbol{A}^{dip}$			DFT	EXP
		δ_{iso} [ppm]	$\Delta\delta$ [ppm]	η	δ_{iso} [ppm]	$\Delta\delta$ [ppm]	η	δ_{iso} [ppm]	$\Delta\delta$ [ppm]	η	δ_{iso} [ppm]	$\Delta\delta$ [ppm]	η	δ_{iso} [ppm]	$\Delta\delta$ [ppm]	η	δ_{iso} [ppm]	$\Delta\delta$ [ppm]	η	δ_{iso} [ppm]	δ_{iso} [ppm]
^{7}Li	$LiMnPO_4$	84.8	0	—	0.3	0	—	0	10.1	0.3	0	1240.1	0.2	0	-1.1	0.5	-0.1	0.2	0.3	84.6	57[a], 68[b]
	$LiFePO_4$	10.6	0	—	5.2	0	—	0	-1.2	0.6	0	886.6	0.2	0	69.3	0.2	-0.9	-14.7	0.7	14.9	-15[a], -8[b]
	$LiCoPO_4$	-25.9	0	—	-10.7	0	—	0	3.4	0.9	0	709.3	0.2	0	64.2	0.2	-11.7	-10.2	0.1	-48.3	-92[a], -86[b]
	$LiNiPO_4$	-64.7	0	—	-23.1	0	—	0	1.7	0.4	0	443.8	0.2	0	48.9	0.1	-0.1	-0.9	0.6	-81.8	-49[b], -41[a]
^{31}P	$LiMnPO_4$	7515.8	0	—	22.7	0	—	0	10.1	0.3	0	1099.3	0.2	0	0.8	0.2	-0.1	-0.1	0.8	7538.4	7296[a]
	$LiFePO_4$	2806.1	0	—	726.4	0	—	0	-310.8	0.6	0	781.9	0.4	0	47.2	0.4	-1.9	10.2	0.2	3530.6	3352[a]
	$LiCoPO_4$	1784.8	0	—	1009.1	0	—	0	-294.9	0.9	0	636.4	0.3	0	80.3	0.3	-2.4	7.3	0.8	2791.5	2756[a]
	$LiNiPO_4$	1235.0	0	—	675.3	0	—	0	-32.4	0.4	0	539.5	0.1	0	50.9	0.1	0.9	-1.7	0.2	1911.2	1706[a]

Table A3 Comparison of the various terms contributing to the shielding tensor for the series of $LiTMPO_4$ compounds (TM= Mn, Fe, Co, Ni) at the ^{7}Li and ^{31}P sites broken down into the contact and dipolar isotropic shift (δ_{iso}, ppm), symmetric anisotropic value ($\Delta\delta$, ppm) and asymmetry parameter (η, dimensionless). The hyperfine tensor for this Table is obtained with the PBE35 hybrid functional and the g-tensor is calculated with GGA. Every tensorial term of the Table is reported oriented with respect to its own principal axis frame. All the reported terms are scaled by the pre-factor $-\frac{\mu_B S(S+1)}{3\hbar\gamma_N K_B(T-\Theta)}$, with the respective Weiss constant of the system. The last column compares the sum of the calculated isotropic terms (a, c, h) with the experimental isotropic shift. [a] Ref. [208]. [b] Ref. [207].

		CONTACT TERMS								DIPOLAR TERMS								ISOTROPIC TERM	
		a) $g_e A^{FC}$			c) $\Delta g_{iso} A^{FC}$			d) $A^{FC} \Delta \tilde{g}$		e) $g_e \boldsymbol{A}^{dip}$			g) $\Delta g_{iso} \boldsymbol{A}^{dip}$			h) $\Delta \tilde{g} \boldsymbol{A}^{dip}$			DFT	EXP
		δ_{iso} [ppm]	$\Delta\delta$ [ppm]	η	δ_{iso} [ppm]	$\Delta\delta$ [ppm]	η	δ_{iso} [ppm]	$\Delta\delta$ [ppm]	η	δ_{iso} [ppm]	$\Delta\delta$ [ppm]	η	δ_{iso} [ppm]	$\Delta\delta$ [ppm]	η	δ_{iso} [ppm]	$\Delta\delta$ [ppm]	η	δ_{iso} [ppm]	δ_{iso} [ppm]
^{7}Li	$LiMnPO_4$	123.9	0	—	0.4	0	—	0	0.2	0.3	0	1230.6	0.2	0	0.9	0.2	-0.1	0.2	0.4	124.2	57^a, 68^b
	$LiFePO_4$	36.4	0	—	11.3	0	—	0	-4.1	0.6	0	869.6	0.2	0	73.1	0.2	-1.2	-16.8	0.7	46.5	-15^a, -8^b
	$LiCoPO_4$	-15.2	0	—	-16.5	0	—	0	4.4	0.9	0	695.7	0.2	0	120.3	0.2	-17.9	-15.4	0.1	-49.6	-92^a, -86^b
	$LiNiPO_4$	-64.6	0	—	-34.3	0	—	0	2.1	0.4	0	434.7	0.2	0	52.6	0.2	-1.1	-1.7	0.6	-100.0	-49^b, -41^a
^{31}P	$LiMnPO_4$	8877.7	0	—	26.8	0	—	0	12.0	0.3	0	1118.8	0.3	0	0.8	0.3	0	-0.1	0.7	8907.5	7296^a
	$LiFePO_4$	3419.3	0	—	1067.1	0	—	0	-445.2	0.6	0	821.9	0.5	0	69.3	0.5	-2.6	15.1	0.4	4483.8	3352^a
	$LiCoPO_4$	2132.7	0	—	1478.1	0	—	0	-400.1	0.9	0	662.7	0.4	0	121.3	0.4	-4.5	10.1	0.4	3606.3	2756^a
	$LiNiPO_4$	1821.9	0	—	853.4	0	—	0	-65.0	0.0	0	595.8	0.1	0	71.0	0.1	1.4	-3.5	0.1	2676.7	1706^a

Table A4 Comparison of the various terms contributing to the shielding tensor for the series of $LiTMPO_4$ compounds (TM= Mn, Fe, Co, Ni) at the ^{7}Li and ^{31}P sites broken down into the contact and dipolar isotropic shift (δ_{iso}, ppm), symmetric anisotropic value ($\Delta\delta$, ppm) and asymmetry parameter (η, dimensionless). The hyperfine tensor for this Table is obtained with the PBE20 hybrid functional and the g-tensor is calculated with GGA+U. Every tensorial term of the Table is reported oriented with respect to its own principal axis frame. All the reported terms are scaled by the pre-factor $-\frac{\mu_B S(S+1)}{3\hbar\gamma_N K_B (T-\Theta)}$, with the respective Weiss constant of the system. The last column compares the sum of the calculated isotropic terms (a, c, h) with the experimental isotropic shift. [a] Ref. [208]. [b] Ref. [207].

		CONTACT TERMS									DIPOLAR TERMS									ISOTROPIC TERM	
		a) $g_e A^{FC}$			c) $\Delta g_{iso} A^{FC}$			d) $A^{FC} \Delta \tilde{g}$			e) $g_e \boldsymbol{A}^{dip}$			g) $\Delta g_{iso} \boldsymbol{A}^{dip}$			h) $\Delta \tilde{g} \boldsymbol{A}^{dip}$			DFT	EXP
		δ_{iso} [ppm]	$\Delta\delta$ [ppm]	η	δ_{iso} [ppm]	$\Delta\delta$ [ppm]	η	δ_{iso} [ppm]	$\Delta\delta$ [ppm]	η	δ_{iso} [ppm]	$\Delta\delta$ [ppm]	η	δ_{iso} [ppm]	$\Delta\delta$ [ppm]	η	δ_{iso} [ppm]	$\Delta\delta$ [ppm]	η	δ_{iso} [ppm]	δ_{iso} [ppm]
^{7}Li	$LiMnPO_4$	84.8	0	—	0.3	0	—	0	10.1	0.3	0	1240.1	0.2	0	-1.1	0.5	-0.1	0.2	0.3	84.6	57[a], 68[b]
	$LiFePO_4$	10.6	0	—	1.4	0	—	0	0.9	0.6	0	886.6	0.2	0	27.9	0.2	-3.2	9.0	0.7	8.8	-15[a], -8[b]
	$LiCoPO_4$	-25.9	0	—	-6.8	0	—	0	0.9	0.9	0	709.3	0.2	0	46.2	0.2	2.6	-5.5	0.1	-30.10	-92[a], -86[b]
	$LiNiPO_4$	-64.7	0	—	-17.4	0	—	0	1.1	0.4	0	443.8	0.2	0	36.2	0.1	0.3	-0.8	0.6	-81.8	-49[b], -41[a]
^{31}P	$LiMnPO_4$	7515.8	0	—	22.7	0	—	0	10.1	0.3	0	1099.3	0.2	0	0.8	0.2	-0.1	-0.1	0.8	7538.4	7296[a]
	$LiFePO_4$	2806.1	0	—	378.4	0	—	0	246.1	0.6	0	781.9	0.4	0	26.4	0.4	-2.4	7.8	0.2	3182.1	3352[a]
	$LiCoPO_4$	1784.8	0	—	465.4	0	—	0	-62.3	0.9	0	636.4	0.3	0	41.5	0.3	-0.5	2.5	0.8	2249.7	2756[a]
	$LiNiPO_4$	1235.0	0	—	331.6	0	—	0	-20.2	0.4	0	539.5	0.1	0	36.2	0.1	0.5	-1.0	0.2	1567.1	1706[a]

Table A5 Comparison of the various terms contributing to the shielding tensor for the series of $LiTMPO_4$ compounds (TM= Mn, Fe, Co, Ni) at the ^{7}Li and ^{31}P sites broken down into the contact and dipolar isotropic shift (δ_{iso}, ppm), symmetric anisotropic value ($\Delta\delta$, ppm) and asymmetry parameter (η, dimensionless). The hyperfine tensor for this Table is obtained with the PBE35 hybrid functional and the g-tensor is calculated with GGA+U. Every tensorial term of the Table is reported oriented with respect to its own principal axis frame. All the reported terms are scaled by the pre-factor $-\frac{\mu_B S(S+1)}{3\hbar\gamma_N K_B(T-\Theta)}$, with the respective Weiss constant of the system. The last column compares the sum of the calculated isotropic terms (a, c, h) with the experimental isotropic shift. [a] Ref. [208]. [b] Ref. [207].

Appendix B

B1 ^{7}Li MAS NMR Spectra of the $LiFePO_4$ Single Crystals

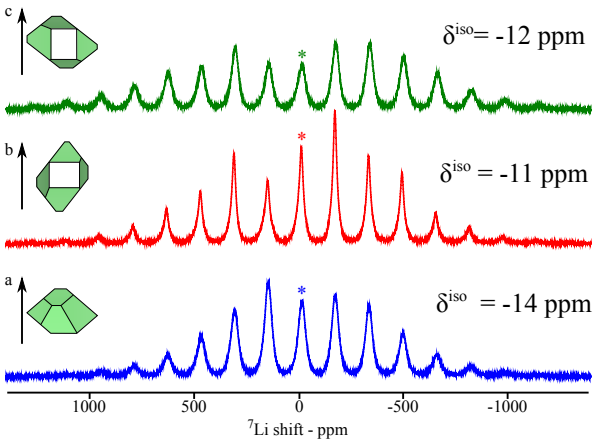

Fig. B1 Experimental ^{7}Li NMR spectra of the $LiFePO_4$ single crystals 1 oriented with the *a*-, *b*- and *c*-axis aligned along the magic angle (blue, red and green spectrum, respectively).

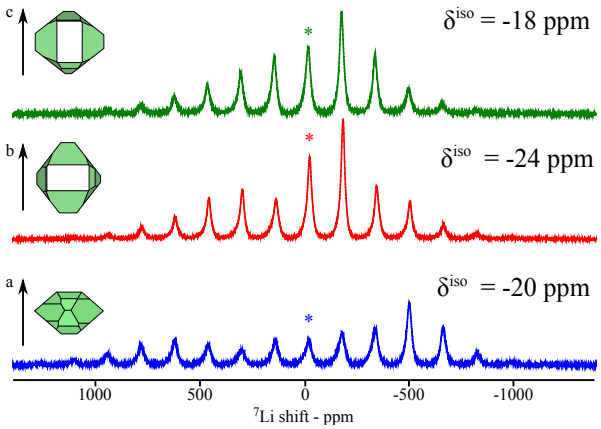

Fig. B2 Experimental ^{7}Li NMR spectra of the $LiFePO_4$ single crystals 2 oriented with the *a*-, *b*- and *c*-axis aligned along the magic angle (blue, red and green spectrum, respectively).

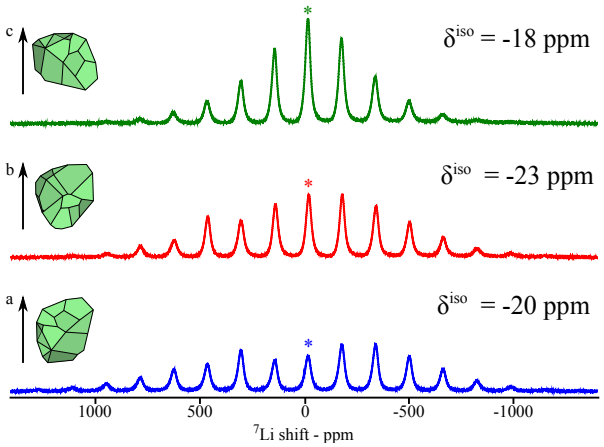

Fig. B3 Experimental ^{7}Li NMR spectra of the $LiFePO_4$ single crystals 3 oriented with the *a*-, *b*- and *c*-axis aligned along the magic angle (blue, red and green spectrum, respectively).

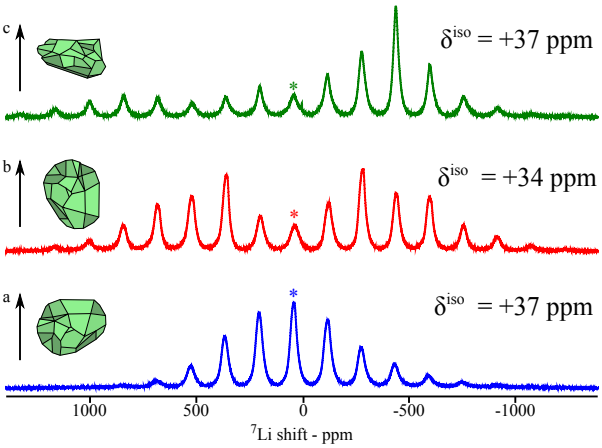

Fig. B4 Experimental ^{7}Li NMR spectra of the $LiFePO_4$ single crystals 4 oriented with the *a*-, *b*- and *c*-axis aligned along the magic angle (blue, red and green spectrum, respectively).